Dissertation

submitted to the

Combined Faculty of the Natural Sciences and Mathematics

of the Ruperto Carola University Heidelberg, Germany

for the degree of

Doctor of Natural Sciences

Presented by

M.Sc. Laura Armbruster

born in: Wolfach

Oral examination: 25th of May 2022

The N^{α}-acetyltransferase NAA50 regulates fertility and stress responses in *Arabidopsis thaliana*

Referees:

Prof. Dr. Rüdiger Hell

Prof. Dr. Irmgard Sinning

Abstract

Even though N^{α}-terminal acetylation (NTA) is conserved throughout the three domains of life, knowledge about its biological function remains limited. In *Arabidopsis thaliana*, NTA affects up to 80 % of all soluble cytosolic proteins and is catalyzed by a set of N^{α}-terminal acetyltransferases (NatA-G). *At*NatA is the major Nat complex and targets approximately 40 % of the plant proteome. The core *At*NatA complex consists of the catalytic subunit *At*NAA10 and the ribosome-binding subunit *At*NAA15.

In humans, this complex associates with the regulatory subunits *Hs*NAA50 and *Hs*HYPK to form the quaternary *Hs*NatA/E complex. Recently, homologs of NAA50 (AT5G11340) and HYPK (AT3G06610) were identified in *A. thaliana*. While *At*HYPK is tethered to the core *At*NatA complex and modulates its activity, the interaction of *At*NAA50 with *At*NatA is still controversially discussed.

This work provides evidence for the association of *At*NAA50 with the core *At*NatA components and the ribosome. *At*NAA50 was found in the proximity of *At*NAA10, *At*NAA15 and *At*HYPK *in vivo*. Co-immunoprecipitation experiments independently confirmed these findings and suggested novel potential binding partners of *At*NAA50.

Unlike *At*HYPK, *At*NAA50 did not modulate *At*NatA activity. This was evidenced by the absence of significant shifts in the NTA yield of known NatA substrates in NAA50-depleted mutants. In line with this finding, the depletion of *At*NAA50 did not impact NatA-mediated proteome stability, either. Nevertheless, *At*NAA50 seemed to exert a critical NatA-independent biological function since its knockout resulted in severe growth retardation and infertility.

The generation of *aminaa50* knockdown mutants revealed that minimal amounts of *At*NAA50 were sufficient to ensure proper plant growth. Global transcriptome and proteome analyses of the mutants showed that the depletion of *At*NAA50 caused a constitutive upregulation of the plant defense response against pathogens. In line with this finding, *aminaa50* plants were resistant to the bacterium *Pseudomonas syringae*. However, the abundance of phytohormones that usually trigger this resistance was not increased in *aminaa50*. Apart from its role in vegetative growth and the regulation of plant defense, complementation studies suggested that NAA50 was required for pollen formation.

In summary, this thesis demonstrates that even though *At*NAA50 interacted with the core *At*NatA complex, it executed functions beyond regulating *At*NatA activity.

Zusammenfassung

Obwohl die N^{α}-terminale Acetylierung (NTA) in allen drei Domänen des Lebens konserviert ist, ist das Wissen um ihre biologische Funktion begrenzt. In *Arabidopsis thaliana* betrifft die NTA bis zu 80 % der löslichen zytosolischen Proteine und wird von N^{α}-terminalen Acetyltransferasen (NatA-G) katalysiert. *At*NatA, der wichtigste Nat-Komplex, acetyliert etwa 40 % des pflanzlichen Proteoms. Der *At*NatA-Kernkomplex besteht aus der katalytischen Untereinheit *At*NAA10 und der Ribosomen-bindenden Untereinheit *At*NAA15.

Im Menschen bindet NatA an die regulatorischen Untereinheiten *Hs*NAA50 und *Hs*HYPK und bildet so den quaternären *Hs*NatA/E-Komplex. Kürzlich wurden Homologe von NAA50 (AT5G11340) und HYPK (AT3G06610) in *A. thaliana* identifiziert. Während HYPK an den *At*NatA-Kernkomplex gebunden ist und dessen Aktivität moduliert, wird die Interaktion von *At*NAA50 mit *At*NatA kontrovers diskutiert.

Diese Arbeit liefert Hinweise auf eine Verbindung von *At*NAA50 mit dem Ribosom und den *At*NatA Kernkomponenten. *At*NAA50 wurde *in vivo* in der Nähe von *At*NAA10, *At*NAA15 und *At*HYPK gefunden. Ein Immunopräzipitationsexperiment bestätigte diesen Befund unabhängig und ließ auf neue potenzielle Bindungspartner von *At*NAA50 schließen.

Im Gegensatz zu HYPK modulierte *At*NAA50 die NatA-Aktivität nicht. Dies wurde durch die Abwesenheit größerer Verschiebungen in der NTA-Ausbeute bekannter NatA-Substrate in *naa50* Mutanten belegt. In Übereinstimmung mit diesem Ergebnis hatte die Abreicherung von *At*NAA50 keinen Einfluss auf die NatA-vermittelte Proteomstabilität. Dennoch scheint *At*NAA50 eine wichtige NatA-unabhängige Funktion auszuüben, da der Verlust von *At*NAA50 zu einer schweren Wachstumsverzögerung und Unfruchtbarkeit führte.

Die Erzeugung von *aminaa50* Knockdown-Mutanten zeigte, dass minimale Mengen von *At*NAA50 ausreichten, um ein normales Pflanzenwachstum zu gewährleisten. Globale Transkriptom- und Proteomanalysen belegten eine konstitutive Aktivierung der pflanzlichen Pathogenabwehr in *aminaa50*. Im Einklang mit diesem Ergebnis waren die Pflanzen resistent gegenüber dem Bakterium *Pseudomonas syringae*. Die Abundanz von Hormonen, die diese Resistenz häufig auslösen, war in den Mutanten jedoch nicht erhöht.

Abgesehen von seiner Rolle beim vegetativen Wachstum und der Regulierung der Pflanzenabwehr legen Komplementationsstudien nahe, dass *At*NAA50 für die Pollenbildung erforderlich ist.

Zusammenfassend belegt diese Arbeit, dass *At*NAA50 zwar mit dem *At*NatA-Komplex interagiert, aber auch NatA-unabängige Funktionen ausübt.

Contents

List of abbreviations

35Sp	cauliflower mosaic virus 35S promotor
A. thaliana	*Arabidopsis thaliana*
A. tumefaciens	*Agrobacterium tumefacines*
ABA	abscisic acid
AcCoA	acetyl-coenzyme A
aminaa10	knockdown mutant of NAA10
aminaa15	knockdown mutant of NAA15
aminaa50	knockdown mutant of NAA50
AmpR	ampicillin resistance
At	*Arabidopsis thaliana*
BastaR	glufosinate ammonium resistance
bp	base pair
BSA	bovine serum albumin
cDNA	complementary DNA
Co-IP	co-immunoprecipitation
cpm	counts per minute
DAPI	4',6-diamidino-2-phenylindole
DNA	deoxyribonucleic acid
dNTP	deoxyribonucleotide triphosphate
DTT	dithiothreitol
E. coli	*Escherichia coli*
EDTA	ethylenediaminetetraacetic acid
ETI	effector-triggered immunity
EGTA	triethylene glycol diamine tetraacetic acid
eYFP	enhanced yellow fluorescent protein
FW	fresh weight
gDNA	genomic DNA
GFP	green fluorescent protein
GO Term	gene ontology term
H.a. Noco 2	*Hyaloperonospora arabidopsidis* Noco 2
HEPES	4-(2-hydroxyethyl)-1-piperazineethanesulfonic acid
Hs	*Homo sapiens*
HYPK	huntingtin yeast partner K

hypk-3	knockout of HYPK line 3
iMet	initiator methionine
IPTG	isopropyl-βD-1-thiogalactopyranoside
JA	jasmonic acid
JA-Ile	7-iso-jasmonoyl-L-isoleucine
KanR	kanamycin resistance
kDa	kilodalton
LC	loading control
LC-MS/MS	liquid chromatography-tandem mass-spectrometry
MES	4-morpholineethanesulfonic acid
MetAP	methionine aminopeptidase
miRNA	micro RNA
mRNA	messenger RNA
MS	mass-spectrometry
MS medium	Murashige Skoog medium
muse6	mutant with point mutation in the *NAA15* gene
N. benthamiana	*Nicotiana benthamiana*
NAA10	N$^{\alpha}$-terminal acetyltransferase 10
NAA15	N$^{\alpha}$-terminal acetyltransferase 15
NAA20	N$^{\alpha}$-terminal acetyltransferase 20
NAA25	N$^{\alpha}$-terminal acetyltransferase 25
NAA30	N$^{\alpha}$-terminal acetyltransferase 30
NAA40	N$^{\alpha}$-terminal acetyltransferase 40
NAA50	N$^{\alpha}$-terminal acetyltransferase 50
NAA50p	NAA50 promoter
NAA60	N$^{\alpha}$-terminal acetyltransferase 60
NAA70	N$^{\alpha}$-terminal acetyltransferase 70
NAA80	N$^{\alpha}$-terminal acetyltransferase 80
NatA	N$^{\alpha}$-terminal acetyltransferase complex A
NatB	N$^{\alpha}$-terminal acetyltransferase complex B
NatC	N$^{\alpha}$-terminal acetyltransferase complex C
NatD	N$^{\alpha}$-terminal acetyltransferase complex D
NatE	N$^{\alpha}$-terminal acetyltransferase complex E
NatF	N$^{\alpha}$-terminal acetyltransferase complex F
NatG	N$^{\alpha}$-terminal acetyltransferase complex G
NatH	N$^{\alpha}$-terminal acetyltransferase complex H
NES	nuclear export sequence

NLS	nuclear localization sequence
NLR	nucleotide-binding leucine-rich-repeat containing receptor
NTA	N^{α}-terminal acetylation
OAS-TL A	*O*-acetylserine(thio)lyase A
OD	optical density
OPDA	12-oxophytodienoic acid
PAGE	polyacrylamide gel electrophoresis
PAMP	pathogen-associated molecular pattern
PCR	polymerase chain reaction
PMSF	phenylmethylsulfonylfluorid
PRR	pathogen-recognition receptor
P. syringae	*Pseudomonas syringae*
PTI	pattern-triggered immunity
PVDF	polyvinylidene difluoride
qRT-PCR	quantitative real-time PCR
RNA	ribonucleic acid
ROS	reactive oxygen species
RPM1	resistance to *P. syringae pv maculicola* 1
RT	room temperature
S. cerevisiae	*Saccharomyces cerevisiae*
SA	salicylic acid
SDS	sodium dodecyl sulfate
SE	standard error
SMC3	structural maintenance of chromosomes 3
SNC1	suppressor of NPR1-1, constitutive 1
SYN4	sister chromatid cohesion 1 protein 4
TAIR	The Arabidopsis Information Resource
tDNA	transfer DNA
TEMED	tetramethylethylenediamine
UPS	ubiquitin-proteasome system
UBQ11	ubiquitin 11
UV	ultraviolet
v/v	volume per volume
w/v	weight per volume
WT	wildtype

1. Introduction

1.1 Protein N^{α}-terminal acetylation (NTA)

Chemical modifications determine key characteristics of proteins, such as their activity, half-life, and localization within the cell. Together with phosphorylation and ubiquitination, acetylation ranges among the most frequent and influential protein processing events (Mann & Jensen, 2003). Acetyl moieties can be transferred from acetyl coenzyme A to the α-amino group of protein N-termini or the ϵ-amino group of internal lysine residues (Fig. 1). These reactions are conserved throughout all kingdoms of life and are catalyzed by various N^{α}-terminal acetyltransferases (Nats) and lysine acetyltransferases (Kats).

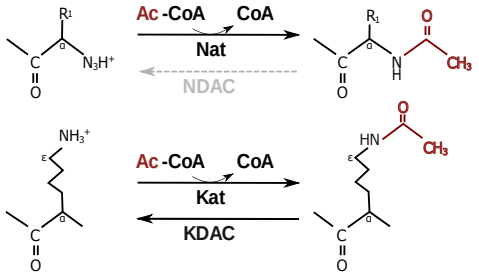

Figure 1: Protein N^{α}- and N^{ϵ}-terminal acetylation. Acetylation can occur at the N-terminus (upper panel) or the internal lysine residues (lower panel) of proteins. N^{α}-terminal acetylation (NTA) is catalyzed by N^{α}-terminal acetyltransferases (Nats). Up to date, no N^{α}-terminal deacetylase (NDAC) has been identified. Hence NTA is thought to be irreversible. Lysine ϵ-acetylation (KAT), however, is catalyzed by lysine acetyltransferases (Kats) and can be reversed by lysine deacetylases (KDACs). Modified from Ree et al., 2018.

While lysine ϵ-acetylation (KAT) is a tightly regulated, reversible post-translational process, N^{α}-terminal acetylation (NTA) is considered irreversible and occurs mainly co-translationally (Bienvenut et al., 2020).

In eukaryotes, NTA is one of the most abundant protein modifications, affecting 80-90 % of soluble proteins in humans and plants, as well as 70-80 % of the fruit fly and 50-60 % of

the yeast proteome (Arnesen et al., 2009; Goetze et al., 2009; Bienvenut et al., 2012). With 20 and 5 % respectively, the degree of acetylation is significantly lower in unicellular prokaryotes such as archaea and eubacteria (Falb et al., 2006; Soppa, 2010). In line with these observations, large-scale proteome analyses of various organisms demonstrate that NTA frequency increases with organismal complexity (Van Damme et al., 2011, 2012; Aksnes et al., 2015).

Despite the prevalence of NTA in higher eukaryotes, the overall significance of the protein modification remains enigmatic. For individual proteins, effects of acetylation on protein-protein interaction (Singer & Shaw, 2003), subcellular localization (Behnia et al., 2004), protein turnover (Hwang et al., 2010) and folding (Trexler & Rhoades, 2012), as well as aggregation (Arnesen et al., 2010) have been demonstrated. Consequently, during the last decade, NTA has emerged as a central regulator of protein fate.

1.1.1 Composition and substrate specificity of the N$^{\alpha}$-terminal acetyltransferase (Nat) complexes NatA-H

Up to date, eight Nat complexes (NatA-H) have been characterized in eukaryotes (Fig. 2). Each complex comprises one catalytic and up to two facultative auxiliary subunits (Aksnes et al., 2015, 2019). Whereas NatA-E are anchored to the ribosome via their auxiliary subunits and co-translationally acetylate nascent polypeptide chains protruding from the ribosome exit tunnel, NatF-NatH are monomeric and operate post-translationally. All eight Nat complexes share a conserved acetyl-CoA binding motif (Q/RxxGxG/A) and belong to the family of GNAT-acetyltransferases (Neuwald & Landsman, 1997; Polevoda & Sherman, 2003). The substrate specificity of the Nats is mainly determined by the first two amino acids of their substrates. The extent of NTA varies between proteins, ranging from infrequent to complete acetylation. Except for the selective Nats (NatD and NatH), the substrate specificity of Nats is broad and, in some cases, overlapping. The two major Nats NatA and NatB together acetylate 50 % of the human (Bienvenut et al., 2012; Van Damme et al., 2012) or 77 % of the plant proteome (Linster et al., 2015; Linster & Wirtz, 2018). NatA targets N-termini starting with small amino acids (A, S, T, C, V, or G), which are exposed due to removal of the initiator methionine (iMet) by methionine aminopeptidases (Mullen et al., 1989; Arnesen et al., 2005; Liszczak et al., 2013; Linster et al., 2015). NatB on the contrary acetylates the iMet of N-termini starting with MD, ME, MN, and MQ (Starheim et al., 2008; Van Damme et al., 2012; Huber et al., 2020). By targeting, among others, N-termini starting

with ML, MI, MF, MY or MK, NatC, NatE, and NatF accept a wider range of substrates (Polevoda et al., 1999; Van Damme et al., 2011; Aksnes et al., 2015; Van Damme et al., 2015, 2016). Despite the considerable overlap between the substrate specificities of NatC, NatE, and NatF, the enzymes acetylate separate substrate pools due to their diverging subcellular localization. Whereas NatC and NatE are attached to the ribosome, NatF resides at the Golgi apparatus in humans (Aksnes et al., 2015; Van Damme et al., 2015) and the plasma membrane in plants (Linster et al., 2020).

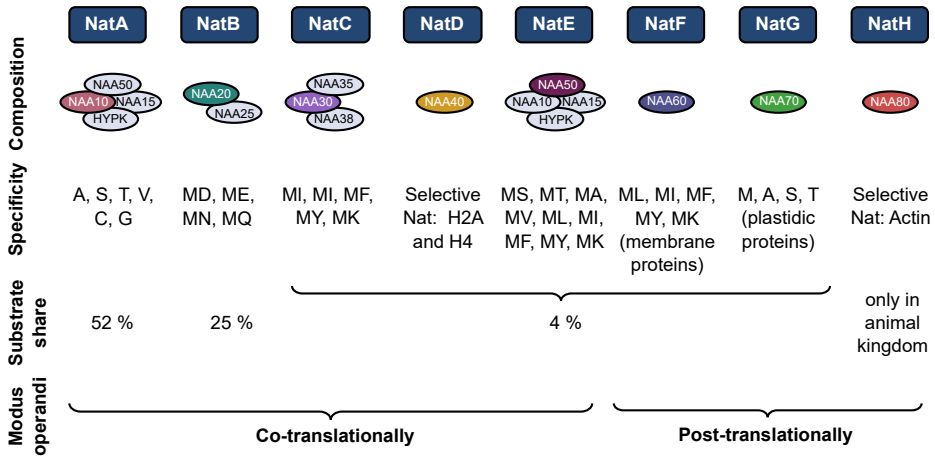

Figure 2: Composition and substrate specificity of the eight eukaryotic Nat complexes. Each Nat consists of one catalytic (dark colors) and up to two auxiliary subunits (grey). The auxiliary subunits attach the Nats to the ribosome and/or mediate their activity and substrate specificity (second row). The substrate specificity of the Nats is determined by the first two amino acids of their substrates (third row). While NatC-G together acetylate only 4 % of the plant proteome, the major Nats NatA and NatB catalyze the acetylation of 52 and 25 % of plant proteins, respectively (fourth row). Unlike NatA-E, which operate co-translationally, NatF-H catalyze NTA in a post-translational manner (fifth row). Modified from Aksnes et al. (2019).

Given the conserved composition and substrate specificity of the ribosome-associated Nats (NatA-E), it was long assumed that Nat diversification had not occurred during the evolution of eukaryotes (Rathore et al., 2016). This dogma was recently called into question by the identification of a highly diversified family of plant-specific post-translationally acting Nats with dual Kat/Nat activity in the chloroplasts of *Arabidopsis thaliana* (Dinh-Van, 2013; Koskela et al., 2018; Bienvenut et al., 2020; Giglione & Meinnel, 2021). The diversification of the post-translational Nat machinery during the evolution of eukaryotes is further evidenced by the previously mentioned diverging localization and concomitant function of NatF in humans and plants and the existence of the animal-specific NatH.

1.1.2 The biological role of the individual Nat complexes

1.1.2.1 NatA/E

In terms of substrate numbers, the NatA complex is the main N$^{\alpha}$-acetyltransferase in higher eukaryotes. It catalyzes the acetylation of 52 % of the human, 36 % of the yeast, and 52 % of the plant proteome (Van Damme et al., 2011; Linster et al., 2015; Aksnes et al., 2016). The core NatA complex consists of the catalytic subunit NAA10 and the auxiliary subunit NAA15, which tethers the complex to the ribosome.

Both proteins are conserved among eukaryotes, and their expression is often co-regulated (Gautschi et al., 2003; Linster et al., 2015; Rathore et al., 2016; Magin et al., 2017). As a monomer, NAA10 post-translationally targets the α-amino groups of proteins with N-terminal D or E residues (Van Damme et al., 2011; Foyn et al., 2013). As a catalytic subunit of the NatA complex, however, NAA10 co-translationally acetylates N-termini starting with small amino acids (A, S, T, C, V or G; Fig. 2). This shift in substrate specificity results from conformational changes induced by the binding of NAA10 to NAA15 (Liszczak et al., 2013).

Decreased NatA activity has been linked to neurodegenerative disorders and developmental impairments in humans (Rope et al., 2011; Esmailpour et al., 2014; Casey et al., 2015; Popp et al., 2015). The first reported example of a human disease caused by a mutation in NatA was Ogden syndrome. The missense mutation in NAA10 (Ser37Pro) reduces NatA activity and translates into a global developmental delay, heart anomalies, and premature death (Rope et al., 2011). Overexpression of NatA, in turn, is associated with various types of tumor diseases, including breast, colon, liver, lung, and prostate cancer. In many cases, the degree of NatA overexpression correlates with the severity of the disease (Wang et al., 2011; Shim et al., 2012; Kuhns et al., 2018). The importance of NatA activity for human cell viability is further underscored by the fact that a knockdown of any of the two core NatA subunits induces cell cycle arrest and ultimately cell death in HeLa cells (Fisher et al., 2005; Arnesen et al., 2006; Lim et al., 2006). In contrast to human cell lines, yeast NatA null-mutants are viable. Nevertheless, they display a variety of defects, including impaired sporulation, decreased growth rates, and increased sensitivity to heat or high salinity (Mullen et al., 1989).

In plants, NatA activity is essential. Whereas a knockout of NAA10 (AT5G13780) or NAA15 (AT1G80410) results in embryo lethality (Feng et al., 2016), a knockdown of either protein leads to perturbations in plant development, such as decreased plant growth

or delayed bolting and flowering (Linster et al., 2015). Interestingly, the transgenic downregulation of NatA induces drought tolerance in *Arabidopsis thaliana*. This remarkable phenotype can be attributed to the enhanced primary root growth and constitutively decreased stomatal aperture of NatA mutants. While it is unclear how NTA regulates primary root growth and stomatal aperture, it is well established that both traits are controlled by the canonical drought stress signaling hormone abscisic acid (ABA). In wildtype plants, the application of exogenous ABA leads to a decrease in NatA expression, providing the first evidence of hormonal control of NTA (Linster et al., 2015). This dynamic control of NTA might constitute an adaptation to the sessile lifestyle of plants that forces them to cope with highly variable adverse environmental conditions (Linster et al., 2020). For additional information on NTA and its implications for plant abiotic stress responses, refer to chapter 1.2.

On the molecular level, NatA-mediated NTA has recently been identified as a crucial factor in controlling protein stability (Timms et al., 2019; Mueller et al., 2021; Linster et al., 2022). In Arabidopsis, the downregulation of NatA activity results in an increased turnover of NatA substrates via the ubiquitin-proteasome system (UPS), suggesting a protective role of NatA-mediated NTA against protein degradation. By masking N-degrons and preventing the ubiquitination of proteins, co-translational NTA via NatA promotes proteome stability and determines the half-life time of proteins when they are synthesized (Linster et al., 2022). The recent identification of E3 ubiquitin ligases, which specifically target non-acetylated NatA substrates in humans, suggests that this novel N-degron pathway is conserved among eukaryotes (Timms et al., 2019; Mueller et al., 2021). This notion is further supported by the fact that yeast NatA mutants display elevated UPS activity, as evidenced by the increased expression of several E3 ligases and the transcription factor RPN4, which acts as a master regulator of proteasome subunits (Kats et al., 2022). While in humans and yeast, E3 ligases specifically targeting NatA substrates with free N-termini have already been characterized, the identification of such enzymes in plants is still pending.

In both humans and plants, the core NatA complex can be joined by an additional subunit termed HYPK (Arnesen et al., 2010; Miklankova, 2019). HYPK is an intrinsically disordered protein that exerts chaperone activity *in vitro* and *in vivo* (Raychaudhuri et al., 2008). It preferentially interacts with aggregation-prone proteins and was initially identified as an interaction partner of the Huntingtin protein. Mutated Huntingtin is the cause of Huntington's disease, a hereditary neurodegenerative disorder (Faber et al., 1998). HYPK not only prevents the aggregation of Huntingtin but also reduces the load of toxic aggregates by

isolating them in sequestration complexes (Ghosh et al., 2018). In addition to Huntingtin, HYPK interacts with proteins involved in protein folding, the response to unfolded proteins, and cell cycle arrest (Choudhury et al., 2012). As previously observed for the knockdown of the core NatA subunits (Fisher et al., 2005; Arnesen et al., 2006; Lim et al., 2006), a knockdown of HYPK induces cell cycle arrest and apoptosis in HeLa cells, suggesting that the presence of HYPK is required for proper NatA function (Arnesen et al., 2010). Indeed, the known NatA substrate PCNP is acetylated less frequently in the absence of HYPK *in vivo* (Arnesen et al., 2010). Interestingly, HYPK exhibits an opposing role *in vitro* as suggested by acetylation assays using cognate NatA substrates (Weyer et al., 2017; Gottlieb & Marmorstein, 2018; Deng et al., 2020). In line with this assumption, the cryo-EM structure of the human NatA/HYPK complex shows that HYPK inhibits NAA10 activity through structural alterations of the NAA10 substrate-binding site (Deng et al., 2020).

While HYPK is absent in yeast (Weyer et al., 2017), the chaperone-like protein is conserved in most other fungi and plants (Macharia et al., 2019; Miklankova, 2019; Gong et al., 2022). Unlike the core NatA subunits, HYPK is dispensable in plants. Similar to the phenotype observed for NAA10 or NAA15 knockdown plants, a knockout of HYPK (AT3G06610) results in reduced growth as well as delayed bolting and flowering in Arabidopsis (Miklankova, 2019). In general, HYPK seems to be a positive regulator of NatA activity in plants since a loss of HYPK decreases NatA activity in both rice and Arabidopsis. In line with this finding, the protein turnover of canonical NatA substrates is increased in loss-of-HYPK mutants of both species (Gong et al., 2022; Miklankova, 2019).

The ternary NatA-HYPK complex can associate with the additional subunit NAA50 to form the tetrameric NatA/E complex (Arnesen et al., 2006). In humans, binding of HYPK and NAA50 to the core NatA complex is competitive. While HYPK and NAA50 make contact with both core NatA subunits, no direct interactions are observed between NAA50 and HYPK (Deng et al., 2019, 2020). In agreement with these findings and the absence of HYPK in yeast, yeast NAA50 resides exclusively at the NatA complex, whereas only 20 % of human NAA50 is found in complex with NAA10 and NAA15 (Gautschi et al., 2003; Hou et al., 2007). Up to date, it is unclear whether *At*NAA50 (AT5G11340) associates with the core NatA complex in *Arabidopsis thaliana* (Armbruster et al., 2020; Neubauer & Innes, 2020). While in yeast two-hybrid experiments, a weak interaction between *At*NAA15 and *At*NAA50 is observed (Weidenhausen et al., 2021), *At*NAA50 does not co-precipitate with *At*NAA10 or *At*NAA50 during *in vivo* protein immunoprecipitation experiments (Feng et al., 2020).

In both humans and plants, NAA50 catalyzes the acetylation of N-termini starting with MS, MT, MA, MV, ML, MI, MF, MY, and MK through a tyrosine and a histidine residue which together coordinate a catalytically important water molecule (Evjenth et al., 2012; Gottlieb & Marmorstein, 2018; Aksnes et al., 2019; Weidenhausen et al., 2021). The mutation of any of those residues results in a loss of enzymatic activity. Even though yeast NAA50 can bind acetyl-CoA, it lacks the aforementioned catalytically important residues and is, in consequence, inactive (Weidenhausen et al., 2021). In line with this view, the knockout of NAA50 in yeast does not affect the acetylation yield of proteins classified as typical NAA50 substrates based on the substrate specificity of human NAA50. Remarkably, the acetylation yield of six known NatA substrates is substantially decreased in yeast loss-of-NAA50 function mutants, indicating a positive regulatory impact of NAA50 on NatA activity in yeast (Van Damme et al., 2015). This hypothesis is supported by structural analyses of the *Sc*NatA/NAA50 complex. Cryo-electron microscopy demonstrates that yeast NAA15 and NAA50 physically interact with rRNA expansion segments to position NAA10 at the ribosome exit tunnel, which facilitates the acetylation of nascent polypeptides (Gautschi et al., 2003; Deng et al., 2019; Knorr et al., 2019; Weidenhausen et al., 2021).

Contrary to the positive impact of NAA50 on NatA activity observed in yeast, *in vitro* assays with human NatA/E components suggest that human NAA50 inhibits NatA activity *in vitro* through structural alteration of the NAA10 substrate binding site (Deng et al., 2019). Interestingly, a knockdown of NAA10 results in decreased NTA of nine putative NAA50 substrates in human cell lines, implicating NAA10 as a positive regulator of NAA50 activity *in vivo* (Van Damme, 2021).

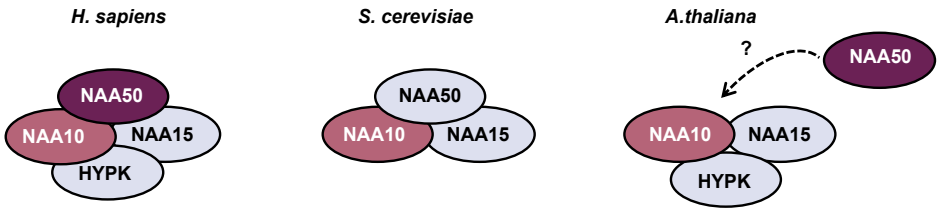

Figure 3: Differences in the composition of the NatA/E complex between humans, yeast, and plants. The NatA/E complex shows the most extensive species-specific variation of all cytosolic Nats identified at present (Weidenhausen et al., 2021). While the NatA/E subunits NAA10, NAA15, NAA50, and HYPK are conserved between humans and plants, HYPK is absent in yeast. Whether NAA50 associates with the core NatA complex in Arabidopsis remains unclear (indicated by a dashed arrow and question mark). In contrast to yeast NAA50, human and plant NAA50 display enzymatic activity. Catalytically active proteins are marked in shades of red.

The NatA/E complex shows the most extensive species-specific variation of all cytosolic Nats identified at present (Fig. 3). While a loss-of-NAA50 in yeast does not result in any phenotype (Gautschi et al., 2003), depletion of human NAA50 causes premature sister chromatid separation in HeLa cell lines (Hou et al., 2007). For additional information on this phenotype, refer to chapter 1.3. In plants, NAA50 is essential for proper development and fertility (Armbruster et al., 2020; Feng et al., 2020; Neubauer & Innes, 2020). While a loss of the core NatA subunits NAA10 or NAA15 arrests embryo development at the globular stage in *Arabidopsis thaliana* (Linster et al., 2015; Feng et al., 2016), NAA50 knockout lines finish embryo development only to terminate growth after the development of the first few leaves. In rare cases, NAA50 knockout plants can flower but even then, they do not produce viable seeds (Armbruster et al., 2020; Feng et al., 2020; Neubauer & Innes, 2020). The growth retardation of NAA50 knockout plants can be rescued by complementation with human but not yeast NAA50, suggesting that the conserved enzymatic activity and substrate specificity of human and plant NAA50 is required for complementation (Armbruster et al., 2020).

Aside from their roles as N$^{\alpha}$-terminal acetyltransferases, NAA10 and NAA50 both may undergo auto-acetylation and subsequently display lysine ϵ-acetyltransferase activity towards a variety of substrates (Jeong et al., 2002; Lim et al., 2006; Shin et al., 2009; Ji Hae et al., 2010; Armbruster et al., 2020; Neubauer & Innes, 2020; Vo et al., 2020). In the case of NAA10, this finding was long discussed controversially since crystal structures suggested that the gate of the NAA10 catalytic pocket was too narrow to fit lysine residues (Arnesen et al., 2005; Magin et al., 2016). However, a recent study demonstrated that in human cell lines, a novel oxygen-sensing process determines the substrate specificity of NAA10. Depending on oxygen availability, NAA10 can be hydroxylated. This modification results in structural changes that widen the gate at the catalytic pocket, allowing for the entrance of lysine residues (Kang et al., 2018).

Furthermore, NAA10 has been implicated in transcriptional regulation. In human cell lines, NAA10 recruits a DNA methyltransferase to the non-methylated E-cadherin promoter, thereby contributing to the silencing of the E-cadherin gene (Lee et al., 2010). In line with its role as a transcriptional regulator, NAA10 localizes to the cytosol and the nucleus of human cells (Arnesen et al., 2006). Similar to NAA10, NAA50 has been observed to localize to the nucleus of human cell lines. Even though both human and plant NAA50 have been reported to acetylate internal lysine residues of the human histone H4 protein *in vitro* (Evjenth et al., 2009; Armbruster et al., 2020; Neubauer & Innes, 2020), no endogenous Nat

or Kat substrates of *At*NAA50 have been identified up to date. Hence the physiological role of NAA50 in plants remains unclear.

1.1.2.2 **NatB**

The NatB complex is conserved among eukaryotes and consists of the catalytic subunit NAA20 and the ribosome-binding subunit NAA25. In humans, yeast, and plants, NatB catalyzes the acetylation of N-termini which retain their iMet followed by the acidic residues D, E, Q, or N (Polevoda et al., 2003; Polevoda & Sherman, 2003; Van Damme et al., 2012; Huber et al., 2020).

In humans, altered NatB expression is associated with various pathologies. An overexpression of NatB, for instance, is linked to hepatocellular carcinoma progression (Ametzazurra et al., 2008; Neri et al., 2017). By acetylating the kinase LKB1, which targets and inactivates a negative regulator of target of rapamycin (TOR), NatB indirectly promotes cell growth through the TOR signaling pathway (Jung et al., 2020). Moreover, depletion of NatB might play an indirect role in the pathogenesis of Parkinson's disease, since NatB-mediated NTA increases the stability of the neuronal protein α-synuclein and reduces its capacity to aggregate (Maltsev et al., 2012; Dikiy & Eliezer, 2014; Iyer et al., 2016; Mason et al., 2016; Fernandez & Lucas, 2018; Watson & Lee, 2019). Misfolding and aggregation of α-synuclein are characteristic of Parkinson's disease (Henderson et al., 2019; Runfola et al., 2020; Vinueza-Gavilanes et al., 2020).

On the molecular level, depletion of NatB results in defects in actin cytoskeleton formation, cell cycle progression, and cell proliferation of human cell lines (Ametzazurra et al., 2008; Starheim et al., 2008; Ametzazurra et al., 2009; Neri et al., 2017). Similarly, in yeast, deletion of NAA20 or NAA25 causes slower growth, abnormal actin cable formation, as well as defective mitochondrial division and vacuolar segregation (Polevoda & Sherman, 2003; Singer & Shaw, 2003). In addition, *Sc*NatB mutants are more susceptible to various stresses, including high temperature and DNA damage. These phenotypes can at least partially be attributed to the lack of NatB-mediated NTA of the actin N-terminus (MDSE-) in NatB mutants (Polevoda et al., 2003; Van Damme et al., 2012).

In plants, orthologous proteins of the NatB subunits NAA20 (AT1G03150) and NAA25 (AT5G58450) have been identified (Bienvenut et al., 2012; Ferrández-Ayela et al., 2013; Huber et al., 2020). Depletion of any of the two NatB subunits results in defects in embryo development and a substantial growth reduction (Ferrández-Ayela et al., 2013; Huber et al.,

2020). In addition to plant development, NatB mediates various stress responses, including the defense against pathogens and the adaptation to salt and osmotic stress (Xu et al., 2015; Huber et al., 2020). Moreover, NatB mutants are hypersensitive to the reductive agent dithiothreitol (DTT) due to a constitutive over-reduction of their cytosol. The cause of this overreduction remains to be elucidated (Huber et al., 2022).

Like NatA-mediated NTA, acetylation via NatB alters the stability of individual stress-related proteins in plants, such as the transcriptional regulator Sigma Factor Binding Protein 1 (SIB1) and several amincyclopropane-1-carboxylate oxidases (ACOs). While SIB1 is implicated in the response to the defense hormone salicylic acid (Li et al., 2020), ACOs catalyze the synthesis of the volatile phytohormone ethylene. Ethylene is responsible for the induction of flowering and fruit ripening (Liu et al., 2021). Moreover, NatA and NatB antagonistically regulate the turnover of the Nod-like immune receptor Suppressor of NPR1 Constitutive 1 (SNC1) and thereby contribute to the defense against the oomycete *Hyaloperonospora arabidopsidis* Noco2 (Xu et al., 2015). For additional information on NTA and its implications for plant biotic stress responses, refer to chapter 1.2.2.

1.1.2.3 **NatC**

The NatC complex consists of a catalytic (NAA30) and two ribosome-binding subunits (NAA35 and NAA38) in humans and yeast. In both organisms, NatC co-translationally acetylates N-termini whose iMet is followed by the hydrophobic amino acids M, L, Y, or F. Those N-termini account for 4.5 and 3.2 % of the yeast and human proteome, respectively (Tercero et al., 1993; Rigaut et al., 1999; Polevoda & Sherman, 2001; Arnesen et al., 2009; Starheim et al., 2009). Several studies show that NatC-mediated NTA steers individual proteins to their target organelles but is no general determinant for protein subcellular localization in yeast (Aksnes et al., 2013). The Golgi proteins Arl3 and Grh1, as well as the nuclear protein Trm1-II, are for instance recruited to the membranes of their respective target organelles by NatC-mediated NTA (Behnia et al., 2004; Setty et al., 2004; Murthi & Hopper, 2005; Behnia et al., 2007). Furthermore, NatC activity is required for the lysosomal localization of the lysosomal positioning and mobility regulator, Arl8b (Starheim et al., 2009).

The knockdown of any of the three NatC subunits results in growth arrest and cell death in human cell lines (Starheim et al., 2009). In addition, a downregulation of the NatC catalytic subunit NAA30 causes a loss of mitochondrial membrane potential and subsequent fragmentation of these organelles, indicating that NatC activity is essential for mitochon-

drial integrity in humans (Van Damme et al., 2016). In yeast, knockdown mutants depleted in any of the three NatC subunits display decelerated growth on non-fermentable carbon sources, indicating that NatC might be responsible for the acetylation of proteins involved in anaerobic energy generation (Tercero et al., 1993).

Putative orthologs of the NatC subunits NAA30 (AT2G38130), NAA35 (AT2G11000), and NAA38 (AT2G23930 and AT3G11500) have been identified in *A. thaliana* (Pesaresi et al., 2003). Even though the interaction of all three NatC components is required for proper NatC function in yeast, the ectopic expression of *At*NAA30 functionally replaced the loss of every single *Sc*NatC subunit, indicating that *At*NAA30 does not rely on NatC complex formation for enzymatic activity. In line with this finding, *At*NAA30 interacts with *At*NAA35 but with none of the putative NAA38 orthologs (Tercero et al., 1993; Pesaresi et al., 2003).

While a mutation in *At*NAA35 does not yield any observable phenotype, the inactivation of *At*NAA30 impairs plant growth. The reduced growth of *At*NAA30 mutants can be attributed to a decreased effective quantum yield of photosystem II due to a downregulation of photosystem II core proteins (Pesaresi et al., 2003).

1.1.2.4 **NatD**

The monomeric NatD is also referred to as NAA40 and exhibits a highly selective substrate recognition pattern, as it only acetylates the N-termini of histones H2A and H4. This narrow substrate specificity is conserved among humans, yeast, and plants (Song et al., 2003; Dinh-Van, 2013; Magin et al., 2015). In humans, NAA40 is present primarily as free Nat in the cytosol or nucleus. Only a small fraction of the enzyme is bound to the ribosome (Hole et al., 2011). While a similar localization pattern has been observed in plants, in yeast, the vast majority of NAA40 is tethered to the ribosome (Song et al., 2003; Dinh-Van, 2013).

In humans, the deregulation of NAA40 and the resulting alterations in chromatin architecture are associated with various malignancies. The downregulation of NAA40, for instance, was linked to decreased apoptosis in hepatocellular carcinoma cells (Liu et al., 2009). Conversely, the upregulation of NAA40 stimulates cancer cell growth in colorectal cancer by modulating the expression of the oncogene PRMT5 (Pavlou & Kirmizis, 2016; Demetriadou et al., 2019). Even though in yeast, NAA40-mediated NTA of histone H4 regulates the expression of specific genes controlling cell growth, depletion of NAA40 leads to no observable phenotype upon growth on a standard culture medium (Song et al., 2003; Schiza

et al., 2013; Molina-Serrano et al., 2016). Similarly, the depletion of NAA40 (AT1G18335) in Arabidopsis does not result in any phenotype under normal growth conditions. Only on medium with a high salt content, decreased germination in comparison to wildtype plants is observed (Dinh-Van, 2013).

1.1.2.5 NatF

The monomeric NatF consists of the catalytic subunit NAA60 and is only expressed in higher eukaryotes where it acetylates the iMet of N-termini starting with MK, MA, MV, MM, MS, ML, MY, MF, MI, or MT. The absence of this promiscuous acetyltransferase in yeast explains the overall lower NTA yield of yeast compared to higher eukaryotes. Indeed, the ectopic expression of *Hs*NAA60 in yeast increases the abundance of N-terminally acetylated proteins by 10 % (Van Damme et al., 2011). In humans, NAA60 is located at the Golgi membrane and post-translationally acetylates membrane proteins with N-termini facing the cytosol. Depletion of NAA60 results in fragmentation of the Golgi apparatus, indicating that the acetyltransferase is indispensable for Golgi integrity (Aksnes et al., 2015). In Arabidopsis, an ortholog of NAA60 (AT5G16800) was identified (Van Damme et al., 2011; Rathore et al., 2016; Linster et al., 2020). Contrary to *Hs*NAA60, *At*NAA60 localizes to the plasma membrane and is, in consequence, not involved in maintaining Golgi integrity. Indeed, depletion of NAA60 in Arabidopsis does not result in any phenotype under standard growth conditions. Only upon cultivation on media with high salt content, decreased germination is observed in NAA60 mutants, implying an important role of NAA60 in salt stress tolerance (Linster et al., 2020). While both *Hs*NAA60 and *At*NAA60 display lysine-acetyltransferase activity *in vitro*, the lysine-acetyltransferase activity of *At*NAA60 is marginal compared to its Nat activity (Yang et al., 2011; Aksnes et al., 2015; Chen et al., 2016; Linster et al., 2020).

1.1.2.6 NatG and further plastidic Nats

Whereas the plant mitochondrial proteome is mostly unaffected by NTA and no mitochondrial Nats have been identified in eukaryotes so far, the N-terminal acetylation of chloroplastic proteins is a widespread phenomenon among photosynthetic organisms (Giglione et al., 2015; Aksnes et al., 2016; Linster & Wirtz, 2018). Chloroplastic proteins which are encoded in the plastid genome can be acetylated co- or posttranslationally, while nuclear-encoded chloroplastic proteins are usually acetylated post-translationally after import into

the plastids and cleavage of their transit peptides (Zybailov et al., 2008; Bienvenut et al., 2011, 2012; Huesgen et al., 2013; Westrich et al., 2021).

The first plastidic Nat to be characterized in Arabidopsis was the monomeric NatG, also referred to as NAA70 (AT2G39000). *At*NAA70 predominantly acetylates N-termini starting with M, A, S, or T and shows a strong structural similarity to *At*NAA50. Like *At*NAA50, *At*NAA70 possesses auto-lysine acetyltransferase activity (Dinh-Van et al., 2015). Recently, an *in silico* search for additional plastidic Nats identified ten candidate enzymes. For eight of them, the localization in the chloroplasts and dual Kat/Nat activity were confirmed (Tab. 2). Compared to the cytosolic Nats, all of the plastid localized enzymes displayed relaxed substrate specificities (Bienvenut et al., 2020).

Table 2: Chloroplast-localized enzymes with dual Kat/Nat activity identified in *Arabidopsis thaliana* after Bienvenut et al. (2020).

Name	Accession number
GNAT1	AT1G26220.1
GNAT2 (NSI1)	AT1G32070.2
GNAT3	AT4G19985.1
GNAT4 (NAA70)	AT2G39000.1
GNAT5	AT1G24040.1
GNAT6	AT2G06025.1
GNAT7	AT4G28030.1
GNAT10	AT1G72030.1

With GNAT2 (NSI1), at least one of the recently identified plastidic Nats is required for the dynamic reorganization of thylakoid protein complexes during state transitions induced by fluctuating light, underscoring the physiological importance of plastidic Nats (Koskela et al., 2018).

1.1.2.7 **NatH**

The monomeric NatH is also referred to as NAA80 and was recently reported to post-translationally acetylate the processed N-termini of β- and γ-actin (Drazic et al., 2018; Goris et al., 2018). NAA80 is exclusive to the animal kingdom. The expression of the acetyltransferase is evolutionarily linked to an animal-specific maturation pathway of actins. While β- and γ-actin are initially N-terminally acetylated by NatB, in animals, a yet-to-be-identified

aminopeptidase cleaves the N-termini of both proteins. The newly generated N-termini of β- and γ-actin are subsequently acetylated by NAA80. In human cell lines, actin acetylation via NAA80 regulates filament assembly, cytoskeleton organization, and cell motility (Drazic et al., 2018).

1.2 NTA in the context of plant stress responses

1.2.1 Response to drought

Prolonged water deficiency hinders plant growth and negatively impacts plant physiology and reproduction. In consequence, drought causes severe yield losses in various agronomically relevant plant species (Yordanov et al., 2000; Barnabas et al., 2008). For wheat and maize, global yield reductions between 1980 and 2015 are estimated to exceed 20 and 40 %, respectively (Daryanto et al., 2016). Because of climate change, yield losses due to water scarcity will further increase in the future (Lobell et al., 2014).

Plants respond to drought by minimizing water loss and optimizing water uptake. To achieve the latter, they prioritize root over shoot growth and stimulate lateral root hair development in response to water shortage (reviewed in Lamers et al., 2020 and Li et al., 2021). Since more than 90 % of the water in plants is lost through transpiration via stomatal pores, plants minimize water loss by closing their stomata at the expense of carbon dioxide uptake (Pei et al., 1998). Drought-induced stomatal closure is regulated primarily by the phytohormone abscisic acid (ABA). ABA is synthesized in the roots and transported to the shoot via the xylem upon drought stress. Once ABA reaches the guard cells surrounding the stomatal pores on the leaf surface, specialized PYR/PYL/RCAR receptors intracellularly perceive the hormone and subsequently bind PP2C-type phosphatases in an inhibitory-manner, triggering an intricate signaling cascade (Pei et al., 2000). The absence of phosphatase activity allows for the activation of sub-class III SnRK2 kinases, which in turn phosphorylate the membrane-localized NADPH oxidase RbohF. Upon phosphorylation, this oxidase participates in producing various reactive oxygen species (ROS). The ROS burst activates ion channels on the plasma membrane, resulting in an efflux of ions and water from the guard cells (Watson & Lee, 2019). Ultimately, the decreased turgor pressure in the guard cells leads to stomatal closure and reduced water loss via transpiration (reviewed in Hsu et al., 2021).

In addition to its role in stomatal closure, ABA also controls the expression of drought-responsive genes through the activation of various transcription factors (Rubio et al., 2009;

Umezawa et al., 2009; Vlad et al., 2009; Singh & Laxmi, 2015; Tan et al., 2018). Many of those drought-responsive genes encode for dehydrins and heat-shock proteins which are required to cope with the dehydration-induced aggregation and misfolding of proteins (Allagulova et al., 2003; Rizhsky et al., 2004; Wang et al., 2004).

Remarkably, ABA is also intricately linked to the frequency of N-terminal acetylation in plants. As first described by Linster et al. (2015), exogenous application of ABA results in a downregulation of the NAA10 and NAA15 subunits of the NatA complex and a subsequent drop in NatA-mediated NTA in *Arabidopsis thaliana*. Conversely, artificial downregulation of NAA10 and NAA15 in transgenic plants causes these plants to mimic the canonical drought stress response even though the mutants do not show any statistically significant increase in ABA levels. NatA mutants display an increased root-to-shoot ratio, higher ROS levels in guard cells, and in consequence, a decreased stomatal aperture. In addition, they constitutively express a subset of drought-responsive genes, including several dehydrins from the late embryogenesis abundant protein family. Moreover, NatA mutants profit from increased protein turnover, enabling them to degrade dehydration-induced misfolded proteins rapidly via the ubiquitin-proteasome system. Due to the aforementioned characteristics, NatA mutants are pre-adapted to desiccation and display a remarkable drought resistance (Linster et al., 2015).

While the exact mechanism by which NTA regulates root growth and stomatal closure and thereby contributes to drought resistance remains unclear, for individual proteins differential degradation of acetylated and non-acetylated proteoforms has been observed upon desiccation. One example is the ϵ-subunit of the ATP synthase, whose non-acetylated form is preferentially degraded in drought-stressed wild watermelons, whereas the abundance of the acetylated isoform remains unchanged (Hoshiyasu et al., 2013). Similar NTA-dependent mechanisms to control protein stability have been observed for various proteins involved in the response to pathogens and will be discussed in the following chapter (see 1.2.2).

1.2.2 Response to pathogens

Plants have evolved a multi-layered defense system to protect them from infections by microbial pathogens. The cuticle and the cell wall form physical barriers that passively prevent microorganisms from entering plant cells (Underwood, 2012). Once pathogens overcome these barriers, they are perceived and attacked by a two-tiered active defense system comprised of pattern-triggered immunity (PTI) and effector-triggered immunity (ETI). Recent

studies show that PTI and ETI work synergistically due to numerous positive interactions between the two branches of the active immune response (Ngou et al., 2021; Yuan et al., 2021). PTI is set off by pattern-recognition receptors (PRRs), which recognize pathogen-associated molecular patterns (PAMPs) at the cell surface. In the presence of PAMPs such as the bacterial flagellin, PRRs recruit and activate cytoplasmic kinases, which initiate signaling cascades leading to the transcriptional reprogramming of plant cells. This reprogramming results in the production of antimicrobial compounds, the fortification of the cell wall, and the synthesis of phytohormones which induce secondary transcriptional waves. Those hormones include salicylic acid, jasmonate, and ethylene (reviewed in Couto & Zipfel, 2016).

Pathogens that adapted to their host plants during evolution can inhibit PTI by secreting virulence effector molecules that sabotage the plant immune response. To counteract these effectors, plants developed intracellular nucleotide-binding leucine-rich-repeat containing receptors (NLRs), which sense virulence effectors and trigger the ETI as a second line of defense (Dodds & Rathjen, 2010). To suppress the spread of infections, ETI is often associated with the hypersensitivity response (HR), a form of programmed cell death restricted to areas under attack by pathogens (Balint-Kurti, 2019).

To prevent unnecessary cell death in the absence of pathogens, plants tightly control the expression, stability, and activity of NLRs governing the ETI. Recent genetic screens implicate NatA-mediated NTA in the turnover of the NLRs RPM1 and SNC1 in *Arabidopsis thaliana*. Both NLRs recognize effectors expressed by one of the most common plant pathogens, the bacterium *Pseudomonas syringae* (Kim et al., 2010; Xu et al., 2015; Wang et al., 2019). In NatA depleted plants, RPM1 and SNC1 accumulate, which contributes to an enhanced resistance of NatA mutants to *P. syringae*. While RPM1 is a typical NatA substrate, SNC1 is subject to alternative translation initiation, generating two distinct SNC1 isoforms. Only one of these isoforms (Met-Met-Asp-SNC1) is acetylated by NatA. The other one (Met-Asp-SNC1) is subject to acetylation via NatB. Remarkably, NTA via NatA and NatB regulate SNC1 stability antagonistically. Whereas acetylation by NatB stabilizes SNC1, acetylation via NatA creates an Ac/N-degron that is recognized by currently unidentified E3 ligases and destabilizes the immune receptor (Xu et al., 2015). The E3 ligase CPR1 and the E4 ligase MUSE3 have already been shown to facilitate the polyubiquitination of SNC1 and hence are good candidates for Ac/N-degron recognition (Huang et al., 2014; Dong et al., 2018). Further evidence for the involvement of NTA in the regulation of immune responses is provided by the stabilization of the immune-activating protein SIB1 via NatB-mediated

acetylation. SIB1 is induced by salicylic acid and enhances the DNA binding capacity of a WRKY transcription factor, which activates genes involved in the regulation of salicylic acid primed cell death during the HR (Li et al., 2020).

It remains to be elucidated whether RPM1, SNC1, and SIB1 are individual cases of immune effectors being regulated by NTA or whether NTA plays a general role in the stabilization and destabilization of proteins involved in the active immune response.

1.3 NTA in the context of sister chromatid cohesion

Mitotic cell division requires the replication of chromatids followed by their equal distribution to two daughter cells. Before the onset of mitosis, cells duplicate their genetic material, which consists of loosely packed chromatin. During the first stage of mitosis, the prophase, cells condense their chromosomes and initiate the mitotic spindle formation. The prophase is followed by the prometaphase, which is characterized by the disintegration of the nuclear envelope. Moreover, the mitotic spindle fibers attach to the centromeres of the chromosomes. During metaphase, the chromosomes are lined up in the middle of the cell (reviewed in McIntosh, 2016). To ensure that sister chromatids are not separated prematurely, they are held together by the ring-like multiprotein cohesin complex. The cohesin complex is loaded onto centromeres and regularly spaced intergenic regions on the chromosome arms. In eukaryotes, the cohesin complex is composed of four core subunits, the structural maintenance of chromosomes proteins SMC1 and SMC3, as well as the sister-chromatid cohesion proteins SCC1 and SCC3 (Fig. 4). Once the chromatids are correctly attached to the mitotic spindle and firmly held together by the cohesin complex, a molecular control mechanism referred to as metaphase checkpoint is passed, and cells proceed to the anaphase. During anaphase, the cohesin complex releases the chromatids and allows them to be pulled towards opposite poles of the cell (reviewed in Peters et al., 2008). In the last phase of mitosis, the telophase, a new nuclear envelope forms around each chromosome set, and the chromosomes unwind into chromatin again. Subsequently, the mitotic cell is ready to divide by cytokinesis to produce two genetically identical daughter cells (reviewed in Pollard & O'Shaughnessy, 2019).

The proper establishment of chromatin cohesion during the prophase and its maintenance during metaphase is essential for mitosis (Nasmyth, 2002). Errors in this process often result in aneuploidy which in humans is associated with tumorigenesis and various developmental disorders referred to as chromatinopathies (Holland & Cleveland, 2012; Parenti &

Kaiser, 2021). Cornelia de Lange syndrome (CdLS) is a prime example of a chromatinopathy caused by mutations in subunits or regulators of the cohesin complex. CdLS results in pre- and postnatal growth delay, intellectual disability, and limb abnormalities (Parenti & Kaiser, 2021). In three cases, patients diagnosed with CdLS displayed mutations in the NAA50 gene instead of classical cohesin components, indicating that NAA50 might be involved in regulating chromatin cohesion (Yavarna et al., 2015; Aoi et al., 2019; Tang et al., 2019).

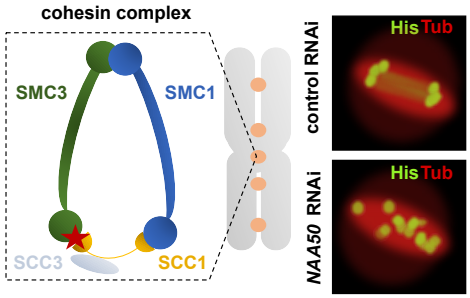

Figure 4: Architecture of the fruit fly cohesin complex. Sister chromatids are held together by the ring-like multisubunit cohesin complex, which consists of the four core subunits SMC1 (blue), SMC3 (green), SCC3 (grey), and SCC1 (yellow). It has been hypothesized that N-terminal acetylation of SCC1 via NAA50 (red star) is required for proper sister chromatid cohesion (left panel). In human and fruit fly cell cultures, NAA50 depletion leads to a disruption of centromeric sister chromatid cohesion, which activates the metaphase checkpoint and ultimately causes mitotic arrest. When cells escape the block, errors in chromosome segregation result in aneuploidy and apoptosis (right panel). Adapted from Peters et al., 2008 and Rong et al., 2016.

Indeed, depletion of NAA50 in human or fruit fly cell cultures disrupts centromeric sister chromatid cohesion, thereby activating the metaphase checkpoint. When cells escape the mitotic arrest, improper chromosome segregation causes aneuploidy followed by apoptosis. Co-IP analyses revealed that in the absence of NAA50, the cohesin complex is still properly loaded onto the chromosomes but cannot maintain its position at the centromeres during metaphase (Williams et al., 2003; Hou et al., 2007; Ribeiro et al., 2016; Rong et al., 2016). Rescue experiments with enzymatically inactive NAA50 variants indicate that NAA50 activity is required for centromeric sister chromatid cohesion (Hou et al., 2007; Ribeiro et al., 2016; Rong et al., 2016). Based on the results of *in vitro* acetylation assays, it has been hypothesized that NAA50 stabilizes the interaction between the C-terminal domain of SMC1 and the N-terminus of SCC1 by N-terminally acetylating the latter. While both human and fruit fly NAA50 can N-terminally acetylate SCC1 *in vitro*, mass-spectrometry analyses of the *in vivo* acetylation status of SCC1 in NAA50 knockout mutants remain inconclus-

ive (Ribeiro et al., 2016; Rong et al., 2016). Nevertheless, complementation experiments in Drosophila underscore the importance of the interaction between SMC3 and SCC1 for chromatin cohesion. Defects in wing development caused by a wing-specific knockdown of NAA50 can, for instance, be rescued by the expression of an SMC3-SCC1 fusion construct in the affected limbs (Ribeiro et al., 2016).

Remarkably, defects in sister-chromatid cohesion induced by the absence of NAA50 can also be counteracted by co-depleting the core NatA subunits NAA10 or NAA15 in human cells. This finding indicates an opposing role for NAA10/NAA15 and NAA50 in sister chromatid cohesion. Since NatA and NAA50 only marginally affect each other's activity *in vivo*, they might impact different downstream regulators of chromatin cohesion (Rong et al., 2016).

Up to date, the impact of NAA10/NAA15 or NAA50 on chromatin cohesion in plants has not been investigated. However, it has been speculated that the lack of NAA50-mediated NTA of the Arabidopsis homolog of SCC1 and the resulting defects in sister chromatid cohesion might explain the infertility and dwarfism of Arabidopsis *naa50* knockout mutants (Feng et al., 2020).

1.4 Aim of this thesis

In Arabidopsis, the *At*NatA complex co-translationally acetylates approximately 40 % of the proteome. The core *At*NatA complex consists of the catalytic subunit *At*NAA10 and the ribosome-binding auxiliary subunit *At*NAA15. While knockouts of *At*NAA10 or *At*NAA15 are lethal, knockdowns result in growth retardation (Linster et al., 2015). The human ortholog of the core NatA complex associates with the regulatory subunits *Hs*NAA50 and *Hs*HYPK to form the NatA/E complex (Deng et al., 2020). Unlike *Hs*HYPK, *Hs*NAA50 displays catalytic activity (Evjenth et al., 2009).

Recently, homologs of NAA50 (AT5G11340) and HYPK (AT3G06610) were identified in *Arabidopsis thaliana* (Miklankova, 2019; Armbruster et al., 2020; Neubauer & Innes, 2020). Contrary to *At*HYPK knockout mutants, which are fertile and display only a slight growth retardation (Miklankova, 2019), *naa50* knockout lines suffer from severe dwarfism and do not produce viable seeds (Armbruster et al., 2020). While *At*HYPK was shown to interact with the core *At*NatA complex, there is conflicting evidence regarding the interaction of *At*NAA50 with *At*NatA (Feng et al., 2020; Weidenhausen et al., 2021).

In this thesis, I aim to elucidate the composition of the NatA/E complex in *A. thaliana*. For this purpose, a split luciferase assay and a co-immunoprecipitation approach are employed. In addition, novel putative interaction partners of *At*NAA50 are identified via mass-spectrometry.

In the second part of this thesis, I investigate the interplay between the core NatA components and *At*NAA50 *in vivo*. Initially, I analyze the impact of *At*NAA50 depletion on typical NatA functions. These include the regulation of protein turnover as well as the adaptation to biotic and abiotic stress. To overcome the experimental limitations posed by the dwarfism and infertility of *naa50* knockout lines, I generate *aminaa50* knockdown lines with an artificial microRNA approach and characterize those novel mutants using global transcriptome and proteome analyses (Schwab et al., 2006).

In the last part of this thesis, I shed light on the role of NAA50 in plant fertility and examine the importance of *At*NAA50 activity for its cellular function. Furthermore, I dissect subcellular compartment-specific functions of *At*NAA50 in a series of complementation experiments with engineered NAA50 proteins targeted exclusively to the nucleus or the cytosol. Finally, I explore the hypothesis that *At*NAA50 is required for sister chromatid cohesion as previously observed in Drosophila (Ribeiro et al., 2016).

2. Results

2.1 Composition of the Arabidopsis NatA/E complex

2.1.1 Subcellular localization of *At*NatA/E components

In humans, the core NatA complex is responsible for the co-translational N-terminal acetylation of approximately 50 % of cytosolic proteins and consists of the catalytic subunit NAA10 and the ribosome-binding subunit NAA15 (Aksnes et al., 2016). Both subunits mainly localize to the cytosol even though *Hs*NAA10 carries a nuclear-localization sequence (NLS) and can be imported into the nuclei of proliferating cells (Park et al., 2014). The core components of the NatA complex are evolutionarily conserved in *Arabidopsis thaliana*. While knockouts of *At*NAA10 (AT5G13780) or *At*NAA15 (AT1G80410) are lethal, knockdowns result in growth retardation (Linster et al., 2015).

Cryo-EM structures provide evidence that the human core NatA complex associates with the regulatory subunits *Hs*NAA50 and *Hs*HYPK to form the quarternary NatA/E complex (Deng et al., 2020). Both *Hs*HYPK and *Hs*NAA50 are predominantly localized in the cytosol but are also found in the nucleus (Arnesen et al., 2006; Ghosh & Ranjan, 2019). Recently, homologs of NAA50 (AT5G11340) and HYPK (AT3G06610) were identified and characterised in *Arabidopsis thaliana* (Stephan, 2011; Bienvenut et al., 2012; Miklankova, 2019; Armbruster et al., 2020; Neubauer & Innes, 2020). While *At*HYPK forms a ternary complex with the core *At*NatA subunits, it remains unclear whether *At*NAA50 participates in the formation of a ribosome-associated *At*NatA/E complex (1.1.2.1).

A common subcellular localization of *At*NAA10, *At*NAA15, and *At*NAA50 in the cytosol is a prerequisite for forming such a complex. To investigate whether this requirement is satisfied, the subcellular localization of the putative *At*NatA/E components was assessed via fluorescence microscopy. For this purpose, *At*NAA10, *At*NAA15, and *At*NAA50 were fused to enhanced yellow fluorescent protein (eYFP), and the fusion proteins were transi-

ently expressed in *N. benthamiana* epidermal leaves under the control of the constitutive 35S promoter (4.3.4 and 4.10.1; for vector maps see Supplementary Fig. S1). The nuclei of the epidermal cells were labelled with mCherry by co-transformation of an NLS-mCherry marker construct (Fig. 5A).

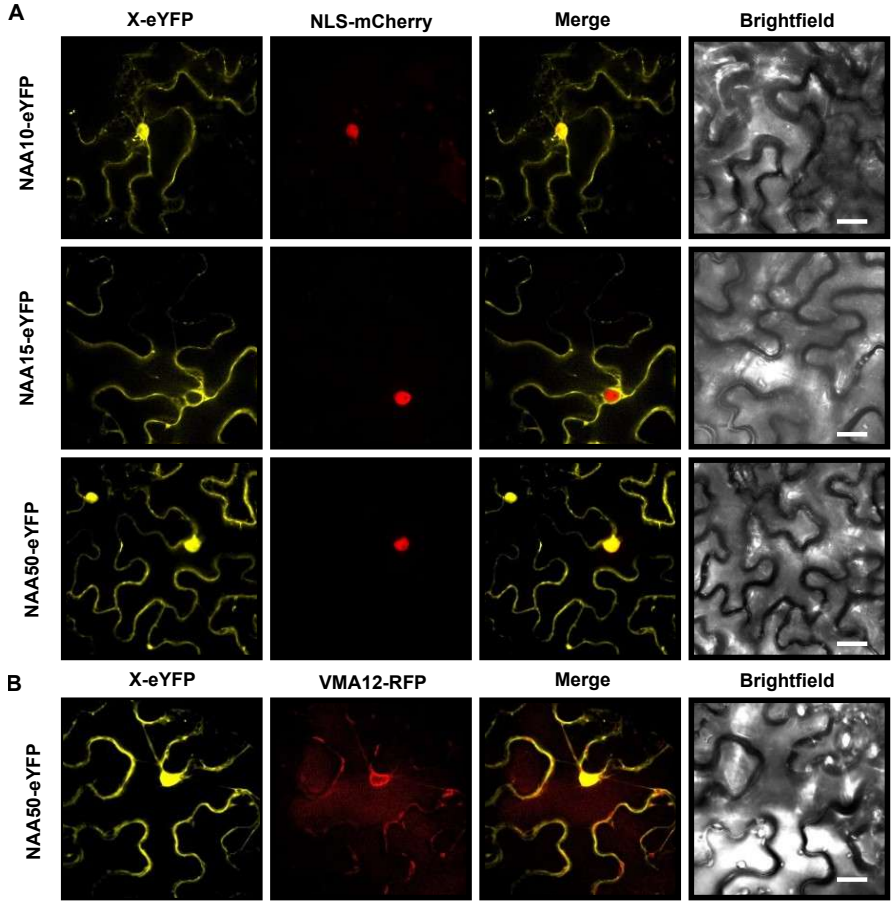

Figure 5: Subcellular localization of putative *At*NatA/E subunits. (A) *N. benthamiana* leaves were transiently transformed (4.3.4) with fusion constructs encoding for *At*NAA10-eYFP (upper panel), *At*NAA15-eYFP (middle panel) or *At*NAA50-eYFP (lower panel). Cells were co-transformed with an NLS-mCherry nuclear marker construct. **(B)** Cells were co-transformed with *At*NAA50-eYFP, and a VMA12-RFP ER marker construct. From left to right, the different columns show the yellow channel (eYFP, 488/527 nm), the red channel (mCherry/RFP, 561/615 nm), an overlay of both channels, and a brightfield image (scale bar = 25 μm). Modified from Armbruster et al., 2020.

To confirm the previously reported ER-localization of *At*NAA50 (Neubauer & Innes, 2020), *At*NAA50-eYFP was co-expressed with the ER-marker VMA12-RFP in an additional experiment (Fig. 5B). The required DNA constructs were generated by Dr. Iwona

Stephan (#1658 for NAA50-eYFP, #1730 for NAA10-eYFP, and #1731 for NAA15-eYFP, all described in Armbruster et al., 2020) or received from B.Sc. Diana Gabler (#1805 for NLS-mCherry, unpublished) and Dr. Melanie Krebs (#1729 for VMA12-RFP, described in Viotti et al., 2013) from the Centre for Organismal Studies, University of Heidelberg.

As reported for their human counterparts, *At*NAA10-eYFP and *At*NAA50-eYFP localized to the cytosol and nucleus, whereas *At*NAA15-eYFP was detected exclusively in the cytosol (Fig. 5A). In addition to its nucleocytoplasmic localization, *At*NAA50-eYFP co-localized with the ER marker VMA12-RFP (Fig. 5B). Considering that eYFP on its own is imported into the nucleus, it cannot be excluded that eYFP, which is cleaved from the *At*NAA50-eYFP fusion construct, contributes to the observed nucleocytoplasmic localization pattern (Chen et al., 2020). To test whether eYFP was cleaved from the *At*NAA50-eYFP fusion protein, leaf material of the transiently transformed tobacco plants was harvested, and proteins were extracted with modified RIPA buffer (4.1.2, after Zhang et al., 2018). The presence of free and *At*NAA50-bound eYFP was verified with a specific antiserum (Fig. 6).

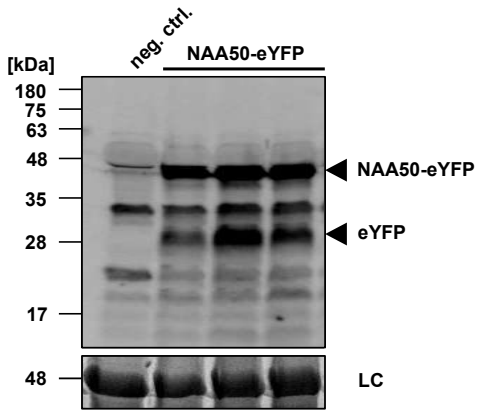

Figure 6: Immunodetection of NAA50-eYFP in protein extracts of transiently transformed *N. benthamiana* plants. Proteins were extracted with modified RIPA buffer (Zhang et al., 2018). eYFP was detected with a polyclonal rabbit α-GFP antibody (#A-6455, Thermo Fisher Scientific). An untransformed plant served as negative control (neg. ctrl.). The expected sizes of the detected proteins are marked with black triangles (NAA50-eYFP: 45 kDa, free eYFP: 27 kDa). A Coomassie-stained PAGE gel loaded with the protein extracts served as a loading control (LC). An uncropped picture of the loading control is shown in Supplementary Fig. S2.

Even though eYFP could have been cleaved from the *At*NAA50-eYFP fusion construct during protein extraction, the detection of free eYFP in the protein extracts of transiently transformed tobacco cells (Fig. 6) calls the nuclear localization of endogenous *At*NAA50 into question since it is unclear whether the observed nuclear fluorescence originates from

free eYFP or the *At*NAA50-eYFP fusion protein (Fig. 5A).

In order to confirm the nuclear localization of *At*NAA50 independently, proteins were extracted from *A. thaliana* wildtype leaf material and separated into cytosolic and nuclear fractions (4.5.3). Subsequently, both fractions were loaded on an SDS-PAGE gel (4.5.8), the proteins were separated and transferred to a PVDF membrane (4.5.10), and *At*NAA50 was detected with a specific antiserum (Fig. 7).

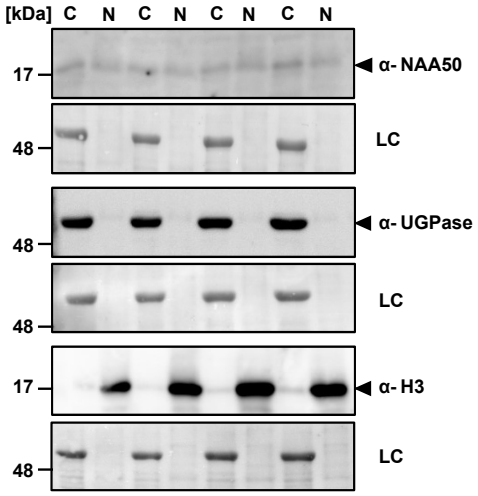

Figure 7: Endogenous *At*NAA50 localizes to the nucleus in wildtype plants. Col-0 wildtype plants were grown on soil for eight weeks under short-day conditions. Subsequently, proteins were extracted from 1.5 g of leaf material per replicate (n=4). The protein extracts were separated into cytosolic (C) and nuclear (N) fractions (4.5.3). The NAA50 protein was detected with a specific antiserum. UDP-glucose pyrophosphorylase (UGPase) and Histon 3 (H3) were used as markers for the cytosolic and nuclear fraction, respectively (18). The expected sizes of the detected proteins are marked with black triangles (NAA50: 18.5 kDa, UGPase: 52 kDa, H3: 17 kDa). Amido black stainings of the membranes served as respective loading controls (LC). Uncropped pictures of the immunoblots are shown in Supplementary Fig. S3.

The detection of *At*NAA50 in the cytosolic and nuclear fractions confirmed the nucleocytoplasmic localization of the acetyltransferase. The nuclear localization of *At*NAA50 is in agreement with a bipartite nuclear localization signal at position 125 of *At*NAA50 as predicted by the cNLS Mapper tool (Kosugi et al., 2009). More importantly, however, the three main components of the putative *At*NatA/E complex are all found in the cytosol, fulfilling the prerequisite for forming a ribosome-associated ternary complex.

2.1.2 Homology modelling of the putative *At*NatA/E complex

Recently, the structures of the human and yeast NatA/E complex were resolved. An analysis of the NAA10-NAA50 and NAA15-NAA50 interface revealed that in both organisms, NAA50 predominantly interacts with NAA15. Even though NAA10-NAA50 interactions were less extensive, important residues for the interaction of NAA50 with both core NatA subunits could be identified (Deng et al., 2019, 2020). To determine whether those residues were conserved in plants, the sequences of NAA10, NAA15, and NAA50 from *Arabidopsis thaliana*, *Homo sapiens*, and *Saccharomyces cerevisiae* were aligned (Fig. 8).

Figure 8: Sequence alignment of NatA/E subunits from *A. thaliana*, *H. sapiens*, and *S. cerevisiae*. Only the sequence stretches at the interface between the subunits are depicted for simplicity. **(A)** Alignment of *At*NAA10 (Q9FKI4, residues 77-137), *Hs*NAA10 (P41227, residues 77-137) and *Sc*NAA10 (P07347, residues 121-180). **(B)** Alignment of *At*NAA15 (Q8VZM1, residues 338-454), *Hs*NAA15 (Q9BXJ9, residues 330-448) and *Sc*NAA15 (C7GPW0, residues 349-458). **(C)** Alignment of *At*NAA50 (Q9LFM3, residues 1-102), *Hs*NAA50 (Q9GZZ1, residues 1-98) and *Sc*NAA50 (Q08689, residues 1-117). Shaded residues mediate the interaction between NAA10-NAA50 (blue) or NAA15-NAA50 (grey). The conserved TPTLxE motif (x either V or I) in the center of the binding interface between NAA15 and NAA50 is marked in red. Residues that were chosen to be mutated in NAA50 to disrupt binding to the other subunits are marked with red asterisks. The alignment was generated with Clustal Omega.

The crystal structure of *Sc*NatA reveals that the interaction between *Sc*NAA10 and *Sc*NAA50 is mainly mediated by electrostatic interactions between three basic residues (R122, R125, and R126) in the *Sc*NAA10 α3-β4 loop and E68 in the *Sc*NAA50 β2-β3 loop (Deng et al., 2019). Similar interactions are observed between R83 in *Hs*NAA10 and D53

in *Hs*NAA50. This pattern of basic amino acids in NAA10 interacting with acidic residues in NAA50 was conserved in *A. thaliana*. Perhaps the most striking conserved feature was, however, the TPTLxE motif (x either V or I) in NAA15, which interacted with conserved residues in NAA50 (Arabidopsis: Y53, V59, and Y87; Human: Y50, V56, Y58; Yeast: Y65, V71, Y102). The TPTLxE motif was nearly completely conserved in Arabidopsis; only the last three amino acids varied slightly (TPTVID instead of TPTLIE in human or TPTLVE in yeast). The importance of this motif is underscored by the fact that mutations in the motif itself (T406Y), as well as its counterpart in NAA50 (Y50A/I54K), disrupt the interaction of *Hs*NAA15 and *Hs*NAA50 (Deng et al., 2019, 2020).

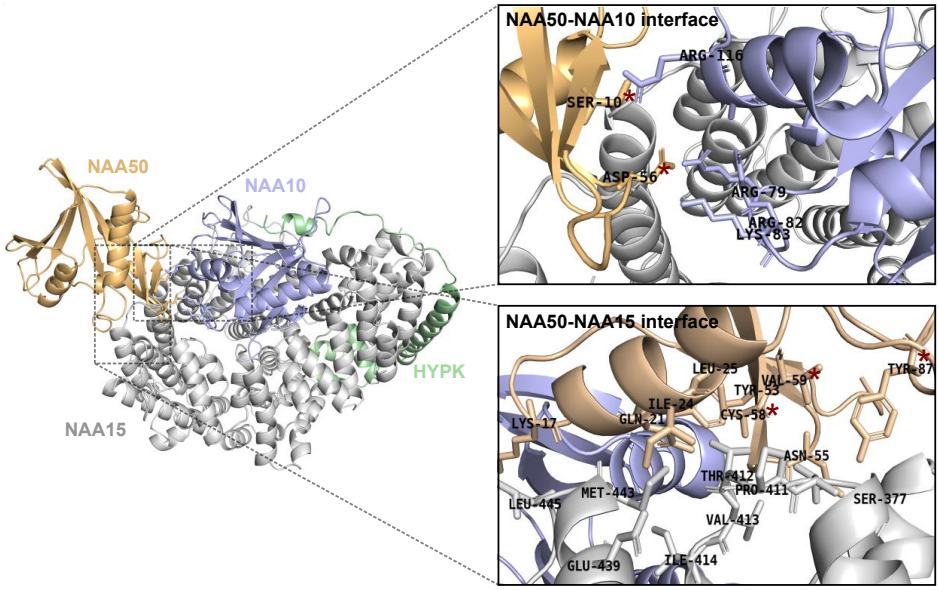

Figure 9: Model of the *At*NatA/E complex. The individual subunits were modeled with SWISS-MODEL based on the templates 6pw9.1 (NAA10, blue), 6pw9.1.A (NAA50, yellow), 6pw9.1 (NAA15, grey) and 6pw9.1.D (HYPK, green) and superimposed with the cryo-EM structure of the human NatA/E complex with PyMOL (4.1.7). The left panel provides an overview of the complex. The right panels show zoom-in views of the interface between NAA50-NAA10 (upper panel) and NAA50-NAA15 (lower panel). Residues mediating the interaction between NAA50 and the core NatA subunits are represented as sticks. Residues which were selected for mutation are marked with red asterisks. The structure of the human NatA/E complex was downloaded from the ProteinDataBank (PDB).

While the alignment suggested that the binding mode of NAA50 to the core NatA complex components was conserved among humans, yeast, and plants, only a 3D structure can reveal whether steric conflicts impede the formation of such a complex *in vivo*. Unfortunately, *At*NAA50 is the only protein among the putative Arabidopsis NatA/E components

which could be crystallized so far (Weidenhausen et al., 2021). To nevertheless investigate the architecture of a putative *At*NatA/E complex, homology models of the individual components were created based on the previously published structures of human NatA/E subunits. Subsequently, the models were superimposed with the experimentally determined human NatA/E structure and visually inspected (Fig. 9).

In agreement with reports by Weidenhausen et al. (2021), no obvious steric clashes were observed in the *At*NatA/E model. To verify complex formation *in vivo*, a split luciferase assay was applied. As a negative control for this experiment, NAA50 versions with disrupted NAA10 and/or NAA15 binding were designed based on the aforementioned alignment and the *At*NatA/E model (Tab. 3).

Table 3: Mutations introduced in *At*NAA50 to disrupt the association with one or both core *At*NatA components.

Name	Mutated residues	Purpose
NAA50^{-NAA10}	S10A, D56A	disrupt NAA10 binding
NAA50^{-NAA15}	Y53T, C58A, V59A, Y87T	disrupt NAA15 binding
NAA50$^{-NAA10/NAA15}$	S10A, Y53T, D56A, C58A, V59A, Y87T	disrupt NAA10 & NAA15 binding

2.1.3 Split luciferase assay to verify interaction between *At*NatA/E components

For the *in planta* detection of protein-protein interactions with the split luciferase proximity assay according to Chen et al. (2008), the full-length coding sequences of *At*NAA10 (AT5G13780), *At*NAA15 (AT1G80410), *At*NAA50 (AT5G11340), *At*HYPK (AT3G06610) and *At*NAA20 (AT1G03150) were PCR-amplified from wildtype cDNA (4.4.4) with specific primers (Supplementary Tab. S6). The primers harboured *Kpn*I and *Sal*I endonuclease restriction sites and - in the case of NAA50 - the necessary mutations to generate the NAA50^{-NAA10}, NAA50^{-NAA15}, and NAA50$^{-NAA10/NAA15}$ constructs. The PCR fragments were ligated into the pCambia-NLuc vector (#1726) upstream of NLuc or in the pCambia-CLuc vector downstream of CLuc (#1725), generating the constructs listed in Tab. 4. Sequencing revealed that the primer pairs #4956 and #4957 (CLuc), as well as #4958 and #4959 (NLuc), did not amplify the main isoform of NAA15 (AT1G80410.2, 991 AA) but a slightly shorter version (AT1G80410.1, 897 AA). Since the C-termini of the two NAA15 isoforms differ

slightly from each other, the split luciferase assay was performed with a truncated NAA15 version containing only the first 893 residues and omitting the variable C-terminus. To amplify this truncated NAA15 version, the primer pairs #4956 and #5204 (CLuc) and #4958 and #5205 (NLuc) were designed.

Table 4: Plasmids generated for the split luciferase assay.

Nr.	Name
1732	pCambia1300-*At*NAA10-NLuc
1733	pCambia1300-CLuc-*At*NAA10
1734	pCambia1300-CLuc-*At*NAA50
1735	pCambia1300-*At*NAA50-NLuc
1736	pCambia1300-*At*HYPK-NLuc
1737	pCambia1300-CLuc-*At*HYPK
1882	pCambia1300-*At*NAA50$^{-NAA10/NAA15}$-NLuc
1883	pCambia1300-CLuc-*At*NAA50$^{-NAA10/NAA15}$
1885	pCambia1300-CLuc-*At*NAA50^{-NAA10}
1886	pCambia1300-*At*NAA50^{-NAA10}-NLuc
1887	pCambia1300-CLuc-*At*NAA50^{-NAA15}
1788	pCambia1300-*At*NAA50^{-NAA15}-NLuc
1889	pCambia1300-CLuc-*At*NAA15
1890	pCambia1300-*At*NAA15-NLuc
1892	pCambia1300-*At*NAA20-NLuc
1893	pCambia1300-CLuc-*At*NAA20

For the split luciferase assay, *N. benthamiana* leaves were co-infiltrated with *A. tumefaciens* expressing different CLuc/NLuc vector pairs and the p19 suppressor. After three days, the leaves were anointed with luciferin, and the luciferase signal was detected in an ImageQuant LAS 4000 biomolecular imager (4.5.11). The reconstitution of luciferase activity revealed that *At*NAA50 was found close to *At*NAA10. The mutations in NAA50^{-NAA10} could not entirely eliminate this interaction (Fig. 10A). The split luciferase assay also verified the interaction between *At*NAA15 and *At*NAA50. The interaction between *At*NAA10 and *At*NAA50 did not seem to be required for the association of *At*NAA15 and *At*NAA50 since the NAA50^{-NAA10} mutant was still able to reconstitute luciferase activity in combination with *At*NAA15 (Fig. 10B).

In addition, luciferase activity was reconstituted upon co-expression of *At*HYPK and any of the other putative *At*NatA/E subunits, including *At*NAA50 (Fig. 10C). Even though the homology model of the *At*NatA/E complex did not indicate a direct interaction between

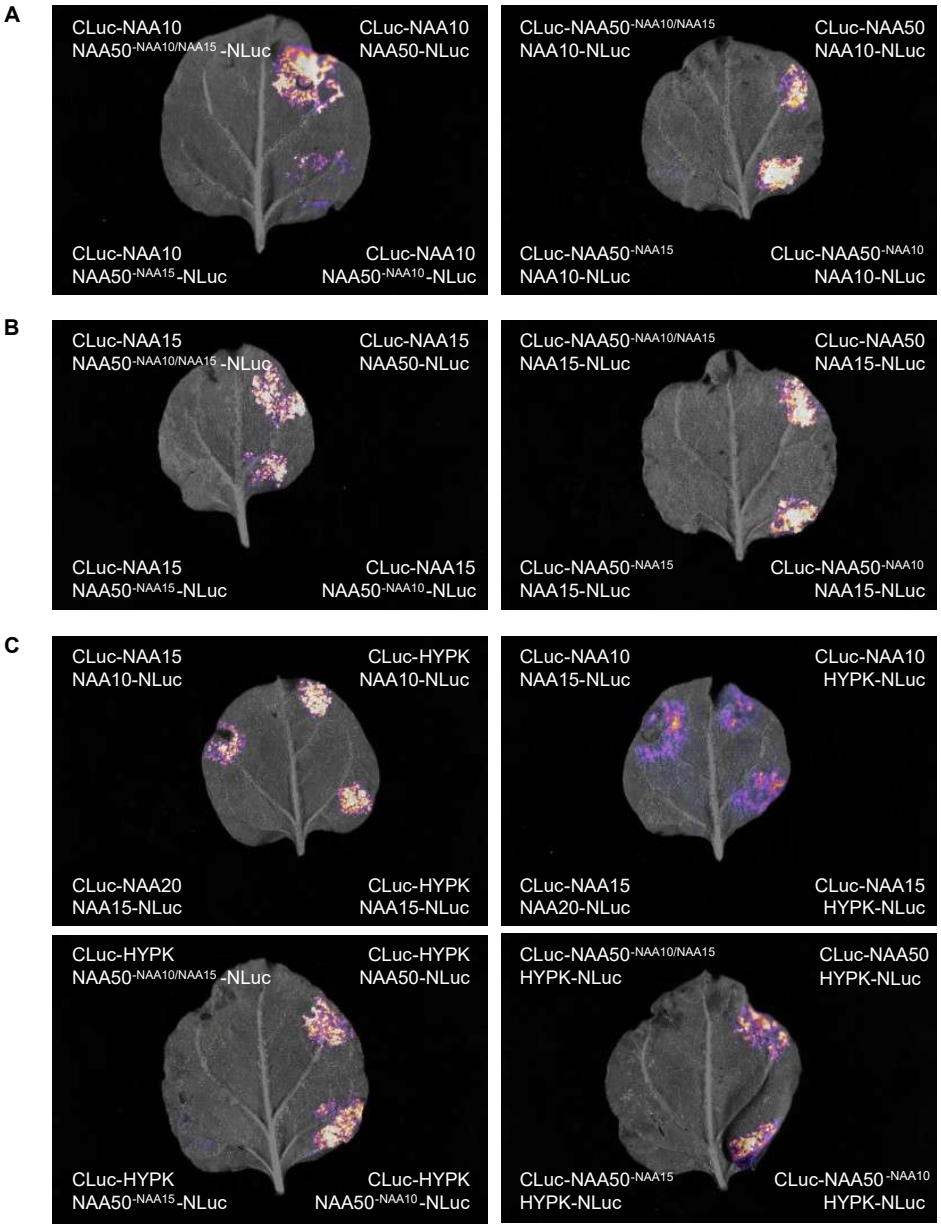

Figure 10: Split luciferase assay to assess the interactions between putative *At*NatA/E subunits. *N. benthamiana* leaves were co-transformed with different split luciferase constructs (4.3.4). After three days, the reconstitution of luciferase activity was assessed by anointing the leaves with luciferin and detecting the resulting bioluminescence in a biomolecular imager (4.5.11). Reconstitution of luciferase activity after expression of split luciferase fusions with **(A)** *At*NAA10 and *At*NAA50, **(B)** *At*NAA15 and *At*NAA50 or **(C)** *At*HYPK and *At*NAA50. Each image is representative of n=3 replicates. The replicates can be found in Supplementary Fig. S4 and S5.

*At*NAA50 and *At*HYPK, this reconstitution of luciferase activity was to be expected since the assay does not only pick up direct interactions but also the close proximity of proteins in multi-protein complexes. Thus, to conclusively demonstrate a direct interaction between *At*NAA50 and the other *At*NatA/E components, further experiments would be required.

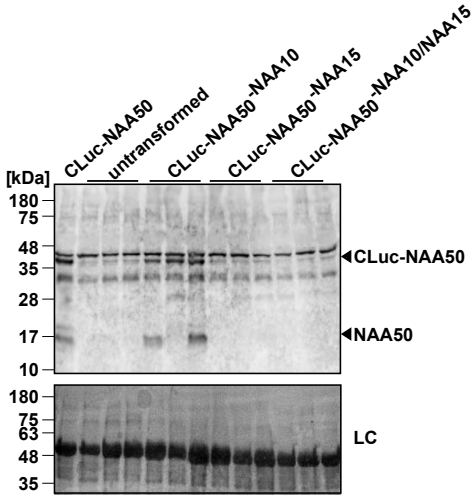

Figure 11: NAA50^{-NAA15} and NAA50$^{-NAA10/NAA15}$ are not expressed in *N. benthamiana* leaves. *N. benthamiana* leaves were co-transformed with NAA15-NLuc and different CLuc-NAA50 versions (n=3). Leaf material was harvested, and proteins were extracted (4.5.1), separated by SDS-PAGE (4.5.8), and transferred to a PVDF membrane (4.5.10). Last, NAA50 expression was detected with a specific antiserum against *At*NAA50 (Tab. 18). Protein extracts from untransformed tobacco plants were used as a negative control. Each lane contains 20 μg protein extract. An Amido black staining of the membrane served as a loading control (LC).

Remarkably, luciferase activity was never reconstituted in leaves transformed with split luciferase combinations which involved NAA50^{-NAA15} or NAA50$^{-NAA10/NAA15}$ (Fig. 10A-C). This finding can be interpreted in two ways. On the one hand, the interaction of *At*NAA50 with *At*NAA10 and *At*HYPK could be mainly mediated by *At*NAA15. This explanation would be well in line with the previously generated model of the *At*NatA/E complex (Fig. 9) and findings reported for the human and yeast NatA/E complex (Deng et al., 2019, 2020). On the other hand, an absence of signal could be attributed to insufficient expression of one or both of the split luciferase constructs. To determine whether NAA50^{-NAA10}, NAA50^{-NAA15}, and NAA50$^{-NAA10/NAA15}$ were properly expressed in the transiently transformed tobacco plants, leaf material was harvested and snap-frozen directly after the split luciferase assay. Subsequently, proteins were extracted from the plant material (4.5.1), separated by SDS-PAGE (4.5.8), and transferred to a PVDF membrane (4.5.10). Last, NAA50 expression was

detected with a specific antiserum against *At*NAA50 (Tab. 18). Protein extracts from untransformed tobacco plants were used as a negative control, whereas a protein extract from tobacco plants transformed with a combination of CLuc-NAA50 and NAA15-NLuc was used as a positive control. While NAA50 expression was verified in the positive control and two of the three NAA50$^{\text{-NAA10}}$ samples, NAA50 could not be detected in any of the protein extracts from leaves transformed with NAA50$^{\text{-NAA15}}$ or NAA50$^{\text{-NAA10/NAA15}}$ (Fig. 11). This suggests that the mutations introduced in NAA50$^{\text{-NAA15}}$ and NAA50$^{\text{-NAA10/NAA15}}$ destabilized the enzymes so that they were quickly degraded right after expression. Hence the split luciferase assay could not provide any information about the interactions between NAA50$^{\text{-NAA15}}$ and NAA50$^{\text{-NAA10/NAA15}}$ with the other NatA/E subunits.

2.1.4 Association of *At*NatA/E components with the ribosome

Since the reconstitution of enzymatic activity in the split luciferase assay (2.1.3) is merely indicative of the proximity of the CLuc-X and Y-NLuc fusion proteins, it remained unclear whether the observed interactions between *At*NAA50 and *At*NAA10 and *At*NAA50 and *At*NAA15 (Fig. 10A-B) were direct interactions or mediated by the association of the *At*NatA/E components with the ribosome or to date undiscovered scaffolding proteins. A co-immunoprecipitation approach was applied to learn more about the postulated interaction of the *At*NatA/E components with the ribosome (2.1.4).

For this purpose, protein extracts from *A. thaliana* wildtype plants were incubated with antibodies against *At*NAA15 or *At*NAA50. Subsequently, the antibodies and the proteins which directly or indirectly interacted with them were captured with protein A/G beads (4.5.4). The beads were collected by centrifugation, and after several washing steps, the antibodies and the co-immunoprecipitated proteins were released from the beads. Following separation by SDS-PAGE (4.5.8), the proteins were transferred to a PVDF membrane (4.5.10) and *At*NAA15, *At*NAA50 and the 40S ribosomal subunit S14 (AT2G36160) were detected with specific antisera (Tab. 18). As expected, *At*NAA15 and *At*NAA50 were strongly enriched among the proteins co-immunoprecipitated with the α-NAA15 and α-NAA50 antibodies, respectively (Fig. 12).

Interestingly, *At*NAA15 was co-immunoprecipitated with *At*NAA50 when the α-NAA50 antibody was used as bait. However, in the reverse constellation, *At*NAA50 could not be co-immunoprecipitated with *At*NAA15. This suggests that although *At*NAA15 and *At*NAA50 interact, most *At*NAA50 is not bound to the NatA complex but is available as a free enzyme.

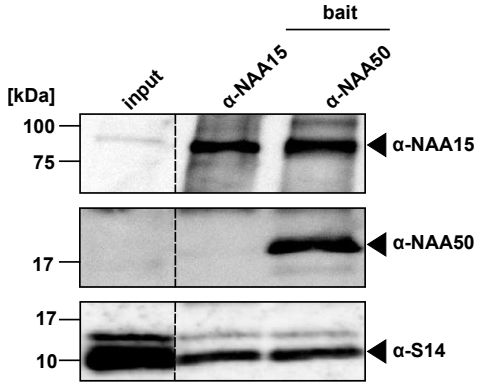

Figure 12: Immunoprecipitation of NatA/E subunits. Protein extracts of six-week-old soil-grown (4.3.2) wildtype plants were divided into two equal fractions, which were incubated with antibodies against *At*NAA15 or *At*NAA50, respectively (Tab. 18). Subsequently, the antibodies and the proteins which interacted with them were captured with protein A/G beads (4.5.4) and separated by SDS-PAGE (4.5.8). The proteins which co-precipitated with the antibodies were detected with specific antisera against *At*NAA15, *At*NAA50, and the 40S ribosomal subunit S14 (Tab. 18). The dotted lines indicate lanes on the same membranes which were rearranged. The original pictures of the membranes can be found in Supplementary Fig. S6.

This is well in line with findings in human cell lines where more than 80 % of *Hs*NAA50 is not associated with the NatA complex (Hou et al., 2007). The fact that equal amounts of the 40S ribosomal subunit S14 were co-immunoprecipitated with NAA15 and NAA50 when the α-NAA50 and α-NAA15 antibodies were used as bait implies that the NatA/E complex mainly forms at the ribosome. Indeed, NAA15 and NAA50 have already been reported to co-localize partially with ribosomal proteins (Huber, 2015).

2.1.5 Identification of *At*NatA/E interaction partners

The co-immunoprecipitation of the 40S ribosomal subunit S14 with NAA15 and NAA50 (Fig. 12) indicates that the experimental approach described in the previous chapter can be harnessed to identify novel interaction partners of *At*NatA/E subunits. For this purpose, the aforementioned co-immunoprecipitation experiment with the α-NAA50 and α-NAA15 antibodies was repeated. In addition, protein extracts incubated without bait antibody or with the α-SAT5 antibody (AT5G56760) were included as negative control and quality control, respectively (4.5.4). The thereby generated samples were loaded on an SDS-PAGE gel (4.5.8). Subsequently, the proteins were fixed, and the gel was stained with Coomassie solution. Fractions of the gel were cut out and subjected to an in-gel digest to prepare the samples for mass-spectrometry (Fig. 13). When cutting the gels, the prominent bands at

50 kDa corresponding to the heavy fragments of the antibodies were omitted to decrease sample complexity. However, the 20 kDa bands corresponding to the light fragments of the antibodies could not be omitted since several of the target proteins (e.g., NAA10 and NAA50 with 20 and 18.5 kDa, respectively) were expected to run at approximately this size.

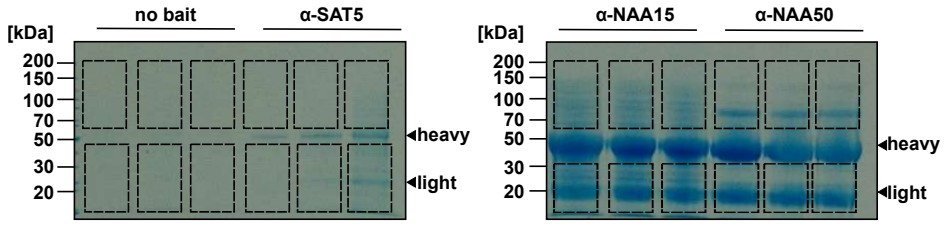

Figure 13: Immunoprecipitation of NatA/E subunits. Protein extracts of six-week-old soil-grown (4.3.2) wildtype plants were incubated with antibodies against *At*SAT5 (quality control), *At*NAA15 and *At*NAA50 (Tab. 18). Protein extracts, which were not incubated with any antibody were used as negative control (no bait). All samples were incubated with protein A/G beads (4.5.4) to capture antibodies and the proteins which interacted with them. After collecting the beads by centrifugation, the bound proteins were released from the beads by adding Laemmli buffer followed by denaturation at 95 °C for 10 min. The thereby generated samples were loaded on an SDS-PAGE gel (4.5.8). After the proteins had penetrated the gel to a depth of 2-3 cm, the proteins were fixed, and the gel was stained with Coomassie solution. The dotted lines indicate fractions of the gel, which were cut and subjected to an in-gel digest to prepare the samples for a mass-spectrometry analysis (4.7.3).

2.1.5.1 The α-SAT5 co-immunoprecipitate as quality control

The protein extracts which had been incubated with α-SAT5 antiserum as bait were selected as quality controls for several reasons. Firstly, the rabbit α-SAT5 antiserum was generated in-house in the same manner as the α-NAA50 and α-NAA15 antisera and could therefore be expected to yield similar unspecific immunoprecipitants (e.g., due to the His-tag used to purify the *At*SAT/NAA10/NAA50 proteins expressed in *E. coli* for the immunization of the rabbits). Secondly, like NAA10 and NAA50, SAT5 is a cytosolic protein with acetylterans-ferase activity. In contrast to NAA10 and NAA15, however, SAT5 is not involved in the N-terminal acetylation of nascent polypeptides at the ribosome. Instead, SAT5 associates with OAS-TL A (AT4G14880.4) to form the cytosolic cysteine synthase complex (cCSC). Only in this complex, the serine acetyltransferase is activated and catalyzes the transfer of an acetyl moiety from acetyl-CoA to free serine to produce *O*-acetylserine (Wirtz et al., 2010). Apart from its primary function in the cCSC, SAT5 has been observed to associate with the serine acetyltransferase SERAT3;1 (AT2G17640.1) and the *O*-acetylserine(thiol)lyases

OAS-TL B (AT2G43750.2) and OAS-TL C (AT3G59760.1), which are usually found in the plastids and mitochondrion, respectively (Haberland, 2017). Together with the aforementioned advantages, this abundance of known SAT5 interaction partners makes the α-SAT5 antiserum an ideal quality control for the co-immunoprecipitation experiment at hand.

Indeed, the mass-spectrometry analysis revealed that 1,652 proteins were identified in all three replicates of the α-SAT5 quality control. Of those, 1,651 were also found in at least one replicate of the negative control so that an enrichment factor could be calculated. In total, only 8 (0.5 %) of the identified proteins were significantly (>2-fold, $p<0.05$ in a Student's t-test) enriched in the α-SAT5 samples. The protein with the highest enrichment factor was SAT5 itself (837-fold), demonstrating that the α-SAT5 antibody effectively precipitated its target. Furthermore, the known SAT5-interactor SERAT3;1 was co-immunoprecipitated (143-fold enrichment). In addition, six previously unknown putative SAT5 interaction partners were up to 12-fold enriched in the α-SAT5 co-immunoprecipitate (Tab. 5). The three known SAT5 interaction partners OAS-TL A-C were enriched as well, although the up to 7-fold accumulation of the enzymes was not statistically significant. In conclusion, the quality control with the α-SAT5 antiserum provided an encouraging proof of principle for the co-immunoprecipitation experiment.

Table 5: Proteins (co)-immunoprecipitated from wildtype protein extracts incubated with a specific α-SAT5 antiserum. Protein extracts of six-week-old soil-grown (4.3.2) wildtype plants were incubated with α-SAT5 antiserum (n=3). Subsequently, the samples were mixed with protein A/G beads (4.5.4) to capture the antibodies and proteins which interacted with them. Protein extracts incubated exclusively with protein A/G beads served as a negative control. After separating the beads from the supernatant, the proteins bound to the beads were released by adding of Laemmli buffer. The proteins were separated by SDS-PAGE and fractions of the gel were subjected to an in-gel digest. The mass-spectrometry analysis of the digested samples was performed by Sabine Merker and Dr. Thomas Ruppert from the Core Facility for Mass Spectrometry & Proteomics (University of Heidelberg). This table shows the abundance ($x10^5$) of proteins as determined by maximum peak height in individual samples (#1-3). Proteins significantly enriched in the α-SAT5 co-immunoprecipitate are marked with an asterisk.

	negative control			**α-SAT5**			
	#1	**#2**	**#3**	**#1**	**#2**	**#3**	**Ratio**
SAT5 (AT5G56760.1)	0	1	0	423	235	310	**837-fold***
SERAT3.1 (AT2G17640.1)	0	0	0	29	16	21	**143-fold***

PP2A-3 (AT2G42500.1)	1	4	2	32	22	34	**12-fold***
EMB2726 (AT4G29060.1)	31	53	29	382	291	482	**10-fold***
CT-BMY (AT4G17090.1)	5	5	3	19	24	24	**5-fold***
GLYR2 (AT1G17650.1)	16	24	12	85	43	109	**5-fold***
SERAT2;2 (AT3G13110.1)	12	12	8	46	23	43	**4-fold***
RPN10 (AT4G38630.1)	2	3	2	8	7	9	**4-fold***
OAS-TL A1 (AT4G14880.4)	33	50	55	297	169	489	**7-fold**
OAS-TL B (AT2G43750.2)	16	46	25	99	71	365	**6-fold**
OAS-TL C (AT3G59760.1)	11	69	9	23	29	275	**4-fold**

2.1.5.2 **Analysis of the α-NAA15 co-immunoprecipitate**

In the α-NAA15 co-immunoprecipitate, 1,237 proteins were identified in all three replicates. Of those, 1,235 were also found in at least one replicate of the negative control so that an enrichment factor could be calculated. In total, only 149 (12 %) of the identified proteins were significantly (>2-fold, $p<0.05$ in a Student's t-test) enriched in the α-NAA15 samples (Fig. 14). None of those proteins accumulated in the α-SAT5 co-immunoprecipitate, suggesting a specific interaction of those proteins with the NAA15 paratope of the α-NAA15 antibody. Surprisingly, the protein with the highest enrichment factor was not NAA15 itself (772-fold; AT1G80410.2), but HYPK (1,070-fold; AT3G06610.1). With NAA10 (528-fold; AT5G13780.1) and NAA50 (3-fold; AT3G06610.1) all NatA/E complex components were significantly enriched by the α-NAA15 co-immunoprecipitation. Compared to NAA10 or HYPK, considerably less NAA50 was detected in the α-NAA15 co-immunoprecipitate. This is in agreement with findings by Hou et al. (2007), who report that in human cell lines, less than 20 % of NAA50 is not bound to the NatA/E complex.

Apart from the NatA/E complex components, three proteins stood out among the most

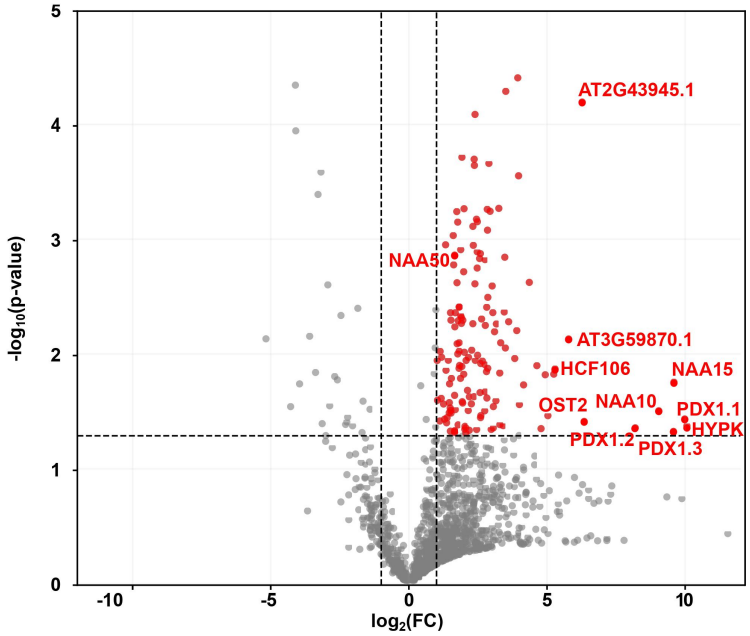

Figure 14: Proteins (co)-immunoprecipitated from wildtype protein extracts incubated with a specific α-NAA15 antiserum. Protein extracts of six-week-old soil-grown (4.3.2) wild-type plants were incubated with α-NAA15 antiserum (n=3). Subsequently, the samples were mixed with protein A/G beads (4.5.4) to capture the antibodies and the proteins which interacted with them. Protein extracts incubated exclusively with protein A/G beads served as a negative control. After separating the beads from the supernatant, the proteins bound to the beads were released by adding Laemmli buffer. The samples were separated by SDS-PAGE, and to omit the 50 kDa band arising from the heavy fragments of the antibodies, the surrounding fractions of the gel were cut out and subjected to an in-gel digest. The digested samples were analyzed by mass-spectrometry. The mass-spectrometry analysis was performed by Sabine Merker and Dr. Thomas Ruppert from the Core Facility for Mass Spectrometry & Proteomics (University of Heidelberg). This volcano plot depicts the significantly (>2-fold, $p<0.05$ in a Student's t-test) enriched proteins identified in the α-NAA15 co-immunoprecipitate in red. The ten most enriched proteins and the components of the NatA/E complex were labelled with their corresponding TAIR symbols.

highly enriched proteins. The PDX1 homologs PDX1.1 (1,013-fold; AT2G38230.1), PDX1.2 (290-fold; AT3G16050.1), and PDX1.3 (763-fold; AT5G01410.1) form heteromeric complexes and - in the case of PDX1.1 and PDX1.3 - associate with PDX2 (AT5G60540, not identified in this dataset) to catalyze the biosynthesis of the essential coenzyme pyridoxal 5'phosphate (Dell'Aglio et al., 2019). Based on their N-terminal sequences, PDX1.1 and PDX1.3 (both MA) are typical NatA substrates, while the pseudoenzyme PDX1.2 is a target of NatB (ME). Hence the presence of PDX1.2 at the NatA complex cannot easily be explained by the nature of its N-terminus and represents an exciting starting point for further studies.

In total, 108 (72.5 %) of the proteins which were identified as putative NatA interaction partners in this screen were typical NatA substrates (MA, MC, MG, MS, MT, MV), whereas only 24 (16.1 %) were classified as NatB substrates (MD, ME, MN, MQ). These numbers differ from an analysis of the nuclear-encoded Arabidopsis proteome (48,076 proteoforms as of TAIR release 10) which encompasses 24,277 (50.5 %) putative NatA and 11,413 (23.7 %) putative NatB substrates. This striking overrepresentation of NatA substrates in the α-NAA15 co-immunoprecipitate suggests that several of the newly identified putative NAA15 interactors are substrates of the NatA complex.

In agreement with a localization of the NatA/E complex at the ribosome, the analysis of the 149 putative NAA15 interactors suggested an association of NAA15 with a number of cytosolic ribosomal proteins (AT1G58380.1, AT3G27830.1, AT1G78630.1, AT2G27720.1, AT1G02780.1, AT5G13510.1, AT3G63490.1, AT5G30510.1, AT5G02870.1, AT2G20450.1 and AT3G47370.3) and a translation elongation factor family protein (AT1G07920.1). Interestingly, three plastid ribosomal proteins (AT3G25920.1, AT1G07320.1, and AT1G32990.1) accumulated in the co-immunoprecipitate. Moreover, several subunits of the proteasome (AT1G13060.1, AT3G05530.1, AT5G35590.1, and AT3G02200.2) and various chaperones (AT3G53990.1, AT2G28000.1, and AT3G11830.1) co-immunoprecipitated with NAA15. A complete list of all 149 putative interactors can be found in the Supplement (Tab. S1).

2.1.5.3 Analysis of the α-NAA50 co-immunoprecipitate

In the α-NAA50 co-immunoprecipitate, a total of 1,388 proteins was reliably quantified in all replicates (n=3). Of those, only 209 (15 %) were significantly (>2-fold, $p<0.05$ in a Student's t-test) enriched in the α-NAA50 samples (Fig. 15). Remarkably, 40 (19 %) of the enriched proteins also accumulated in the α-NAA15 co-immunoprecipitate. This considerable

overlap includes the NatA/E subunits NAA10 (AT5G13780.1), NAA50 (AT5G11340.1), and NAA15 (AT1G80410.2) as well as the ribosome subunits EMB1473 (AT1G78630.1) and EMB3126 (AT3G63490.1) and the translation elongation factor AT1G07920.1. This supports the hypothesis that NAA50 associates with the core NatA complex at the ribosome. Although HYPK accumulated 35-fold in the α-NAA50 co-immunoprecipitate, the enrichment was not statistically significant. Given that in *in vitro* experiments with human NatA/E components, negative cooperative binding of *Hs*NAA50 and *Hs*HYPK to the core NatA complex was observed, this does not come as a surprise. Moreover, Tab. 6 revealed that after normalizing for the amount of NAA50 co-immunoprecipitated with α-NAA15 and α-NAA50, the α-NAA15 antibody co-immunoprecipitated more than 2000-fold more NAA10 and NAA15 than the α-NAA50 antibody, indicating that as previously observed for human NAA50 (Hou et al., 2007), *At*NAA50 is mostly found outside of the *At*NatA/E complex.

Table 6: Proteins (co)-immunoprecipitated from wildtype protein extracts incubated with a specific α-NAA15 or α-NAA50 antiserum. Protein extracts of six-week-old soil-grown (4.3.2) wildtype plants were incubated with antiserum (n=3). Subsequently, the samples were mixed with protein A/G beads (4.5.4) to capture the antibodies and proteins which interacted with them. Protein extracts incubated exclusively with protein A/G beads served as a negative control. After separating the beads from the supernatant, the proteins bound to the beads were released by adding Laemmli buffer. The proteins were separated by SDS-PAGE, and fractions of the gel were subjected to an in-gel digest. The mass-spectrometry analysis of the digested samples was performed by Sabine Merker and Dr. Thomas Ruppert from the Core Facility for Mass Spectrometry & Proteomics (University of Heidelberg). This table shows the abundance (x10^5) of proteins as determined by maximum peak height in individual samples (#1-3).

	negative control			**anti-NAA15**			**anti-NAA50**		
	#1	**#2**	**#3**	**#1**	**#2**	**#3**	**#1**	**#2**	**#3**
NAA10 (AT5G13780.1)	2	5	4	1,756	2,514	1,367	72	34	56
NAA15 (AT1G80410.2)	18	37	16	15,765	23,471	16,358	433	423	325
NAA50 (AT5G11340.1)	11	14	8	33	38	30	1,954	1,963	2,358
HYPK (AT3G06610.1)	0	0	0	223	290	131	9	9	3

EDR1 (AT1G08720.1)	1	1	2	0	0	0	37	42	44

Among the proteins which accumulated exclusively upon immunoprecipitation with α-NAA50, EDR1 (AT1G08720.1) stood out. EDR1 is an ER-localized negative regulator of plant stress responses. Recently, this kinase was identified as an interaction partner of NAA50 (Neubauer & Innes, 2020). Since NAA50 and EDR1 both localize to the ER and EDR1 was not detected in the α-NAA15 immunoprecipitate, it can be assumed that the interaction between NAA50 and EDR1 occurs outside of the NatA/E complex at the ER or the ER membrane. According to their annotation in TAIR10, apart from EDR1 and NAA50 itself, eight additional proteins with ER-localization were identified in the α-NAA50 co-immunoprecipitate.

As previously observed for the putative NAA15 interaction partners, typical NatA substrates (MA, MC, MG, MS, MT, MV) were overrepresented among the proteins in the α-NAA50 co-immunoprecipitate. While NatA substrates accounted for 146 of 209 significantly enriched proteins (70.0 %), only 28 (13.4 %) and 22 (10.5 %) of the significantly enriched proteins in the α-NAA50 co-immunoprecipitate were classified as NatB (MD, ME, MN, MQ) or NatC/E/F (MF, MI, MK, ML, MM, MY) substrates, respectively. Two of the putative NatC/E/F targets (AT5G19140.1 and AT3G09980.1) are predicted to localize to the cytosol and have previously been identified as N-terminally acetylated according to the N-ter database.

In addition to putative NAA50 substrates, the α-NAA50 antiserum immunoprecipitated a variety of ribosomal (AT3G06040.3, AT1G78630.1, AT3G63490.1, AT3G53430.1, AT2G31610.1, AT3G24830.1, AT4G16720.1, AT5G61170.1, AT5G07090.1, AT5G40950.1, AT1G33140.1, and AT3G04840.1) and translation related proteins such as the translation initiation factor AT2G39990.1 and the translation elongation factor AT1G07920.1. Moreover, several molecular chaperones (AT3G13860.1, AT3G44110.1, AT4G35450.5, AT3G09440.4, AT5G56010.1, and AT5G20890.1), proteasome subunits (AT1G53850.1, AT4G38630.1, AT2G32730.1, and AT1G53750.1) and proteases (AT1G02560.1, AT1G09130.3) were identified in the co-immunoprecipitate. A complete list of all 209 putative interactors can be found in the Supplement (Supplementary Tab. S2).

In summary, the co-immunoprecipitation assay confirmed the association of *At*NAA50 with the core *At*NatA components as previously observed in a split luciferase assay (2.1.3). The enrichment of the ribosomal proteins EMB1473 and EMB3126 in both the α-NAA15

and α-NAA50 co-immunoprecipitate suggests that this interaction occurs at the ribosome. However, in agreement with the hypothesis that the NatA complex does not bind the majority of *At*NAA50, several ER-localized proteins such as the known NAA50-interactor EDR1 were co-immunoprecipitated exclusively by α-NAA50. Moreover, the detection of putative NAA50 substrates in the α-NAA50 co-immunoprecipitate opens up new avenues for identifying the first *in vivo* substrate of *At*NAA50.

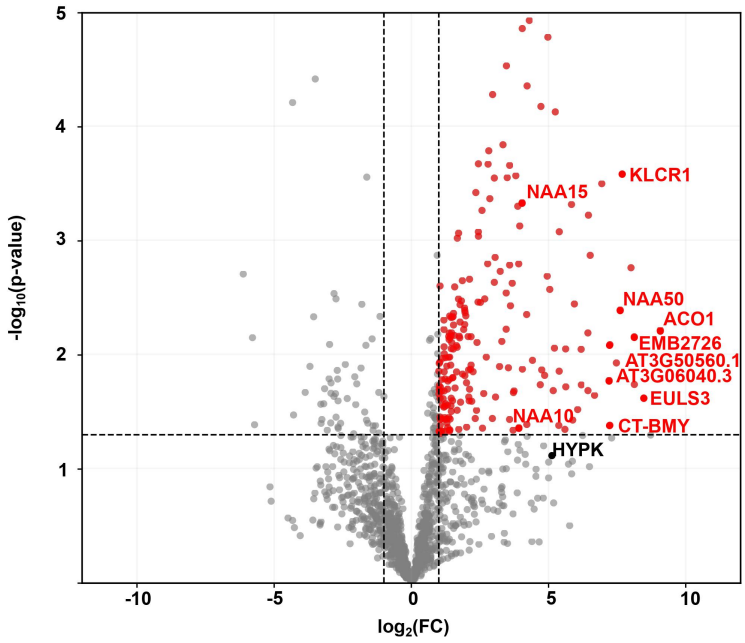

Figure 15: Proteins (co)-immunoprecipitated from wildtype protein extracts incubated with a specific α-NAA50 antiserum. Protein extracts of six-week-old soil-grown (4.3.2) wildtype plants were incubated with α-NAA50 antiserum (n=3). Subsequently, the samples were mixed with protein A/G beads (4.5.4) to capture the antibodies and the proteins which interacted with them. Protein extracts incubated exclusively with protein A/G beads served as a negative control. After separating the beads from the supernatant, the proteins bound to the beads were released by adding Laemmli buffer. The samples were separated by SDS-PAGE, and two fractions of the gel ($\leq$20 kDa and $\geq$50 kDa) were cut out and subjected to an in-gel digest. The digested samples were analyzed by mass-spectrometry. The mass-spectrometry analysis was performed by Sabine Merker and Dr. Thomas Ruppert from the Core Facility for Mass Spectrometry & Proteomics (University of Heidelberg). This volcano plot depicts the significantly ($>$2-fold, $p<0.05$ in a Student's t-test) enriched proteins identified in the α-NAA50 co-immunoprecipitate in red. The ten most enriched proteins and the NatA/E subunits NAA10, NAA15, and HYPK were labelled with their corresponding TAIR symbols.

2.2 The interplay between *At*NAA50 and the core NatA subunits *in vivo*

In the previous chapter it was established that *At*NAA10, *At*NAA15, *At*HYPK and *At*NAA50 interact to form the ribosome-associated *At*NatA/E complex. The following chapter explores the biological role of *At*NAA50 in the context of classical NatA functions such as the regulation of protein turnover (2.2.3) and plant stress responses (2.2.4). To prepare for these *in vivo* analyses, the *naa50* knockout lines *naa50-1* (SAIL_1210_A02, Col-0 background) and *naa50-2* (SAIL_1186_A03, Col-3 background) were characterized (2.2.1).

2.2.1 Characterization of *naa50* knockout mutants

According to The Arabidopsis Information Resource (TAIR), the tDNA insertions in SAIL_1186_A03 and SAIL_1210_A02 map to the first (*naa50-2*) and second (*naa50-1*) intron of *At*NAA50 (AT5G11340). Indeed, PCR amplification of genomic DNA with a left border primer (#321) and a gene-specific primer (#646 for *naa50-1* and #604 for *naa50-2*) followed by sequencing of the PCR products confirmed the location of the tDNA insertions 1,159 bp (*naa50-2*) and 1,468 bp (*naa50-1*) upstream of the start codon (Fig. 16A; Stephan, 2011).

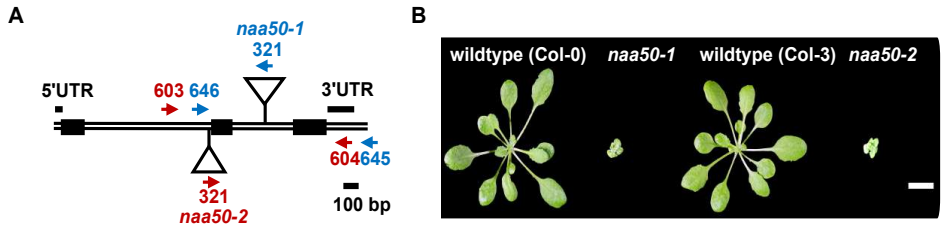

Figure 16: Gene model and phenotype of *naa50* knockout mutants. A) Gene model for AT5G11340 (NAA50). Black boxes represent exons. Triangles mark the tDNA insertion sites of *naa50-1* (SAIL_1210_A02) and *naa50-2* (SAIL_1186_A03). Blue (*naa50-1*) and red (*naa50-2*) arrows represent the primers used for genotyping. **B)** Representative images of homozygous six-week-old *naa50* mutants and wildtype plants. Plants were cultivated on 1/2 MS medium for four weeks (4.3.3) under short-day conditions and subsequently transferred to soil and grown under short-day conditions for an additional two weeks (scale bar = 1 cm).

For both tDNA insertion lines, homozygous mutants could be identified. As reported recently (Armbruster et al., 2020; Feng et al., 2020; Neubauer & Innes, 2020), homozygous *naa50* mutants displayed a dramatic growth retardation with most plants terminating growth after the formation of the first small leaves (Fig. 16B). Only rarely *naa50* mutants reached

the flowering stage and if they did, no seeds were produced. Plants heterozygous for the tDNA insertion into the *NAA50* gene however were indistinguishable from wildype plants.

To determine the impact of the tDNA insertions in the *NAA50* gene on the transcription of *NAA50* and the putative NatA/E subunits *NAA10*, *NAA15* and *HYPK*, a qRT-PCR analysis of wildtype plants (Col-0 and Col-3) as well as the *naa50* knockout mutants was performed. Since the knockout mutants do not germinate well on soil, plants were grown on 1/2 MS medium for four weeks (4.3.3) and subsequently transferred to soil where they were grown for an additional two weeks under short-day conditions (4.3.2). Afterwards, leaf material was harvested for RNA extraction (4.4.11) and subsequent cDNA synthesis (4.4.12). While qRT-PCR (4.4.13) verified the abscence of *NAA50* transcripts in *naa50-1* and *naa50-2*, the transcription of the genes encoding for the remaining NatA/E subunits was not affected by the tDNA insertions (Fig. 17).

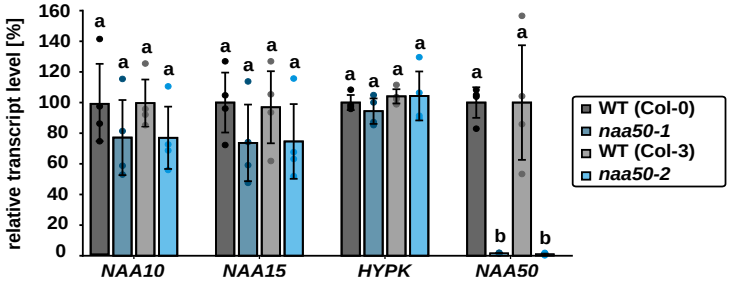

Figure 17: Knockout of *NAA50* does not impact the transcription of genes encoding for the other *At*NatA/E subunits. Transcript levels of *NAA10*, *NAA15*, *HYPK*, and *NAA50* as determined via qRT-PCR (4.4.13) with specific primers (Supplementary Tab. S8) in leaf material of six-week-old *naa50* mutants and wildtype plants cultivated under short-day conditions. Plants were germinated on 1/2 MS medium (4.3.3) and transferred to the soil after four weeks. Data given as means ± standard deviation. Different letters indicate individual groups identified by multiple pairwise comparisons with a Holm-Sidak, One-way ANOVA test ($p<0.05$, n=4).

To confirm those findings on the protein level, the amount of NAA10, NAA15, and NAA50 protein in leaf material collected from four-week-old wildtype plants and *naa50* mutants grown on 1/2 MS plates under short-day conditions (4.3.3) was quantified. To this end, total soluble proteins were extracted (4.5.1), separated with SDS-PAGE (4.5.8), and transferred to a PVDF membrane (4.5.10) where NAA10, NAA15, and NAA50 were detected with specific antisera (Tab. 18). While the NAA50 protein was readily detectable in the wildtype, it was absent in both tDNA insertion lines (Fig. 18), demonstrating that *naa50-1* and *naa50-2* are full knockout mutants. At the same time, the NAA10 and NAA15 protein levels remained unchanged. This finding is remarkable since the downregulation of

NAA10 or NAA15 with an artificial microRNA approach results in co-downregulation of the respective other subunit on the transcript and protein level (Linster et al., 2015).

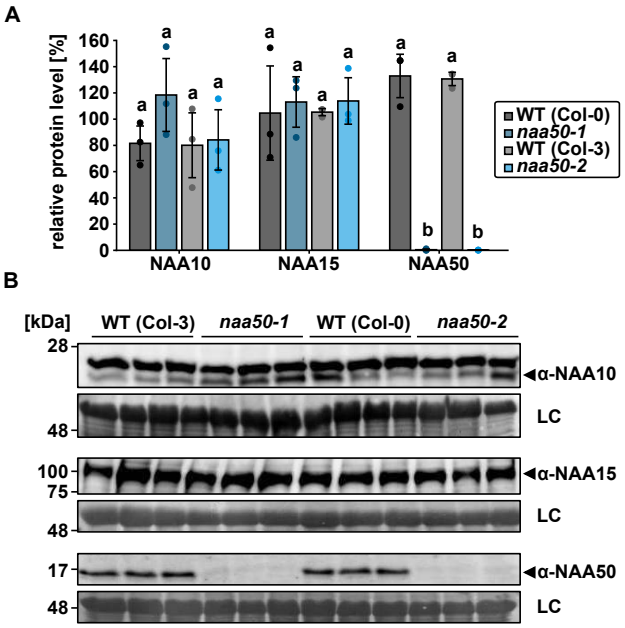

Figure 18: Knockout of NAA50 does not impact the abundance of other *At*NatA/E subunits on the protein level. **(A)** Quantification of the blots shown in **(B)**. Protein levels of NAA10, NAA15, and NAA50 were determined with specific antisera (4.5.10) in four-week-old *naa50* mutants and wildtype plants cultivated on 1/2 MS plates (4.3.3) under short-day conditions. Data given as means ± standard deviation. Different letters indicate individual groups identified by multiple pairwise comparisons with a Holm-Sidak, One-way ANOVA test ($p<0.05$, n=3). The expected sizes of the detected proteins are marked with black triangles (NAA10: 20 kDa, NAA15: 100 kDa, NAA50: 18.5 kDa). 25 μg raw protein extract was loaded per lane. Amido black stainings of the membranes served as respective loading controls (LC). Uncropped pictures of the immunoblots are shown in Fig. S7.

2.2.1.1 Whole proteome analysis of *naa50-2*

The severe dwarf phenotype of the *naa50* knockout mutants suggests a crucial role of NAA50 for plant growth and development. In order to understand this vital function, a mass-spectrometry based proteome analysis (4.7.3) was performed on protein extracts of four-week-old wildtype and *naa50-2* seedlings grown under short-day conditions on 1/2 MS medium (4.3.3). The experiment was carried out by Dr. Annika Brünje and Dr. Jürgen Eirich under the supervision of Prof. Dr. Iris Finkemayer (Institute for Plant Biology and Biotechnology, University of Münster) and identified 4,507 protein groups, of which 621

(13.8 %) were differentially expressed (>1.5-fold up- or downregulated, p<0.05 in a Student's t-test) between wildtype and mutant (Fig. 19). While the abundance of 476 protein groups increased significantly in *naa50-2*, only 145 protein groups were downregulated in the tDNA insertion line. The abundance of the NatA subunits NAA10 and NAA15 was not differentially regulated between mutant and wildtype, confirming the qRT-PCR and immunodetection results (Fig. 17 and Fig. 18). NAA50 and HYPK were not detected in either genotype and are therefore not included in the dataset.

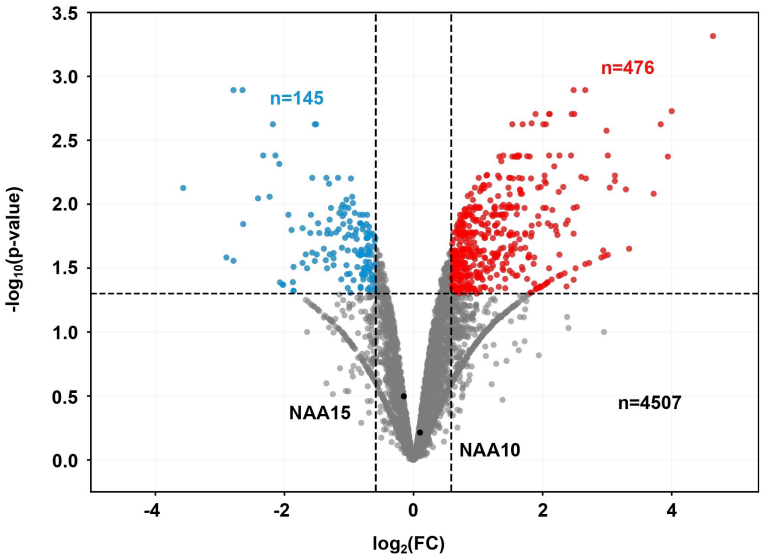

Figure 19: Differentially expressed proteins between wildtype and *naa50-2*. Volcano plot depicting the significantly (>1.5-fold, p<0.05 in a Student's t-test) regulated protein groups in red (upregulated) and blue (downregulated). Proteins with unchanged abundance are labeled in grey. Proteins were extracted from four-week-old seedlings grown under short-day conditions on 1/2 MS medium (4.3.3). For each replicate (n=4), >20 individual seedlings were pooled to harvest a total mass of 100 mg plant material per replicate. Plants were grown by Dr. Eric Linster from the Centre for Organismal Studies, University of Heidelberg. The mass-spectrometry analysis (4.7.3) was performed by Prof. Dr. Iris Finkemeier, Dr. Annika Brünje, and Dr. Jürgen Eirich from the Institute for Plant Biology and Biotechnology, University of Münster. Adapted from Armbruster et al., 2020.

Even though the protein extracts contained proteoforms originating from a wide array of subcellular compartments (3,508 mapped to the chloroplast; 1,794 to the cytoplasm; 1,542 to the nucleus; 1,139 to the mitochondrion; 953 to the plasma membrane and 451 to the ER according to TAIR), proteoforms localizing to specific subcellular compartments were significantly (>2-fold, p<0.05 in a Fisher's Exact test) overrepresented among the differentially regulated proteoforms (Fig. 20A).

Those compartments were identified in a GO-Term enrichment analysis with the DAVID functional annotation tool (4.11.3) and included the ER lumen (5.5-fold, 15 proteoforms), the vacuole (5.3-fold, 5 proteoforms), the cell wall (2.6-fold, 47 proteoforms), the extracellular region (2.2-fold, 101 proteoforms) and components of the plasma membrane (2.9-fold for integral and 2.0-fold for anchored components, 17 and 12 proteoforms, respectively). Remarkably, sorting to all of the aforementioned cellular compartments requires the processing of proteins through the secretory pathway starting at the ER. This is especially interesting in the context of the previously uncovered ER-localization of *At*NAA50 (Armbruster et al., 2020; Neubauer & Innes, 2020).

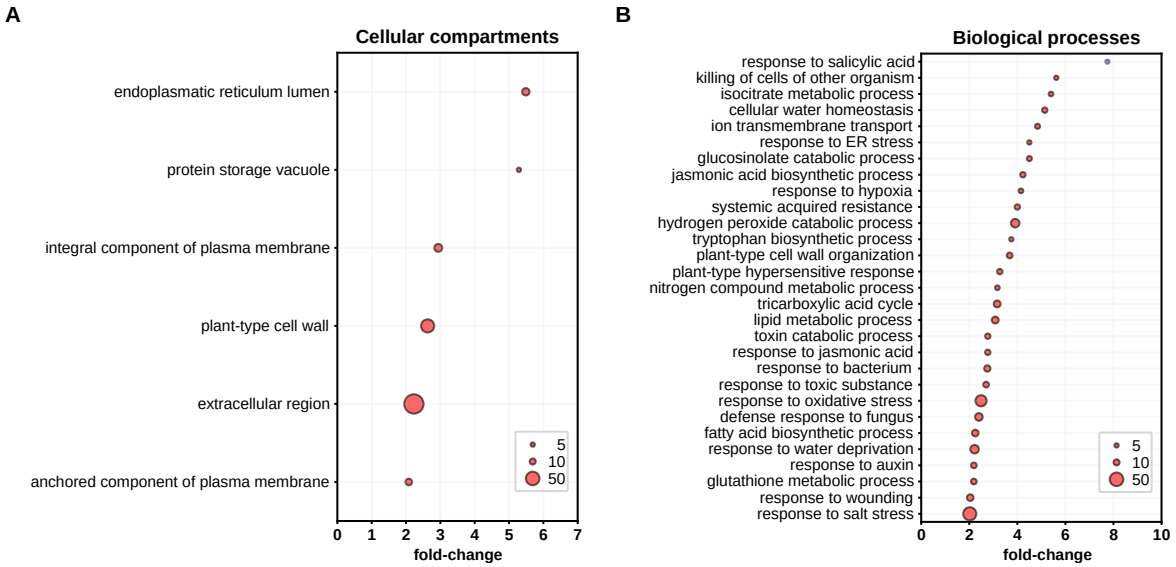

Figure 20: GO-Term enrichment analysis of differentially expressed proteins in *naa50-2*. The significantly (>1.5-fold, p<0.05 in a Fisher's Exact test) up- and downregulated protein groups as identified by mass-spectrometry (4.7.3, Fig. 19) were subjected to separate GO-Term enrichment analyses with the DAVID functional annotation tool v.6.8. The entirety of identified proteoforms in the dataset was used as background. Dots indicate **(A)** cellular compartments or **(B)** biological processes significantly (>2-fold, p<0.05 in a Fisher's Exact test) overrepresented among upregulated (red) and downregulated (blue) transcripts, respectively. The size of the dots represents the number of proteoforms assigned to each GO-Term. Only compartments and biological processes encompassing at least five differentially expressed proteoforms were considered.

In addition, the GO-Term enrichment analysis (4.11.3) revealed that among the proteins accumulating in *naa50-2*, proteins involved in the adaptation to a variety of adverse conditions were significantly (>2-fold, p<0.05 in a Fisher's Exact test) overrepresented (Fig. 20B). These conditions included ER stress (4.5 fold, 5 proteoforms), hypoxia (4.2-fold,

6 proteoforms), oxidative stress (2.5- fold, 34 proteoforms), water deprivation (2.2-fold, 20 proteoforms), and salt stress (2.0-fold, 47 proteoforms). Furthermore, proteins involved in the adaptation to biotic stress were overrepresented among the proteoforms upregulated in the knockout mutant *naa50-2*. Specifically, those proteins mediated the systemic acquired resistance (4-fold, 8 proteoforms), the responses to bacteria (2.8-fold, 11 proteoforms), fungi (2.4-fold, 16 proteoforms), and wounding (2.0-fold, 12 proteoforms) as well as the plant-type hypersensitive response (3.2-fold, 8 proteoforms), which triggers apoptosis in infected tissues to block the spread of pathogen invasions. In line with these findings, the regulation of several stress-related phytohormones was disturbed in *naa50-2*. Among the upregulated proteoforms, proteoforms involved in the response to auxin (2.2-fold, 9 proteoforms) and jasmonic acid (2.7-fold, 8 proteoforms) were overrepresented, whereas proteoforms mediating the response to salicylic acid (7.7-fold, 5 proteoforms) were enriched among the downregulated proteoforms in *naa50-2*.

In essence, *naa50-2* mutants accumulated several proteins involved in the regulation of biotic and abiotic stress responses. Whether the observed changes in the protein expression profile of *naa50* were direct results of a lack of acetylation via *At*NAA50 remains unclear. Based on their N-terminal sequence (MF, MI, MK, ML, MM, or MY), approximately 12.2 % of all nuclear-encoded proteoforms identified in this proteome analysis were putative substrates of NatC, NatE, or NatF. The share of NatC/E/F substrates was similar among the upregulated (11.4 %) and downregulated (10.5 %) proteoforms in *naa50*, indicating that most of the differentially regulated proteoforms were not direct targets of NatC, NatE, or NatF. To identify direct *At*NAA50 targets, the stable-isotope protein N-terminal acetylation quantification (SILProNAQ) method (4.7.4) for comparative N-terminome profiling of wildtype and *naa50* was applied (2.2.1.2).

2.2.1.2 **N-terminome profiling of *naa50-2***

The SilProNAQ approach relies on the chemical acetylation of free N-termini in wildtype and mutant protein extracts with N-acetoxy-[2H3]-succinimide, followed by trypsin digestion and enrichment of N-terminal peptides with strong cation exchange. Subsequently, the N-termini are characterized via mass-spectrometry, and the NTA yields of individual proteins identified in wildtype and mutant are compared (4.7.4). For the experiment at hand, SilProNAQ was applied to protein extracts of whole four-week-old wildtype and *naa50-2* seedlings grown under short-day conditions on 1/2 MS medium (4.3.3). The mass-spectrometry

analysis was carried out by Dr. Willy V. Bienvenut, and Dr. Jean-Baptiste Boyer under the supervision of Dr. Carmela Giglione and Dr. Thierry Meinnel (Institute of Integrative Biology, University of Paris-Saclay) and led to the identification of 108 N-termini with quantifiable NTA yield in wildtype and *naa50-2*. For only two proteins (AT2G14880 and AT5G03370), the acetylation yield differed significantly (>2-fold, p<0.05) between the two genotypes (Fig. 21A).

A

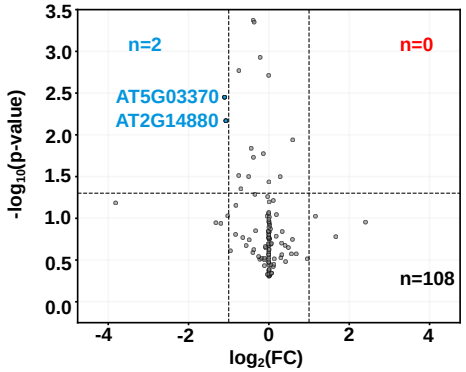

B

	NTA ratio (*aminaa10*:WT) [%]	NTA ratio (*naa50-2*:WT) [%]
AT5G11670	41.6	107.3
AT5G46790	46.0	100.8
AT1G65930	52.3	100.2
AT3G23810	59.8	100.3
AT3G53870	69.1	100.1
AT2G36530	78.3	100.0
AT3G52230	78.6	100.1

Figure 21: N-terminal protein acetylation yield in wildtype and *naa50-2*. **(A)** Volcano plot depicting acetylated N-termini quantified in both wildtype and *naa50-2*. Proteins with statistically significantly (>1.5-fold change, p<0.05 in a Student's t-test) changed N-terminal acetylation yields are labeled in red (increased acetylation in *naa50-2*) or blue (decreased acetylation in *naa50-2*). Proteins were extracted from four-week-old seedlings grown under short-day conditions on 1/2 MS medium (4.3.3). For each replicate (n=3 for *naa50-2* and n=2 for wildtype), > 20 individual seedlings were pooled to harvest a total mass of 100 mg plant material per replicate. Plants were grown by Dr. Eric Linster from the Centre for Organismal Studies, University of Heidelberg. The N-terminome profiling (4.7.4) was performed by Dr. Thierry Meinnel, Dr. Carmela Giglione, Dr. Jean-Baptiste Boyer and Dr. Willy V. Bienvenut from the Institute of Integrative Biology, University of Paris-Saclay. **(B)** The NTA yield of confirmed *At*NatA substrates remained unaffected in *naa50-2*. Proteins were quantified in at least two replicates of wildtype and the NatA knockdown mutant *aminaa10* (Linster et al., 2015). Adapted from Armbruster et al., 2020.

Both proteins localize to the chloroplast and harbour typical NatA-type N-termini. The acetylation yields in the wildtype were poor for both proteins (1.9 % for AT2G14880 and 13.9 % for AT5G03370) and dropped to even lower levels upon depletion of *At*NAA50 (0.9% for AT2G14880 and 6.4% for AT5G03370). Although these changes were statistically significant, it is unclear whether they have any biological relevance. It is conceivable that the SilProNAQ approach only picked up natural fluctuations in NTA yield. Given that *At*NAA50 is thought to acetylate less than 4 % of all soluble proteins in plants (Linster et al., 2020),

it does not surprise that the SilProNAQ approach did not allow for the identification of true *At*NAA50 *in vivo* substrates. The unbiased identification of *At*NAA50 substrates most likely requires the analysis of a higher number of N-termini.

Nevertheless, the results of the SilProNAQ analysis allowed for relevant conclusions regarding the biological function of *At*NAA50. Since *At*NatA is thought to acetylate more than half of all soluble proteins in *Arabidopsis thaliana*, the depletion of *At*NAA50 should result in significant shifts in NTA yield between wildtype and *naa50-2* if *At*NAA50 regulated *At*NatA activity in a similar manner than *At*HYPK. The absence of such shifts in NTA yield (Fig. 21A) indicates that *At*NAA50 did not modulate *At*NAA50 activity to a substantial degree. Indeed, there were seven previously identified NatA substrates among the 108 quantified N-termini (Linster et al., 2015). All seven retained their NTA levels in the *naa50-2* background (Fig. 21B).

Even though the proteome analysis of the *naa50* knockout mutants gave some interesting indications for possible physiological functions of *At*NAA50, the dwarf phenotype of the *naa50* knockout mutants did not allow for physiological experiments (e.g., pathogen infections) to further investigate these putative functions of *At*NAA50. To overcome this limitation, constitutive *NAA50* knockdown lines with a milder phenotype were generated with an artificial microRNA approach (2.2.2).

2.2.2 Generation and characterization of *aminaa50* knockdown plants

A *NAA50* microRNA precursor (Supplementary Fig. S8A) was designed with the Web microRNA Designer and synthesized in two consecutive PCRs using the primers #849 + #850 and #4726-#4729 as well as the pRS300 vector (#1082) as a template (Supplementary Fig. S4B). Subsequently, the miRNA precursor was cloned into the empty pBinAR expression vector (#1834), which harbours a kanamycin resistance gene and allowed for the expression of the microRNA precursor under the control of the constitutive CaMV 35S promoter (Supplementary Fig. S4C). The final pBinAR-35Sp-aminaa50 construct (#1655) was stably transformed into *Arabidopsis thaliana* wildtype plants (T0 generation). Through selection on plates containing AT-medium (4.1.2) supplemented with kanamycin (4.3.6), 16 positive transformants (*aminaa50* #1-16) were identified (T1 generation). To verify the presence of the microRNA construct in T1, the transformants were genotyped using the primers #3915 and #4839. Since all 16 transformants contained the microRNA construct (data not shown), seeds were harvested, and the growth phenotype of T2 plants was analyzed. For

this purpose, the rosette radius of four individual plants of each *aminaa50* line was assessed and correlated with the relative *NAA50* transcript level as determined by qRT-PCR (4.4.13). All of the 64 analyzed *aminaa50* plants displayed lower *NAA50* transcript levels than the average wildtype, indicating a successful knockdown of *NAA50* with the microRNA approach (Fig. 22). Interestingly, there was no correlation (R^2=0.01) between rosette radius and relative *NAA50* transcript levels. In total, 40 of 64 plants (62.5 %) displayed relative *NAA50* transcript levels below 15 % of the wildtype level. Of those 40 plants, 28 (70 %) had a rosette radius within $\pm 2\sigma$ of the radius measured for wildtype plants, suggesting that minimal *NAA50* transcript levels are sufficient to ensure normal plant growth and survival. While the *NAA50* transcript levels fluctuated heavily within most *aminaa50* lines due to ongoing segregation, the lines #2, #7, #9, #13 and #16 displayed consistently low relative *NAA50* transcript levels (<15 % of wildtype) in all four analyzed individuals per line.

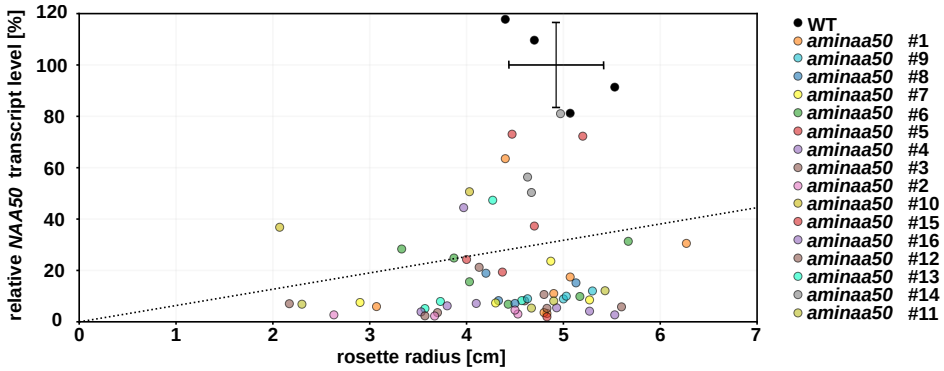

Figure 22: Downregulation of *NAA50* does not correlate with diminished rosette radius. Correlation between the relative *NAA50* transcript level and the growth phenotype of *aminaa50* plants. The rosette radius of six-week-old T2 plants grown on soil (4.3.2) under short-day conditions was correlated with the relative *NAA50* transcript level as determined by qRT-PCR (4.4.13). Each data point represents an individual plant (n=64 for *aminaa50* and n=4 for wildtype). The independent *aminaa50* lines #1-16 are marked with different colors. For each line, four plants were assessed. The dotted line shows the correlation (R^2=0.01) between rosette radius and relative *NAA50* transcript level determined over all plants. The standard deviation of the wildtype *NAA50* transcript level and rosette radius are marked with a black cross.

To assess the segregation patterns of the *aminaa50* lines #2, #7, #9, #13, and #16, seeds of the twenty individual plants were harvested, and the T3 generation was germinated on plates containing AT-medium (4.1.2) supplemented with kanamycin (4.3.6). The selection revealed that the lines #2.2, #9.4, #9.7, and #13.6 exhibited a 100 % survival rate indicative of multiple insertions of the microRNA construct. Among those four T3 lines, *aminaa50* #9.4 and #13.6 had displayed the lowest relative *NAA50* transcript levels in the T2 generation

(2.2 % for *aminaa50* #9.4 and 8.2 % for *aminaa50* #13.6) and were hence selected for further characterization.

While there was no statistically significant ($p<0.05$ in a One-way ANOVA test) difference between the average rosette radius measured for the four wildtype plants and the *aminaa50* #9 and #13 lines in the T2 generation, the selected individuals *aminaa50* #9.4 and #13.6 were slightly smaller than wildtype plants (3.7 and 4.6 cm rosette radius compared to 4.9 cm for the average wildtype). To determine whether this phenotype persisted in the T3 generation, the fresh weight (Fig. 23A) and rosette radius (Fig. 23B) of eight-week-old *aminaa50* #9.4 and #13.6 plants grown under short-day conditions were determined. No statistically significant ($p<0.05$ in a One-way ANOVA test) differences between the wildtype and the *aminaa50* lines could be detected for the two traits. In line with this finding, the visual phenotype of the *aminaa50* plants resembled that of the wildtype (Fig. 23C).

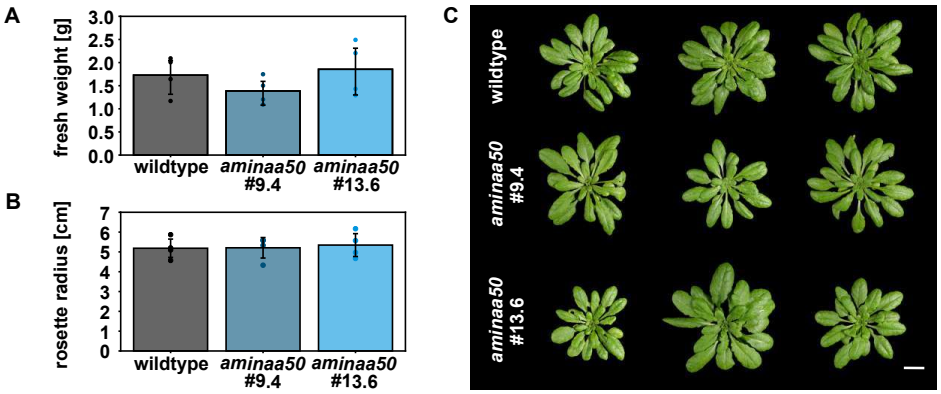

Figure 23: Growth phenotype of selected *aminaa50* knockdown lines. (A) Fresh weight and **(B)** rosette radius of wildtype, *aminaa50* #9.4 and *aminaa50* #13.6 T3 plants. Data given as means ± standard deviation. Different letters indicate individual groups identified by multiple pairwise comparisons with a Holm-Sidak, One-way ANOVA test ($p<0.05$, n=4). **(C)** Representative images of eight-week-old *aminaa50* mutants and wildtype plants germinated on standard AT-medium (wildtype, 4.1.2) or AT-medium supplemented with kanamycin (*aminaa50*, 4.3.6). After four weeks of growth on solid medium, the surviving plants were transferred to soil and left to grow for an additional four weeks. Growth occurred under short-day conditions (scale bar = 2 cm).

To determine the impact of the microRNA insertion in *aminaa50* #9.4 and #13.6 on the expression of NAA50 and the other NatA subunits, leaf material of the previously analyzed plants (Fig. 23) was harvested and subjected to protein (4.5.1) and RNA (4.4.11) extraction. Whereas the protein extracts were frozen away until further usage, the RNA was used for cDNA synthesis (4.4.12) followed by a qRT-PCR (4.4.13). The analysis revealed a strong

downregulation of *NAA50* transcription in the *aminaa50* #9.4 and #13.6 lines to 4.3 and 3.5 % of the wildtype level, respectively (Fig. 24). At the same time, the transcription of the genes encoding for the remaining NatA/E subunits was not affected by the microRNA expression as previously observed for the *naa50* knockout lines (2.2.1).

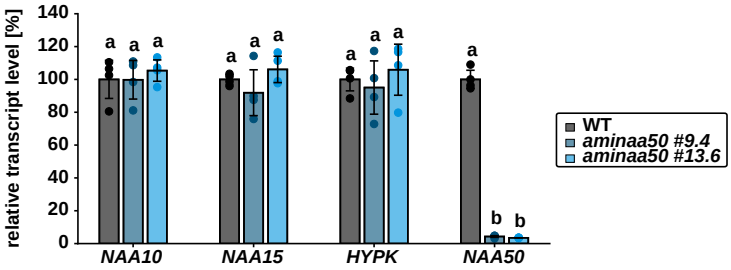

Figure 24: Knockdown of *NAA50* does not impact the transcription of other *At*NatA/E subunits. Transcript levels of *NAA10*, *NAA15*, *HYPK*, and *NAA50* as determined via qRT-PCR (4.4.13) with specific primers (Supplementary Tab. S8). T3 plants were germinated on standard AT-medium (wildtype, 4.1.2) or AT-medium supplemented with kanamycin (*aminaa50*, 4.3.6). After four weeks of growth on solid medium, the surviving plants were transferred to soil and left to grow for an additional four weeks. Growth occurred under short-day conditions. Data given as means ± standard deviation. Different letters indicate individual groups identified by multiple pairwise comparisons with a Holm-Sidak, One-way ANOVA test ($p<0.05$, n=4).

The amount of NAA10, NAA15, and NAA50 protein in the previously generated protein extracts was quantified to confirm those findings on the protein level. To this end, proteins were separated with SDS-PAGE (4.5.8), and transferred to a PVDF membrane (4.5.10), where NAA10, NAA15 and NAA50 were detected with specific antisera (Tab. 18). While the NAA10 and NAA15 protein levels remained unchanged, the NAA50 protein was readily detectable in the wildtype but seemingly absent in both *aminaa50* mutant lines (Fig. 25). The apparent absence of NAA50 protein in the wildtype-like *aminaa50* lines was astonishing in light of the dwarf phenotype previously observed for the *naa50-1* and *naa50-2* knockout mutants (Fig. 16).

One possible explanation for the absence of growth defects in *aminaa50* is the expression of minimal amounts of NAA50 protein. These low levels of NAA50 could be sufficient to ensure normal plant growth and development but might not be detectable with the specific antiserum used in this thesis. To determine the detection limit of the aforementioned antiserum, proteins were extracted from wildtype plants (4.5.1), and dilutions of the protein extracts (1:2, 1:4, 1:10) were prepared. Subsequently, the dilutions were loaded on an SDS-PAGE gel (4.5.8) and later transferred to a PVDF membrane (4.5.10), where the

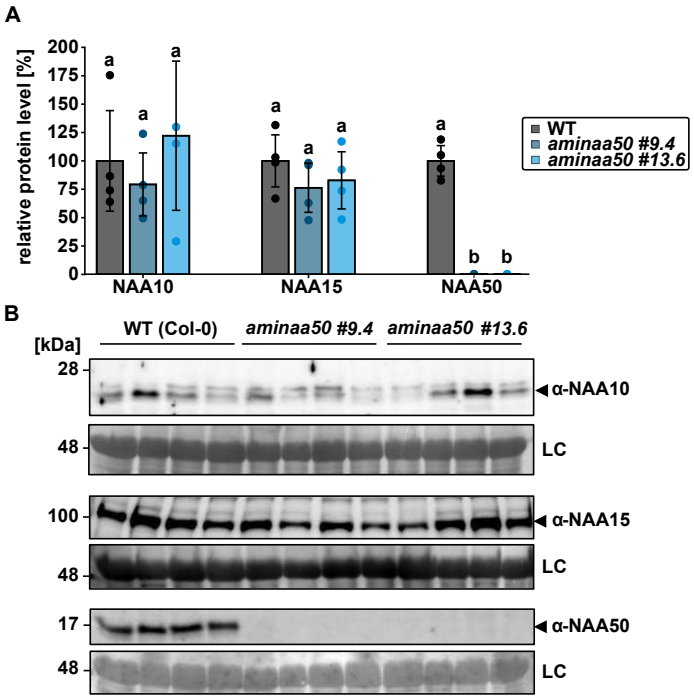

Figure 25: Knockdown of *NAA50* does not impact the abundance of other *At*NatA/E subunits on the protein level. (A) Quantification of the blots shown in **(B)**. Data given as means ± standard deviation. Different letters indicate individual groups identified by multiple pairwise comparisons with a Holm-Sidak, One-way ANOVA test ($p<0.05$, n=4). Plants were germinated on standard AT-medium (wildtype, 4.1.2) or AT-medium supplemented with kanamycin (*aminaa50*, 4.3.6). After four weeks of growth on solid medium, the surviving plants were transferred to soil and left to grow for an additional four weeks. Growth occurred under short-day conditions. Protein levels of NAA10, NAA15, and NAA50 were determined with specific antisera (4.5.10) in 25 μg raw protein extract (4.5.1) per lane. The expected sizes of the detected proteins are marked with black triangles (NAA10: 20 kDa, NAA15: 100 kDa, NAA50: 18.5 kDa). Amido black stainings of the membranes served as respective loading controls (LC). Uncropped pictures of the immunoblots are shown in Supplementary Fig. S9.

NAA50 protein was detected with the antiserum in question (Fig. 26). While the NAA50 protein was readily detectable in the 1:2 (15 μg raw extract) and 1:4 dilutions (12.5 μg raw extract), there was only a faint signal in the 1:10 dilutions (3 μg raw extract), indicating that the detection limit of the analyzed antiserum lies at approximately 10 % of wildtype protein levels under the here-applied conditions (1:2,500 dilution of the antiserum; 3 h incubation at RT; detection with the SuperSignal West Extended Duration Substrate by Thermo Scientific after 5 sec exposure time). In light of this detection limit, it is conceivable that the *aminaa50* lines #9.4 and #13.6 harbour up to 10 % of the NAA50 wildtype protein level despite of the seemingly absent NAA50 signal upon immunodetection (Fig. 25).

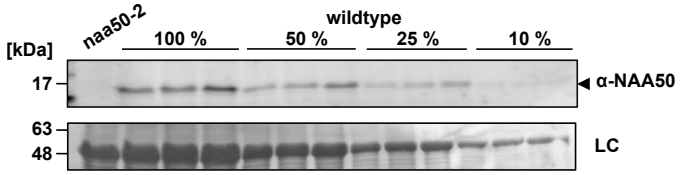

Figure 26: Detection limit of the specific antiserum against *At*NAA50. (A) Proteins were extracted from *naa50-2* and wildtype (n=3) plants. Dilutions were prepared starting from 30 μg of raw extract (= 100 %). The *At*NAA50 level was detected with a specific antiserum (diluted 1:2.500 in TBS-T supplemented with 0.5 % BSA, 3 h incubation at RT). **(B)** An Amido black staining of the membrane (lower panel) served as a loading control (LC). An uncropped picture of the immunoblot is shown in Supplementary Fig. S10.

In summary, the artificial microRNA approach led to the generation of the *aminaa50* lines #9.4 and #13.6, which displayed a robust knockdown of NAA50 (>90 %) on the transcript and protein level but nevertheless closely resembled the wildtype phenotype.

2.2.2.1 Whole transcriptome analysis of *aminaa50* #13.6

As previously determined, loss of NAA50 results in the accumulation of stress-related proteins in *naa50-2* knockout mutants (2.2.1.1). To determine whether the same was true for *aminaa50* despite the wildtype-like rosette diameter, whole transcriptome (2.2.2.1) and proteome (2.2.2.2) analyses of the knockdown line #13.6 were performed. For both analyses, leaf material of seven-week-old plants grown on soil under short-day conditions was harvested. Subsequently, RNA (4.4.11) and total soluble proteins (4.5.1) were extracted. Since the electropherogram of the RNA showed no signs of contaminants or RNA degradation, the samples were hybridized on a microarray of the Arabidopsis Gene 1.0 ST type (Affymetrix, Santa Clara, USA), and a global transcriptome analysis (4.8) was performed in collaboration with Dr. Carsten Sticht and Dr. Carolina De La Torre (NGS Core Facility,

University of Heidelberg). To determine inter- and intragroup variability and to identify biological outliers, the Pearson's correlation coefficient was calculated between all samples and visualized as a heatmap (Fig. 27). While the heatmap showed little variance among the wildtype replicates, the divergence among the *aminaa50* #13.6 replicates was more pronounced, mostly due to sample #4 which seemed to exhibit a slightly different expression pattern than the remaining three *aminaa50* #13.6 replicates. Nevertheless, the wildtype and *aminaa50* samples were found in clearly separated clusters, allowing for further analysis of the data.

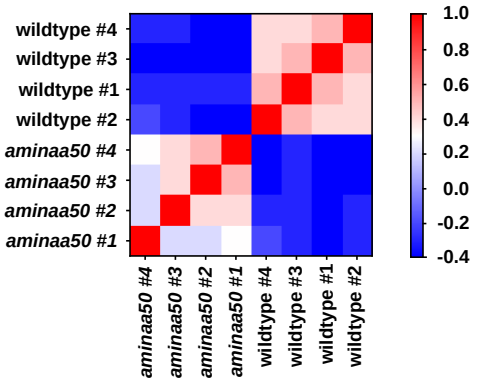

Figure 27: Gene expression profile of wildtype and *aminaa50* #13.6. Heatmap depicting the correlation between wildtype and *aminaa50* #13.6 samples as quantified by the Pearson's correlation coefficient (n = 27,826 genes). RNA was extracted from seven-week-old plants grown under short-day conditions on soil (n=4). The transcriptome analysis (4.8) was performed by Dr. Carsten Sticht and Dr. Carolina De La Torre from the NGS Core Facility, University of Heidelberg.

The microarray covered 27,826 transcripts, of which 27,059 (97.2 %) were protein coding. In total, 1,001 of all transcripts (3.6 %) were differentially regulated (>2-fold up- or downregulated, $p<0.05$ in a Student's t-test) between wildtype and mutant (Fig. 28). While the abundance of 721 transcripts increased significantly in *aminaa50* #13.6, only 280 transcripts were downregulated in the knockdown line. As previously quantified via qRT-PCR (Fig. 24), *NAA10*, *NAA15*, and *HYPK* were unaffected in *aminaa50* #13.6, whereas *NAA50* transcription was 4.3-fold downregulated.

Among the differentially regulated transcripts, transcripts encoding for proteins localizing to specific subcellular compartments were significantly (>2-fold, $p<0.05$ in a Fisher's Exact test) overrepresented. Those compartments were identified in a GO-Term enrichment analysis with the DAVID functional annotation tool (4.11.3) and - in the case of the upregulated transcripts - included the plasma membrane (5.1-fold, 33 transcripts), the cell

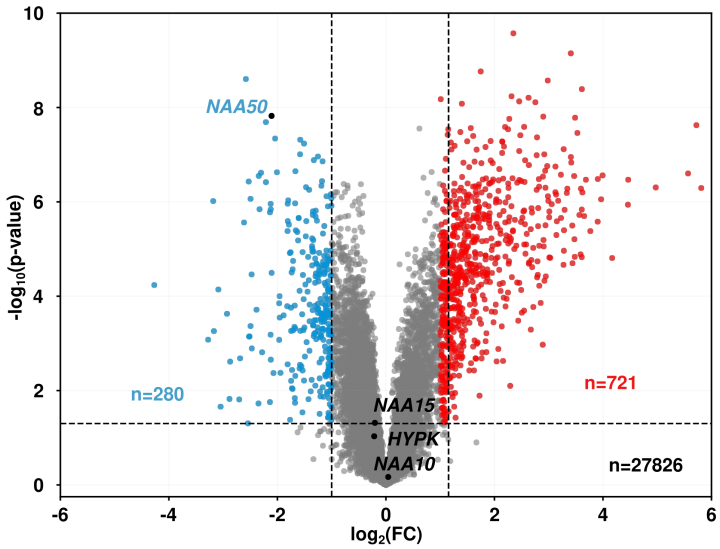

Figure 28: Differentially transcribed genes between wildtype and *aminaa50* #13.6. Volcano plot depicting the significantly (>2-fold, p<0.05 in a Student's t-test) regulated transcripts in red (upregulated) and blue (downregulated). Transcripts with unchanged abundance are labeled in grey. RNA was extracted from seven-week-old plants (n=4) grown under short-day conditions on soil (4.3.2). The transcriptome analysis (4.8) was performed by Dr. Carsten Sticht and Dr. Carolina De La Torre from the NGS Core Facility, University of Heidelberg.

wall (4.3-fold, 39 transcripts), the plasmodesmata (2.4- fold, 64 transcripts) and the apoplast (2.2-fold, 29 transcripts). Among the downregulated transcripts, transcripts encoding for proteins localizing to the vacuole (3.0-fold, 19 transcripts) or the peroxisome (3.0-fold, 7 transcripts) were overrepresented (Fig. 29A). A similar pattern was observed in *naa50-2* knockout mutants where proteins localizing to the vacuole (5.3-fold, 5 proteoforms), the cell wall (2.6-fold, 47 proteoforms) and the plasma membrane (2.0-fold, 12 proteoforms) accumulated (2.2.1.1).

Furthermore, the GO-Term enrichment analysis (4.11.3) revealed that among the transcripts accumulating in *aminaa50* #13.6, transcripts involved in the adaptation to abiotic stress were significantly (>2-fold, p<0.05 in a Fisher's Exact test) overrepresented (Fig. 29B). These stress responses included the response to hypoxia (7.0-fold, 5 transcripts), the response to the absence of light (7.0-fold, 5 transcripts), the response to osmotic stress (3.0-fold, 10 transcripts), the response to cold (2.4-fold, 20 transcripts), the response to water deprivation (2.3-fold, 18 transcripts) and the response to oxidative stress (2.3-fold, 18 transcripts). In addition, transcripts mediating the defense response to biotic stress (2.5-fold, 46 transcripts) were upregulated in *aminaa50* #13.6. Specifically, those transcripts regu-

lated glucosinolate metabolism (4.7-fold, 5 transcripts), the response to bacteria (5-fold, 14 transcripts), viruses (4.7-fold, 5 transcripts), and fungi (4.5-fold, 9 transcripts) as well as the plant-hypersensitive response (5.4-fold, 11 transcripts). Another cluster of biological processes which was strikingly upregulated in *aminaa50* #13.6 was related to cell wall organization (2.8-fold, 25 transcripts) and cell wall biogenesis (6.7-fold, 11 transcripts). In line with these findings, the regulation of several stress and growth-related phytohormones was disturbed in *aminaa50* #13.6. Among the upregulated transcripts, transcripts involved in the response to brassinosteroids (8.5-fold, 8 transcripts), salicylic acid (4.7-fold, 20 transcripts), abscisic acid (3.5-fold, 19 transcripts), ethylene (2.8-fold, 14 transcripts), and auxin (2.2-fold, 18 transcripts) were overrepresented.

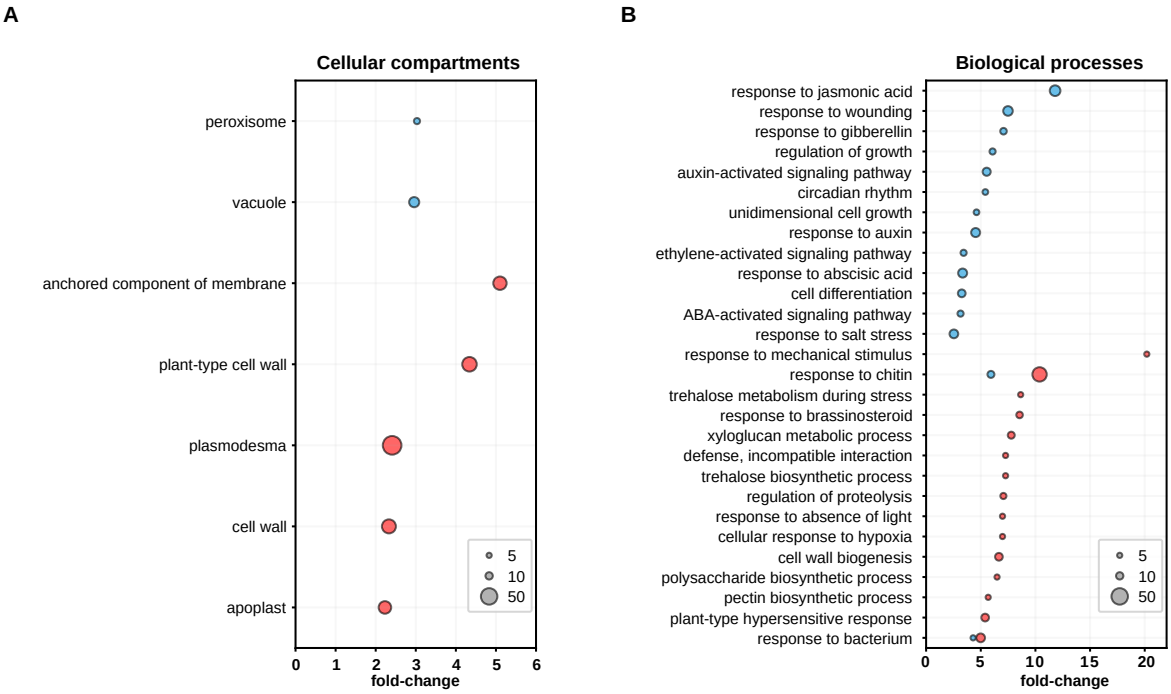

Figure 29: GO-Term enrichment analysis of differentially expressed transcripts in *aminaa50* #13.6. The significantly (>2-fold, p<0.05 in a Fisher's Exact test) up- and downregulated transcripts as identified in Fig. 28 were subjected to separate GO-Term enrichment analyses with the DAVID functional annotation tool v.6.8. The Arabidopsis transcriptome was used as background. Dots indicate **(A)** cellular compartments or **(B)** biological processes significantly (>2-fold, p<0.05 in a Fisher's Exact test) overrepresented among upregulated (red) and downregulated (blue) transcripts, respectively. The size of the dots represents the number of transcripts assigned to each GO-Term. Only compartments and biological processes encompassing at least five differentially regulated transcripts were taken into account. This figure shows only the fifteen most upregulated and downregulated processes; a complete list can be found in the Supplement (Tab. S3 and S4).

Interestingly, transcripts involved in the response to jasmonic acid (11.8-fold, 21 transcripts), gibberellin (7.0-fold, 8 transcripts), auxin (5.5-fold, 12 transcripts), and ethylene (3.4-fold, 7 transcripts) were also overrepresented among the downregulated transcripts in *aminaa50* #13.6. Moreover, the downregulated transcripts were involved in the regulation of growth (6-fold, 7 transcripts), cell differentiation (3.3-fold, 11 transcripts), and multicellular organism development (2.3-fold, 10 transcripts). This finding is striking given the wildtype-like phenotype of the *aminaa50* mutants.

To determine whether the gene expression profile of *aminaa50* #13.6 resembled that of the core NatA mutants *aminaa10* and *aminaa15*, transcriptome data generated by Dr. Pavlina Miklankova from six-week-old soil-grown plants were included in the following analysis (Miklankova, 2019). In order to provide a comparative overview, a clustered heatmap was prepared based on the fold changes measured for each gene and genotype with respect to the corresponding wildtype. The dendrogram shows that *aminaa10*, *aminaa15*, and *hypk-3* clustered together, whereas the *aminaa50* #13.6 gene expression profile was considerably different from the other three genotypes (Fig. 30).

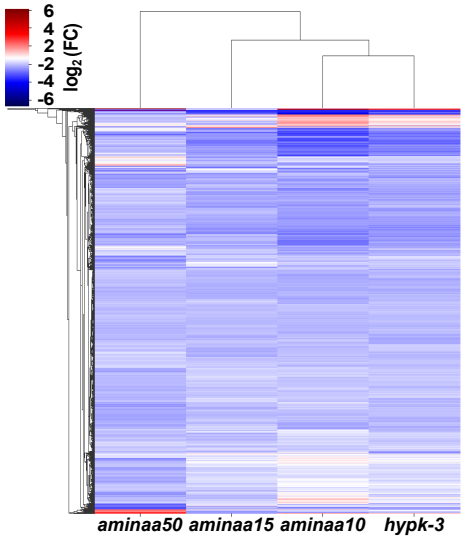

Figure 30: Clustered heatmap showing the gene expression profiles of *At*NatA/E mutants. The clustering was determined based on the euclidean distance between the average fold changes measured for each gene (n = 27,826) and genotype with respect to the corresponding wildtype using the seaborn.heatmap (Waskom, 2021) and matplot.lib (Hunter, 2007) libraries in Python 2.7. Expression data for *aminaa10*, *aminaa15* and *hypk-3* was obtained from Dr. Pavlina Miklankova (Miklankova, 2019).

The first observation that the gene expression profile of *aminaa50* #13.6 differed from

the patterns observed in the other three *At*NatA/E mutants was confirmed by a quantitative analysis using Venn diagrams (Fig. 31). The diagrams show the overlap between the significantly (>2-fold, p<0.05) up- or downregulated transcripts in the four mutants. Of the 721 transcripts that were upregulated in *aminaa50* #13.6, 611 (84 %) were not significantly upregulated in neither *aminaa10* nor *aminaa15*. In comparison, the *hypk-3* mutant upregulated 455 transcripts, of which only 33 (7 %) were not overexpressed in *aminaa10* or *amiaa15*. With 103 commonly upregulated transcripts, *aminaa50* displayed the most considerable overlap with *aminaa10*. However, the overexpression of those 103 transcripts did not seem to be a common feature of *At*NatA/E mutants since only 13 of those transcripts were also upregulated in *aminaa15*. Interestingly, 50 and 48 (7 %) of the transcripts that were found to be upregulated in *aminaa50* #13.6 were antagonistically regulated in *aminaa10* and *aminaa15*, respectively. Of the 455 transcripts that were found to be upregulated in *hypk-3*, none were antagonistically regulated in the core NatA mutants (data not shown).

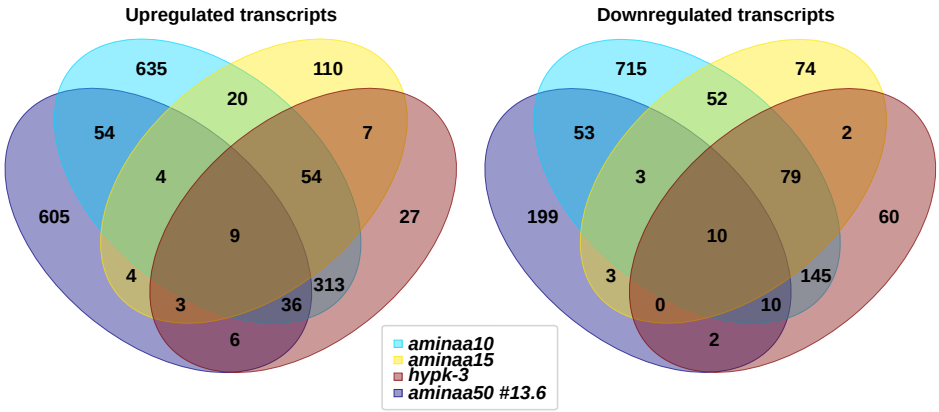

Figure 31: Venn diagrams showing the gene expression profiles of *At*NatA/E mutants. Comparison between significantly (>2-fold, p<0.05) up- or downregulated transcripts in different *At*NatA/E mutants (n=4 for *aminaa50* and n=3 for all other genotypes). Expression data for *aminaa10*, *aminaa15* and *hypk-3* was obtained from Dr. Pavlina Miklankova (Miklankova, 2019).

Among the 280 downregulated genes identified in *aminaa50*, 201 (72 %) were not significantly downregulated in neither *aminaa10* nor *aminaa15*. In comparison, a total of 308 transcripts was downregulated in *hypk-3*, of which only 62 (20 %) were not depleted in *aminaa10* or *amiaa15*. With 76 commonly downregulated transcripts, *aminaa50* displayed the biggest overlap with *aminaa10*. As previously observed for the commonly upregulated genes, the downregulation of those 76 transcripts was not a common feature between all *At*NatA/E mutants since only 13 of those transcripts were also downregulated in *aminaa15*.

Interestingly, 10 (3 %) and 24 (9 %) of the 280 transcripts which were found to be downregulated in *aminaa50* #13.6 were upregulated in *aminaa10* and *aminaa15*, respectively. In comparison, only one of the 308 transcripts which were downregulated in *hypk-3* was antagonistically regulated in *aminaa15*, and none were antagonistically regulated between *hypk-3* and *aminaa10* (data not shown).

In conclusion, *aminaa50* #13.6 displayed a considerably different gene expression profile than other *At*NatA/E mutants.

2.2.2.2 Whole proteome analysis of *aminaa50* #13.6

To determine whether the altered gene expression patterns observed in *aminaa50* #13.6 translated into changes on the protein level, a global proteome analysis (4.7.3) was performed on total soluble protein extracts (4.5.1) of seven-week-old wildtype and *aminaa50* #13.6 plants grown under short-day conditions on soil (4.3.2).

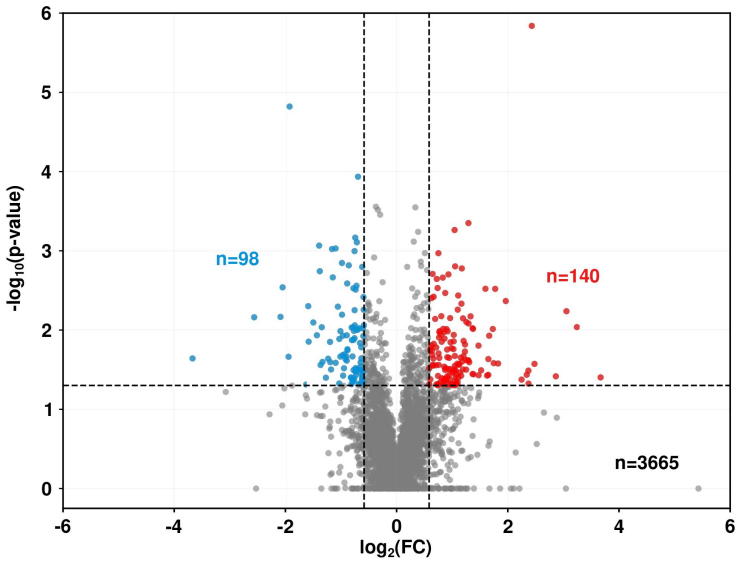

Figure 32: Differentially expressed proteins between wildtype and *aminaa50* #13.6. Volcano plot depicting the significantly (>1.5-fold, p<0.05 in a Student's t-test) regulated protein groups in red (upregulated) and blue (downregulated). Proteins with unchanged abundance are labeled in grey. Proteins were extracted from leaves of seven-week-old plants (n=4) grown on soil (4.3.2) under short-day conditions (4.5.1). The mass-spectrometry analysis (4.7.3) was performed by Prof. Dr. Iris Finkemeier, Dr. Annika Brünje, and Dr. Jürgen Eirich from the Institute for Plant Biology and Biotechnology, University of Münster.

The experiment was carried out by Dr. Annika Brünje and Dr. Jürgen Eirich under the supervision of Prof. Dr. Iris Finkemayer (Institute for Plant Biology and Biotechnology,

University of Münster) and identified 3,665 protein groups of which 238 (6.5 %) were differentially expressed (>1.5-fold up- or downregulated, p<0.05 in a Student's t-test) between wildtype and mutant (Fig. 32).

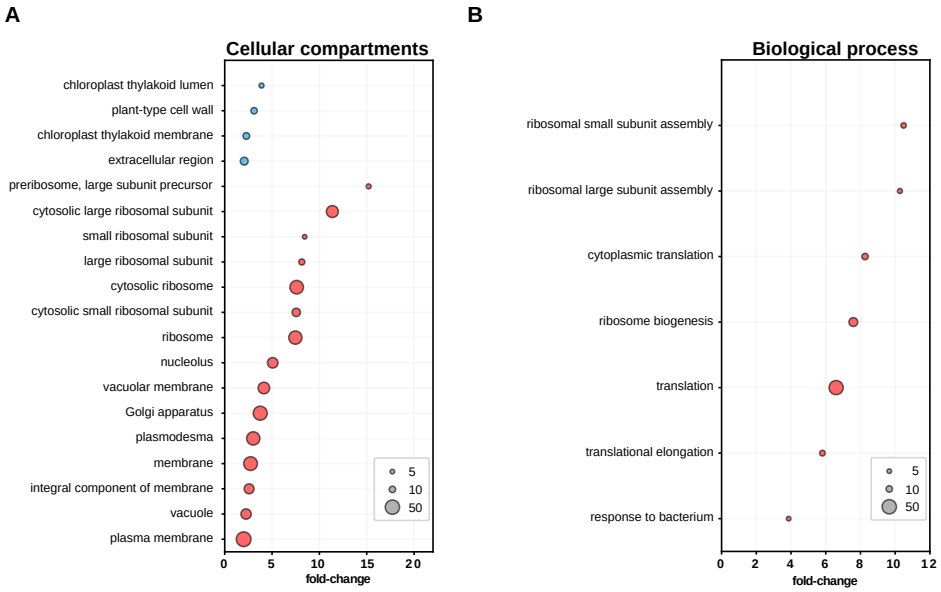

Figure 33: GO-Term enrichment analysis of differentially expressed proteins in *aminaa50* #13.6. The significantly (>1.5-fold, p<0.05 in a Fisher's Exact test) up- and downregulated protein groups identified in Fig. 32 were subjected to separate GO-Term enrichment analyses with the DAVID functional annotation tool v.6.8. The entirety of identified proteoforms in the dataset was used as background. Dots indicate **(A)** cellular compartments or **(B)** biological processes significantly (>2-fold, p<0.05 in a Fisher's Exact test) overrepresented among upregulated (red) and downregulated (blue) transcripts, respectively. The size of the dots represents the number of proteoforms assigned to each GO-Term. Only compartments and biological processes encompassing at least five differentially expressed proteoforms were considered.

While the abundance of 140 protein groups increased significantly in *aminaa50* #13.6, 98 protein groups were downregulated in the knockdown line. The NatA subunits NAA10, NAA15, and HYPK were not among the identified proteins. Remarkably, NAA50 was detected in all four wildtypes but none of the *aminaa50* #13.6 samples, confirming a strong knockdown of the protein. Besides NAA50, 15 additional proteins were exclusively identified in the wildtype (Supplementary Tab. S5). Based on their N-termini (MF, MI, MK, ML, MM, or MY), only two of those proteins were putative NAA50 substrates, indicating that the differential expression of those proteins might be a pleiotropic effect. Similarly, for the rest of the up- or downregulated proteins in *aminaa50* #13.6, no overrepresentation of NAA50-type N-termini could be detected. Of the 3,681 identified nuclear-encoded proteo-

forms in the dataset 449 (12.2 %) were putative substrates of NAA50. The share of putative NAA50 substrates was similar among the differentially expressed proteoforms (30 of 237 proteoforms, 12.6 %), indicating that most of them were not direct targets of NAA50.

Even though the protein extracts contained proteoforms originating from various subcellular compartments (1,552 mapped to the chloroplast; 1,543 to the cytoplasm; 1,183 to the nucleus; 678 to the mitochondrion; 644 to the plasma membrane; 223 to the Golgi apparatus and 183 to the ER according to TAIR), proteoforms localizing to specific subcellular compartments were significantly (>2-fold, $p<0.05$, in a Fisher's Exact test) overrepresented among the differentially regulated proteoforms (Fig. 33A). Those compartments were identified in a GO-Term enrichment analysis with the DAVID functional annotation tool (4.11.3). While among the downregulated proteoforms, proteoforms localizing to the chloroplast thylakoid lumen (3.9-fold, 6 proteoforms), the cell wall (3.1-fold, 10 proteoforms), the chloroplast thylakoid membrane (2.2-fold, 11 proteoforms), and extracellular regions (2.0-fold, 15 proteoforms) were overrepresented, proteoforms localizing to the ribosome (7.5-fold, 43 proteoforms), the Golgi apparatus (3.8-fold, 48 proteoforms), the vacuole (2.3-fold, 26 proteoforms) and the plasma membrane (2.0-fold, 53 proteoforms) were enriched among the proteoforms accumulating in *aminaa50* #13.6.

In agreement with the observed localization of the upregulated proteoforms at the ribosome, the GO-Term enrichment analysis (4.11.3) revealed that among the proteins accumulating in the knockdown mutant, proteins involved in ribosome biogenesis (7.6-fold, 19 proteoforms) and translation (6.6-fold, 49 proteoforms) were significantly (>2-fold, $p<0.05$ in a Fisher's Exact test) overrepresented (Fig. 33B). In addition, *aminaa50* #13.6 accumulated proteins involved in the response to bacteria (3.9-fold, 5 proteoforms) which is well in line with the changes in gene expression reported in the transcriptome analysis (2.2.2.1).

Since the samples for the transcriptome and proteome analysis had been harvested from the same plants, it was possible to verify whether the previously detected transcriptional changes could account for the observed deregulation at the protein level.

For this purpose, the transcriptome and proteome data were analyzed comparatively. In total, expression data for 3,603 genes were collected on the transcript and the protein level. The transcript level of 162 of those genes was significantly (>1.5-fold, $p<0.05$) upregulated in *aminaa50* #13.6. For only 14 of those 162 genes (9 %), this aberrant transcription translated into an increased protein abundance (>1.5-fold, p-value not taken into account). Similarly, the transcript levels of 210 genes were significantly (>1.5-fold, $p<0.05$) downregulated with only 31 proteins (15 %) following this trend (>1.5-fold, p-value not taken

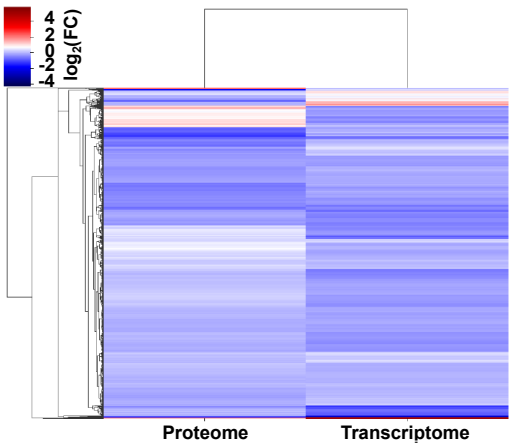

Figure 34: Clustered heatmap correlating proteome and transcriptome data from *aminaa50* #13.6. The clustering was determined based on the euclidean distance between the average fold changes (n=4) measured on the transcriptome and proteome level with respect to the wildtype using the seaborn.heatmap (Waskom, 2021) and matplot.lib (Hunter, 2007) libraries in Python 2.7.

into account). Conversely, for 140 proteins, increased expression was observed (>1.5-fold, p<0.05) but only for 16 of them (11 %), an increase in transcription (>1.5-fold, p-value not taken into account) could explain the aberrant expression. Of the 98 downregulated proteins in the dataset, only 6 (6 %) were encoded by transcripts that were downregulated (>1.5-fold, p-value not taken into account). The poor correlation between transcriptome and proteome data could also be visually assessed when correlating the data in a clustered heatmap (Fig. 34). Low correlation between transcriptome and proteome data is, however, not unusual and supports the view that post-transcriptional processes such as the regulation of translation efficiency or post-translational protein modifications play a major role in shaping the proteome (Liang et al., 2016; Soto-Suárez et al., 2016; Ding et al., 2020). In this context, the co-translational imprinting of the proteome with acetylation marks, in particular, is crucial for coordinating proteome stability (2.2.3).

2.2.3 Role of *At*NAA50 in protein turnover

Recent targeted analyses in *Arabidopsis thaliana* revealed that non-acetylated NatA substrates are destabilized via conserved non-Ac/N-degrons, which are recognized by E3-ligases of the ubiquitin-proteasome system. Consequently, depletion of NatA activity results in increased degradation of NatA substrates lacking acetylation marks. Remarkably, those elev-

ated degradation rates are balanced out by a concomitant increase in translation facilitated by a target-of-rapamycin induced biosynthesis of ribosomes (Miklankova, 2019; Gong et al., 2022; Linster et al., 2022). As *At*NAA50 associated with the ribosome and the components of the NatA/E complex (2.1.3 and 2.1.4) and *aminaa50* mutants accumulated proteins involved in cytoplasmic translation and ribosome biogenesis (2.2.2.2), a role of *At*NAA50 in the regulation of protein translation is conceivable.

2.2.3.1 Impact of *At*NatA/E depletion on protein biosynthesis

To determine whether the depletion of *At*NAA50 affects protein translation as previously observed for the downregulation of *At*NAA10, *At*NAA15, and *At*HYPK, the translation rates in *aminaa50* and *hypk-3* were assessed. The *hypk-3* mutant suffers from a tDNA insertion in the *HYPK* gene, resulting in a total knockout of HYPK and a decrease in NatA activity (Miklankova, 2019).

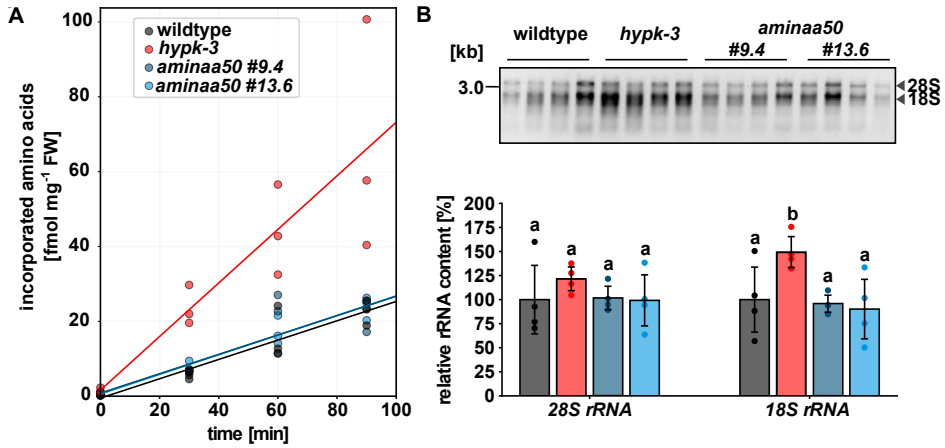

Figure 35: Translation rate and rRNA content of *aminaa50* and *hypk-3*. **(A)** Incorporation of ^{35}S-labelled amino acids into soluble proteins extracted from leaf discs of seven-week-old plants (n=3) grown on soil (4.3.2) under short-day (4.6.1). **(B)** Visualization (upper panel) and quantification (lower panel) of 28S (4.0 kb) and 18S (1.6 kb) rRNA extracted from equal amounts of leaf material from nine-week-old plants grown on soil (4.3.2) under short-day conditions. Total RNA was extracted (4.4.11), and equal volumes of RNA were loaded on an agarose gel. The signal intensity was measured with Fiji (4.1.7). Data given as means ± standard deviation. Different letters indicate individual groups identified by multiple pairwise comparisons with a Holm-Sidak, One-way ANOVA test ($p<0.05$, n=4).

To measure the protein translation rate, leaf discs of seven-week-old soil-grown plants (4.3.2) were incubated in 1/2 Hoagland medium (4.1.2) supplemented with radioactively

labelled methionine and cysteine for different time-spans (0, 30, 60, and 90 min). Subsequently, proteins were extracted, free amino acids were removed via gel filtration columns, and the incorporation of radioactively labelled amino acids into proteins was measured with a scintillation counter (4.6.1). The analysis revealed that after 90 min, the *hypk-3* leaf discs had incorporated approximately 3-fold more radioactively labeled amino acids than the leaf discs originating from wildtype plants. However, no differences between the *aminaa50* lines #9.4 and #13.6 and the wildtype were detected (Fig. 35A). In line with this finding, *hypk-3* but not *aminaa50* lines displayed 1.5-fold higher 18S rRNA and 1.2-fold higher 28S rRNA levels than wildtype plants when RNA was extracted from leaf material of nine-week-old plants and visualized on an agarose gel (Fig. 35B).

Taken together, these observations indicate that contrary to other NatA/E mutants, the *aminaa50* lines #9.4 and #13.6 did not display increased global protein translation.

2.2.3.2 **Impact of NatA/E depletion on protein degradation**

To determine whether the second aspect of protein turnover - protein degradation - was impacted by depletion of NAA50, the abundance of ubiquitinylated proteins was assessed in *aminaa50*. To this end, leaf discs of seven-week-old soil-grown plants were incubated in 1/2 Hoagland medium (4.1.2) supplemented with 50 μM of the proteasome inhibitor MG132. After 24 h, proteins were extracted from the leaf discs (4.5.1), loaded on an SDS-PAGE gel (4.5.8), blotted onto a PVDF membrane (4.5.10), and finally detected with an α-UBQ11 antibody (Tab. 18, AT4G05050).

Whereas in *hypk-3* plants, the ubiquitinylation levels rose 2.4-fold upon MG132 exposure, only a mild increase of 1.3 to 1.7-fold was observed in the wildtype and the *aminaa50* lines (Fig. 36). This difference between *hypk-3* and the other three plant lines observed after MG132 treatment was statistically significant ($p<0.05$, One-way ANOVA, n=3).

The fact that the differences in ubiquitinylation levels between *hypk-3* and the other genotypes only became apparent after proteasome inhibition suggests that *hypk-3* plants can efficiently degrade ubiquitinylated proteins under control conditions. Usually, ubiquitinylated proteins are cleared via the proteasome. To assess the activity of this multiprotein complex, protein extracts of six-week-old soil-grown plants were incubated with the fluorogenic proteasome substrate Z-Leu-Leu-Leu-AMC (Sigma-Aldrich, Steinheim), and the fluorescence emitted upon cleavage of Z-Leu-Leu-Leu-AMC was assessed with a plate reader (4.6.3). This time, not only wildtype, *hypk-3*, and *aminaa50* #9.4 and #13.6, but also *muse6* plants

were included in the experiment. The *muse6* mutant harbours a point mutation in the *NAA15* gene and, consequently, displays diminished NatA activity (Xu et al., 2015).

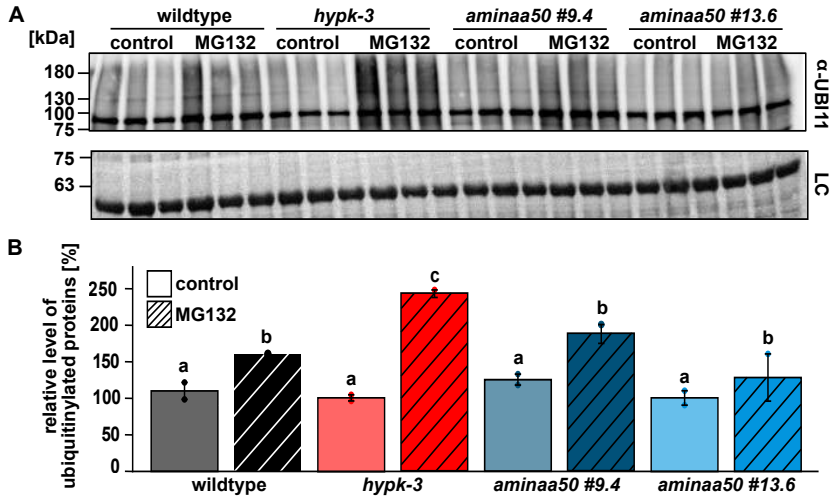

Figure 36: Accumulation of ubiquitinylated proteins in NatA/E mutants after proteasome inhibition. **(A)** Leaf discs of seven-week-old soil-grown (4.3.2) plants were incubated in 1/2 Hoagland medium (control, plain bars) or 1/2 Hoagland medium supplemented with 50 μM proteasome inhibitor (+MG132, striped bars). After 24 h, proteins were extracted from the leaf discs (4.5.1), loaded on an SDS-PAGE gel (4.5.8), and blotted onto a PVDF membrane (4.5.10). Ubiquitinylated proteins were detected with a specific antiserum (diluted 1:5.000 in TBS-T supplemented with 0.5 % BSA, 1.5 h incubation at RT). An Amido black staining of the membrane (lower panel) served as a loading control (LC). Uncropped pictures of the immunoblots are shown in Supplementary Fig. S11. **(B)** Quantification of (A). Values are shown relative to the wildtype. Data given as means ± standard deviation. Different letters indicate individual groups identified by multiple pairwise comparisons with a Holm-Sidak, One-way ANOVA test ($p<0.05$, n=3).

While the *aminaa50* lines behaved similarly to the wildtype, *hypk-3* and *muse6* displayed a 2.3 and 3.0-fold increase in proteasome activity with respect to the wildtype (Fig. 37). This is well in line with previous reports about increased proteasome activity in the NatA knockdown lines *aminaa10* and *aminaa15* (Miklankova, 2019; Linster et al., 2022).

The accumulation of the 20S proteasome β-subunit PBA1 (AT4G31300) may contribute to the increased proteasome activity observed in NatA mutants. As evidenced by immunological detection (4.5.10), PBA1 abundance was elevated 1.6-fold in six-week-old *aminaa10* and *aminaa15* plants grown on soil under standard growth conditions (Fig. 38A-B). This increase in PBA1 abundance on the protein level could not be attributed to an increased transcription of *PBA1* (Fig. 38C), indicating that altered translation efficiency or

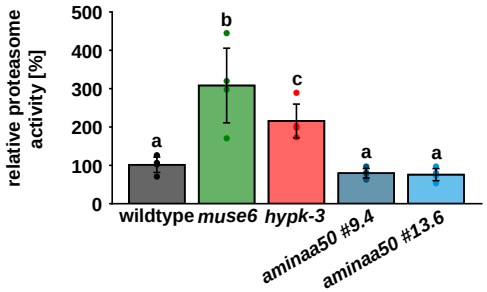

Figure 37: Proteasome activity in NatA/E mutants. The proteasome activity was measured in protein extracts from leaves of six-week-old plants grown on soil (4.3.2) under short-day conditions. For this purpose, the protein extracts were supplemented with the fluorogenic proteasome substrate Z-Leu-Leu-Leu-AMC (Sigma-Aldrich, Steinheim), and the fluorescence emitted upon cleavage of Z-Leu-Leu-Leu-AMC was assessed with a plate reader (4.6.3). Values are shown relative to the wildtype. Data given as means ± standard deviation. Different letters indicate individual groups identified by multiple pairwise comparisons with a Holm-Sidak, One-way ANOVA test ($p<0.05$, n=5).

post-translational modifications of the PBA1 protein might be responsible for the accumulation of PBA1 in the NatA knockdown lines.

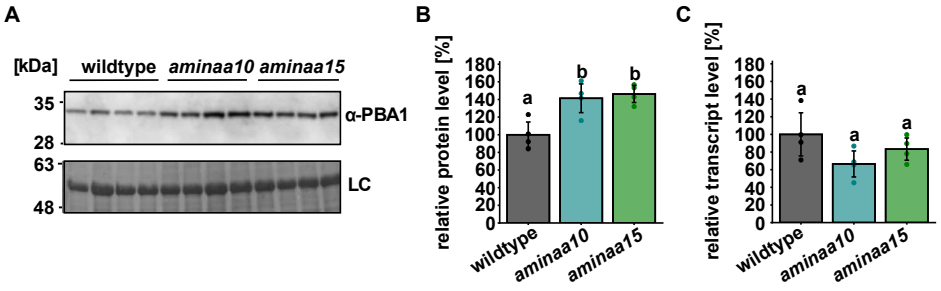

Figure 38: Expression of the 20S proteasome subunit PBA1. (A) Proteins were extracted (4.5.1) from leaves of six-week-old plants grown on soil (4.3.2) under short-day conditions, separated by SDS-PAGE (4.5.8), and transferred onto a PVDF membrane (4.5.10) where PBA1 was detected with a specific antiserum (Tab. 18). An Amido black staining of the membrane served as a loading control (LC). Uncropped pictures of the immunoblot and the loading control are shown in Supplementary Fig. S12. **(B)** Quantification of the blot shown in (A). **(C)** *PBA1* transcription as determined by qRT-PCR (4.4.13). Values are shown relative to the wildtype. Data given as means ± standard deviation. Different letters indicate individual groups identified by multiple pairwise comparisons with a Holm-Sidak, One-way ANOVA test ($p<0.05$, n=4).

2.2.3.3 Impact of NatA/E depletion on NTA frequency

The fact that increased global protein turnover was observed in NatA knockdown mutants but not the *aminaa50* plants is well in line with the assumption that, unlike the core NatA

subunit NAA10, NAA50 targets only very few substrates. Indeed, an analysis of the Arabidopsis proteome (48,076 proteoforms as of TAIR release 10) revealed that based on their N-terminal sequence, 50.5 % of the nuclear-encoded proteins were putative NatA substrates (MA, MC, MG, MS, MT, MV), whereas only 18.6 % were predicted to be acetylated by NatC, NatE or NatF (MF, MI, MK, ML, MM, MY). This difference in the estimated size of the NAA10 and NAA50 substrate pools became even more apparent when only N-termini with experimentally verified Ac-status were included in the analysis. The N-ter database harbours information about 2,212 proteoforms with experimentally verified acetylated N-termini (>10 % acetylation frequency). Of those, 62.7 % were predicted NatA, and only 5.4 % putative NatC/E/F substrates (Fig. 39).

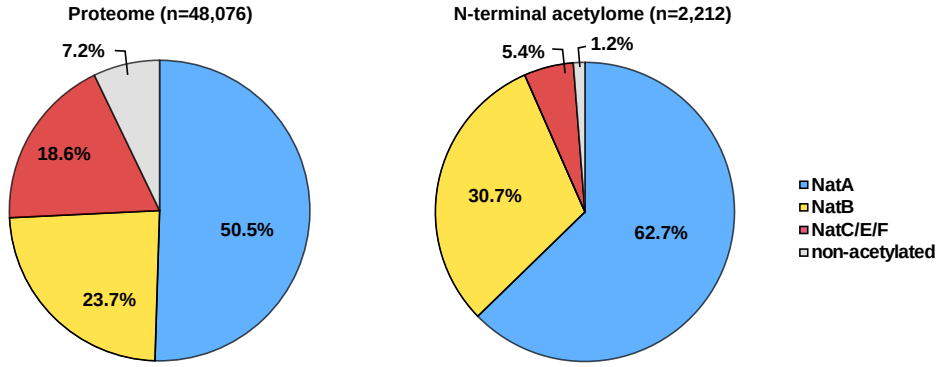

Figure 39: Composition of the N-terminal acetylome in *Arabidopsis thaliana*. Contribution of NatA (blue), NatB (yellow) and NatC/E/F (red) to the N-terminal acetylome in Arabidopsis. Numbers are based on the nuclear-encoded Arabidopsis proteome (n=48,076 proteoforms; left panel) or experimentally verified N-terminally acetylated proteins as documented in the N-ter database (n=2,212). Proteins were assigned to the substrate pools of the different Nats based on their N-terminal sequence (NatA: MA, MC, MG, MS, MT, MV; NatB: MD, ME, MN, MQ; NatC/E/F: MF, MI, MK, ML, MM, MY; remainder: non-acetylated).

Experimental data supported this bioinformatic analysis. A quantification of free N-termini in mutants with impaired NatA activity revealed that with respect to wildtype, *muse6* and *hypk-3* displayed a 1.8-fold increase in free N-termini. In the *aminaa50* lines #9.4 and #13.6, however, only a 1.5-fold increase was detected (Fig. 40). This observation agrees with the finding that NAA50 depletion does not impair the acetylation of typical NatA substrates (2.2.1.2). Moreover, it aligns with previously published data on NTA frequency in NatA mutants (Linster et al., 2015).

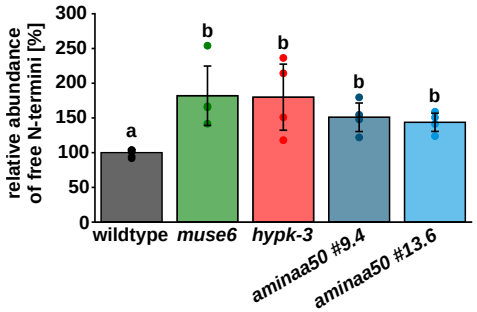

Figure 40: Soluble free N-termini detected in NatA/E mutants. The level of free N-termini was assessed in protein extracts from seven-week-old soil-grown (4.3.2) plants. To this end, 75 μg of protein extract (4.5.1) were mixed with 0.5 mM NBD-Cl and incubated at RT in the dark. After 16 h, the resulting fluorescence was measured with a plate reader (4.6.4). Data given as means ± standard deviation. Different letters indicate individual groups identified by multiple pairwise comparisons with a Holm-Sidak, One-way ANOVA test ($p<0.05$, n=4).

2.2.3.4 Identification of E3 ligases targeting free N-termini

Previous studies demonstrated that the bulk of proteins affected by the increased protein degradation and translation observed in NatA depleted plants are NatA substrates (Linster et al., 2022). Although an increasing amount of evidence suggests that this enhanced protein turnover results from non-acetylated N-termini being marked for proteasomal degradation by E3 ubiquitin ligases, it remains unclear which of the myriad E3 ligases target unshielded N-termini (Miklankova, 2019; Linster et al., 2022). About 5 % of the Arabidopsis genome encode for proteins involved in the ubiquitination pathway. Of those, over one thousand are putative E3 ligases (Mazzucotelli et al., 2006). To identify (a subset of the) E3-ligases which are responsible for the degradation of proteins with unshielded N-termini, custom-synthesized peptides (4.1.6) mimicking the acetylated and free N-terminus of the known NatA substrate OAS-TL A (AT4G14880) were coupled to sepharose beads and incubated with wildtype protein extracts (4.7.2). Beads that had not been coupled to peptides served as a negative control. After 16 h, the beads were collected via centrifugation and washed several times to elute proteins bound unspecifically to the beads or the peptides coupled to them. Last, the proteins bound specifically to the bait peptides were eluted with 1x Laemmli buffer. Subsequently, the eluted proteins were loaded on an SDS-PAGE gel (4.5.8) and visualized via Silver staining (4.5.9).

The staining revealed that there was a high background of proteins binding unspecifically to the beads irrespective of whether there was peptide coupled to the beads or not (Fig. 41). However, the staining also demonstrated that slightly more proteins were eluted from beads

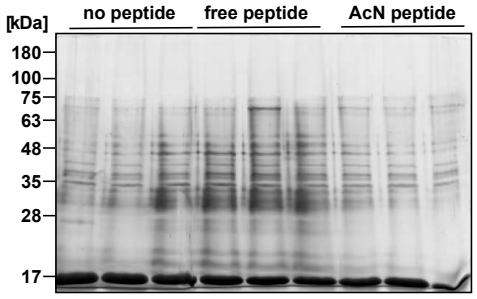

Figure 41: Silver-stained PAGE gel depicting proteins bound to beads coated with acetylated or free OAS-TL A peptides. Protein extracts (4.5.1) from leaves of six-week-old soil-grown wildtype plants (4.3.2) were incubated with peptide-coated sepharose beads (4.7.2) for 16 h. As a negative control, protein extracts were incubated with beads not coupled to peptides. Subsequently, the beads were washed, and the proteins binding specifically to the free or N-terminally acetylated peptides were eluted with 1x Laemmli buffer. The eluted proteins were separated by SDS-PAGE (4.5.8) and visualized via Silver staining (4.5.9). This experiment was performed in cooperation with Dr. Xiaodi Gong, Centre for Organismal Studies (University of Heidelberg).

coupled to peptides with free N-termini ("free peptide") than from beads coupled to N-terminally acetylated peptides ("AcN peptide"). To identify these proteins, the experiment was repeated, but instead of eluting the proteins on the beads with 1x Laemmli buffer, the samples were digested via on-bead proteolysis and identified by mass-spectrometry (4.7.2).

The following analysis only includes proteins that were identified by at least three peptides and which were detected in at least three of four replicates in one of the two treatment groups ("free peptide" or "AcN peptide"). Using these criteria, the mass-spectrometry analysis of N-terminal interactors in the wildtype protein extract identified 584 proteins. Four of those (0.7 %) interacted exclusively with the acetylated peptide, while nine (1.5 %) interacted only with the free peptide. In addition, five proteins (0.9 %) interacted significantly ($>$2-fold, $p<0.05$ in a Students t-test) more with the free than the acetylated N-terminal peptide (Tab. 7). There were no proteins that interacted significantly more with the acetylated N-terminal peptide.

Most of the putative N-terminal interactors listed in Tab. 7 were enzymes with functions unrelated to protein degradation and turnover. The most remarkable interactor identified in this first screen was CCT2 (AT5G20890), a subunit of the multiprotein chaperonin containing T (CTT) complex. The CCT complex contributes to protein folding by encapsulating nascent polypeptides in its central cavity, providing a sequestered environment. In eukaryotes, approximately 7 % of nascent polypeptides with mostly complex topologies bind to

the CCT complex after or during translation (Yam et al., 2008).

Table 7: Proteins interacting specifically with the free or acetylated N-terminus of the known NatA substrate OAS-TL A. N-terminal interactors were identified by mass-spectrometry (4.7.2). Each treatment group ("free peptide" and "AcN peptide") contained four samples. Proteins were only included in the analysis if they were identified by more than three peptides and detected in at least three replicates in one of the two treatment groups. In total, the mass-spectrometry analysis identified 584 proteins, of which four interacted exclusively with the acetylated peptide, nine interacted exclusively with the free peptide, and five significantly (>2-fold, $p<0.05$ in a Student's t-test) more with the free than the acetylated peptide. The mass-spectrometry analysis was performed by Sabine Merker and Dr. Thomas Ruppert from the Core Facility for Mass Spectrometry & Proteomics (University of Heidelberg).

ID	Symbol	Description	fold-change	p-value
AT1G01320	REC1	Protein with similarity to the FLOURY locus in maize	only in free	-
AT2G43970	LARP6B	RNA-binding protein	only in free	-
AT3G08030	ATHA2-1	DUF642 cell wall protein	only in free	-
AT3G24830	-	Ribosomal L13 family protein	only in free	-
AT3G26420	RBGB2	Zinc finger-containing RNA-binding protein	only in free	-
AT3G48000	ALDH2B4	Putative (NAD+) aldehyde dehydrogenase	only in free	-
AT4G04020	FIB	Fibrillin precursor protein	only in free	-
AT4G37980	ELI3-1	NADPH-dependent cinnamaldehyde reductase	only in free	-
AT5G20890	CCT2	TCP-1 chaperonin family protein	only in free	-
AT1G23740	AOR	Alkenal/one oxidoreductase	only in Ac	-
AT1G31230	AK-HSDH	Aspartate kinase/homoserine dehydrogenase	only in Ac	-
AT2G41530	SFGH	S-formylglutathione hydrolase	only in Ac	-
AT4G11175	-	Nucleic acid-binding protein	only in Ac	-
AT2G45770	CPFTSY	Chloroplast SRP receptor homolog	25.80	7.60E-06
AT5G40370	GRXC2	Glutaredoxin family protein	4.20	9.45E-04

AT4G13930	SHM4	Serine hydroxymethyltransferase	3.28	5.75E-04
AT3G06580	GALK	Galactose kinase	2.75	3.35E-02
ATCG00160	RPS2	Chloroplast ribosomal protein S2	2.48	1.26E-02

The aforementioned screen was repeated to identify further proteins interacting specifically with free or N-terminally acetylated peptides. To increase the chances of identifying E3 ligases involved in the turnover of proteins with unshielded N-termini, this time protein extracts from six-week-old *muse6* mutants instead of wildtype plants were used. The rationale behind this change in the experimental setup was that the elevated protein turnover observed in *muse6* might be associated with an increased expression of E3 ligases, making it easier to detect those enzymes in a mass-spectrometry based screen. The analysis of N-terminal interactors in the *muse6* protein extract (4.7.2) identified 1,614 proteins. Eleven of those (0.7 %) interacted exclusively with the acetylated peptide, while ten (0.6 %) interacted only with the free peptide. In addition, six proteins (0.4 %) interacted significantly (>2-fold, $p<0.05$ in Student's t-test) more with the free than the acetylated N-terminal peptide (Tab. 8). There were no proteins that interacted significantly more with the acetylated N-terminal peptide. As observed in the last screen, most of the identified putative N-terminal interactors had no known function in protein degradation and turnover. The most promising candidate for a non-Ac degron-recognizing E3 ligase identified in this second screen was the E3 ligase MAC3A (AT1G04510). MAC3A is a subunit of the MOS4-Associated Complex (MAC), which represents a regulatory hub in the plant pathogen response (Monaghan et al., 2009). The connection between protein N-terminal acetylation and plant immunity will be the focus of one of the following chapters (2.2.4.3).

Table 8: Proteins interacting specifically with the free or acetylated N-terminus of the known NatA substrate OAS-TL A. N-terminal interactors were identified by mass-spectrometry (4.7.2). Each treatment group ("free peptide" and "AcN peptide") contained four samples. Proteins were only included in the analysis if they were identified by more than three peptides and detected in at least three replicates in one of the two treatment groups. In total, the mass-spectrometry analysis identified 1,614 proteins of which eleven interacted exclusively with the acetylated peptide, ten interacted exclusively with the free peptide, and six significantly (>2-fold, $p<0.05$ in a Student's t-test) more with the free than the acetylated peptide. The mass-spectrometry analysis was performed by Sabine Merker and Dr. Thomas Ruppert from the Core Facility for Mass Spectrometry & Proteomics (University of Heidelberg).

ID	Symbol	Description	fold-change	p-value
AT1G04510	MAC3A	MOS4-associated complex 3A	only free	-
AT1G13870	ATKTI12	KTI12-like 2C chromatin associated protein	only free	-
AT2G15320	-	Leucine-rich repeat (LRR) family protein	only free	-
AT2G20190	CALSP	CLIP-associated protein	only free	-
AT2G20900	DGK5	Diacylglycerol kinase 5	only free	-
AT2G24050	EIFISO4G2	Eukaryotic translation initiation factor	only free	-
AT2G37020	-	Translin family protein	only free	-
AT3G11270	IRP4	Mov34/MPN/PAD-1 family protein	only free	-
AT3G53580	-	Diaminopimelate epimerase family protein	only free	-
AT5G15530	BCCP2	Biotin carboxyl carrier protein 2	only free	-
AT1G10700	PRPP3	Phosphoribosyl pyrophosphate (PRPP) synthase 3	only Ac	-
AT1G32050	SCAMP5	SCAMP family protein	only Ac	-
AT1G78830	MNB1	Curculin-like lectin family protein	only Ac	-
AT2G31390	FRK1	PfkB-like carbohydrate kinase family protein	only Ac	-
AT2G36580	-	Pyruvate kinase family protein	only Ac	-
AT3G14130	HAOX1	Aldolase-type TIM barrel family protein	only Ac	-

AT3G22950	ARL5	ADP-ribosylation factor C1	only Ac	-
AT3G52560	UEV1D	Ubiquitin E2 variant 1D-4	only Ac	-
AT3G63080	GPX5	Glutathione peroxidase 5	only Ac	-
AT4G21150	RPN2	Ribophorin II (RPN2) family protein	only Ac	-
ATCG01090	-	NADPH dehydrogenase	only Ac	-
AT1G03090	MCCA	Methylcrotonyl-CoA carboxylase alpha chain	31.72	1.25E-03
AT5G16390	BCCP	Chloroplastic AcCo-A carboxylase 1	16.02	8.16E-04
AT5G35360	CAC2	AcCo-A biotin carboxylase subunit	11.71	1.21E-05
AT1G76010	ALBA1	Alba DNA/RNA-binding protein	2.97	1.50E-03
AT1G20220	ALBA2	Alba DNA/RNA-binding protein	2.97	3.62E-03

In summary, the N-terminal interactor screens suggested that the free but not the acetylated N-terminus of the OAS-TL A peptide was targeted by the E3 ligase MAC3A and the chaperone CCT2. This finding requires confirmation e.g., by heterologous expression and purification of both proteins from *E. coli* and subsequent *in vitro* interaction assays. As the Arabidopsis genome encodes for more than 1,000 E3 ubiquitin ligases, it is highly unlikely that MAC3A is the only E3 ligase involved in recognizing unshielded N-termini (Mazzucotelli et al., 2006). Hence in the future, interactor screens with other N-terminal peptides as bait might identify more E3 ligases involved in the turnover of proteins lacking N-terminal acetylation marks.

2.2.4 Impact of *At*NAA50 on the adaptation to stress

Previous publications implicate the NatA complex in adapting to a variety of biotic and abiotic stresses. Those include the response to the virulent oomycete *Hyaloperonospora arabidopsidis* (*H.a.*) Noco2 and the bacterium *Pseudomonas syringae* pathovar *maculicola* (*P.s.m.*) ES4326 (Xu et al., 2015) as well as the resistance to drought (Linster et al., 2015). The analysis of the *aminaa50* transcriptome (2.2.2.1) and proteome (2.2.2.2) suggested that NAA50 as well might mediate plant stress responses. In the knockdown mutants, the de-

pletion of NAA50 resulted in an accumulation of transcripts and proteins involved in the response to pathogenic infection by bacteria. Moreover, the *aminaa50* plants overexpressed transcripts involved in the response to the absence of light, osmotic stress, and water deprivation. To determine whether these changes on the transcript and protein level translated into altered stress responses, the phenotype of the *aminaa50* lines was assessed upon UV-B light exposure (2.2.4.1), drought (2.2.4.2), and pathogen attack (2.2.4.3).

2.2.4.1 **UV stress**

UV-B light is a form of electromagnetic radiation with wavelengths of 280-315 nm, which is emitted by the sun. Even though most of it is absorbed by ozone in the earth's stratosphere, up to ten percent of the UV-B radiation produced by the sun reach the earth's surface. Prolonged exposure to UV-B light reduces plant genome stability, growth, and productivity. These detrimental effects are caused by reactive oxygen species (ROS) generated in plant cells upon UV-B exposure. ROS induce damage to nucleic acids, proteins, and membrane lipids (Kunz et al., 2006; Meyer et al., 2021). As obligate phototrophs, plants cannot altogether avoid exposure to UV-B light. However, they can remediate its damaging effects by synthesizing secondary metabolites that absorb UV light and neutralize ROS. Those metabolites include flavonoids, anthocyanins, alkaloids, phenolic compounds, carotinoids, and glucosinolates (Schreiner et al., 2014). NatA mutants and *hypk-3* plants constitutively downregulate the expression of genes involved in carotinoid and flavonoid biosynthesis and are more susceptible to UV-B exposure (Linster, 2014; Miklankova, 2019). To determine whether the same was true for the *aminaa50* lines, six-week-old soil-grown (4.3.2) wildtype, *hypk-3* and *aminaa50* #9.4 and #13.6 plants were exposed to UV-B radiation for 6 h (4.3.12). Directly after the UV-B treatment, no phenotypical changes could be observed (data not shown). However, after four days of recovery, the UV-B treated plants of all four genotypes looked paler than the control plants. In addition, *hypk-3* mutants which had been exposed to UV-B light displayed lesions and necrotic leaves. This was not the case for the other genotypes, indicating an increased sensitivity of *hypk-3* but not *aminaa50* to UV-B radiation. This first impression was further corroborated by an analysis of the fresh weight loss caused by the treatment. On average, six-week-old UV-B treated *hypk-3* mutants were 68 % lighter than their counterparts which had been growing under control conditions. For wildtype and the *aminaa50* lines, less severe average growth retardations of 36 and 39-49 % fresh weight were measured, respectively. Since the six-week-old wildtype and *aminaa50*

plants were slightly larger than *hypk-3* mutants of the same age, eight-week-old *hypk-3* plants were included in the experiment as an additional control. The effect of increased UV sensitivity persisted independent of the size of the *hypk-3* mutants (Fig. 42). This is consistent with previously reported findings (Linster, 2014; Miklankova, 2019).

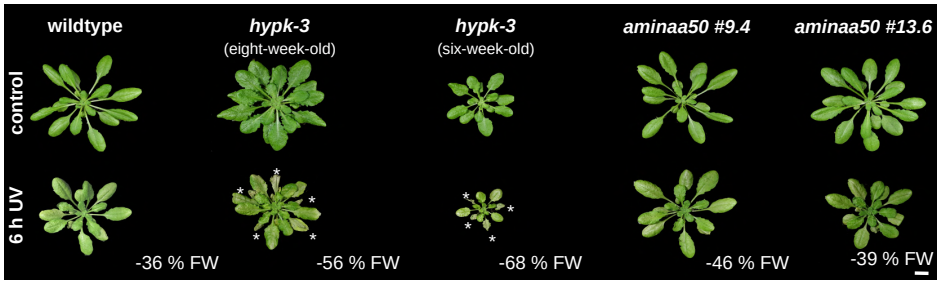

Figure 42: NatA mutants are sensitive to UV-B stress. Representative pictures of wildtype, *hypk-3*, and *aminaa50* plants after UV-B treatment. Six-week-old soil-grown (4.3.2) plants were either kept under standard growth light (upper panel) or exposed to UV-B light (0.04 $mWcm^{-2}$) for 6 h (lower panel). To account for the size difference between *hypk-3* and the wildtype, eight-week-old *hypk-3* mutants were included as additional controls. After four days of recovery, the phenotypical changes were documented, and the fresh weight (FW) of the plants was assessed (4.3.12). Fresh weight losses are given as means (n=4). Necrotic leaves are marked with white asterisks (scale bar = 1 cm).

In order to understand the connection between the depletion of NatA activity and the increased sensitivity to UV-B stress in *hypk-3* but not *aminaa50* mutants, the transcription of the NatA/E subunits NAA10, NAA15, HYPK, and NAA50 was assessed in UV-stressed wildtype plants (4.3.12). For this purpose, eight-week-old soil grown plants were exposed to UV-B light for 5 h (4.3.12). Directly afterwards, leaf material was harvested and snap-frozen in liquid nitrogen for RNA extraction (4.4.11), followed by cDNA synthesis (4.4.12) and qRT-PCR (4.4.13).

The qRT-PCR revealed a >15,000-fold induction of chalcone synthase transcription upon UV-B exposure, thereby confirming the effectiveness of the treatment. Chalcone synthase (CHS, AT5G13930) is a key enzyme of the flavonoid biosynthesis pathway and a well-known marker for UV-B stress (Dao et al., 2011). Moreover, the analysis revealed a statistically highly significant ($p>0.001$, Student's t-test) 3.6-fold increase in *NAA10* transcription. Similarly, a slight tendency for increased transcription was observed for *NAA15* and *HYPK*. This agrees with previous analyses, which revealed increased transcription of the core NatA components upon UV-B exposure (Miklankova, 2019). Remarkably, a 2.2-fold increase of *NAA50* transcription was detected after UV-treatment even though the expression

of *NAA50* and the core NatA subunits is usually not co-regulated (Fig. 43).

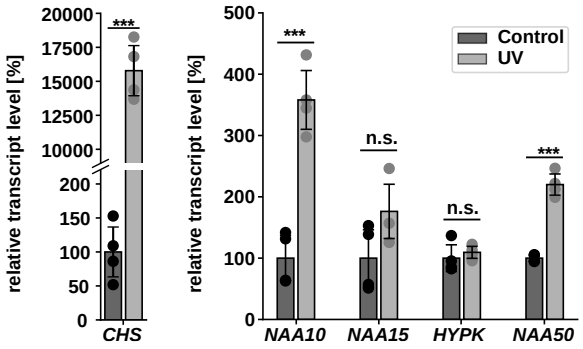

Figure 43: Transcript levels of NatA/E subunits after UV-B stress. RNA was extracted (4.4.11) from eight-week-old soil-grown (4.3.2) plants treated for 5 h with UV-B light (4.3.12). Subsequently, cDNA was synthesized (4.4.12), and a qRT-PCR (4.4.13) was performed with the primers specified in Supplementary Tab. S8. Data given as means ± standard deviation. Asterisks indicate significant differences as determined with a Student's t-test ($p<0.05$, n=4).

The immunodetection of NAA10, NAA15, and NAA50 in protein extracts (4.5.1) of the previously harvested leaves suggested that the accumulation of transcripts encoding for the NatA/E subunits translated into an increased abundance on the protein level. While the 1.3-fold and 1.4-fold overexpression observed for NAA10 and NAA50 was statistically significant ($p>0.01$, Student's t-test), the NAA15 protein level remained unchanged (Fig. 44).

In conclusion, the expression of both catalytic subunits of the NatA/E complex was upregulated under UV-B exposure. The fact that unlike mutants depleted in NatA activity, *aminaa50* #9.4 and #13.6 were not susceptible to UV-B damage indicates that the core NatA subunits but not NAA50 might be required for the adaptation to UV-B radiation.

2.2.4.2 **Drought stress**

Under field conditions, UV-B stress is often accompanied by drought. Drought severely impacts crop quality and yield quantity and hence is an environmental constraint for agriculture (Yordanov et al., 2000; Barnabas et al., 2008). As outlined in 1.2.1, prolonged water deficiency brings about a reduction in shoot growth, increased root branching and elongation, as well as stomatal closure. The latter is regulated primarily by the phytohormone abscisic acid (ABA), which is synthesized in the roots of plants during drought stress. As first described by Linster et al. (2015), ABA is also intricately linked to the frequency of N-terminal acetylation in *Arabidopsis thaliana*. Exogenous application of ABA leads to a decrease in NAA10 and NAA15 abundance, causing a drop in NatA-mediated NTA. Conversely, the

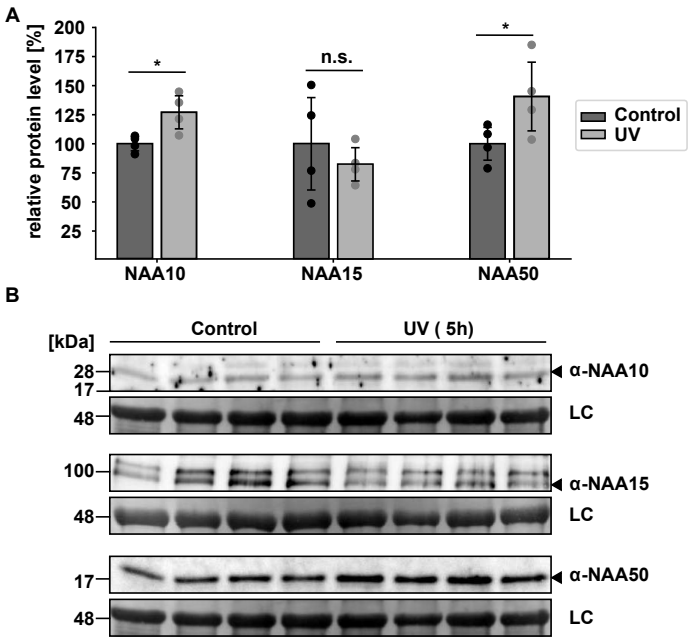

Figure 44: NatA/E subunits accumulate upon UV-B treatment. (A) Quantification of the blots shown in **(B)**. Data given as means ± standard deviation. Asterisks indicate significant differences as determined with a Student's t-test ($p<0.05$, n=4). Proteins were extracted (4.5.1) from eight-week-old soil-grown (4.3.2) plants treated for 5 h with UV-B light (4.3.12). Subsequently, the protein levels of NAA10, NAA15, and NAA50 were determined with specific antisera. The expected sizes of the detected proteins are marked with black triangles (NAA10: 20 kDa, NAA15: 100 kDa, NAA50: 18.5 kDa). Amido black stainings of the membranes served as loading controls (LC). Since the membrane where NAA10 was detected was stripped for the detection of NAA50, only one Amido black staining is available and was used as a loading control for both membranes. Uncropped pictures of the immunoblots are shown in Fig. S13.

artificial downregulation of NAA10 and NAA15 in transgenic plants causes these plants to mimic the canonical drought stress response. In consequence, NatA depleted plants are resistant to drought (Linster et al., 2015). Even though the downregulation of HYPK does not result in a co-regulation of the NatA core subunits, *hypk-3* mutants are also resistant to water scarcity, indicating that HYPK plays a vital role in drought sensing (Miklankova, 2019).

To address whether NAA50 as a component of the NatA/E complex is involved in the drought stress response, plants were grown on soil under short-day conditions (4.3.2) and exposed to a prolonged period of drought (4.3.10). During this experiment, the physical appearance of the plants was monitored. To account for the difference in size between the wildtype-like *aminaa50* plants and *hypk-3*, eight-week-old *hypk-3* plants were included in the experiment (Fig. 45).

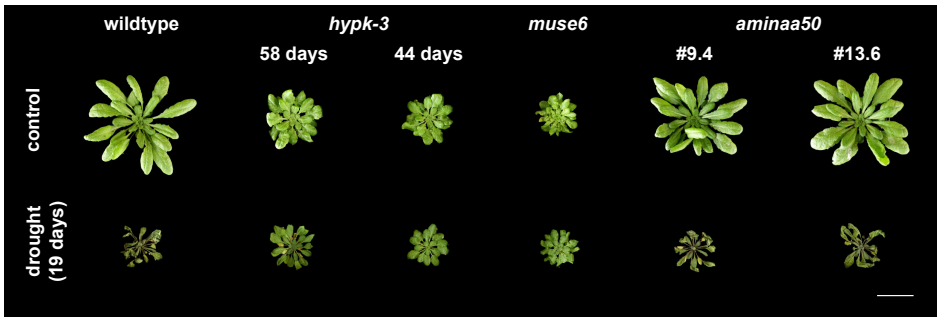

Figure 45: Unlike NatA mutants, *aminaa50* plants are not able to survive prolonged periods of drought. To address whether NAA50 as a component of the NatA/E complex was involved in the drought stress response, plants were grown on soil for six weeks under short-day conditions (4.3.2) and subsequently exposed to 19 days of drought (4.3.10). The control plants (upper panel) were watered further. To account for the difference in size between the wildtype-like *aminaa50* plants and *hypk-3*, eight-week-old *hypk-3* plants were included. Each plant is representative of at least five replicates. Pictures of the replicates can be found in Supplementary Fig. S14 and Fig. S15 (scale bar = 6 cm).

After fifteen days of drought, the first wildtype and *aminaa50* plants displayed wilted leaves and a faint yellow coloring. At the same time, the *hypk-3* and *muse6* plants seemed visually unaffected by the treatment. After nineteen days of drought stress, the wildtype and *aminaa50* plants had completely dried out, while the leaves of the *hypk-3* and *muse6* mutants were still green. The apparent absence of drought resistance in the *aminaa50* lines suggested that unlike HYPK and the core NatA subunits, NAA50 was not involved in regulating the plant drought stress response.

As NatA transcript levels decrease upon desiccation (Forero Ruiz, 2017), the transcrip-

tion of *NAA50* was assessed in wildtype plants subjected to fourteen days of drought. The RNA extracted from leaves of drought-stressed and control plants was kindly provided by M.Sc. Marlena Pozoga (Centre for Organismal Studies, University of Heidelberg). After cDNA synthesis (4.4.12), a qRT-PCR analysis was performed (4.4.13). As expected, the qRT-PCR revealed a 10-fold induction of the drought-inducible dehydrin *RD29B* (AT5G52300) upon desiccation (Virlouvet et al., 2014). Moreover, a statistically significant ($p>0.05$, Student's t-test) 15 % decrease in *NAA10* transcription was observed under drought conditions (Fig. 46A). A similar tendency for reduced transcription was observed for *NAA15*. The transcription of *HYPK* and *NAA50*, however, remained unaffected by the treatment. This is in agreement with previous reports (Miklankova, 2019).

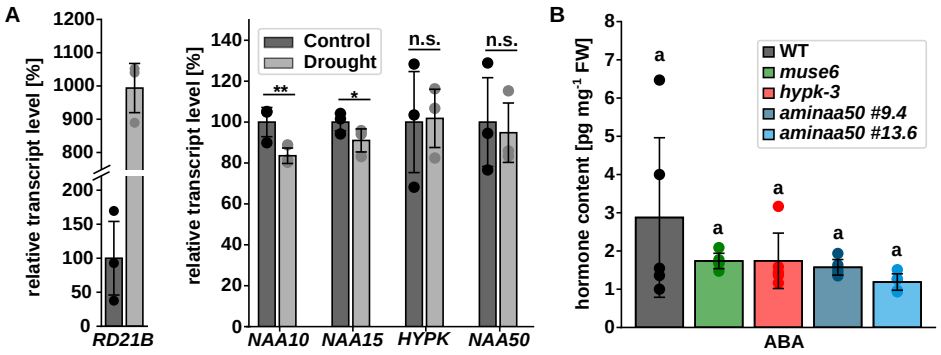

Figure 46: Transcript levels of NatA/E subunits after drought stress. (A) RNA was extracted (4.4.11) from eight-week-old soil-grown (4.3.2) plants (n=3) which had been subjected to two weeks of drought (4.3.10). Subsequently, cDNA was synthesized (4.4.12), and a qRT-PCR (4.4.13) was performed with the primers specified in Supplementary Tab. S8. Data given as means ± standard deviation. Asterisks indicate significant differences as determined with a Student's t-test ($p<0.05$, n=3).**(B)** Abscisic acid (ABA) content of six-week-old NatA/E mutants grown on soil (4.3.2) under short-day conditions. The measurement (4.9.1) was performed in cooperation with Michael Schulz from the Metabolomics Core Technology Platform, University of Heidelberg. Data given as means ± standard deviation. Different letters indicate individual groups identified by multiple pairwise comparisons with a Holm-Sidak, One-way ANOVA test ($p<0.05$, n=5).

Previous reports also showed that neither in the root, nor in the shoot, the ABA content of core NatA mutants is significantly altered compared to the wildtype. Thus, the reduced stomatal opening and altered root growth in NAA10 and NAA15 depleted plants cannot be explained by an accumulation of ABA in the mutants (Linster et al., 2015). The analysis of the ABA content (4.9.1) of six-week-old soil-grown (4.3.2) NatA/E mutants reinforced this notion and, on top, revealed that the *aminaa50* lines #9.4 and #13.6 also displayed wildtype like ABA levels (Fig. 46B). This is in line with the observed absence of drought tolerance

in those lines.

In summary, the drought stress experiments confirmed the drought tolerance of the core NatA mutants and proved that, unlike *muse6* and *hypk-3*, the *aminaa50* lines were sensitive to prolonged water scarcity.

2.2.4.3 **Plant immunity**

Many pathogens, including bacteria, oomycetes, and fungi, exploit stomatal pores as invasion routes. Thus, stomata closure is not only an integral part of the drought stress response but also strengthens plant immunity by actively preventing pathogens from entering plant leaves. To circumvent this physical barrier, pathogens have evolved virulence effector molecules which trigger stomatal reopening (Melotto et al., 2006; Ye et al., 2020; Bharath et al., 2021). Those effectors can be recognized by specialized nucleotide-binding leucine-rich-repeat containing receptors (NLRs) which induce the effector-triggered immunity (ETI) as the second line of defense (1.2.2). NatA mutants display not only constitutively closed stomata (Linster et al., 2015; Miklankova, 2019) but also overexpress the NLRs RPM1 (AT3G07040) and SNC1 (AT4G16890). Hence it is not surprising that depletion of NatA is associated with increased resistance to attacks by the virulent oomycete *H.a.* Noco2 and the bacterium *P.s.m.* ES4326 (Xu et al., 2015).

Unfortunately, neither RPM1 nor SNC1 were among the proteins identified in the global proteome analysis of *naa50-2* and *aminaa50* #13.6. Nevertheless, the *naa50-2* knockout (2.2.1.1) and the *aminaa50* #13.6 knockdown line (2.2.2.2) accumulated several other proteins involved in the immune response. To assess whether these changes in protein expression resulted in increased resistance to pathogens, the *aminaa50* lines #9.4 and #13.6 were challenged with the virulent oomycete *H.a.* Noco2 and the bacterium *P.s.m.* ES4326 (4.3.11). For this purpose, four-week-old soil-grown plants were infiltrated with a *P. syringae* bacterial suspension. Leaf discs were collected on the day of infection and three days later. The number of colony-forming units (CFUs) was assessed after serial dilution and bacterial incubation on LB plates (Fig. 47A). For the infection of plants with *H.a.* Noco2, two-week-old soil-grown seedlings were sprayed with *H.a.* Noco2 spores. The sporulation was quantified after one week of growth (Fig. 47B).

Compared to the wildtype, *muse6*, *hypk-3*, and the *aminaa50* lines displayed an increased resistance to *P. syringae*. Even though all genotypes had been inoculated with the same amount of bacteria at the beginning of the experiment, after three days of growth, the

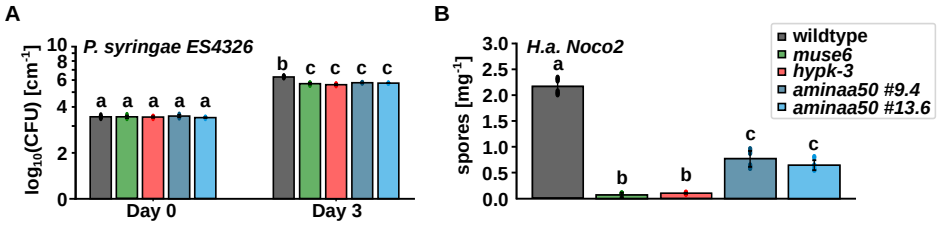

Figure 47: NatA/E mutants are resistant to pathogens. **(A)** Four-week-old soil-grown NatA/E mutants were infiltrated with a *P. syringae* bacterial suspension of OD_{600}=0.001. Leaf discs were collected on the day of infection (Day 0) and three days later (Day 3). After incubation of the plant material on LB plates, the number of colony-forming units (CFUs) was assessed. **(B)** Two-week-old soil-grown NatA/E mutants were sprayed with *H.a.* Noco2 spores. The sporulation was quantified after one week of growth using a hemocytometer (4.3.11). Both pathogen challenges were performed by Dr. Zhongshou Wu under the supervision of Prof. Dr. Xin Li from the Michael Smith Laboratories, University of British Columbia. Data given as means ± standard deviation. Data shown in (A) were log-transformed. Different letters indicate individual groups identified by multiple pairwise comparisons with a Holm-Sidak, One-way ANOVA test ($p<0.05$, n=4).

average amount of colony-forming units (CFUs) detected on wildtype leaf discs exceeded the measurements taken for the other genotypes approximately five times (Fig. 45A). Similarly, resistance to *H.a.* Noco2 was observed in all NatA/E mutants, even though the effect was more pronounced in the NatA mutants than in the *aminaa50* lines (Fig. 45B). One week after being sprayed with *H.a.* Noco2 spores, *muse6* and *hypk-3* displayed a 30-fold lower amount of spores on their leaves than wildtype plants. For the *aminaa50* lines, however, only a 3-fold decrease in spores was observed compared to the wildtype.

In essence, the pathogen challenges confirmed previous findings of the resistance of mutants with depleted NatA activity to *H.a.* Noco2 and the bacterium *P. syringae* (Xu et al., 2015). In addition, the experiments uncovered the resistance of the *aminaa50* lines to both pathogens. The more pronounced resistance to *H.a.* Noco2 observed for *muse6* and *hypk-3* in comparison to the *aminaa50* lines indicates that the depletion of NatA activity and the knockdown of NAA50 contributed to pathogen resistance via different mechanisms.

The plant defence against pathogens is mainly orchestrated by the three phytohormones salicylic acid (SA), jasmonic acid (JA), and ethylene (Dong, 1998). A global transcriptome analysis (2.2.2.1) revealed that transcripts involved in the response to salicylic acid were 4.7-fold overrepresented among the upregulated transcripts in *aminaa50* #13.5. In addition, transcripts associated with ethylene-activated signalling and the response to jasmonic acid were enriched among the up- and the downregulated transcripts in NAA50-depleted plants.

To determine whether this disturbed response to hormones was accompanied by an altered expression of the latter, the salicylic acid and jasmonic acid content of leaves excised from six-week-old soil-grown (4.3.2) NatA/E mutants was quantified (Fig. 48).

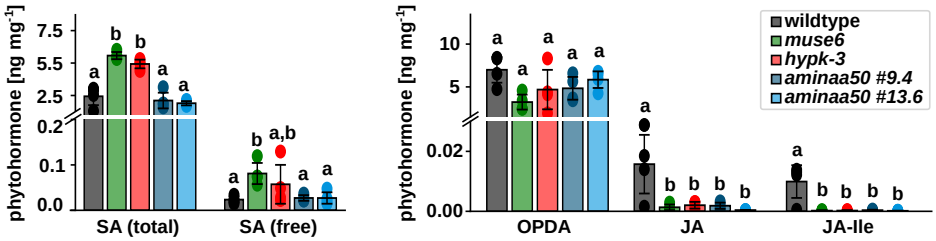

Figure 48: Phytohormone content of NatA/E mutants. Plants were grown for six weeks on soil (4.3.2) under short-day conditions. The total SA content was determined by Dr. Zhongshou Wu under the supervision of Prof. Dr. Xin Li from the Michael Smith Laboratories, University of British Columbia as described in Li et al. (1999). All other phytohormone measurements (4.9.1) were performed in cooperation with Michael Schulz from the Metabolomics Core Technology Platform, University of Heidelberg. Data given as means ± standard deviation. Different letters indicate individual groups identified by multiple pairwise comparisons with a Holm-Sidak, One-way ANOVA test ($p<0.05$, n=5).

Whereas the NatA depleted *muse6* and *hypk-3* accumulated 3.2-fold and 1.8-fold more SA than the wildtype, the SA content of both *aminaa50* mutant lines remained unchanged. This is in agreement with previous observations of SA accumulation in *aminaa10* and *aminaa15* plants (Linster, 2014) and suggests that depletion of NatA activity is associated with an activation of the immune response even in the absence of a pathogen infestation. Although the JA precursor 12-Oxophytodienoic acid (OPDA) had previously been reported to accumulate in the leaves of NatA depleted plants (Linster, 2014), no changes in the OPDA content were observed between wildtype, *muse6*, *hypk-3*, and the *aminaa50* lines in this experimental setup. Nevertheless, the jasmonic acid (JA) content was decreased approximately 6-fold in all NatA/E mutants. In line with this finding, the activated form of JA, 7-iso-Jasmonoyl-L-isoleucine (JA-Ile), was downregulated up to 50-fold in the NatA/E mutants.

During a pathogen attack, SA accumulates at the site of infection and mediates the systemic acquired resistance towards biotrophic pathogens. JA as an antagonist of the SA response is usually produced during the defense against herbivores or necrotrophic pathogens (Buerger & Chory, 2019). The substantial depletion of JA and JA-Ile in the NatA/E mutants might activate the SA response, which could explain the resistance of *muse6*, *hypk-3*, and the *aminaa50* lines towards the biotrophic pathogens *H.a.* Noco2 and *P. syringae*.

Indeed, certain *P. syringae* pathovars are known to produce coronatine, a molecular mimic of JA-Ile, to suppress SA-mediated immunity and trigger the reopening of closed stomata to allow for bacterial entry (Zheng et al., 2012). The additional accumulation of SA observed exclusively in the NatA mutants might explain the different extent of resistance observed for *muse6* and *hypk-3* compared to the *aminaa50* lines.

In brief, the previous chapters provided evidence for an association of *At*NAA50 with the core *At*NatA complex (2.1.3 and 2.1.5) but at the same time demonstrated that, unlike HYPK, *At*NAA50 did not act as a modulator of *At*NatA activity (2.2.1.2). Instead, *At*NAA50 seemed to execute important NatA-independent functions in vegetative growth (2.2.2) and the regulation of plant immunity (2.2.4.3). The diverging functions of NAA50 and the core NatA subunits manifested as phenotypical differences between the NatA/E mutants, e.g., regarding the resistance to UV-B exposure (2.2.4.1), drought (2.2.4.2), or pathogens (2.2.4.3). Therefore, the following chapter is dedicated to the NatA-independent functions of *At*NAA50.

2.3 Relevance of NAA50 catalytic activity for plant growth

Even though NAA50 is conserved among eukaryotes, the enzyme shows the most notable species-specific variation of all cytosolic Nats identified up to date (Weidenhausen et al., 2021). While in humans, only 20 % of NAA50 is bound to the core NatA complex, in yeast, NAA50 is exclusively found in complex with NatA and seems to play a major role in positioning the complex at the ribosome exit tunnel (Gautschi et al., 2003; Hou et al., 2007; Van Damme et al., 2011; Knorr et al., 2019). In agreement with this scaffolding function, *Sc*NAA50 is catalytically dead (Deng et al., 2019; Weidenhausen et al., 2021). *Hs*NAA50 and *At*NAA50 in contrast are both enzymatically active (Armbruster et al., 2020; Neubauer & Innes, 2020; Weidenhausen et al., 2021). Complementation experiments revealed that the ectopic expression of human but not yeast NAA50 rescues the dwarf phenotype of the *naa50-2* knockout mutant, suggesting that the enzymatic activity of NAA50 is required for proper growth and development in *A. thaliana* (Armbruster et al., 2020).

The active site of *At*NAA50 includes the residues Y77 and H115 and a catalytically important water molecule. In the presence of AcCoA, this water molecule is coordinated by Y77, I78, and H115. Single mutations in any of those residues result in a dramatically decreased activity of *At*NAA50 (Weidenhausen et al., 2021). Interestingly, all three residues are conserved between human and Arabidopsis, but not yeast (Fig. S16). In order to investigate the hypothesis that *At*NAA50 activity is required for plant growth, *naa50-2* knockout mutants were transformed with a construct encoding for *At*NAA50 harboring a mutation in H115A. To this end, the full-length coding sequence of NAA50(H115A) was PCR-amplified (4.4.4) from the pET24d-T7p-NAA50(H115A) vector (#1720, received from M.Sc. Jonas Weidenhausen, Heidelberg University Biochemistry Center) with the primers #4868 and #4869. The primers harboured *Kpn*I and *Sal*I endonuclease restriction sites which allowed for the insertion of the resulting PCR fragment into the empty pBinAR vector (#1834) under the control of the constitutive CaMV 35S promoter. The final pBinAR-35Sp-NAA50(H115A) construct (#1722) was stably transformed (4.3.5) into heterozygous *naa50-2* mutants (T0 generation). Through selection on plates containing AT-medium (4.1.2) supplemented with kanamycin (4.3.6), 28 positive transformants were identified (T1 generation). Of those 28, 12 (43 %) were homozygous and eight (28 %) heterozygous for the tDNA insertion in the *NAA50* gene. Since the homozygous T1 transformants displayed a wildtype-like phenotype (data not shown), after eight weeks of growth under short-day conditions, they were were transferred to the long-day chamber for seed produc-

tion. Remarkably, all of the 12 homozygous transformants displayed aborted pistils instead of developing elongated siliques so that no offspring were obtained. Since the heterozygous transformants had already been disposed of, the remaining seeds of the T0 generation were germinated on plates containing AT-medium (4.1.2) supplemented with kanamycin (4.3.6) to re-start the selection process. This time, 22 positive transformants were identified (T1 generation), of which seven (32 %) were homozygous and ten (45 %) heterozygous for the tDNA insertion in the *NAA50* gene. As observed for the previously selected T1 transformants, the homozygous *naa50-2:35Sp-NAA50(H115A)* plants resembled the wildtype habitus (Fig. 49).

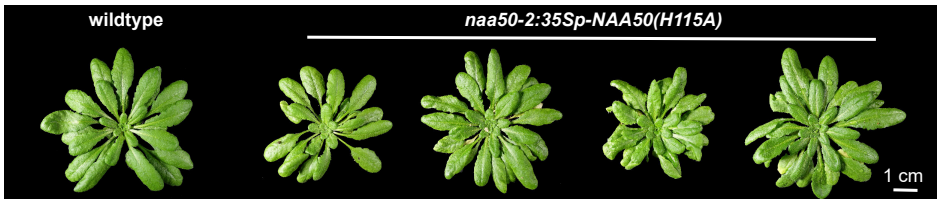

Figure 49: Growth phenotype of homozygous *naa50-2:35Sp-NAA50(H115A)* lines. Representative images of eight-week-old *naa50-2:35Sp-NAA50(H115A)* mutants (T1 generation) and wildtype plants germinated on standard AT-medium (Col-3 wildtype, 4.1.2) or AT-medium supplemented with kanamycin (*naa50-2:35Sp-NAA50(H115A)*, 4.3.6). After four weeks of growth on solid medium, the surviving plants were transferred to soil and left to grow for an additional four weeks. Plants homozygous for the tDNA insertion in the *NAA50* gene were identified by genotyping with the primers #321 and #604 as well as #603 and #604 (Supplementary Tab. S7). Growth occurred under short-day conditions (scale bar = 1 cm).

Since again, none of the seven homozygous *naa50-2:35Sp-NAA50(H115A)* lines produced any offspring, the seeds of the ten heterozygous lines were collected, and all further experiments were performed with the homozygous offspring of the heterozygous *naa50-2:35Sp-NAA50(H115A)* line #25. To identify the cause of the previously observed infertility of the homozygous mutants, the flowers, and siliques of eight-week-old soil-grown (4.3.2) homozygous *naa50-2:35Sp-NAA50(H115A)* #25 plants (T2) were examined. For this purpose, the flowers were removed with forceps and visually inspected under a binocular microscope. The inspection revealed that the flowers of homozygous *naa50-2:35Sp-NAA50(H115A)* mutants had short filaments which could not reach the pistil. In addition, the mutant anthers remained closed so that no pollen grains could be detected. The extraction of pollen from newly opened flowers (4.3.8) confirmed the absence of pollen in the mutants (Fig. 50).

An analysis of the mutant siliques demonstrated that whereas the wildtype developed

normally after self-pollination, the *naa50-2:35Sp-NAA50(H115A)* plants merely displayed aborted pistils. To assess whether the infertility of the *naa50-2:35Sp-NAA50(H115A)* mutants was caused exclusively by the absence of pollen, the stigma of wildtype plants and mutants were manually pollinated with wildtype pollen. While the wildtype developed siliques that contained seeds, the *naa50-2:35Sp-NAA50(H115A)* plants displayed aborted pistils, suggesting that NAA50 is not only essential for normal pollen formation but also involved in regulating stigma and female gametophyte development. This is well in line with findings by Feng et al. (2020), who report to not have obtained any seeds upon pollination of *naa50* knockout mutants with wildtype pollen.

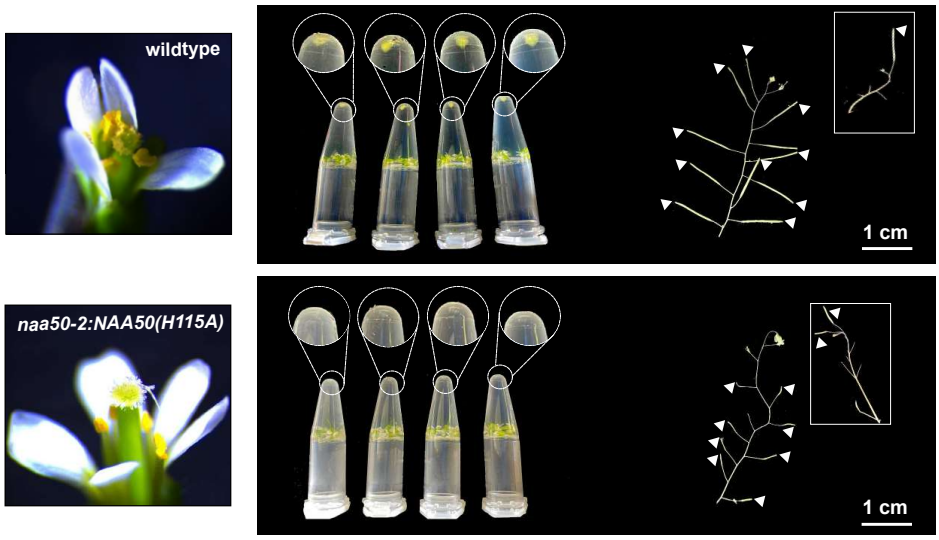

Figure 50: Homozygous *naa50-2:35Sp-NAA50(H115A)* plants are infertile. Contrary to the flowers of wildtype plants (upper panel), the flowers of homozygous *naa50-2:35Sp-NAA50(H115A)* mutants (lower panel) had short filaments which could not reach the pistil. Upon visual inspection under a binocular microscope, all mutant anthers remained closed, and no pollen grains were detected on them. Pollen extraction (4.3.8) from six flowers per replicate (n=4) revealed that, indeed, pollen was absent in the mutants but not the wildtype plants (circular magnification). Consequently, the siliques of the wildtype plants developed normally after self-pollination, whereas the mutant plants displayed merely aborted pistils (white triangles). Even when the stigma of wildtype plants and mutants were manually pollinated with wildtype pollen, only the wildtype plants were able to develop siliques that contained seeds (white inlays). Pictures are representative of at least four individual plants per genotype.

In summary, the expression NAA50(H115A) under the control of the 35S promoter could only partially complement *naa50-2*. While the dwarf phenotype of the knockout mutants was rescued, their infertility persisted upon NAA50(H115A) expression. At first glance, this partial rescue seemed to imply that NAA50 activity was dispensable for nor-

mal plant growth and development but essential for plant fertility. There are, however, two caveats. First of all, NAA50(H115A) expression might have varied between different tissues and organs. Indeed, 35S promoter-driven transgenes are considerably less expressed in *Arabidopsis thaliana* leaves and roots than in the inflorescences. Even more importantly there is no promoter activity at all in pollen (Wilkinson et al., 1997; Kiselev et al., 2021). Hence it is conceivable that the NAA50(H115A) construct under the control of the 35S promoter was well expressed in the leaves but poorly or not at all expressed in the inflorescence, explaining the complementation of *naa50-2* phenotypes in some but not all plant organs. As Neubauer & Innes (2020) point out, most research on NTA has been performed in unicellular organisms such as yeast, making it impossible to investigate whether acetyltransferases display tissue-specific functions.

The second caveat concerns the assumption that the mutation in NAA50(H115A) results in complete inactivation of the enzyme. While the expression of NAA50(H115A) in pollen could not be assessed due to the absence of pollen in the transformants, the activity of NAA50(H115A) could be quantified with an *in vitro* acetyltransferase assay. To this end, Trx-His_6-*At*NAA50 and His_6-*At*NAA50(H115A) were expressed in *E. coli* (4.5.5) using the vectors #831 and #1720. Subsequently, the His-tagged enzymes were purified from the bacteria by immobilized metal affinity chromatography (4.5.6, Fig. 51A and 51B). Subsequently, both enzymes were incubated with 45 μM [^{3}H]acetyl-CoA and 0.2 mM of the custom-synthesized MLGP peptide. The MLGP peptide (4.1.6) was chosen since it is a model substrate of *Hs*NAA50 and was recently shown to be acetylated by *At*NAA50 *in vitro* (Evjenth et al., 2009; Armbruster et al., 2020). After incubation, the MLGP peptide was enriched via specific interaction of its C-terminus with SP-sepharose, and the amount of incorporated [^{3}H]acetyl was measured by scintillation counting. As a negative control, heat-inactivated NAA50 was included in the experiment. The *in vitro* assay revealed that within one hour, 5 μg of the endogenous *At*NAA50 enzyme acetylated 411 pmol of MLGP peptides (Fig. 51C). During the same time, 5 μg of the mutated NAA50(H115A) version only acetylated 49 pmol peptides. When accounting for the size difference due to the absence of the thioredoxin reductase tag in His_6-NAA50(H115A), the mutated NAA50 version retained approximately 19 % of the wildtype activity. As the amount of acetylated peptide increased linearly with increasing amounts of NAA50(H115A) enzyme (Fig. 51D) and over time (Fig. 51E), it is unlikely that the observed signals arose from chemical acetylation rather than enzymatic activity.

Since the NAA50(H115A) enzyme retained a considerable amount of activity despite

the mutation introduced in its catalytic center, it is impossible to conclude whether or not NAA50 activity is required for plant growth and development from the aforementioned complementation experiment. As demonstrated by the generation of the wildtype-like *aminaa50* knockdown lines (2.2.2), minimal amounts of NAA50 are sufficient to ensure proper plant growth. Hence it does not come as a surprise that 19 % enzymatic activity combined with a strong overexpression of the enzyme under the control of the 35S promoter achieved a rescue of the *naa50-2* dwarf phenotype. Nevertheless, the complementation experiments showed that *At*NAA50 is required for both vegetative and generative growth.

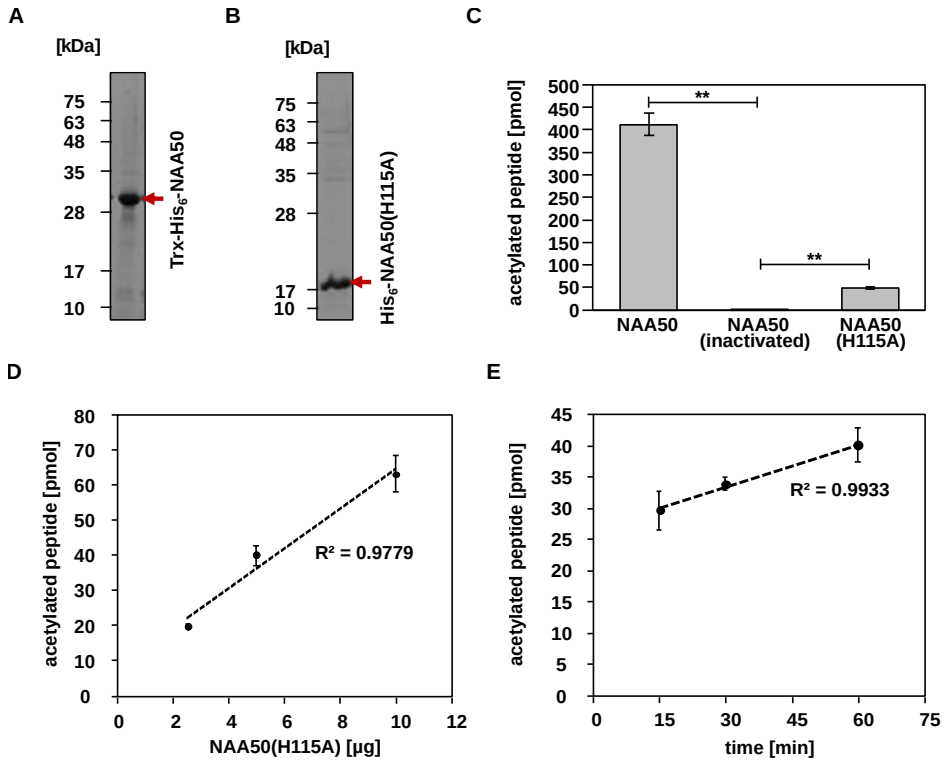

Figure 51: *At*NAA50(H115A) displays dramatically reduced enzymatic activity. (A) Trx-His$_6$-*At*NAA50 (33.2 kDa) and **(B)** His$_6$-*At*NAA50(H115A) (20.0 kDa) were purified from *E. coli* by immobilized metal affinity chromatography. **(C)** 5 μg of purified enzyme were incubated for 1 h at 37 °C with 45 μM [^{3}H]acetyl-CoA and 0.2 mM of the synthetic MLGP peptide (Tab. 4.1.6). After incubation, the peptide was enriched via specific interaction with SP-sepharose, and the amount of incorporated [^{3}H]acetyl was measured by scintillation counting. As a negative control, Trx-His$_6$-*At*NAA50 was heat-inactivated at 95 °C for 10 min. The average background was determined in reaction mixes incubated without peptide and was subtracted from the respective measurements. **(D)** Concentration-dependency and **(E)** Time-dependency of the His$_6$-*At*NAA50(H115) *in vitro* acetyltransferase activity. Data are presented as mean ± standard error (n=4, $p < 0.05$ in a Student's t-test).

To learn more about the role of *At*NAA50 during vegetative growth, a transcriptome analysis (4.8) of homozygous *naa50-2:35Sp-NAA50(H115A)* plants (T2) was performed. For this purpose, leaf material of seven-week-old plants grown on soil (4.3.2) under short-day conditions was harvested. Subsequently, RNA (4.4.11) was extracted, and the samples were hybridized on a microarray of the Arabidopsis Gene 1.0 ST type (Affymetrix, Santa Clara, USA) by Dr. Carsten Sticht and Dr. Carolina De La Torre (NGS Core Facility, University of Heidelberg). To determine inter- and intragroup variability and to identify biological outliers, the Pearson's correlation coefficient was calculated between all samples and visualized as a heatmap (Fig. 52). While the heatmap showed little variance among the *naa50-2:35Sp-NAA50(H115A)* replicates, the divergence among the wildtype replicates was more pronounced. Nevertheless, the wildtype and *naa50-2:35Sp-NAA50(H115A)* samples were found in clearly separated clusters, allowing for further analysis of the data.

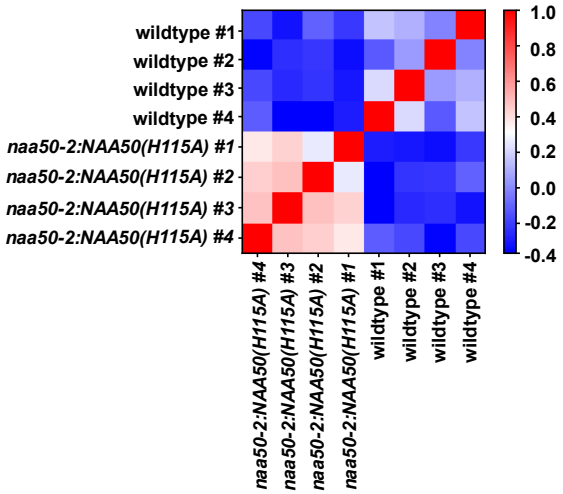

Figure 52: Gene expression profile of wildtype and *naa50-2:35Sp-NAA50(H115A)*. Heatmap depicting the correlation between wildtype and *naa50-2:35Sp-NAA50(H115A)* samples as quantified by the Pearson's correlation coefficient (n = 27,826 genes). RNA was extracted from seven-week-old plants grown under short-day conditions on soil (n=4). The transcriptome analysis (4.8) was performed by Dr. Carsten Sticht and Dr. Carolina De La Torre from the NGS Core Facility, University of Heidelberg.

The microarray covered 27,826 transcripts, of which 27,059 (97.2 %) were protein coding. In total, 694 of all transcripts (2.6 %) were differentially regulated (>2-fold up- or downregulated, $p<0.05$ in a Student's t-test) between wildtype and mutant (Fig. 53). While the abundance of 446 transcripts increased significantly in *naa50-2:35Sp-NAA50(H115A)*, only 248 transcripts were downregulated in the mutant line. Whereas the transcription of

NAA10, *NAA15*, and *HYPK* was unaffected in *naa50-2:35Sp-NAA50(H115A)*, *NAA50* was 63.4-fold overexpressed.

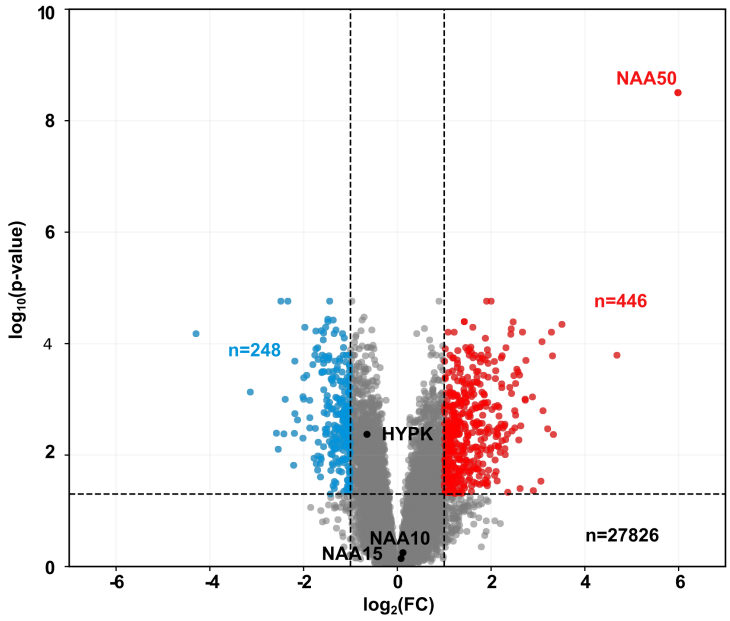

Figure 53: Differentially transcribed genes between wildtype and *naa50-2:35Sp-NAA50(H115A)*. Volcano plot depicting the significantly (>2-fold, p<0.05 in a Student's t-test) regulated transcripts in red (upregulated) and blue (downregulated). Transcripts with unchanged abundance are labeled in grey. RNA was extracted from seven-week-old plants (n=4) grown under short-day conditions on soil (4.3.2). The transcriptome analysis (4.8) was performed by Dr. Carsten Sticht and Dr. Carolina De La Torre from the NGS Core Facility, University of Heidelberg.

Among the differentially regulated transcripts, transcripts encoding for proteins localizing to specific subcellular compartments were significantly (>2-fold, p<0.05 in a Fisher's Exact test) overrepresented. Those compartments were identified in a GO-Term enrichment analysis with the DAVID functional annotation tool (4.11.3) and - in the case of the upregulated transcripts - included the cell wall (4.0-fold, 23 transcripts), integral components of the plasma membrane (2.4-fold, 11 transcripts), the apoplast (2.3- fold, 19 transcripts) and the plasmodesmata (2.3-fold, 38 transcripts). Among the downregulated transcripts, transcripts encoding for proteins localizing to the chloroplast thylakoid (3.7-fold, 7 transcripts), the chloroplast stroma (2.3-fold, 14 transcripts), or the vacuolar membrane (2.2-fold, 11 transcripts) were overrepresented (Fig. 54A). A similar pattern was observed in *aminaa50* #13.6 mutants where transcripts encoding for proteins localizing to the cell wall (4.3-fold, 39 transcripts), the plasmodesmata (2.4- fold, 64 transcripts), and the apoplast (2.2-fold, 29

transcripts) accumulated (2.2.2.1).

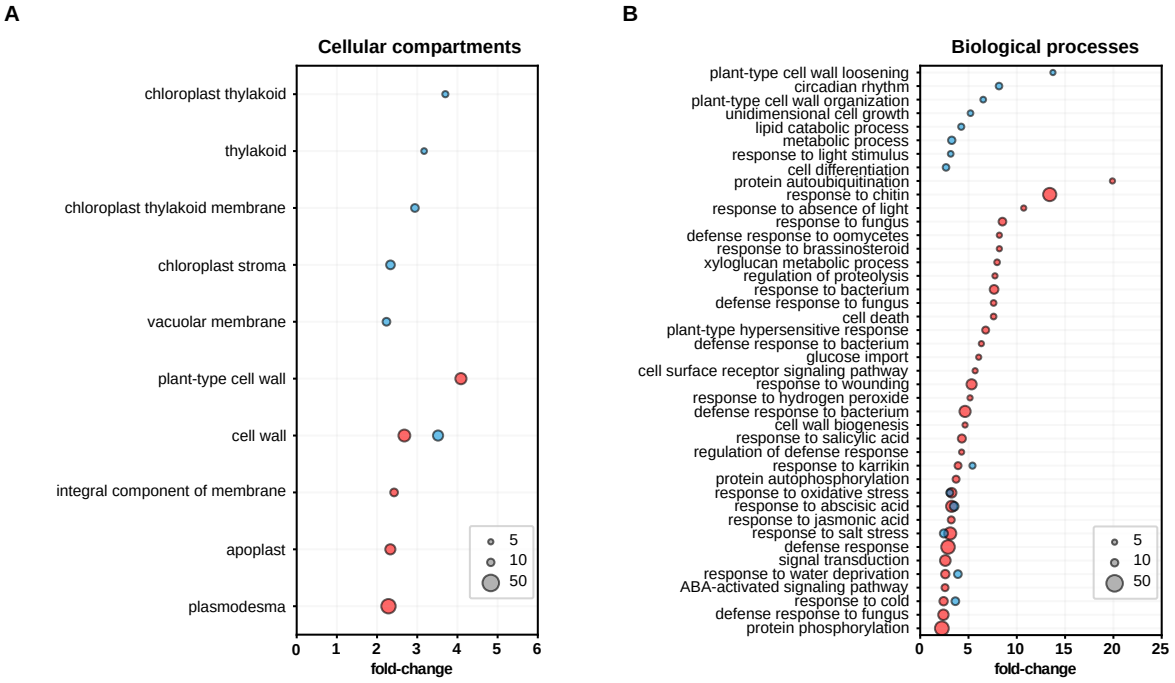

Figure 54: GO-Term enrichment analysis of differentially expressed transcripts in *naa50-2:35Sp-NAA50(H115A)*. The significantly (>2-fold, p<0.05 in a Fisher's Exact test) up- and downregulated transcripts, identified in Fig. 53 were subjected to separate GO-Term enrichment analyses with the DAVID functional annotation tool v.6.8. The Arabidopsis transcriptome was used as background. Dots indicate **(A)** cellular compartments or **(B)** biological processes significantly (>2-fold, p<0.05 in a Fisher's Exact test) overrepresented among upregulated (red) and downregulated (blue) transcripts, respectively. The size of the dots represents the number of transcripts assigned to each GO-Term. Only compartments and biological processes encompassing at least five differentially regulated transcripts were considered.

In addition, the GO-Term enrichment analysis (4.11.3) revealed that among the transcripts accumulating in *naa50-2:35Sp-NAA50(H115A)*, transcripts involved in the adaptation to abiotic stress were significantly (>2-fold, p<0.05 in a Fisher's Exact test) overrepresented (Fig. 54B). These stress responses included the response to the absence of light (10.7-fold, 5 transcripts), the response to oxidative stress (3.2-fold, 17 transcripts), the response to salt stress (3.1-fold, 27 transcripts), the response to water deprivation (2-6-fold, 13 transcripts) and the response to cold (2.4-fold, 13 transcripts). Furthermore, transcripts mediating the defense response to biotic stress (2.5-fold, 46 transcripts) were upregulated in *naa50-2:35Sp-NAA50(H115A)*. Specifically, those transcripts regulated the response to fungi (8.5-fold, 11 transcripts), oomycetes (8.2-fold, 5 transcripts), bacteria (7.6-fold, 14

transcripts) as well as the plant-type hypersensitive response (6.8-fold, 9 transcripts). In line with these findings, the regulation of several stress and growth-related phytohormones was disturbed in *naa50-2:35Sp-NAA50(H115A)*. Among the upregulated transcripts, transcripts involved in the response to brassinosteroids (8.2-fold, 5 transcripts), salicylic acid (4.3-fold, 12 transcripts), abscisic acid (3.3-fold, 23 transcripts), and jasmonic acid (3.2-fold, 9 transcripts) were overrepresented.

Interestingly, transcripts involved in the response to water deprivation (3.9-fold, 11 transcripts), salt stress (2.4-fold, 12 transcripts), oxidative stress (3.1-fold, 9 transcripts), the response to cold (3.6-fold, 11 transcripts), and the response to abscisic acid (3.5-fold, 14 transcripts) were also overrepresented among the downregulated transcripts in *naa50-2:35Sp-NAA50(H115A)*. Moreover, the downregulated transcripts were involved in cell wall loosening (13.7-fold, 5 transcripts), cell wall organization (6.5-fold, 6 transcripts), unidimensional cell growth (5.2-fold, 6 transcripts), and cell differentiation (2.7-fold, 8 transcripts). This is striking given the wildtype-like phenotype of the *naa50-2:35Sp-NAA50(H115A)* mutants but was already observed in the *aminaa50* #13.6 plants which also downregulated processes mediating cell growth and at the same time displayed a wildtype-like habitus.

In conclusion, the gene expression profile of *naa50-2:35Sp-NAA50(H115A)* seemed to resemble that of the *aminaa50* #13.6 knockdown mutants on a pathway level. To provide a better comparative overview and a more quantitative analysis, Venn diagrams were prepared. The diagrams show the overlap between the significantly (>2-fold, p<0.05) up- or downregulated transcripts in the two mutants (Fig. 55).

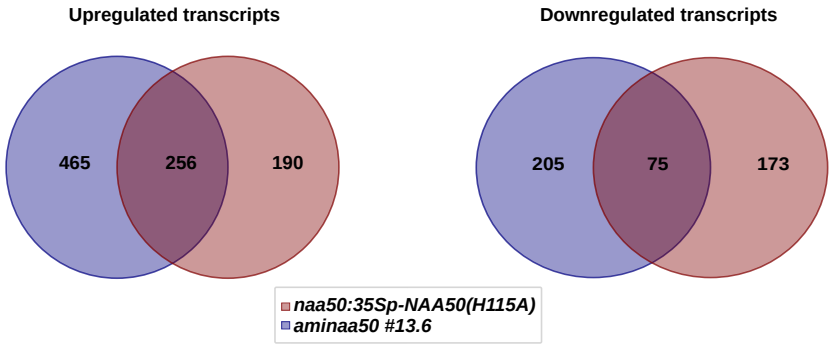

Figure 55: Venn diagrams showing the gene expression profiles of *naa50-2:35Sp-NAA50(H115A)* and *aminaa50* #13.6. Comparison between significantly (>2-fold, p<0.05) up- or downregulated transcripts (n=4). Since the plants for the transcriptome analysis were grown side-by-side and the *naa50-2:35Sp-NAA50(H115A)* and *aminaa50* samples were analyzed in one run, the gene expression profiles of the two mutants are comparable.

Among the 446 genes found to be upregulated in *naa50-2:35Sp-NAA50(H115A)*, 256 (57 %) were also accumulating in *aminaa50* #13.3. Similarly, of the 248 genes which were downregulated in *naa50-2:35Sp-NAA50(H115A)*, 75 (30 %) were also transcribed significantly less in aminaa50 #13.6. In addition, the comparison of the gene expression profiles revealed that only one transcript (AT5G11340) was expressed antagonistically between *aminaa50* and *naa50-2:35Sp-NAA50(H115A)*. This transcript encoded for NAA50, which was 4.3-fold downregulated in *aminaa50* but 63.4-fold overexpressed in *naa50-2:35Sp-NAA50(H115A)*. Hence the expression profiles of *aminaa50* and the complemented *naa50-2* knockout lines strongly resembled each other, indicating that both mutants suffered from decreased NAA50 activity - in one case caused by the depletion of transcripts encoding for NAA50 via artificial microRNA and in the other case as a result of the mutation in the overexpressed genetically engineered NAA50(H115A). In both genotypes, this decrease in NAA50 activity affected the gene expression patterns but not the physical appearance of the plants.

In essence, the complementation of the *naa50-2* knockout mutant with NAA50(H115A) under the control of the 35S promoter revealed the importance of NAA50 expression for pollen development and fertility. Moreover, it once again confirmed that minimal amounts of NAA50 activity are sufficient to ensure proper plant growth in the vegetative phase.

2.4 Compartment-specific complementation of *naa50-2*

Given its localization in the nucleus and the ER (2.1.1), *At*NAA50 might carry out additional functions besides catalyzing the N-terminal acetylation of nascent polypeptides at the ribosome. To understand in which subcellular compartment(s) *At*NAA50 is required, *naa50-2* knockout mutants were complemented with *At*NAA50-eYFP fusion proteins expected to localize exclusively to the nucleus (NLS-*At*NAA50-eYFP), the cytosol (NES-*At*NAA50-eYFP), or the nucleus, the cytosol and the ER (*At*NAA50-eYFP).

To this end, the full-length sequence encoding for the NAA50-eYFP fusion protein was PCR-amplified (4.4.4) from the pB7YWG2-35Sp-NAA50-eYFP vector (#1658) generated by Dr. Iwona Stephan. The primers (#4864 and #4867) used for the amplification harbored *BamH*I and *Sal*I endonuclease restriction sites (Supplementary Tab. S6). To generate the pBinAR-35Sp-NAA50-eYFP construct (#1727), the PCR fragment was directly ligated into the empty pBinAR vector (#1834) under the control of the constitutive CaMV 35S promoter. In order to exclusively target the *At*NAA50-eYFP fusion protein to the nucleus, the nuclear

localization sequence (NLS) of the simian virus SV40 large T antigen was amplified from the GreenGate entry module pGGD003 (#1762) with the primers #4865 and #4866 (Kalderon et al., 1984). The primers carried *Kpn*I and *BamH*I restriction sites (Supplementary Tab. S6) so that the NLS could be joined with the previously generated *At*NAA50-eYFP PCR fragment and the empty pBinAR vector (#1727) in a three-way ligation. As a result, the pBinAR-35Sp-NLS-NAA50-eYFP construct (#1723) was generated. To prevent nuclear localization of *At*NAA50-eYFP, the nuclear export signal (NES) of the rabbit heat-stable protein kinase inhibitor α was harnessed (Wen et al., 1995; Matsushita et al., 2003). The NES was constructed by annealing two primers (#4876 and #4877) which encoded for the short 19 amino acid NES sequence and harbored *Kpn*I and *BamH*I endonuclease restriction sites (Supplementary Tab. S6). Since previous experiments with the NES had shown that one NES repeat was insufficient to completely remove NAA50 from the nucleus (data not shown), the primers encompassed three repeats of the NES sequence. Finally, the 3xNES PCR product was joined with the *BamH*I-*At*NAA50-eYFP-*Sal*I PCR fragment and the empty pBinAR vector (#1727) in a three-way ligation resulting in the generation of the pBinAR-35Sp-3xNES-NAA50-eYFP construct (#1724).

All three constructs (#1723, #1724, and #1727) were transiently expressed in *N. benthamiana* (4.3.4) to verify the subcellular localization of the *At*NAA50-eYFP fusion proteins. Fluorescence microscopy (4.10.1) confirmed that the *At*NAA50-eYFP fusion protein without targeting sequence localized to the cytosol and the nucleus (Fig. 56).

As expected, the NLS-*At*NAA50-eYFP fusion protein localized exclusively to the nucleus. However, the 3xNES-*At*NAA50-eYFP fusion protein was found in both the nucleus and the cytosol, even though the nuclear fluorescence signal seemed to be less intense than the nuclear signal emitted by the fusion construct without targeting sequence. Quantification of the fluorescence in the cytosol and the nucleus in images taken from at least five different leaves revealed an average ratio of approximately 1:2 for the *At*NAA50-eYFP fusion protein, which dropped to 1:0.7 upon fusion with the 3xNES. A possible explanation for the unexpected nuclear signal observed after transient expression of 3xNES-*At*NAA50-eYFP is the high activity of the 35S promoter. The overexpression of 3xNES-*At*NAA50-eYFP might have overcharged the nuclear export machinery so that not all fusion proteins could be returned from the nucleus to the cytosol. To solve this problem, the rat glucocorticoid receptor (GR) ligand-binding domain was amplified from the pSW181 vector (#1769) using the primers #4888 and #4889 and fused to *At*NAA50-eYFP. The final pBinAR-35Sp-GR-NAA50-eYFP vector (#1891) was generated in a three-way ligation of the GR and the

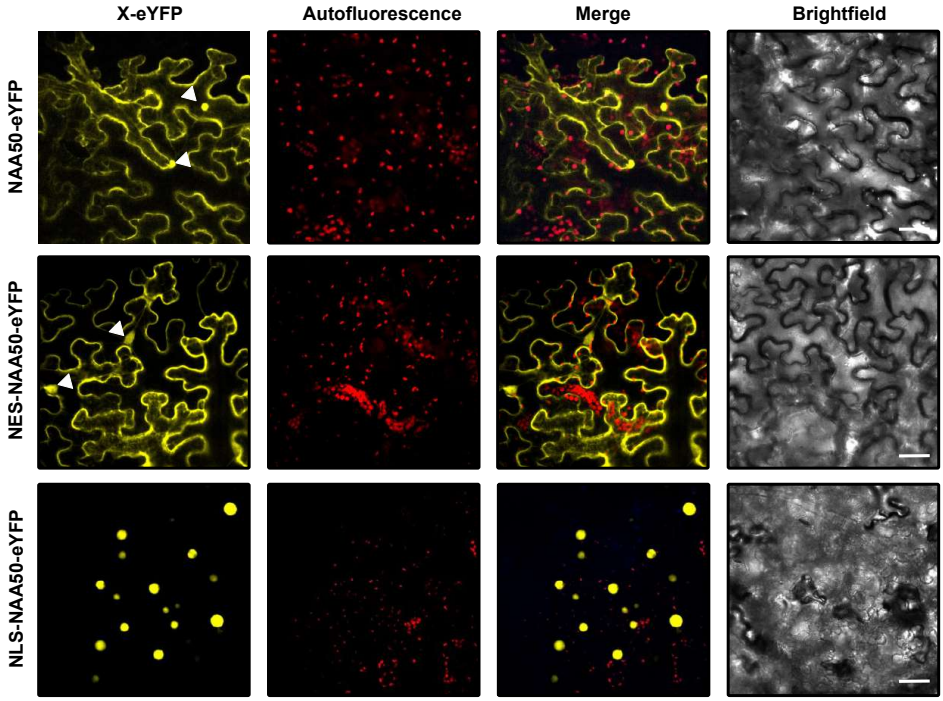

Figure 56: Subcellular localization of *At*NAA50-eYFP fusion constructs. *N. benthamiana* leaves were transiently transformed (4.3.4) with fusion constructs encoding for *At*NAA50-eYFP (upper panel), 3xNES-*At*NAA50-eYFP (middle panel) or NLS-*At*NAA50-eYFP (lower panel) under the control of the constitutive 35S promoter. From left to right, the different columns show the yellow channel (eYFP, 488/527 nm), the red channel (chloroplast autofluorescence, 561/615 nm), an overlay of both channels, and a brightfield image (scale bar = 25 μm).

NAA50-eYFP PCR fragment and the empty pBinAR vector. In the absence of hormones, the GR forms part of a molecular chaperone complex and is retained in the cytosol. Only upon hormone binding, the receptor undergoes a conformational change and translocates into the nucleus (Brockmann et al., 2001; Lopez-Salmeron et al., 2019). Since glucocorticoid hormones do not occur naturally in plants, the GR-*At*NAA50-eYFP fusion protein was expected to localize exclusively to the cytosol. Unfortunately, the transient expression of the construct in *N. benthamiana* (4.3.4) followed by fluorescence microscopy (4.10.1) demonstrated that the GR-*At*NAA50-eYFP fusion protein nevertheless partially localized to the nucleus (Fig. 57). One possible explanation for this behaviours is a predicted bipartite nuclear localization signal at position 125 of *At*NAA50 (Armbruster et al., 2020), which might override the GR cytosolic retention signal.

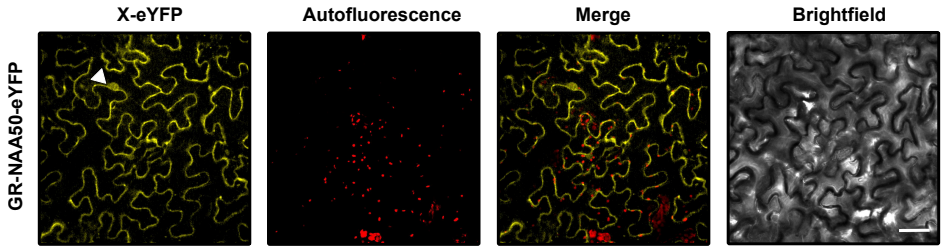

Figure 57: Subcellular localization of GR-*At*NAA50-eYFP fusion constructs. *N. benthamiana* leaves were transiently transformed (4.3.4) with a fusion construct encoding for GR-*At*NAA50-eYFP under the control of the constitutive 35S promoter. From left to right, the different columns show the yellow channel (eYFP, 488/527 nm), the red channel (chloroplast autofluorescence, 561/615 nm), an overlay of both channels, and a brightfield image (scale bar = 25 μm).

While the GR-*At*NAA50-eYFP fusion protein displayed a lower nuclear to cytosolic fluorescence ratio than *At*NAA50-eYFP (1:1.5 vs. 1:2), the general fluorescence intensity in GR-*At*NAA50-eYFP was rather low, indicating poor expression of the GR-*At*NAA50-eYFP fusion construct. For this reason, the 3xNES-*At*NAA50-eYFP fusion construct was chosen for future experiments.

In a next step, the *At*NAA50-eYFP fusion constructs (#1723, #1724 and #1727) were stably transformed (4.3.5) into heterozygous *naa50-2* mutants (T0 generation). Through selection on plates containing AT-medium (4.1.2) supplemented with kanamycin (4.3.6), several positive transformants for were identified (T1 generation, Tab. 9).

Table 9: Transformants identified after complementation of *naa50-2* knockout mutants with compartment-specific *At*NAA50-eYFP versions.

Genotype	# of homozygous T1 plants
naa50-2:35Sp-*At*NAA50-eYFP	12/37 (32 %)
naa50-2:35Sp-3xNES-*At*NAA50-eYFP	10/26 (38 %)
naa50-2:35Sp-NLS-*At*NAA50-eYFP	2/11 (18 %)

Since the homozygous T1 transformants displayed a wildtype-like phenotype, after eight weeks of growth under short-day conditions, they were were transferred to the long-day chamber for seed production. As previously observed for the *naa50-2* knockout lines complemented with *At*NAA50(H115A) under the control of the 35S promoter, all homozygous transformants produced aborted pistils instead of developing siliques. For this reason, the following experiments were conducted with the homozygous T2 offspring of the heterozygous lines #48 (*naa50-2*:35Sp-*At*NAA50-eYFP), #80 (*naa50-2*:35Sp-3xNES-*At*NAA50-eYFP) and #32 (*naa50-2*:35Sp-NLS-*At*NAA50-eYFP).

Remarkably, the expression of all three *At*-NAA50-eYFP variants complemented the *naa50-2* dwarf phenotype (Fig. 58A), as demonstrated by fresh weight measurements (Fig. 58B). However, the infertility of *naa50-2* was not rescued by any of the three constructs, as none of the homozygous transformants produced any pollen (Fig. 58C). The fact that once again, constructs under the control of the 35S promoter could rescue the dwarfism but not the infertility of the *naa50-2* lines reinforces the notion that *At*NAA50 is required for proper generative growth but cannot be expressed in the tissues where it is needed due to the limitations of the promoter.

To better understand why both the 35Sp-3xNES-*At*NAA50-eYFP and the 35Sp-NLS-*At*NAA50-eYFP construct ensured proper plant development in the vegetative phase, the localization of *At*NAA50-eYFP was verified by fluorescence microscopy in the roots of five-day old complemented *naa50-2* seedlings (Fig. 59).

Unlike previously observed in the transiently transformed *N. benthamiana* plants (Fig. 56), no nuclear signal was detected in the roots of *naa50-2* knockout mutants complemented with *At*-NAA50-eYFP. Similarly, the complementation with 3xNES-*At*NAA50-eYFP did not yield any nuclear fluorescence signal. Only upon expression of NLS-*At*NAA50-eYFP, a nuclear localization of the *At*NAA50-eYFP fusion protein was observed. While the absence of nuclear signal in plants complemented with the 3xNES-*At*NAA50-eYFP construct was

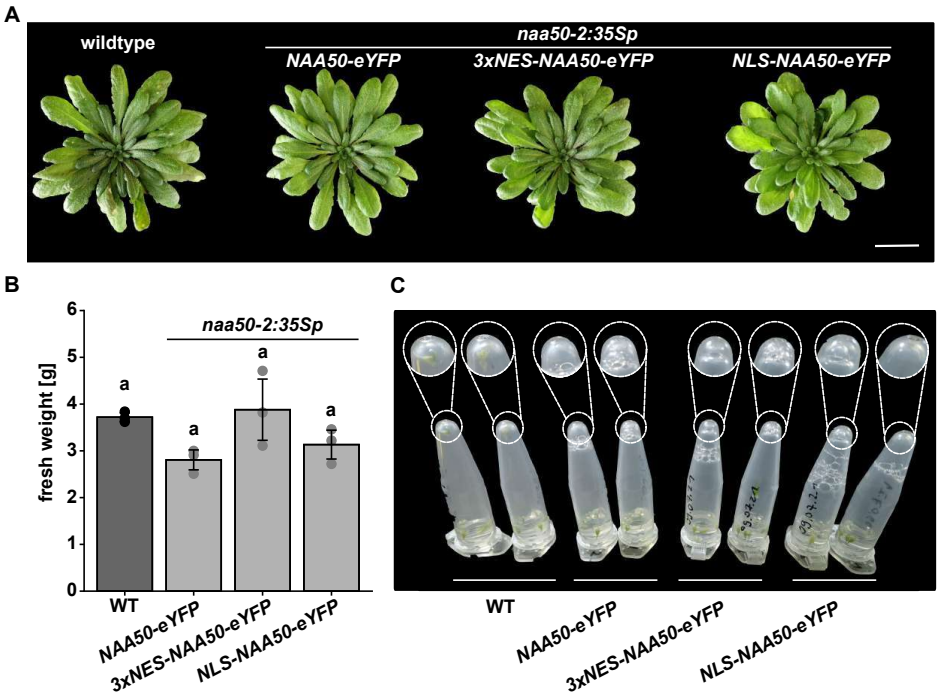

Figure 58: Compartment-specific expression of *At*NAA50-eYFP rescues the dwarf phenotype but not the infertility of *naa50-2* knockout mutants. **(A)** Phenotype of nine-week-old soil-grown (4.3.2) wildtype plants and the complemented lines homozygous for the tDNA insertion in the *NAA50* gene as determined by genotyping with the primers #321 and #604 as well as #603 and #604 (Supplementary Tab. S7). **(B)** Quantification of rosette fresh weight. Data given as means ± standard deviation. Different letters indicate individual groups identified by pairwise multiple comparisons with a Holm-Sidak, One-way ANOVA test ($p<0.05$, n=3). **(C)** Pollen extraction (4.3.8) from six flowers per replicate (n=2) revealed that pollen was absent in the mutants but not the wildtype plants (circular magnification).

expected, the expression of *At*NAA50-eYFP should have yielded a nuclear signal. This apparent difference in the localization of *At*NAA50-eYFP in the leaves of *N.benthamiana* plants and roots of *A. thaliana* might be tissue-dependent. The fact that *At*NAA50 was detected in the nuclear fractions of protein extracts derived from wildtype *A. thaliana* leaves (Fig. 7) supports this hypothesis.

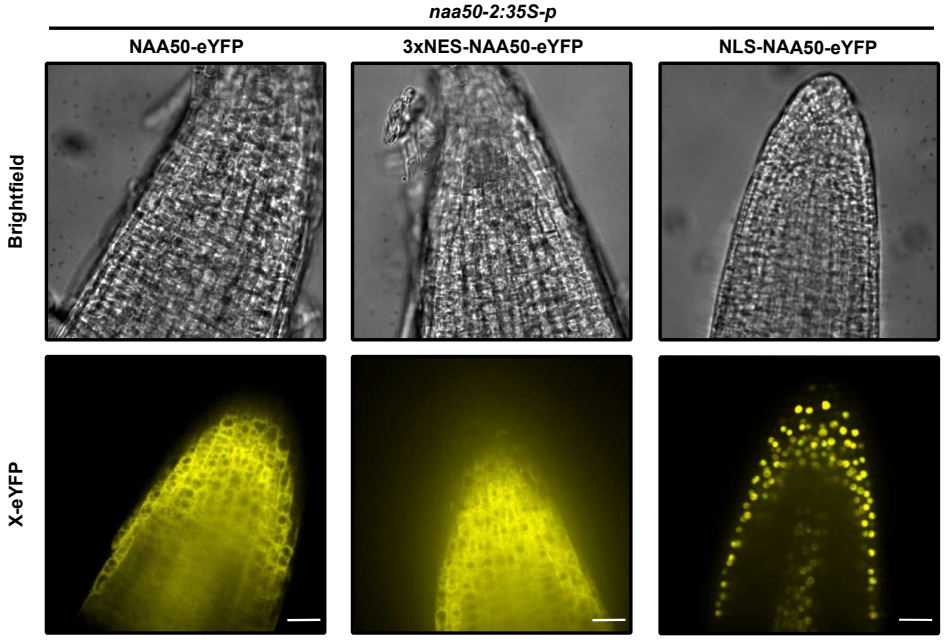

Figure 59: Subcellular localization of *At*NAA50-eYFP fusion constructs stably expressed in *A. thaliana*. After five days of growth on 1/2 MS plates (4.3.3) under short-day conditions, the roots of *naa50-2* seedlings complemented with different *At*NAA50-eYFP fusion constructs were examined under a fluorescence microscope (4.10). A brightfield image (upper panel) and an image of the yellow channel (eYFP, 488/527 nm) were taken. Pictures are representative of at least four individual plants per genotype (scale bar = 20 μm).

Based on the results of the complementation experiments, it is impossible to assert whether exclusively nuclear or cytosolic *At*NAA50 is sufficient for proper plant growth. The fact that the 3xNES-*At*NAA50-eYFP construct rescued NAA50 expression seemed to imply that *At*NAA50 is not required in the nucleus of plants. However, as observed in the tobacco plants, 3xNES-*At*NAA50-eYFP is not entirely absent from the nucleus. While the 3xNES was effective in exporting *At*NAA50 from the nucleus, minimal amounts of the acetyltransferase would always be found there. Those minimal amounts might not be detectable by fluorescence microscopy but might be sufficient to ensure proper plant growth. Similarly, the purely nuclear signal observed for the NLS-*At*NAA50-eYFP construct should not

be confused with the complete absence of *At*NAA50 from the cytosol. Indeed, the protein is synthesized in the cytosol and will therefore inevitably localize to this compartment for a short time. This short timespan could be enough for NLS-*At*NAA50-eYFP to perform any cytosolic acetyltransferase functions.

In conclusion, the complementation of the *naa50-2* knockout mutant with all three *At*NAA50-eYFP constructs rescued dwarfism of the sporophyte, but not the infertility of *naa50-2*, further empathizing the importance of the acetyltransferase for pollen development.

2.5 Role of NAA50 in chromatin cohesion

The previous chapters clearly showed that NAA50 is required for both vegetative and generative growth in *A. thaliana*. One possible explanation for the importance of *At*NAA50 during both phases might be the proposed role of NAA50 in sister chromatid cohesion (Feng et al., 2020). Sister chromatid cohesion is essential for the correct segregation of chromosomes during cell division and is mediated by the multi-subunit chromatin cohesion complex. This complex is conserved among eukaryotes and consists of the structural maintenance of chromosomes (SMC) and sister chromatid cohesion (SCC) proteins SMC1, SMC3, SCC3, and an α-kleisin subunit (1.3). In Drosophila, *Ds*NAA50 has been reported to N-terminally acetylate the α-kleisin SCC1, promoting its interaction with SMC3 and enabling the formation of the cohesion complex (Ribeiro et al., 2016). Since the N-terminal sequence of *Ds*SCC1 is shared by the three Arabidopsis α-kleisin subunits *At*SYN2-4 (Fig. 60) and the substrate specificity of NAA50, which mainly depends on the first few amino acids of the target proteins is conserved between fruit flies and plants, *At*SYN2-4 might be targets of *At*NAA50.

```
Dm.Q9U6D9           ----------MFYEHIILAKKGPLARIWLAAHWDKKITKAHVFETNIEKSVEGILQPKV  49
AT5G05490.1 (SYN1)  MLRLESLIVTVWGPATLLARKAPLGQIWMAATLHAKINRKKLDKLDIIQICEEILNPSV- 59
AT5G40840.2 (SYN2)  ----------MFYSHCLVSRKGPLGAIWVAAYFFKKLKKSQVKATHIPSSVDQILQKELD 50
AT3G59550.1 (SYN3)  ----------MFYSHTLLARKGPLGTVWCAAHVHQRLKKSQYTSINIPDTVDNIMFPEV- 49
AT5G16270.1 (SYN4)                                                              49
```

Figure 60: Sequence alignment of α-kleisins from *D. melanogaster* and *A. thaliana*. For simplicity, only the N-termini are depicted. The conserved MFY residues at the N-terminus are marked in green. Sequences of the main isoforms were downloaded from TAIR (AT5G05490.1, AT5G40840.2, AT3G59550.1, and AT5G16270.1) or PDB (Q9U6D9). The alignment was generated with Clustal Omega.

Indeed, an *in vitro* acetylation assay (4.5.7) with ectopically expressed *At*NAA50 (4.5.5) purified from *E. coli* (4.5.6) revealed that a custom synthesized peptide modeled after the

conserved α-kleisin N-terminus (4.1.6) could be N-terminally acetylated by *At*NAA50 (Fig. 61A). In direct comparison with the previously mentioned model substrate of human NAA50, the MLGP peptide, however, the activity of *At*NAA50 towards the α-kleisin N-terminus was relatively low. While 4.6 μg of purified NAA50 on average acetylated 643 pmol of the MLGP peptide in one hour, the same amount of *At*NAA50 only acetylated 137 pmol and hence 4.7-fold less of the MFYS-peptide in the same timespan (data not shown). To ensure that the minimal activity of *At*NAA50 towards the MFYS-peptide was not merely the result of chemical acetylation, the MPFY-peptide was included in the experiment as a negative control. The MPYF-peptide displays the same sequence as the MFYS-peptide, with the sole difference of harboring a proline as a second residue at the N-terminus. This proline residue is thought to inhibit enzymatic but not chemical N-terminal acetylation (Van Damme et al., 2011). Since the MFYS, but not the MPFY peptide, was acetylated by *At*NAA50, the enzyme seemed to possess genuine activity towards the α-kleisin N-terminus. An assessment of the concentration- and time-dependency of the *in vitro* acetyltransferase activity of *At*NAA50 reinforced this notion (Fig. 61B and C). Both measurements showed that the amount of acetylated MFYS peptide increased linearly with increasing amounts of NAA50 enzyme and over time.

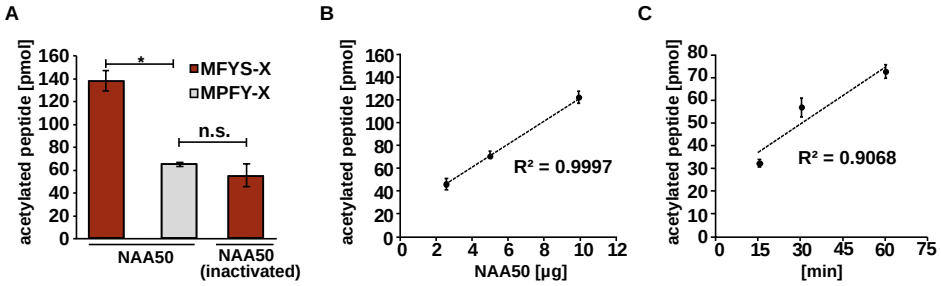

Figure 61: *At*NAA50 displays activity towards the MFY-X N-terminus. (A) Trx-His_6-*At*NAA50 waw purified from *E. coli* by immobilized metal affinity chromatography. 4.6 μg of purified enzyme were incubated for 1 h at 37 °C with 45 μM [^{3}H]acetyl-CoA and 0.2 mM of the synthetic MFYS-X or MPFYS-X peptide (4.1.6). After incubation, the peptides were enriched via specific interaction with SP-sepharose, and the amount of incorporated [^{3}H]acetyl was measured by scintillation counting. As a negative control, Trx-His_6-*At*NAA50 was heat-inactivated at 95 °C for 10 min. The average background was determined in reaction mixes incubated without peptide and was subtracted from the respective measurements. **(B)** Concentration-dependency and **(C)** time-dependency of the *in vitro* acetyltransferase activity. Data are presented as mean ± standard error (n=4, $p < 0.05$ in a Student's t-test).

In Drosophila, a wing-specific knockout of NAA50 leads to severe chromosome segregation defects during mitosis resulting in abnormal wing development. The extreme

dwarfism, spontaneous cell death, nuclear enlargement, and infertility documented in *naa50* knockout mutants imply that in *Arabidopsis thaliana* the depletion of NAA50 might lead to similar problems (Feng et al., 2016). Remarkably, the developmental defects caused by a wing-specific knockout of NAA50 in fruit flies can be rescued by expressing a fusion of the structural maintenance of chromosomes protein SMC3 and the sister chromatid cohesion protein SCC1 in the affected limbs. Based on the results of *in vitro* acetylation assays, it has been hypothesized that NAA50 stabilizes the interaction between the C-terminal domain of SMC3 and the N-terminus of the α-kleisin SCC1 by N-terminally acetylating the latter (Ribeiro et al., 2016). Since *At*NAA50 is in principle capable of N-terminally acetylating the Arabidopsis SCC1 homologs SYN2-4, the acetyltransferase might play a similar role in plants. To test whether the acetylation of α-kleisins is required for proper development in Arabidopsis, an *At*SMC3-*At*SYN4 fusion construct under the control of the constitutive CaMV 35S promoter was generated. For this purpose, the full-length coding sequences of SMC3 (AT2G27170.1) and SYN4 (AT5G16270.1) were amplified from cDNA (4.4.4). While the primers used to amplify SMC3 (#4966 and #4687) harbored *Xho*I and *Kpn*I endonuclease restriction sites, the SYN4 primers (#4995 and #4997) encompassed *Xho*I and *Sal*I recognition sites. In addition, the reverse primer of SMC3 and the forward primer of SYN4 each encoded for a part of a 53 amino acid long polypeptide linker (Eichinger et al., 2013). The SMC3 and the SYN4 PCR fragments were digested (4.4.5) and ligated (4.4.8) into the empty pBinAR vector (#1834). The final pBinAR-35Sp-SMC3-SYN4 construct (#1659) was stably transformed (4.3.5) into heterozygous *naa50-2* mutants (T0 generation). Through selection on plates containing AT-medium (4.1.2) supplemented with kanamycin (4.3.6), one positive transformant was identified (T1 generation). This plant was homozygous for the tDNA insertion in the *NAA50* gene and displayed a *naa50-2*-like dwarf phenotype (Fig. 62).

The fact that the SMC3-SYN4 fusion construct could not rescue the *naa50-2* growth defect can be interpreted in two ways. Either the construct was not properly expressed after stable transformation, or the dwarfism of *naa50* mutants is unrelated to SMC3/SYN4-mediated sister chromatid cohesion.

Unfortunately, the expression of the SMC3-SYN4 fusion construct could not be verified in the dwarfish *naa50-2:35Sp-SMC3-SYN4* line since the available leaf material was not sufficient for neither RNA or protein extraction. For this reason, a second round of selection was started with the remaining seeds of the heterozygous *naa50-2* T0 plants transformed with the SMC3-SYN4 fusion construct. This time, three positive transformants were iden-

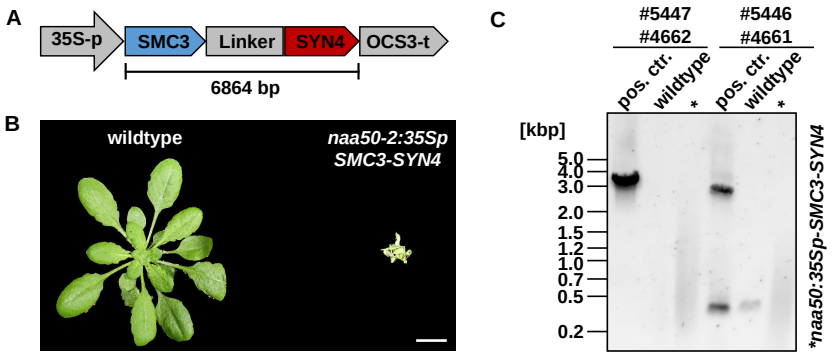

Figure 62: Expression of a SMC3-SYN4 fusion protein could not rescue the dwarf phenotype of *naa50-2* knockout mutants. (A) Schematic representation of the SMC3-SYN4 construct under the control of the 35S promoter. **(B)** Phenotype of six-week-old soil-grown (4.3.2) wildtype and the complemented *naa50-2:35Sp-SMC3-SYN4* line homozygous for the tDNA insertion in the *NAA50* gene as determined by genotyping with the primers #321 and #604 as well as #603 and #604 (Supplementary Tab. S7). **(C)** The SMC3-SYN4 fusion construct is not expressed in *naa50-2:35Sp-SMC3-SYN4* as verified by RNA extraction (4.4.11), followed by cDNA synthesis (4.4.12) and PCR reactions (4.4.4) amplifying SMC3-Linker (#5447 and #4662) and SYN4-Linker (#5446 and #4661) fragments. Wildtype cDNA and the original pBinAR-SMC3-SYN4 vector (#1659) were included as negative and positive controls, respectively.

tified. Genotyping revealed that two of those (66 %) were homozygous, and one (33 %) was heterozygous for the tDNA insertion in the *NAA50* gene. Additionally, genotyping with primers specific for the kanamycin resistance gene confirmed the integration of the SMC3-SYN4 fusion construct. As previously observed, the homozygous transformants retained their dwarfish phenotype. However, the heterozygous line displayed a wildtype like habitus so that RNA could be extracted (4.4.11) and transcribed into cDNA (4.4.12). Subsequently, the primer pairs #5446 and #4661 (expected *SYN4* PCR product size: 3,220 bp) as well as #5447 and #4662 (expected *SMC3* PCR product size: 3,661 bp) were used to verify the expression of the SMC3-SYN4 fusion construct. The original pBinAR-SMC3-SYN4 vector (#1659) used to transform the plants was included as a positive control, whereas wildtype cDNA served as a negative control. Since neither *SMC3* nor *SYN4* could be amplified from the cDNA, the SMC3-SYN4 fusion construct under the control of the constitutive 35S promoter was most likely not transcribed in the transformants.

In human cells, defects in sister-chromatid cohesion induced by the absence of NAA50 can also be counteracted by co-depleting the core NatA subunits NAA10 or NAA15. Since *Hs*NatA and *Hs*NAA50 only marginally affect each other's activity *in vivo*, it was hypothes-

ized that NAA10 and NAA50 might impact different downstream regulators of chromatin cohesion (Rong et al., 2016). To test whether the same was true in *A. thaliana*, eight-week-old soil-grown (4.3.2) heterozygous *naa50-2* knockout mutants were crossed with *aminaa10* knockdown mutants. Subsequently, seeds were collected from the T0 siliques, which developed as a result of the crossing. The seeds were germinated on 1/2 MS medium (4.3.3) under short-day conditions. After two weeks, the seedlings were transferred to soil and genotyped. Out of 20 plants, seven (35 %) tested positive for the presence of a tDNA insertion in the *NAA50* gene. Of those seven, three (42 %) also carried the construct encoding for the artificial microRNA against *NAA10*. Those three T1 plants were transferred to the long-day chamber for seed production. The resulting seeds were germinated on 1/2 MS medium (4.3.3) under short-day conditions, and once again, the developing seedlings were genotyped to verify the presence of the tDNA insertion in the *NAA50* gene and the construct encoding for the artificial microRNA against *NAA10*. Only one homozygous *naa50-2xaminaa10* mutant was identified (Fig. 63).

Figure 63: Co-depletion of NAA10 could not rescue the dwarf phenotype of *naa50-2* knockout mutants. Heterozygous *naa50-2* knockout mutants were crossed (4.3.7) with *aminaa10* lines. In the T2 generation, plants that were homozygous for the tDNA insertion in the *NAA50* gene and carried the construct encoding for the amiRNA against *NAA10* were identified by genotyping (4.4.4) with the primers #321 and #604, #603 and #604 as well as #3166 and #3915 (Supplementary Tab. S7). Seeds were germinated on 1/2 MS medium (4.3.3) and transferred to soil after two weeks of growth under short-day conditions. The phenotype of the plants was documented after four weeks (scale bar = 1 cm).

The co-depletion of NAA10 and NAA50 did not alleviate the dwarf phenotype of *naa50-2* knockout mutants, indicating that either defects in sister chromatid cohesion were not responsible for the growth defects in *naa50-2* or that, contrary to the situation in humans, NAA10 and NAA50 did not take over opposing roles in the mediation of chromatid cohesion.

In summary, it remains unclear whether *At*NAA50 is implicated in sister chromatid cohesion in *A. thaliana*. Similarly, it remains uncertain whether *At*NAA50 acetylates the α-kleisins SYN2-4 *in vivo*, even though the enzyme was shown to accept a custom-synthesized peptide mimicking the kleisin N-terminus as substrate.

3. Discussion

Up to 80 % of cytosolic proteins in humans and plants are targeted by N^{α}-terminal acetyltransferases (Nats), making N^{α}-terminal acetylation (NTA) the most widespread protein modification in higher eukaryotes (Arnesen et al., 2009; Goetze et al., 2009; Bienvenut et al., 2012; Linster & Wirtz, 2018). Even though the global protein imprinting mechanism alters key protein characteristics such as their activity, half-life, and subcellular localization (Ree et al., 2018), NTA is only starting to gain recognition as a regulator of proteome plasticity (Shemorry et al., 2013; Mueller et al., 2021; Linster et al., 2022).

In Arabidopsis, the dominant N-acetyltransferase is the *At*NatA complex, which co-translationally targets more than 40 % of the plant proteome. The core *At*NatA complex is composed of the catalytic subunit *At*NAA10 and the ribosome-anchoring subunit *At*NAA15 (Linster et al., 2015). The human ortholog of NatA associates with the regulatory subunits *Hs*NAA50 and *Hs*HYPK to form the quarternary *Hs*NatA/E complex (Deng et al., 2020).

Recently, homologs of NAA50 (AT5G11340) and HYPK (AT3G06610) were identified in *Arabidopsis thaliana* (Bienvenut et al., 2012; Miklankova, 2019; Armbruster et al., 2020; Neubauer & Innes, 2020). While *At*HYPK interacts with the core *At*NatA complex and regulates its activity (Miklankova, 2019), the biological role of *At*NAA50 and whether the protein contributes to the formation of a ribosome-associated *At*NatA/E complex remain unclear (Feng et al., 2020; Weidenhausen et al., 2021). To answer these questions, the first chapter of this work set out to identify *At*NAA50 interaction partners (2.1).

3.1 *At*NAA50 associates with the core NatA complex and the ribosome

Given the composition of the human NatA/E complex and the conservation of its components in Arabidopsis, the core NatA subunits *At*NAA10, *At*NAA15 and *At*HYPK were obvi-

ous candidates for possible interactions with *At*NAA50. Indeed, a co-immunoprecipitation experiment confirmed the interaction between *At*NAA15 and the remaining three putative *At*NatA/E components (Fig. 14). Similarly, the association of *At*NAA50 with the core *At*NatA components was corroborated (Fig. 15).

Interestingly, *At*HYPK was not enriched in the α-*At*NAA50 co-immunoprecipitate (Tab. 6). This agrees with reports by Weidenhausen et al. (2021), who did not observe any direct interactions between *At*NAA50 and *At*HYPK in their homology model of the *At*NatA/E complex. Moreover, the fact that the core *At*NatA components but not *At*HYPK were co-immunoprecipitated with *At*NAA50 could imply that *At*NAA50 and *At*HYPK associate with the core *At*NatA complex in a negative-cooperative manner. Such a behaviour was previously demonstrated for the human NatA/E complex *in vitro*. Even though *Hs*NAA50 and *Hs*HYPK interact with *Hs*NatA via independent binding surfaces, the tethering of one of the two subunits to *Hs*NatA destabilizes the binding of the other by inducing conformational changes in *Hs*NAA15. Nevertheless, in humans the formation of the quarternary *Hs*NatA/E complex can be observed, indicating that *Hs*NAA50 and *Hs*HYPK do not completely displace each other from the core *Hs*NatA complex (Deng et al., 2020). A similar mechanism is conceivable in *A. thaliana* and could explain why not only *At*NAA50 and the *At*NatA core subunits, but also *At*NAA50 and *At*HYPK were found in close proximity to each other in a split luciferase assay (Fig. 10). However, to definitively prove or disprove the existence of a quarternary *At*NatA/E complex, further experiments such as the heterologous expression and purification of all four *At*NatA/E components followed by size-exclusion chromatography are required. In addition, the interaction between *At*NAA50 and the *At*NatA core subunits could be studied in wildtype plants and *hypk* mutants via fluorescence resonance energy transfer to learn more about a possible negative-cooperative binding of *At*NAA50 and *At*HYPK to the core NatA complex.

In addition to confirming the interaction between all four *At*NatA/E components, the co-immunoprecipitation experiment suggested novel *At*NAA15 and *At*NAA50 interactors. Interestingly, many of these putative interactors were found in both the α-*At*NAA15 and the α-*At*NAA50 co-immunoprecipitate. The fact that the forty common interactor candidates included the ribosomal subunits EMB1473 (AT1G78630.1) and EMB3126 (AT3G63490.1) as well as a translation elongation factor (AT1G07920.1) supported the hypothesis that *At*NAA50 and the core *At*NatA complex associate with the ribosome. Indeed, *At*NAA15 and *At*NAA50 partially co-localize with ribosomal proteins upon polysome purification (Huber, 2015).

However, it remains unclear whether *At*NAA50 interacts with the ribosome independently or whether its ribosome-association requires the formation of the *At*NatA/E complex. In yeast, *Sc*NAA10 and *Sc*NAA50 are not found at the ribosome in the absence of *Sc*NAA15, even though *Sc*NAA50 makes direct contact with ribosomal rRNA expansion segments (Gautschi et al., 2003; Knorr et al., 2019). This indicates that *Sc*NAA50 contributes to the ribosome binding of the *Sc*NatA-NAA50 complex but is not sufficient to tether itself or *Sc*NAA10 to the ribosome. It has been speculated that in humans, *Hs*NAA50 and *Hs*HYPK both contribute to the interaction of the *Hs*NatA/E complex with the ribosome and that the competition between the two proteins could displace the respective other from the ribosome (Gottlieb & Marmorstein, 2018; Deng et al., 2020). Such a competition between *At*NAA50 and *At*HYPK for ribosome binding via *At*NAA15 could explain why upon polysome purification a considerable fraction of *At*NAA50 is not located at the ribosome (Huber, 2015). To test whether *At*NAA15 is required for the ribosomal localization of *At*NAA50 and whether *At*HYPK can displace *At*NAA50 from the ribosome, polysomes could be purified from wildtype plants and mutants depleted of NAA15 and HYPK. Subsequently, the amount of co-purified *At*NAA50 could be compared between the genotypes.

In humans and plants, a non-ribosome-bound, cytosolic fraction of NatA was identified, suggesting that the NAA10 and NAA15 associate in the cytosol and transiently interact with the ribosome for the recognition and acetylation of NatA substrates (Linster et al., 2015; Weyer et al., 2017; Miklankova, 2019). It is currently unknown whether *At*NAA50 already joins this complex in the cytosol or whether the ribosome is required as scaffold for *At*NatA-NAA50 complex formation.

Regardless of where the NatA-NAA50 complex forms and which subunits are directly involved in ribosome binding, the area around the ribosome exit tunnel is notoriously crowded. Various ribosome-associated factors compete for access to nascent polypeptides protruding from the ribosome exit channel. Among those factors are methionine aminopeptidases (MetAPs), which cleave the initiator methionine (iMet) from the N-termini of nascent protein chains (Kramer et al., 2009). In eukaryotes, approximately two thirds of the proteome are potential MetAP substrates (Giglione et al., 2004). The cotranslational removal of the iMet by MetAPs is a prerequisite for the acetylation of protein N-termini by NAA10 (Giglione et al., 2015; Ree et al., 2018). It has been proposed that NatA-bound NAA50 and MetAP compete for access to the N-termini of nascent polypeptides. Once NAA50 acetylates a protein, its N-terminus is blocked for NatA since MetAP cannot act on acetylated iMet residues (Van Damme et al., 2015). Although there is no direct structural information

regarding the human or yeast MetAP–ribosome complex, it is assumed that in both organisms, concomitant MetAP/NatA binding is possible and that after iMet cleavage, MetAP substrates are directly handed over to NatA (Knorr et al., 2019; Wild et al., 2020). Remarkably, in this thesis neither of the two Arabidopsis MetAPs (AT2G45240 and AT3G59990) was co-immmunoprecipitated with *At*NAA15 or *At*NAA50. To test whether the *At*NatA/E components are neverthless found in close proximity to MetAPs *in vivo*, a luciferase split assay or a biotin-based proximity labeling approach could be applied.

In contrast to MetAP, chaperones or targeting and translocation factors cannot bind to *Sc*NatA and the ribosome simultaneously due to steric clashes (Knorr et al., 2019). Still, *At*NAA50 co-immunoprecipitated with a number of chaperones, including the heat-shock proteins HSP60 (AT3G13860), HSP70 (AT3G09440), and HSP90 (AT5G56010) as well as the CCT2 (AT5G20890) subunit of the chaperonin containing T-complex (Tab. S2). Similarly, *At*NAA15 co-immunoprecipitated the universal chaperone ATSUP (AT3G53990) and CCT7 (AT3G11830), another component of the chaperonin containing T-complex (Tab. S1). The importance of those chaperones in the context of NatA-mediated protein turnover will be discussed later in this chapter (3.2).

In conclusion, the co-immunoprecipitation experiment independently confirmed the results of the split luciferase assay and implied that - in agreement with its presumed function as co-translational acetyltransferase - *At*NAA50 associates with the core *At*NatA complex at the ribosome.

3.2 The depletion of *At*NAA50 has no impact on *At*NatA function *in vivo*

In humans, the role of HYPK in NatA-mediated protein acetylation remains unclear. While *Hs*HYPK is required for the acetylation of the known *Hs*NatA substrate PCNP *in vivo* (Arnesen et al., 2010), both *Hs*HYPK and *Hs*NAA50 contribute to *Hs*NAA10 activity inhibition through structural alteration of the *Hs*NAA10 substrate-binding site *in vitro* (Deng et al., 2020). In plants, on the other hand, a global decline of NTA frequency was observed specifically for NatA substrates upon depletion of HYPK, indicating that the regulatory subunit was required for NatA-mediated NTA *in vivo* (Miklankova, 2019).

Since the first chapter of this thesis revealed that in *A. thaliana*, *At*NAA50 interacted with the core *At*NatA components (2.1), the question arose whether *At*NAA50 had a regu-

latory impact on *At*NatA-mediated NTA just like previously observed for *At*HYPK. There are various non-mutually exclusive scenarios which would allow *At*NAA50 to modulate *At*NAA10 activity. On the one hand, *At*NAA50 binding could alter the conformation of the *At*NAA10 catalytic center or limit the access of *At*NAA10 to potential targets. On the other hand, *At*NAA50 could acetylate NatA-type N-termini and thereby protect them from iMet cleavage by MetAP and subsequent acetylation via *At*NatA. Since *At*HYPK is required for the proper function of *At*NatA *in vivo* (Miklankova, 2019), an indirect contribution of *At*NAA50 to the regulation of *At*NatA activity could be the displacement of *At*HYPK from the ribosome. However, changes in the N-terminal acetylation frequency of NatA substrates upon depletion of NAA50 could also arise from the co-regulation of the core *At*NatA subunits. The expression of *At*NAA10 and *At*NAA15 for instance is co-regulated in various eukaryotes (Gautschi et al., 2003; Linster et al., 2015; Rathore et al., 2016; Magin et al., 2017).

The analysis of two independent *naa50* knockout lines (SAIL_1210_A02 and SAIL_1186_A03) and the newly generated *aminaa50* knockdown lines #9.4 and #13.6 (2.2.2) revealed that the depletion of *At*NAA50 did not impair the transcription or protein accumulation of core *At*NatA subunits (Figs. 17, 18, 24 and 25). To assess the impact of NAA50-depletion on the overall acetylation status of cellular proteins, the level of free N-termini was determined in protein extracts from various NatA/E mutants. Given that NatA is responsible for nearly half of all acetylation events in plant cells (Linster et al., 2015), it did not come as a surprise that in comparison to wildtype plants, the abundance of free N-termini was strongly increased in NatA-depleted *muse6* mutants. In contrast, the abundance of free N-termini was only slightly elevated in *aminaa50* knockdown lines (Fig. 40). The marginal but statistically significant increase observed for the *aminaa50* mutants was in agreement with previous reports of a 4 % increase in the abundance of free N-termini in *naa50* knockout plants and can most likely be attributed to the decreased NTA of *At*NAA50 substrates (Linster, 2014). This view was supported by a bioinformatical analysis of the nuclear-encoded Arabidopsis proteome (Fig. 39). Based on their N-terminal sequence, 50.5 % of the 48,076 characterized proteoforms were putative *At*NatA substrates (MA, MC, MG, MS, MT, MV), whereas only 18.6 % were predicted to be acetylated by *At*NatC, *At*NatE or *At*NatF (MF, MI, MK, ML, MM, MY). This difference in the estimated size of the NatA and NatC/E/F substrate pools became even more apparent when only N-termini with experimentally verified Ac-status were included in the analysis. Of the 2,212 proteoforms which were annotated as N-terminally acetylated in the N-ter database, 62.7 % were predicted NatA and

only 5.4 % putative NatC/E/F substrates. The exact number of putative NatE substrates in the Arabidopsis proteome is however difficult to estimate due to the considerable overlap between the *in vitro* substrate specificities of *At*NAA30, *At*NAA50 and *At*NAA60 (Pesaresi et al., 2003; Armbruster et al., 2020; Linster et al., 2020; Neubauer & Innes, 2020). Even though in general, no substantial changes were observed in the abundance of free N-termini in *aminaa50* plants, the influence of NAA50-depletion on the acetylation status of NatA substrates, in particular, remained unclear. In humans, the interaction of *Hs*NAA50 with the core *Hs*NatA complex promotes the activity of both *Hs*NAA10 and *Hs*NAA50 *in vitro* (Deng et al., 2020). Similarly, in yeast the association of *Sc*NAA50 with the core *Sc*NatA complex facilitates the binding of acetyl-CoA to *Sc*NAA10 and enhances *Sc*NatA activity *in vitro* (Deng et al., 2020). Moreover, *Sc*NAA50 was shown to be required for the acetylation of at least six known NatA substrates *in vivo* (Van Damme et al., 2015). To determine whether the depletion of *At*NAA50 had any impact on *At*NatA-mediated NTA in *A. thaliana*, data generated via an N-terminome profiling approach were re-analyzed. Initially, the SilProNAQ method (4.7.4) was devised to identify Nat substrates by comparing the acetylation profiles of wildtype plants and Nat mutants (Armbruster et al., 2020). Unfortunately, the SilProNAQ method did not identify any *At*NAA50 substrates when applied on proteins extracted from wildtype and *naa50-2* plants (Fig. 21). However, based on their N-terminal sequence, the vast majority (>80 %) of the 108 N-termini, which were characterized in wildtype and *naa50-2*, were predicted NatA substrates. Seven of them had even been experimentally verified as NatA substrates in a previous SilProNAQ screen (Linster et al., 2015). Based on the observation that the acetylation yield of neither the confirmed nor the predicted NatA substrates was significantly altered in *naa50-2* mutants, it was reasoned that contrary to *Sc*NAA50, *At*NAA50 did not contribute to proper NatA function *in vivo*.

To further strengthen this hypothesis, it would have been required to assess the NTA status of additional NatA substrates in NAA50 depleted plants. However, due to practical limitations of the SilProNAQ method which could only cover a few N-termini of highly abundant proteins, this was impossible (Bienvenut et al., 2017). Instead, global protein turnover and the response of plants to drought stress were used as alternative readouts for proper NatA function *in vivo*.

Global protein turnover was chosen since co-translational acetylation by NatA was recently reported to shield proteins from degradation by the proteasome. Hence, plants devoid of NatA activity display enhanced degradation of non-acetylated NatA substrates via the ubiquitin-proteasome system. Remarkably, the increased degradation of NatA targets is

compensated for by a concomitant increase in protein translation, resulting in an overall elevated turnover of NatA substrates while maintaining the state-state protein level (Linster et al., 2022). Since NatA-mediated NTA is dynamically controlled by the stress-related phytohormone abscisic acid (Linster et al., 2015), it has been hypothesized that the co-translational protein modification might contribute to stimulus-induced proteostasis and proteome surveillance (Linster et al., 2022). Indeed, the N-terminal acetylation of NatA substrates seems to be intricately linked to the drought stress response in *A. thaliana*. The exogenous application of ABA results in a decrease in NAA10 and NAA15 abundance, leading to a drop in NatA-mediated NTA. Conversely, artificial downregulation of NAA10 and NAA15 in transgenic plants causes these plants to mimic the canonical drought stress response. In consequence, NatA depleted plants are tolerant to desiccation (Linster et al., 2015). The fact that *hypk* mutants recapitulate both the increased protein turnover and stress resistance observed in core NatA mutants strengthens the link between NatA-mediated NTA and stimulus-induced protein surveillance, even though the mechanism linking those processes is currently unknown (Miklankova, 2019).

To test whether the absence of the *At*NatA/E subunits *At*HYPK and *At*NAA50 affected protein degradation in a similar manner, the accumulation of polyubiquitinated proteins after proteasome inhibition (Fig. 36) and the steady-state proteasome activity (Fig. 37) were comparatively assessed in various *At*NatA/E mutants. Unlike the core *At*NatA and the *hypk* mutants, which displayed an elevated proteasome activity as well as a significant accumulation of polyubiquitinated proteins after proteasome inhibition, the two independent *aminaa50* lines both behaved like wildtype plants. In agreement with this finding, the core *At*NatA and the *hypk* mutants but not the *aminaa50* lines were resistant to desiccation when watering of the plants was suspended for approximately three weeks (Fig. 47). Taken together, those observations once more indicated that *At*HYPK but not *At*NAA50 was required for the *At*NatA-mediated regulation of protein turnover *in vivo*.

As previously mentioned, it is unclear how NatA-mediated NTA contributes to stimulus-induced protein surveillance in plants. In humans, ubiquitin E3 ligases known as inhibitor of apoptosis proteins (IAPs) have recently been identified as agents of protein quality control. Under normal conditions, IAPs prevent the untimely assembly of pro-apoptotic protein complexes by associating with caspases and sequestering them. To interact with IAPs, the caspases require non-modified N-termini and special IAP binding motifs (IBMs). Interestingly, up to five percent of the human proteome - including many NatA substrates - carry cryptic IBMs. In consequence, the depletion of *Hs*NatA results in the generation of a multitude of

new potential IAP binding partners with free N-termini. Similar to known endogenous mitochondrial IAP antagonists, those proteins outcompete the caspases for IAP binding, thereby triggering apoptosis (Mueller et al., 2021). Currently it is unclear, whether this process is conserved in plants. On the one hand, the existence of apoptosis in plants is discussed controversially (Dickman et al., 2017). On the other hand, direct homologs of IAPs are missing in plants. Moreover, the only IAP-like protein of Arabidopsis (AT4G19700) lacks a domain which is required for the interaction with free N-termini in human IAPs, suggesting that IAPs do not act as N-recognins in plants (Kim et al., 2011).

Nevertheless, protein N-termini are hotspots for determining protein stability in plants. This is evidenced by the fact that in Arabidopsis, NatA-depletion triggers an increase in polyubiquitinated proteins, which are subsequently degraded by the ubiquitin-proteasome-system (Linster et al., 2022). However, the E3 ligases responsible for the specific polyubiquitination of NatA substrates with free N-termini have not yet been identified. In order to close this knowledge gap, custom-synthesized peptides mimicking the acetylated and free N-terminus of the known NatA substrate OAS-TL A (AT4G14880, Linster et al., 2022) were coupled to sepharose beads and incubated with protein extracts. Subsequently, the proteins bound specifically to the bait peptides were identified via mass-spectrometry (Tab. 7 and 8). While most of the putative N-terminal interactors were enzymes with functions unrelated to protein degradation and turnover, two remarkable candidates showed up in the N-terminal interactor screen. The first one was the CCT2 (AT5G20890) subunit of the multiprotein chaperonin containing T (CTT) complex. In Arabidopsis, the hetero-oligomeric complex consists of the subunits CCT1-CCT8 and contributes to protein folding by encapsulating proteins in its central cavity and providing them with a self-contained environment for proper folding. The complex is conserved among eukaryotes and binds to 7 % of nascent polypeptides directly after or during translation. Instead of recognizing specific motifs, the CCT-substrate selection depends on the context of translation, e.g. the presence of co-translational modifications such as NTA and/or cooperating chaperone systems (Yam et al., 2008). Interestingly, CCT2 was already identified as putative interactor of *At*NAA50 in the previously described co-immunoprecipitation experiment. Moreover, another component of the CCT complex, CCT7 (AT3G11830), was identified as a putative interactor of *At*NAA15 in the same assay (3.1). Hence it is conceivable that *At*NatA/E and the CCT complex work together at the ribosome to ensure proper folding of non-acetylated NatA substrates and thereby contribute to protein quality control. Indeed, in plant stem cells the CCT complex mitigates protein aggregation and confers resistance to proteotoxic stress (Llamas et al.,

2021). In the future, this possible link between acetylation via NatA and CCT-mediated protein folding could be investigated by confirming the interaction between *At*NAA15 and one or more of the eight components of the CCT complex. Furthermore, the formation of protein aggregates in NatA/E depleted mutants could be investigated. This is a particularly interesting line of research since in yeast, NatA and NatB mutants accumulate protein aggregates. Remarkably, this aggregation was not restricted to NatA or NatB substrates, implying a general protein folding deficiency conferred e.g. by reduced chaperone activity. In consequence it has been hypothesized that Nats might affect the activity of chaperones acting co-translationally at the ribosome exit tunnel (Friedrich et al., 2021).

The second N-terminal interactor of interest was the E3 ligase MAC3A (AT1G04510). MAC3A is a subunit of the nuclear MOS4-Associated Complex (MAC), which represents a regulatory hub in the plant pathogen response. Together with MAC3B (AT2G33340), the second E3 ligase of the MAC complex, MAC3A has been hypothesized to target defense repressors for degradation upon pathogen attack. Indeed, several components of the MAC complex, including MAC3A and MAC3B, but also the eponymous MOS4 (AT3G18165) itself, are required for pathogen resistance (Monaghan et al., 2009). MOS4 was identified in a forward genetic screen (Li et al., 1999), targeting unknown positive regulators of pathogen resistance. Interestingly, a second forward genetic screen for negative regulators of MOS4-mediated immunity identified MUSE1 (AT3G58030), MUSE2 (AT2G42030) and MUSE3 (AT5G15400). While MUSE1 and MUSE2 act as E3 ubiquitin ligases, MUSE3 is a putative E4 ubiquitin-conjugating enzyme (Huang et al., 2013; Dong et al., 2018). Remarkably, the same genetic screen also identified MUSE6 (AT1G80410) as suppressor of MOS4 absence. MUSE6 was later on characterized as NAA15 subunit of the *At*NatA complex.

If the interaction of MAC3A with the free N-terminus of an archetypical NatA substrate observed in this thesis were independently confirmed, this could indicate that MAC3A recognizes and ubiquitinates non-acetylated NatA-type defense repressors upon pathogen attack. Indeed, this thesis links NatA-mediated NTA to pathogen resistance by reporting the accumulation of the defense-triggering phytohormone salicylic acid in NatA-depleted mutants (Fig. 48). In addition, an increased resistance of those mutants to the virulent oomycete *H.a.* Noco2 and the bacterium *P. syringae* was observed (Fig. 47). This pathogen resistance of NatA-depleted plants was previously reported by Xu et al. (2015), who curiously attributed it to the stabilization of the immune receptors SNC1 (AT4G16890) and RPM1 (AT3G07040) as a consequence of diminished NatA-mediated NTA (Xu et al., 2015). This is in sharp contrast to the recently discovered stabilizing role of NatA-mediated NTA

in global protein turnover, where NTA protects NatA substrates from degradation (Linster et al., 2022). However, it cannot be excluded that individual proteins deviate from this rule, especially if their stability must be as tightly regulated as that of SNC1 and RPM1. Both proteins belong to the class of nucleotide-binding leucine-rich-repeat containing receptors (NLRs) which sense virulence effectors and in response trigger the biosynthesis of SA and the expression of pathogenesis-related (PR) genes (Dodds & Rathjen, 2010). Ideally, NLRs should be readily activated upon infection but remain inactive in the absence of pathogens to avoid uncontrolled immune activation and massive fitness costs (Karasov et al., 2017). Moreover, the acetylation of SNC1 is a particular case since the immune receptor is subject to alternative translation initiation. This process generates two distinct SNC1 isoforms which are targeted by NatA (Met-Met-Asp-SNC1) and NatB (Met-Asp-SNC1). Whereas acetylation via NatB stabilizes SNC1, acetylation via NatA creates an Ac/N-degron that is recognized by an at present unknown E3 ligases and destabilizes the immune receptor (Xu et al., 2015).

In essence, the N-terminal interactor screens suggested that the free but not the acetylated N-terminus of the OAS-TL A peptide was targeted by the E3 ligase MAC3A and the chaperone CCT2. The interaction of free NatA-type N-termini with the immune-associated E3 ligase MAC3A is plausible in the context of the enhanced pathogen resistance observed for NatA-depleted mutants. In the absence of pathogens, NatA-mediated acetylation could stabilize suppressors of pathogen resistance and prevent autoimmmunity. Upon depletion of NAA15, the free N-termini of those suppressors could target them for degradation via MAC3A or MAC3B, leading to an activation of the immune response. However, as the Arabidopsis genome encodes for more than 1,000 E3 ubiquitin ligases, it is very likely that more than one E3 ligase is involved in recognizing unshielded N-termini (Mazzucotelli et al., 2006). Hence in the future, interactor screens with other N-terminal peptides (e.g., resembling the SNC1 or the RPM1 N-terminus) as bait might identify more E3 ligases involved in the turnover of proteins lacking N-terminal acetylation marks.

3.3 *At*NAA50 modulates plant stress responses and fertility

The previous sections lined out that even though *At*NAA50 interacted with *At*NatA (3.1), it did not act as an *At*NatA modulator (3.2). Nevertheless, a knockout of *At*NAA50 was associated with severe growth defects and infertility (Fig. 16), which indicates that *At*NAA50 has other vital functions in vegetative plant growth and reproductive development.

The generation and characterization of the *aminaa50* knockdown lines #9.4 and #13.6 (2.2.2) revealed that minimal amounts of *At*NAA50 were sufficient to ensure proper plant growth and development (Fig. 23). Although the enzymatic activity of NAA50 has been demonstrated *in vitro* (Fig. 51), it is currently unclear whether *At*NAA50 must be catalytically active to fulfill its function. Unfortunately, no conclusions could be drawn from a complementation experiment with NAA50(H115A) because the activity of the mutated NAA50 version was - albeit significantly reduced - not completely abolished (Figs. 51 and 49). Given that the enzymatically active *Hs*NAA50 but not the catalytically dead *Sc*NAA50 rescue the dwarfism of *naa50* knockout mutants (Armbruster et al., 2020), it is plausible that *At*NAA50 activity is required for proper plant growth. However, this experiment has to be interpreted with caution. Despite the high degree of sequence conservation between the human and yeast NatA/NAA50 interfaces, purified *Sc*NatA and *Sp*NAA50 but not *Hs*NatA and *Sp*NAA50 form a complex, indicating that the mechanisms of NatA/NAA50 binding diverged during evolution. Those changes might reflect the regulatory role of HYPK, which is present in higher eukaryotes and most fungal species, but absent in fission and baker's yeast (Weyer et al., 2017; Deng et al., 2019). Hence the failure of *Sc*NAA50 to complement the Arabidopsis *naa50* knockout mutant might be attributed to the slightly different 3D structure or the missing activity of the yeast enzyme. However, an observation by Neubauer & Innes (2020) supports the notion that the activity of *At*NAA50 is required for its function. While the expression of inactive NAA50(I145A) in the *naa50* knockout background rescues the rosette radius of the mutants, the transgenic plants continue to display root dwarfism and a disturbed root morphology and do not develop viable seeds (Neubauer & Innes, 2020).

Despite the apparent importance of *At*NAA50 activity for its function, no *in vivo* NatA substrates have been identified up to date. This is most likely not due to the absence of substrates but due to the experimental limitations of the current SilProNaq approach, as the detection of free N-termini with NBD-Cl demonstrated an increase in free N-termini in the *aminaa50* knockdown lines (Fig. 40). A literature search suggested three interesting putative *At*NAA50 targets. The first one is the Arabidopsis homolog of the Drosophila α-kleisin subunit SCC1. *Ds*NAA50 has been reported to N-terminally acetylate the α-kleisin SCC1, promoting its interaction with the structural maintenance of chromosomes (SMC) protein SMC3 and enabling the formation of the chromatin cohesion complex (Ribeiro et al., 2016). Sister chromatid cohesion is essential for the correct segregation of chromosomes during cell division and is mediated by the multi-subunit chromatin cohesion complex. This complex is conserved among eukaryotes and consists of the structural maintenance of

chromosomes (SMC) and sister chromatid cohesion (SCC) proteins SMC1, SMC3, SCC1, and SCC3. Since the substrate specificity of NAA50 is conserved between fruit flies and plants (Rong et al., 2016; Armbruster et al., 2020) and the N-terminal sequence of *Ds*SCC1 (MFY) is shared by the three Arabidopsis α-kleisin subunits *At*SYN2-4 (Fig. 60), *At*SYN2-4 (AT5G40840, AT3G59550, and AT3G59550) might be targets of *At*NAA50. While *At*SYN2 and *At*SYN4 play an important role in repairing DNA damage in somatic cells and partially compensate for each other, *At*SYN3 is essential for megagametogenesis and pollen development (Yuan et al., 2014). Defects in DNA damage repair or chromatid cohesion might cause faulty cell division, aneuploidy and changes in cell properties. For these reasons, the lack of *At*NAA50-mediated NTA of α-kleisins might explain the phenotypes of *naa50* knockout mutants, including spontaneous cell death, nuclear enlargement, and pollen abortion (Feng et al., 2020). While *At*NAA50 could indeed acetylate a custom-made peptide with a SYN-like N-terminus *in vitro* (Fig. 61), the *in vivo* acetylation status of the plant α-kleisin subunits remains unknown. In the future, complementation experiments with genetically engineered NatA-type or non-acetylatable α-kleisin subunits in the *naa50* background could help elucidate the role of *At*NAA50 in sister chromatin cohesion.

A second putative *At*NAA50 target is the cysteine endopeptidase CEP1 (AT5G50260). The CEP1 N-terminus (MKR) fits the *At*NAA50 substrate specificity as determined by global acetylome profiling (Armbruster et al., 2020). CEP1 is expressed specifically in the tapetum during anther development and is required for functional pollen formation. Interestingly, NAA50-depletion is associated with an increased transcription of CEP1 and an impaired expression of several genes involved in pollen wall deposition and pollen mitotic division (Feng et al., 2022). In agreement with this finding, the knockout of NAA50 results in defects in pollen formation and ultimately infertility (Armbruster et al., 2020; Feng et al., 2020, 2022). These defects in pollen formation were also visible in *naa50* knockout mutants complemented with a variety of genetically engineered *At*NAA50 versions under the control of the 35S promoter, even though the rosette radius of those transformants was recovered (Figs. 49, 50, and 58). The fact that the expression of these *At*NAA50 constructs could rescue the dwarfism but not the infertility of the *naa50-2* lines suggests that *At*NAA50 is required for proper pollen development but could not be expressed in the tissues where it was needed due to the limitations of the promoter. No seeds were obtained, when the stigma of complemented *naa50* mutant plants were pollinated with wildtype pollen. These results are well in line with findings by Feng et al. (2020) and indicate that *At*NAA50 is involved in male and female fertility. To determine whether the role of *At*NAA50 in generative growth

is tied to the N-terminal acetylation of CEP1, it might be worthwhile to investigate whether or not *At*NAA50 can acetylate CEP1 *in vitro*.

The third and last potential *At*NAA50 substrate is EDR1 (AT1G08720). Mutations in the protein kinase result in an increased sensitivity to various stimuli, including drought and the phytohormones ABA and ethylene (Frye et al., 2001; Tang et al., 2005; Wawrzynska et al., 2008). EDR1 was identified as interactor of *At*NAA50 in a yeast two-hybrid screen (Neubauer & Innes, 2020). This interaction was confirmed by co-immunoprecipitation of NAA50 and EDR1 in this thesis (Fig. 15). According to Neubauer & Innes (2020), EDR1 and NAA50 are both negative regulators of the plant defense response. In agreement with this assumption, this thesis demonstrates that *aminaa50* knockdown lines not only over-expressed transcripts (Figs. 28 and 29) and proteins (Figs. 32 and 33) involved in plant immunity, but also displayed an enhanced resistance to the bacterium *P. syringae* and the oomycete *H.a.* Noco2 (Fig. 45). Interestingly, this resistance was not associated with an accumulation of salicylic acid as previously observed for NatA depleted plants (Fig. 48). While the mechanism which drives the pathogen resistance of *aminaa50* remains unclear, the role of EDR1 in plant immunity has recently been elucidated. The kinase interferes with the association of EDS1 (AT3G48090) and PAD4 (AT3G52430) and thereby impedes the activation of intracellular NLR receptors which usually trigger the biosynthesis of salicylic acid and the expression of PR genes (Neubauer et al., 2020). Like NAA50 (Fig. 5), EDR1 localizes to the ER (Christiansen et al., 2011; Neubauer & Innes, 2020). However, for none of the two proteins, direct ER-associated functions have been described so far. While the loss of EDR1 leads to enhanced sensitivity to ER stress, NAA50 depletion induces constitutive ER stress signaling, indicating that both proteins are negative regulators of ER stress (Neubauer & Innes, 2020). Based on these observations, Neubauer & Innes (2020) propose that phosphorylation of NAA50 via EDR1 is required for NAA50-mediated NTA which in turn ensures proper protein folding and thereby inhibits ER stress. However, up to date, the phosphorylation of *At*NAA50 has not been observed. Hence it is unclear if NAA50 is indeed a substrate of EDR1. Since the N-terminus of EDR1 (MKH) fits the reported *At*NAA50 substrate specificity, EDR1 might just as well be a NAA50 substrate. In the future, *in vitro* and *in vivo* acetylation screens might be valuable tools to assess the role of *At*NAA50 and EDR1 in plant immunity and the response to ER stress.

Since the localization of proteins determines their access to substrates and potential interaction partners, knowledge about the subcellular localization of *At*NAA50 is key to understanding its function within the cell. This thesis reports the localization of an *At*NAA50-

eYFP fusion protein to the cytosol, the nucleus and the ER (Fig. 5). While the cytosolic and ER-associated localization of *At*NAA50 is in agreement with its function as a ribosome-associated acetyltransferase, the function of *At*NAA50 in the nucleus remains elusive. A nuclear localization of *At*NAA50 is, however, in agreement with a predicted bipartite nuclear localization signal at position 125 of NAA50 (Kosugi et al., 2009) and the nucleocytoplasmic localization of its human counterpart *Hs*NAA50 (Arnesen et al., 2006). Moreover, *At*NAA10 (Fig. 5) and *Hs*NAA10 both also localize to the nucleus (Arnesen et al., 2005), demonstrating that a nuclear localization of acetyltransferases is not unusual. In the nucleus, *Hs*NAA10 regulates the response to hypoxia by ϵ-lysine acetylation of the transcription factor HIF-1α (Kang et al., 2018). Since *At*NAA50 has also been shown to operate as auto-lysine acetlytransferase *in vitro*, a similar function of *At*NAA50 in the nucleus is conceivable (Armbruster et al., 2020).

In essence, this thesis demonstrates that *At*NAA50 is crucial for plant growth and fertility. While the association of *At*NAA50 with the core *At*NatA complex and the ribosome was confirmed, no regulatory impact of *At*NAA50 on *At*NatA-mediated NTA was observed. Instead of acting as a NatA-modulator, *At*NAA50 executed various NatA-independent functions, such as the regulation of the plant defense response against pathogens. Whether those functions depend on the acetyltransferase activity of *At*NAA50 and if so, which proteins are targeted by *At*NAA50 *in vivo*, remains to be elucidated.

4. Materials and methods

4.1 Technical equipment and materials

Chemicals, consumables, and devices not listed below are standard laboratory equipment and were obtained from AppliChem (Karlsruhe), Macherey-Nagel (Düren), or Sigma-Aldrich (Steinheim).

4.1.1 Technical equipment

Autoclave Sanoclav	Sanoclav, Bad Überkingen-Hausen
Binocular microscope MZFLIII	Leica, Wetzlar
Camera DSC-RX100 M3	Sony Deutschland, Cologne
Centrifuge 5417R	Eppendorf, Hamburg
Centrifuge Mikro200R	Hettich Zentrifugen, Tuttlingen
Centrifuge Rotanta 460R	Hettich Zentrifugen, Tuttlingen
Centrifuge Sorvall LYNX 6000	Thermo Fisher, Waltham (USA)
Centrifuge Sorvall RC5C	DuPont, Bad Homburg
Climate chamber Percival CU-3GL14	CLF Laborgeräte GmbH, Emersacker
Climate chamber ThermoTEC	ThermoTEC, Weilburg
Confocal microscope A1R	Zeiss, Jena
DM IRB epifluorescence microscope	Leica, Wetzlar
DNA gel chamber 40-1214	PeqLab, Erlangen
Electrophoresis chamber PerfectBlue Twin ExW	PeqLab, Erlangen
Electrophoresis chamber Mini Preotean III	Bio-Rad, Feldkirchen
Electrophoresis chamber Mini Preotean Tetra	Bio-Rad, Feldkirchen
ERS-VoX spinning disk confocal microscope	Nikon, Tokyo (JPN)
Gas burner gasprofi 2 accu	WLD-Tec GmbH, Arenshausen
Gel Jet Imager 2000	Intas, Göttingen
Heatblock HBT-2 132	Labor Consult HLC, Bovenden

Heater (80°C) B6120	Heraeus Instruments, Hanau
Horizontal shaker KS 260 Basic	IKA Werke, Staufen
Horizontal shaker Belly Dancer	Stovall, Greensboro (USA)
Ice machine	Ziegra Eis Maschinen, Isernhagen
ImageQuantTM LAS 4000	GE Healthcare, Freiburg
Incubator (28°C / 37°C)	Heraeus Instruments, Hanau
Incubator Multitron Standard	Infors, Bottmingen (CH)
Magnetic stirrer MR 3001	Heidolph Instruments, Schwabach
NanoDrop ND-2000	Peqlab, Erlangen
Orbital shaker Rotamax 120	Heidolph Instruments, Schwabach
PCR cycler Biometra T-Gradient	Analytik Jena, Jena
PCR cycler Mastercycler Gradient 5531	Eppendorf, Hamburg
PCR cycler Mastercycler Personal 5332	Eppendorf, Hamburg
Photometer Kontron UVIKON 923	Secoman, Kandsberg
Plate reader Fluostar Omega	BMG, Offenburg
Power supply Power Pac 1000	Bio-Rad, Feldkirchen
Precision balance AUW120D	Shimadzu, Griesheim
Precision balance CY323C	Waagen Friedrichs, Heidelberg
RT PCR cycler Rotor-Gene 6000	Qiagen, Hilden
Scintillation counter Tri-Carb 2810TR	PerkinElmer, Waltham (USA)
Sterile bench Lamin Air 2448/HB 2472	Heraeus Instruments, Osterode
Ultra-low temperature freezer C660-86	New Brunswick Scientific, Nürtingen
Ultrasonic homogeniser UW70	Bandelin Electronic, Berlin
Vortex 444-1372	VWR International, Darmstadt
Water purification system PURELAB Classic	ELGA LabWater, Celle
Western Blot system Trans-Blot	Bio-Rad, Feldkirchen

4.1.2 Buffers and solutions

1/2 Hoagland medium	2.5 mM $Ca(NO_3)_2$, 0.5 mM $MgSO_4$, 2.5 mM KNO_3, 0.5 mM KH_2PO_4, 4 μM Fe-EDTA, 25 μM H_2BO_3, 2.25 μM $MnCl_2$, 1.9 μM $ZnCl_2$, 0.15 μM $CuCl_2$, 0.05 μM $(NH_4)_6Mo_7O_{24}$; pH 5.8
1/2 MS medium	2.21 g l^{-1} Murashige Skoog salts, 0.4 g l^{-1} MES; pH 5.8
5 x Laemmli buffer	10 % (w/v) SDS, 20 % (v/v) glycerine, 100 mM Tris, 0.1 % (w/v) bromophenol blue; 25 % (v/v) β-mercaptoethanol; pH 7.0

AT medium	5 mM KNO_3, 2.5 mM KH_2PO_4, 2 mM $MgSO_4$, 2 mM $Ca(NO_3)_2$, 0.05 mM Fe-EDTA, 0.01 μM $CoCl_2$, 0.02 μM Na_2MoO_4, 0.5 μM $CuSO_4$, 1 μM $ZnSO_4$, 10 μM NaCl, 14 μM $MnCl_2$; pH 5.8
LB medium	1 % (w/v) Bacto™ Tryptone, 0.5 % (w/v) Bacto™ Yeast Extract, 1 % (w/v) NaCl
Resolving gel buffer	1.5 M Tris, 0.4 % (w/v) SDS; pH 8.8
RIPA buffer	50 mM HEPES-KOH, 100 mM KCl, 5 mM EDTA, 5 mM EGTA, 50 mM NaF, 10 % (v/v) glycerol, 1 % (v/v) IGEPAL, 0.5 % (w/v) deoxycholate, 0.10 % (w/v) SDS, 1 mM Na_4VO_3, 1 mM PMSF; pH 7.8 supplemented with 1 × protease inhibitor cocktail (Roche)
Stacking gel buffer	0.5 M Tris, 0.4 % (w/v) SDS; pH 6.8

4.1.3 Chemicals

$(NH_4)_6Mo_7O_{24}$	AppliChem, Darmstadt
2-log-DNA-Marker	New England Biolabs, Beverly (USA)
^{3}H-acetylCoA	Hartmann Analytic, Braunschweig
ABA	Sigma-Aldrich, Steinheim
Acetic acid	Fluka Biochemika, Fuchs
Acetonitrile	Sigma-Aldrich, Steinheim
Acetosyringone	Sigma-Aldrich, Steinheim
Agar	Fluka Biochemika, Fuchs
Agarose	Biozym Scientific, Oldendorf
Albumin fraction V	Roth, Karlsruhe
Ampicillin	Roth, Karlsruhe
BactoTM Tryptone	BD Biosciences, Heidelberg
BactoTM Yeast Extract	BD Biosciences, Heidelberg
β-mercaptoethanol	Merck, Darmstadt
Beetle luciferin	Promega, Madison (USA)
BlueStar Prestained Protein Marker	NIPPON Genetics, Düren
Bromophenol blue	Kallies Feinchemie, Sebnitz
$Ca(NO_3)_2$	Fluka Biochemika, Fuchs
$CaCl_2$	AppliChem, Darmstadt
Citric acid	AppliChem, Darmstadt
$CoCl_2$	Duchefa, Haarlem (NLD)

cOmplete protease inhibitor cocktail	Roche, Mannheim
$CuCl_2$	Roth, Karlsruhe
$CuSO_4$	Merck, Darmstadt
Cycloheximide	Sigma-Aldrich, Steinheim
Deoxynucleotide Solution Mix	New England Biolabs, Beverly (USA)
DMSO	Roth, Karlsruhe
DTT	AppliChem, Darmstadt
EDTA	Roth, Karlsruhe
EGTA	Fluka Biochemika, Fuchs
Ethanol	Merck, Darmstadt
Ethidium bromide	Sigma-Aldrich, Steinheim
Fe-EDTA	Duchefa, Haarlem (NLD)
Gentamicin	Duchefa, Haarlem (NLD)
Glucose	Merck, Darmstadt
Glufosinate ammonium	Bayer, Leverkusen
Glycerine	Merck, Darmstadt
H_3BO_3	Merck, Darmstadt
H_3BO_3	Merck, Darmstadt
HCl	Sigma-Aldrich, Steinheim
Hepes	Roth, Karlsruhe
IGEPAL	Sigma-Aldrich, Steinheim
Imidazole	Sigma-Aldrich, Steinheim
IPTG	Sigma-Aldrich, Steinheim
Isopropanol	Roth, Karlsruhe
Kanamycin	Duchefa, Haarlem (NLD)
KCl	Merck, Darmstadt
KH_2PO_4	Merck, Darmstadt
KNO_3	Roth, Karlsruhe
KOH	Sigma-Aldrich, Steinheim
Mannitol	VWR International, Darmstadt
MES	AppliChem, Darmstadt
Methanol	Fisher Scientific, Schwerte
MG132	Sigma-Aldrich, Steinheim
$MgCl_2$	AppliChem, Darmstadt
$MgSO_4$	Merck, Darmstadt
Microagar	Duchefa, Haarlem (NLD)
$MnCl_2$	AppliChem, Darmstadt

Murashige Skoog salts	Duchefa, Haarlem (NLD)
Na_2MoO_4	AppliChem, Darmstadt
NaCl	AppliChem, Darmstadt
NaOH	AppliChem, Darmstadt
NP-40 Detergent Solution	Abcam, Cambridge (UK)
Phenol	Riedel-de Haen, Seelze
Phenylmethanesulfonylfluoride	Serva, Heidelberg
Polyethylenglycol 4000	Roth, Karlsruhe
Quick Coomassie Stain	Serva, Heidelberg
Rifampicin	Duchefa, Haarlem (NLD)
Rotiphorese Gel 30	Roth, Karlsruhe
Roti-Quant Bradford reagent	Roth, Karlsruhe
SDS	Fluka Biochemika, Seelze
Silwet Gold	Spiess-Urania Chemicals, Hamburg
Sodium citrate	Riedel-de Haen, Seelze
Sodium hypochlorite	Fluka Biochemika, Seelze
Spectinomycin	Sigma-Aldrich, Steinheim
Streptomycin	AppliChem, Darmstadt
Sucrose	Roth, Karlsruhe
TEMED	Roth, Karlsruhe
Tris	Roth, Karlsruhe
Triton X-100	Sigma-Aldrich, Steinheim
Tween 20	Sigma-Aldrich, Steinheim
Western blocking reagent	Roche, Mannheim
Z-Leu-Leu-Leu-AMC Proteasome Substrate I	Sigma-Aldrich, Steinheim
ZnCl	Merck, Darmstadt
$ZnSO_4$	Riedel-de Haen, Seelze

4.1.4 Consumables

12-well plates	Greiner Bio-One, Frickenhausen
96-well plates	Greiner Bio-One, Frickenhausen
Cover glass	Menzel, Braunschweig
EASYstrainer	Greiner Bio-One, Frickenhausen
GeneChip Arabidopsis Gene 1.0 ST Array	Affymetrix, High Wycombe (UK)
HiTrapTM Chelating column	GE Healthcare, Freiburg
Immobilon-P PVDF transfer membrane	Merck Millipore, Darmstadt

Microscope slides	Marienfeld, Laude-Königshofen
PD SpinTrap G-25 desalting columns	GE Healthcare, Freiburg
Petri dishes (round, 94 x 16 mm)	Greiner Bio-One, Frickenhausen
Petri dishes (square, 120 x 120 x 17 mm)	Greiner Bio-One, Frickenhausen
Rotilabo syringe filter (0.22-0.45 μm)	Roth, Karlsruhe
Semi-micro cuvettes (10 x 4 x 45 mm)	Sarstedt, Nümbrecht
Streptavidin-coated sepharose beads	Cytvia, Chalfont St. Gilles (UK)
Single-use syringe Luer-Look (10 ml)	BD Biosciences, Heidelberg
STRIP Tubes 0.1 ml for qRT-PCR	LTF-Labortechnik

4.1.5 Enzymes and kits

CloneJET PCR Cloning Kit	Thermo Scientific, Waldorf
EasyTag Express 35S Labeling Mix	PerkinElmer, Waltham (USA)
E.Z.N.A. Plasmid DNA Midi Kit	Omega Biotek, Norcross (USA)
Fast Gene Scriptase II cDNA Synthesis Kit	NIPPON Genetics, Düren
FastGene TAQ Ready Mix	NIPPON Genetics, Düren
NucleoSpin Gel and PCR Clean-up Kit	Macherey-Nagel, Düren
NucleoSpin Plasmid Kit	Macherey-Nagel, Düren
PCRBIO HiFi polymerase and buffer	PCR Biosystems, London (UK)
peqGOLD total RNA kit	Peqlab, Erlangen
peqGOLD DNase I Digest Kit	Peqlab, Erlangen
Phusion High-Fidelity DNA polymerase	New England Biolabs, Beverly (USA)
PlusOne Silver Staining Kit	GE Healthcare, Freiburg
qPCRBIO SyGreen Mix Lo-ROX	PCR Biosystems, London (UK)
Restriction enzymes	New England Biolabs, Beverly (USA)
RevertAid H Minus cDNA Synthesis Kit	Thermo Scientific, Walldorf
SuperSignal West Extended Duration Substrate	Thermo Scientific, Walldorf
T4 DNA Ligase and Buffer	New England Biolabs, Beverly (USA)
Universal RNA Kit	Roboclon, Berlin
RNA Extraction Kit	VWR, Radnor (USA)

4.1.6 Oligopeptides

The following peptides were custom-synthesized by GeneCust (Boynes, FRA) or Royobiotech (Shanghai, CHN) for *in vitro* acetylation assays and pulldown experiments:

Sequence	N-terminus	Manufacturer
SESSSRSRWGRPVGRRRRPVRVYP	*Hs*HMG-1 (P17096)	GeneCust
MLGPEGGRWGRPVGRRRRPVRVYP	*Hs*RNPF (P52597)	GeneCust
MFYSQFIRWGRPVGRRRRPVRVYP	*At*SYN4 (AT5G16270)	GeneCust
MPYSQFIRWGRPVGRRRRPVRVYP	*At*SYN4 (AT5G16270)	GeneCust
Ac-ASRIAKDVTELIG-(K)-Biotin	*At*OAS-TL A (AT4G14880)	Royobiotech
ASRIAKDVTELIG-(K)-Biotin	*At*OAS-TL A (AT4G14880)	Royobiotech

4.1.7 Software

EndNote X2	Thomson Reuters, New York (USA)
Fiji	Schindelin et al., 2012
Geneious	Biomatters, Auckland (NZL)
ImageQuant TL 8.1	GE Helathcare, München
Inkscape 1.1	Inkscape Project
Matplot.lib library in Python 2.7	Hunter (2007)
MS Office 365	Microsoft, Redmond (USA)
NanoDrop ND-2000	Peqlab, Erlangen
Overleaf	Overleaf
Photoshop CS5	Adobe Systems, San Jose (USA)
Pymol	Schrödinger Inc, New York City (USA)
Rotor-Gene Q Series Software	Qiagen, Hilden
Sigma Plot 12	SPPS Inc, München
SWISS-MODEL	Center for Molecular Life Sciences, Basel (CH)
Vector NTI 11	Invitrogen, Karlsruhe

4.2 Microbiological methods

4.2.1 Bacterial strains

For cloning and multiplication of vectors, chemocompetent *E. coli* XL1 Blue were used. Recombinant proteins were expressed in *E. coli* Rosetta (DE3). Transformation of *A. thaliana* or *N. benthamiana* was performed with chemocompetent *A. tumefaciens* GV3101.

Table 10: Bacterial strains used in this thesis.

Strain	Manufacturer	Genotype
E. coli XL1 Blue	Stratagene	*recA1 endA1 gyrA96 thi-1 hsdR17 supE44 relA1 lac- [F' proAB lacI^q, ZΔM15Tn10*(Tet^r)]
E. coli Rosetta (DE3)	Novagen	F- *ompT hsdSB(r_B^- m_B^-) gal dcm* pLysSRARE (Cam^r)
A. tumefaciens GV3101	GoldBio	C58, pMP90, pTiC58DT-DNA, Gent^r, Rif^r

4.2.2 Cultivation of bacteria

The bacteria were grown in liquid LB medium (4.1.2). To solidify the medium, 1.5 % agar was added. For selection, media were supplemented with the appropriate antibiotic (ampicillin: 100 μg ml^{-1}; kanamycin: 50 μg ml^{-1}; rifampicin: 50 μg ml^{-1}; gentamycin: 30 μg ml^{-1}; streptomycin: 100 μg ml^{-1}; spectinomycin: 100 μg ml^{-1}). *E. coli* were grown for 16 h at 37 °C and *A. tumefaciens* for 24-48 h at 28 °C in a shaking incubator (220 U min^{-1}).

4.2.3 Preparation and transformation of chemocompetent cells

4.2.3.1 Chemocompetent *E. coli*

500 ml LB medium (4.1.2) without antibiotics were inoculated with 10 ml of an overnight culture of chemocompetent bacteria (LB medium with corresponding antibiotics). The culture was incubated at 37 °C while shaking at 220 U min^{-1} until its OD_{600} reached 0.5-1.0. After incubation on ice for 20 min, the bacteria were centrifuged at 3,500 g for 10 min at 4 °C. Subsequently, the supernatant was discarded, and the pellet was resuspended in 100 ml LB medium (4.1.2) supplemented with 10 % (w/v) polyethylene glycol, 5 % (v/v) dimethyl sulfoxide and 50 mM Mg^{2+} at pH 6.5. The chemocompetent cells were aliquoted, snap-frozen in liquid nitrogen, and stored at -80 °C until further usage.

For transformation, 100 μl *E. coli* were thawed on ice and mixed with up to 10 µl vector DNA. The mixture was incubated on ice for 30 min. Subsequently, the bacteria were heat-shocked for 1 min at 42 °C. After a recovery of 2 min on ice, 500 μl LB medium (4.1.2) were added and the bacteria were incubated for 1 h at 37 °C while shaking (220 U min^{-1}).

4.2.3.2 Chemocompetent *A. tumefaciens*

250 ml LB medium (4.1.2) with antibiotics (50 μg ml^{-1} rifampicin, 30 μg ml^{-1}gentamycin) were inoculated with 5 ml of an overnight culture of chemocompetent bacteria. The culture was incubated at 28 °C while shaking at 220 U min^{-1}until its OD_{600} reached 0.8-1. After incubation on ice for 20 min, the bacteria were centrifuged at 3,500 g for 10 min at 4 °C. Subsequently, the supernatant was discarded and the pellet was resuspended in 10 ml 20 mM $CaCl_2$. After repeating this step once, the chemocompetent cells were aliquoted, snap-frozen in liquid nitrogen and stored at -80 °C until further usage.
For transformation, 200 μl *A. tumefacines* were thawed on ice and mixed with 1 µg vector DNA. The mixture was incubated on ice for 10 min and then transferred to liquid nitrogen for 5 min. After a 10 min heat-shock at 37 °C, 1 ml LB medium (4.1.2) was added to the bacteria and the mixture was incubated for 3-4 h at 28 °C while shaking (220 U min^{-1}).

4.2.4 Glycerol stocks

500 μl of bacterial liquid culture with an OD_{600} of 0.5-2 were mixed with 500 μl autoclaved 50 % glycerol (v/v), snap-frozen in liquid nitrogen, and stored at -80 °C.

4.3 Methods of plant work

4.3.1 Plant material

This work refers to the *Arabidopsis thaliana* ecotypes Col-0 (CS1092) and Col-3 (CS908) as wildtype (WT). In addition to these plants, the transgenic plants listed in Tab. 11 were used.

Table 11: Transgenic plant lines used in this thesis.

#	Name	Description
#325	*naa50-1* (SAIL_1210_A02)	T-DNA insertion, NAA50 knockout (Armbruster et al., 2020; Neubauer & Innes, 2020)
#329	*naa50-2* (SAIL_1186_A03)	T-DNA insertion, NAA50 knockout (Armbruster et al., 2020; Neubauer & Innes, 2020)
#1083	*aminaa10* #23	amiRNA, NAA10 knockdown (Linster et al., 2015)
#1297	*muse6*	point mutation, NAA15 knockdown (Xu et al., 2015)
#1386	*hypk-3* (SALK_080671)	T-DNA insertion, HYPK knockout (Miklankova, 2019)
#1791	*aminaa50* #9.4	amiRNA, NAA50 knockdown
#1840	*aminaa50* #13.6	amiRNA, NAA50 knockdown
#1792	*naa50-2* x NAA50-eYFP	*naa50-2* complemented with eYFP-tagged NAA50 under 35Sp
#1793	*naa50-2* x NAA50(H115A)	*naa50-2* complemented with inactive NAA50 under 35Sp
#1794	*naa50-2* x NLS-NAA50-eYFP	*naa50-2* complemented with nuclear-localized eYFP-tagged NAA50 under 35Sp
#1795	*naa50-2* x NES-NAA50-eYFP	*naa50-2* complemented with cytosolic eYFP-tagged NAA50 under 35Sp
#1881	*naa50-2* x SMC3-SYN4	*naa50-2* complemented with SMC3-SYN4 fusion construct under 35Sp

4.3.2 Cultivation on soil and seed collection

Arabidopsis thaliana seeds were sown in pots containing a well-watered turf mixture (Ökohum GmbH, Herbertingen) supplemented with 10 % (v/v) vermiculite and 2 % (v/v) quartz sand. The seeds were stratified in the dark at 4 °C. After three days, the pots were transferred

to the short-day growth chamber (8 h light at 100 µmol m^{-2} s^{-1} and 22 °C followed by 16 h darkness at 18 °C; relative humidity 50 %). After two weeks, the seedlings were separated into individual pots. If not stated otherwise, plants were watered twice a week. In order to prevent an infestation with mildew, lice, or greenhouse whiteflies, the plants were treated biweekly with 0.0175 % (w/v) Discus and 0.03 % (w/v) Mospilan SG (both Cheminova, Aarhus, Denmark). An additional alternating biweekly treatment with nematodes protected the plants against fly larvae. For seed production, plants were transferred to the long-day chamber (16 h light at 100 µmol m^{-2} s^{-1} and 22 °C followed by 8 h darkness at 18 °C; relative humidity 50 %). When the first siliques formed, the shoots were fixed to wooden sticks, and the plants were covered with a paper bag. Upon the first signs of senescence, watering was suspended. When the plants had completely dried out, seeds were harvested and stored in reaction tubes which were kept in a dry and cool environment.

4.3.3 Cultivation under sterile conditions on plates

For cultivation of *Arabidopsis thaliana* under sterile conditions, seeds were surface-sterilized with 70 % (v/v) ethanol (2x 5 min) and 6 % sodium hypochlorite (1x 3 min). Subsequently, the seeds were washed trice with ddH_2O and sown on 1/2 MS plates (4.1.2) for physiological experiments or AT medium plates supplemented with antibiotics for selection (4.3.6). In both cases, the seeds were stratified at 4 °C in the dark for three days before they were germinated under short-day conditions in the Percival growth chamber.

4.3.4 Transient transformation of *N. benthamiana*

For the transient transformation of *N. benthamiana*, overnight cultures of *A. tumefaciens* in LB medium (4.1.2) supplemented with antibiotics were prepared (4.2.2). When the OD_{600} of the cultures reached 1-1.5, the cells were harvested via centrifugation at 6,000 g and 4 °C for 15 min. The supernatant was discarded, and the pellet was washed twice with ice-cold water. Subsequently, the bacteria were diluted to an OD_{600} of 0.8-1.2 in transformation buffer (10 mM MES, 10 mM $MgCl_2$, 0.2 mM acetosyringone; pH 5.6) and incubated for 3 h at RT. Meanwhile, approximately six-week-old *N.benthamiana* plants were incubated at 100 % humidity for 1 h. In the last step, the bacterial suspension was injected into the abaxial side of the youngest *N.benthamiana* leaves using a syringe. The infiltrated leaves were marked with adhesive tape, and the expression was evaluated 47-72 h after infiltration. When several constructs were co-expressed, the respective bacterial cultures were mixed

1:1 before infiltration. For poorly expressed constructs, the efficiency was boosted by co-expression of the silencing suppressor p19 (Voinnet et al., 2003).

4.3.5 Stable transformation of *A. thaliana*

For stable transformation after Clough & Bent (1998), *A. thaliana* was grown for eight weeks under short-day conditions and then transferred to the long-day chamber. As soon as the first flowers formed, the transformation procedure was initiated. For that purpose, any siliques already present were clipped off. Moreover, 300 ml LB medium (4.1.2) were inoculated with *A. tumefaciens* containing the plasmid of interest and left to incubate at 28 °C (4.2.2). When the OD_{600} of the culture reached 0.8-1, the bacteria were centrifuged at 6,000 g and 4 °C for 15 min. The supernatant was removed, and the pellet was washed twice with ice-cold ddH_2O. Subsequently, the pellet was resuspended in transformation medium (50 g l^{-1} saccharose, 200 μl l^{-1} Silwet Gold) to an OD_{600} of 1. *A. thaliana* plants were dipped into the suspension, bringing the flowers into direct contact with the bacteria. Afterwards, the plants were positioned horizontally on a plastic tray, covered with a plastic hood, and left to incubate at high humidity in the darkness for 24 h. After a recovery phase of a week at long-day growth conditions, the procedure was repeated up to four times to increase the transformation efficiency.

4.3.6 Selection of transformants

To select plants carrying a kanamycin resistance gene, seeds were sterilized (4.3.3) and germinated on AT medium (4.1.2) supplemented with kanamycin (50 μg ml^{-1}). After four weeks of growth under short-day conditions in the Percival chamber, the surviving seedlings were transferred to soil. To select plants carrying a glufosinate-ammonium resistance gene, seeds were germinated on humid soil (4.3.2). After two weeks of growth, the seedlings were sprayed with 200 mg l^{-1}glufosinate-ammonium. The treatment was repeated every two days until the non-transformed plants died. The remaining plants were transferred to individual pots.

In both cases, the presence of the transgene of interest was confirmed by PCR-based genotyping (4.4.4).

4.3.7 Crossing of *A. thaliana*

To cross two genotypes, the parent plants were cultivated on soil under short-day conditions (4.3.2). Approximately two weeks after the plants started flowering, the cross was performed on flowers of the primary inflorescence. For this purpose, flowers that had already opened were removed from the mother plant and sepals, petals, and stamina were removed from the remaining closed flower buds with precision forceps to expose the unfertilized stigmata. Afterwards, the stamina of freshly opened flower buds of the father plant were isolated, and the pollen was transferred to the stigmata of the mother plant. For each inflorescence, at least three stigmata were pollinated. The inflorescences used for crossing were marked with adhesive tape. Successful crossing led to the development of siliques. Seeds from those siliques were harvested and stored in a dark and dry reaction tube until further use.

4.3.8 Extraction of mature pollen from *A. thaliana*

For the extraction of mature pollen from *A. thaliana*, newly opened flowers were pulled off the inflorescence with forceps. The flowers were added to a reaction tube filled with 500 μl of pollen isolation buffer (100 mM $NaPO_4$, 1 mM EDTA, 0.1 % (v/v) Triton-X-100; pH 7.5) and vortexed 20 sec. The released pollen was harvested by 30 sec of centrifugation at 1,500 g. Subsequently, the presence or absence of pollen in the reaction tube was photo-documented. For fluorescence microscopy, the pollen was resuspended in 20-50 μl pollen isolation buffer supplemented with 1 μg ml^{-1}DAPI.

4.3.9 Visualization of aborted seeds from *A. thaliana*

To quantify and analyze seeds, *A. thaliana* plants were grown on soil (4.3.2). Four to five weeks after the induction of flowering, fully developed siliques of the primary shoot were carefully opened using syringe needles and forceps. The results were documented under a binocular microscope (MZFLIII, Leica).

4.3.10 Drought stress

To perform a drought stress treatment, plants were grown in individual pots on equal amounts of soil as determined by weight (4.3.2). Before the beginning of the treatment, the plants were supplied with an excess of water for 2 h and then transferred to a dry tray. Afterwards,

watering was suspended for the drought-stressed plants and continued for the control plants. To account for the size difference between wildtype and smaller mutants, mutants of the same age but also the same size as the wildtype plants were included in the experiment. Those controls are referred to as “same size” and “same age” control.

4.3.11 Pathogen challenge

Infection experiments with *H.a. Noco2* and *P.s.m.* ES4326 were performed as described by Huang et al. (2013). In brief, two-week-old soil-grown seedlings were sprayed with *H.a.* Noco2 spores at a concentration of 105 spores per ml water. Sporulation was quantified using a hemocytometer after plants were grown at 18°C for 7 days. For bacterial infections, four-week-old plants under short-day conditions were infiltrated with bacterial solution at OD_{600}=0.001. Leaf discs were collected and ground on the day of infection (Day 0) and 3 days later (Day 3). Colony-forming units were counted after incubation on LB plates with streptomycin selection. Pathogen challenges were performed by Dr. Zhongshou Wu under the supervision of Prof. Dr. Xin Li from the Michael Smith Laboratories, University of British Columbia (Canada).

4.3.12 UV stress treatment

For the UV stress treatment, six to eight week-old soil-grown plants (4.3.2) were transferred from the climate chambers to the greenhouse and exposed to UV-B light (0.04 $mWcm^{-2}$) for up to 6 h. After the treatment, the plants were left in the greenhouse to continue their growth under standard short-day conditions. After four days of recovery, the fresh weight of the plants was assessed, and phenotypical changes caused by the UV treatment were documented with a digital camera.

4.4 Molecular biology methods

4.4.1 Isolation of genomic DNA from plant tissue

Genomic DNA (gDNA) was extracted from *A. thaliana* according to Edwards et al. (1991). After approximately four weeks of growth, a small leaf was excised, placed in a reaction tube, and ground with a re-usable plastic pestle. After a few seconds of grinding, 400 μl Edwards buffer (0.2 M Tris, 250 mM NaCl, 25 mM EDTA, 0.5% (w/v) SDS; pH 7.5) were

added and the sample was vortexed for 10 sec. The samples were centrifuged at 14,000 g for 5 min, and 300 μl of supernatant were collected. The supernatant was mixed with an equal volume of 100 % isopropanol by inversion of the reaction tube. After incubation for 2 min at RT, the DNA was precipitated by centrifugation of the samples at 14,000 g for 10 min. The supernatant was removed, and the pellet was washed with 70 % (v/v) ethanol. After the last centrifugation step of 2 min at 14,000 g, the ethanol was discarded, and the DNA pellet was dried either overnight at RT or for 1 h at 37 °C. The dried pellet was resuspended in up to 50 μl sterile ddH_2O and stored at -20 °C until further usage.

4.4.2 Isolation of plasmid DNA from *E. coli*

Plasmids were extracted from *E. coli* liquid cultures using the NucleoSpin Plasmid kit by Macherey-Nagel (Düren) according to the manufacturer's instructions. Plasmids were eluted in 50 μl ddH_2O and stored at -20 °C until further usage.

4.4.3 Primer design

Primers for cloning (4.4.9), genotyping (4.4.4), and qRT-PCR (4.4.13) were ordered from Sigma-Aldrich (Steinheim). When designing the primers, GC clamps were added to the 5' and 3' ends and the melting temperature was kept between 55 and 65 °C whenever possible. Lyophilized primers were resuspended in ddH_2O to a stock concentration of 100 μM and stored at -20 °C until further usage.

4.4.4 Polymerase chain reaction (PCR)

For PCR-based genotyping, the FastGene TAQ Ready Mix (Nippon Genetics, Düren) was used. For each PCR reaction, 2 μl gDNA, 1 μl of each primer (10 μM), 10 μl FastGene TAQ Ready Mix, and 6 μl sterile ddH_2O were mixed. The reaction mix was treated according to the PCR program outlined in Table 12.

Table 12: PCR program for the FastGene polymerase.

Cycle	Step	Temperature	Duration
1	Initial denaturation	95 °C	3 min
35	Denaturation	95 °C	30 sec
35	Annealing	55-68 °C	30 sec
35	Extension	72 °C	1 min/kb
1	Final extension	72 °C	5 min
1	Hold	16 °C	Infinite

The Phusion High-Fidelity DNA polymerase (New England Biolabs, Beverly) was used to amplify *At*SYN4 (AT5G16270) from cDNA for subsequent cloning. Up to 10 μl DNA template were mixed with 10 μl GC buffer, 1 μl dNTPs (10 mM), 2.5 μl of each primer (10 μM), 1.5 μl DMSO and 0.5 μl Phusion High-Fidelity DNA polymerase. The reaction mix was topped up to 50 μl with ddH_2O and treated according to the PCR program outlined in Table 13.

Table 13: PCR program for the Phusion High-Fidelity polymerase.

Cycle	Step	Temperature	Duration
1	Initial denaturation	98 °C	30 sec
35	Denaturation	98 °C	10 sec
35	Annealing	55-68 °C	30 sec
35	Extension	72 °C	30 sec/kb
1	Final extension	72 °C	5 min
1	Hold	16 °C	Infinite

For all other PCR reactions, the PCRBIO HiFi polymerase was used. Up to 2 μl template (plasmid or cDNA) were mixed with 10 μl 5x PCRBio HiFi buffer, 2 μl of each primer (10 μM) and 0.5 μl PCRBio HiFi polymerase. The reaction mix was topped up to 50 μl with ddH_2O and treated according to the PCR program outlined in Table 14.

Table 14: PCR program for the PCRBIO HiFi polymerase.

Cycle	Step	Temperature	Duration
1	Initial denaturation	95 °C	1 min
35	Denaturation	95 °C	15 sec
35	Annealing	55-68 °C	15 sec
35	Extension	72 °C	30 sec/kb
1	Hold	16 °C	Infinite

The annealing temperature of the individual primers was estimated using OligoCalc and adjusted to 60 °C whenever possible. The result of the PCR amplification was validated by visualization on an agarose gel (4.4.6) and sequencing (4.4.10).

4.4.5 Restriction of DNA

Restriction digests either served to confirm the identity of previously generated plasmids (4.4.9) or to digest PCR products (4.4.4) and target vectors for subsequent ligation. For test digests, 5 μl DNA, 1 μl of each restriction enzyme (New England Biolabs, Beverly), and 2 μl of restriction buffer were mixed. The reaction mix was topped up to 20 μl with ddH_2O and left to incubate for 1 h at 37 °C.
For the digestion of PCR fragments and target vectors for subsequent cloning, 1 μg target vector or PCR fragment were mixed with 1 μl of each restriction enzyme (New England Biolabs, Beverly) and 5 μl of the required restriction buffer as specified by the manufacturer. The reaction mix was topped up to 50 μl with ddH_2O and left to incubate for 3 h at 37 °C. The resulting DNA fragments were separated by agarose gel electrophoresis (4.4.6) and extracted from the gel (4.4.7).

4.4.6 Agarose gel electrophoresis

PCR products (4.4.4) or digested DNA fragments (4.4.5) were separated by agarose gel electrophoresis. For this purpose, 0.6-2 % agarose was heated in 1 x TAE buffer (90 mM Tris, 90 mM H_2BO_3, 0.5 mM EDTA, supplemented with 0.7 μg ml^{-1}ethidium bromide). The mixture was poured into a gel chamber equipped with a gel comb. After cooling, the DNA samples were either directly loaded onto the gel (e.g., when a pre-stained reaction mix had been used for PCR) or mixed with 6 x loading dye (New England Biolabs, Beverly). The 2-Log DNA Ladder (New England Biolabs, Beverly) served as a size standard. The

electrophoretic separation of DNA fragments by size was carried out at 120 V in 1 x TAE buffer. The results were documented on the Gel Jet Imager 2000 (Intas, Göttingen) under UV light.

4.4.7 Isolation of DNA from agarose gels

DNA fragments were purified from agarose gels using the NucleoSpin Gel and PCR Clean-up kit (Macherey-Nagel, Düren) according to the manufacturer's instructions. DNA fragements were eluted in 15 μl ddH_2O.

4.4.8 Ligation of DNA fragments

For ligation of blunt-end PCR products into the pJET1.2 vector, the CloneJET PCR Cloning Kit (Thermo Scientific, Waldorf) was used according to the manufacturer's instructions. Ligations into the pJET1.2 vector were performed for PCR products which were only obtained in low concentrations and needed to be amplified once again before attempting a restriction digest.

In all other cases, linearized vector and digested PCR fragments with compatible ends were ligated using the T4 DNA ligase (New England Biolabs, Beverly). 2 μl T4 buffer were mixed with 1 μl T4 ligase and up to 300 ng DNA (3:1 molar ratio insert : vector). The reaction mix was topped up to 20 μl with ddH_2O and incubated for 10 min at RT followed by 2 h at 16 °C for shorter PCR fragments ($<$ 1 kb) or overnight at 16 °C for longer PCR fragments ($>$ 1 kb).

Irrespective of the ligase used, the ligation mix was inactivated by incubation at 65 °C for 10 min and directly used for transformation of chemocompetent *E. coli* (4.2.3.1).

4.4.9 Cloning using restriction sites

The PCR product (4.4.4) and the target vector were digested with the corresponding restriction enzymes (4.4.5). The resulting fragments were visualized on an agarose gel (4.4.6), and the bands of the desired size were cut and purified (4.4.7). The purified fragments were ligated (4.4.8) and transformed into *E. coli* (4.2.3.1). Overnight cultures of *E. coli* were prepared, and the plasmids were extracted (4.4.2). The presence of the insert was verified via a test digest (4.4.5) and sequencing (4.4.10). The constructs used in this thesis are listed in Table 15. Maps can be found in Supplementary Fig. S1.

Table 15: Plasmids used in this thesis.

#	Name	Purpose
831	pETM20-T7p-NAA50	expression of NAA50
1655	pBinAR-35Sp-aminaa50	knockdown of NAA50
1658	pB7YWG2-35Sp-NAA50-eYFP	localization of NAA50
1659	pBinAR-35Sp-SMC3-SYN4	complementation of *naa50*
1720	pET24d-T7p-NAA50(H115A)	expression of mutated NAA50
1722	pBinAR-35Sp-NAA50(H115A)	complementation of *naa50*
1723	pBinAR-35Sp-NLS-NAA50-eYFP	complementation of *naa50*
1724	pBinAR-35Sp-NES-NAA50-eYFP	complementation of *naa50*
1725	pCambia1300-35Sp-CLuc	split luciferase assay
1726	pCambia1300-35Sp-NLuc	split luciferase assay
1727	pBinAR-35Sp-NAA50-eYFP	complementation of *naa50*
1729	pURT2-Ubip-VMA12-RFP	ER marker
1730	pB7YWG2-35Sp-NAA10-eYFP	localization of NAA10
1731	pB7YWG2-35Sp-NAA15-eYFP	localization of NAA15
1732	pCambia1300-NAA10-NLuc	split luciferase assay
1733	pCambia3000-CLuc-NAA10	split luciferase assay
1734	pCambia3000-CLuc-NAA50	split luciferase assay
1735	pCambia1300-NAA50-NLuc	split luciferase assay
1736	pCambia1300-HYPK-NLuc	split luciferase assay
1737	pCambia1300-CLuc-HYPK	split luciferase assay
1808	pGG-Ubip-NLS-mCherry	nuclear marker
1882	pCambia1300-NAA50$^{\text{-NAA10/NAA15}}$-NLuc	split luciferase assay
1883	pCambia1300-CLuc-NAA50$^{\text{-NAA10/NAA15}}$	split luciferase assay
1885	pCambia1300-CLuc-NAA50$^{\text{-NAA10}}$	split luciferase assay
1886	pCambia1300-NAA50$^{\text{-NAA10}}$-NLuc	split luciferase assay
1887	pCambia1300-Cluc-NAA50$^{\text{-NAA15}}$	split luciferase assay
1888	pCambia1300-NAA50$^{\text{-NAA15}}$)-NLuc	split luciferase assay
1889	pCambia1300-CLuc-NAA15	split luciferase assay
1890	pCambia1300-NAA15-NLuc	split luciferase assay
1892	pCambia1300-NAA20-NLuc	split luciferase assay
1893	pCambia1300-CLuc-NAA20	split luciferase assay

4.4.10 Sequencing

Sequencing of the cloned constructs was performed by Eurofins Genomics (Ebersberg). The samples were prepared according to the instructions on the Eurofins homepage (50-100 ng μl^{-1} plasmid DNA or >10 ng μl^{-1} of purified PCR fragment in ddH_2O). The sequencing results were analyzed with either ContigExpress (Invitrogen, Karlsruhe) or Geneious (Biomatters, Auckland).

4.4.11 Isolation of total RNA from plant tissue

RNA was isolated from 50-100 mg leaf material with the peqGOLD Total RNA Kit (Peqlab, Erlangen), the Universal RNA Kit (Roboclon, Berlin), or the RNA Extraction Kit (VWR, Radnor). For this purpose, leaf material was snap-frozen and ground in an M400 grinding system (Retsch) at 20 Hz for 30 sec. For the following steps, the manufacturer's protocols were followed. The optional on-column DNA digestion step was carried out as suggested by the manufacturers. In the end, RNA was eluted with up to 50 μl sterile RNAase free ddH_2O, and the resulting RNA concentration was determined with the Nanodrop ND-2000 (Peqlab, Erlangen). The choice of RNA extraction kit was not influenced by scientific considerations, but by the availability of the kits. Due to the corona crisis, RNA extraction kits were in high demand and kits had to be obtained from different manufacturers.

4.4.12 cDNA synthesis

cDNA was synthesized with the Fast Gene Scriptase II cDNA Synthesis Kit (NIPPON Genetics, Düren). For this purpose, 0.5-3 μg RNA (4.4.11) were mixed with 0.5 μl oligo(dT)-Primer and DEPC-treated ddH_2O to a final volume of 6.25 μl. This pre-mix was incubated at 65 °C for 5 min and subsequently cooled down on ice. Afterwards, 2 μl FastGene Scriptase II buffer, 1 μl 0.1 M DTT and 0.25 μl RNase inhibitor were added and the mixture was incubated at 42 °C for 2 min. Subsequently, it was cooled down on ice and 0.5 μl FastGene Scriptase II were added. The reaction mix was incubated at 42 °C for 50 min before the reaction was inactivated by incubation at 70 °C for 15 min.
Alternatively, cDNA was synthesized with the RevertAid H Minus First Strand cDNA Synthesis Kit (Thermo Scientific, Walldorf). For this purpose, 0.5-3 μg RNA (4.4.11) were mixed with 1 μl Oligo(dT)-Primer and DEPC treated ddH_2O to a final volume of 12 μl. This pre-mix was incubated at 65 °C for 5 min and subsequently cooled down on ice. Af-

terwards, 4 μl reaction buffer, 2 μl dNTP mix, 1 μl RiboLock RNase inhibitor and 1 μl RevertAid H minus M-MuLV reverse transcriptase were added to the pre-mix. The reaction mix was incubated in a PCR Cycler at 42 °C for 1 h followed by incubation at 72 °C for 5 min. In both cases, the resulting cDNA was stored at -80 °C until further usage.

4.4.13 Quantitative real-time polymerase chain reaction (qRT-PCR)

To analyze the expression of selected genes via qRT-PCR, cDNA (4.4.12) was diluted with 180 μl ddH_2O. 2 μl of diluted cDNA were mixed with 0.5 μl primer mix (5 μM each), 3.75 μl ddH_2O and 6.25 μl qPCRBIO SyGreen Mix Lo-ROX (PCR Biosystems, London). The PCR program was designed according to the manufacturer's instructions. All samples were measured in duplicates. One control sample was diluted (1:10 and 1:20) and used as a reference to generate a standard curve. The expression of the genes of interest was normalized to the housekeeping genes *PP2A* (AT1G69960), *SAND* (AT3G28390), and *TIP41* (AT4G34270).

4.5 Protein biochemical methods

4.5.1 Extraction of soluble proteins from plant tissue

To extract soluble proteins from plant tissue, 50-200 mg snap-frozen plant material was ground with stainless steel beads in an M400 grinding system (Retsch) at 20 Hz for 30 sec. Subsequently, 200-800 μl protein extraction buffer (50 mM HEPES-KOH, 10 mM KCl, 1 mM EDTA, 1 mM EGTA, 10 mM DTT, 0.5 mM PMSF; pH 7.4) were added to the plant powder. The samples were kept on ice and vortexed alternately for 15 min to bring all soluble proteins into solution. In the last step, the samples were centrifuged at 16,400 g and 4 °C for 10 min. The supernatant containing the soluble proteins was transferred to a fresh reaction tube, and the protein concentration was assessed with a Bradford assay (4.5.2).

4.5.2 Determination of protein concentration

In order to quantify their protein concentration, samples were diluted 1:10 in ddH_2O. 10 μl of each sample, as well as a blank of 10 μl ddH_2O, were loaded on a 96 well plate together with 250 μl of RotiQuant Bradford Reagent (Roth, Karlsruhe). The absorption at 595 nm

was measured on the FLUOstar Omega plate reader (BMG Labtech, Ortenberg). For quantification, a BSA standard curve was applied (0.1, 0.2 and 0.4 μg ml^{-1}). Measurements were taken in duplicates.

4.5.3 Nucleocytoplasmic fractionation of protein extracts

To separate nuclear and cytoplasmic proteins, 1.5 g of leaf material were harvested by pooling up to four plants. The leaf material was snap-frozen in liquid nitrogen and ground to a fine powder using a mortar and a pestle. The powder was mixed with 2 ml lysis buffer (10 mM Tris, 10 mM NaCl, 10 mM MgCl, 10 % (v/v) glycerol, 10 mM β-mercaptoethanol; pH 7.5 supplemented with 1 × protease inhibitor cocktail) by continuous vortexing for 15 min and subsequently filtered through a 100 μm cell strainer (EASYstrainer, Greiner BioOne) by centrifugation at 1,500 g for 3 min. The pellet was resuspended by gentle tapping and the filtrate was centrifuged again at 2,500 g and 4 °C for 10 min. While the remaining cell debris was pelleted and discarded, the supernatant was transferred to a new reaction tube and centrifuged at 13,000 g and 4 °C for 15 min. The resulting supernatant represented the cytoplasmic fraction and was diluted 1:10 in 5 x Laemmli buffer (4.1.2) for denaturation. In the meantime, the pellet which contained the nuclei was resuspended in 1 ml washing buffer (10 mM Tris, 10 mM NaCl, 10 mM MgCl, 0.5 % (v/v) Triton X-100, 1 M hexylene glycol, 10 mM β-mercaptoethanol; pH 7.5 supplemented with 1 × protease inhibitor cocktail) and centrifuged at 1,500 g and 4 °C for 10 min. The washing step was repeated until the nuclei pellet had a thoroughly white colour (8-10 times). At this point, the pellet was resuspended in 1 x Laemmli buffer. The cytoplasmic and the nuclear fraction were denatured by incubation at 95 °C for 10 min and 10 μl of the cytoplasmic and 30 μl of nuclear fraction were loaded on an SDS-PAGE gel (4.5.8). After Western Blotting (4.5.10), the quality of the fractionation was verified by immunodetection of the marker proteins UGPase (cytosol: AT3G03250) and Histone 3 (nucleus: AT1G09200, AT1G19890, AT3G27360, AT4G40030, AT4G40040, AT5G10390, AT5G10400, AT5G10980, and AT5G65360) with specific antibodies (Table 18).

4.5.4 Co-immunoprecipitation of proteins

In order to identify physiologically relevant protein–protein interactions, 3 g of wildtype leaf material were harvested and snap-frozen in liquid nitrogen. Subsequently, the material was ground to a fine powder using a mortar and a pestle. The powder was mixed with 6 ml

protein extraction buffer (50 mM HEPES-KOH, 10 mM KCl, 1 mM EDTA, 1 mM EGTA, 10 mM DTT, 0.5 mM PMSF; pH 7.4) supplemented with 1 x protease inhibitor cocktail (Roche, Mannheim) and 0.1 % NP-40 (Abcam, Cambridge, UK). The samples were kept on ice and vortexed in an alternating manner for 20 min. After 20 min of centrifugation at 16,400 g and 4 °C, the supernatant containing the soluble cellular proteins was collected. The protein concentration was determined with a Bradford assay (4.5.2), and 80 μl of the sample were set aside as input control. The rest of the sample was split and redistributed in two reaction tubes. While one reaction tube served as background control, the protein extract in the second tube was mixed with 10 μl of a specific *At*NAA15 or *At*NAA50 antiserum (Tab. 18). Both reaction tubes were incubated for 2 h at 4 °C in an overhead shaker. In the meantime, 60 μl slurry A/G agarose beads (Thermo Fisher, Waltham) were washed trice with 1 ml protein extraction buffer (centrifugation at 400 g for 1 min). After the last washing step, the beads were split into two aliquots and added to the previously generated protein extract and background control. The mixture was incubated for another 4 h at 4 °C. As a last step, the beads were washed with extraction buffer five times (centrifugation at 400 g for 1 min) and the proteins bound to the beads were eluted with 30 μl 1 × Laemmli buffer (4.1.2). For Western Blotting, the samples were loaded on 10-15 % SDS-PAGE gels (4.5.8) and transferred to PVDF membranes (4.5.10) which were incubated with antisera specific for the expected interactors. To identify previously unknown interactors of *At*NAA15 and *At*NAA50, the samples were passed on to the Core Facility for Mass Spectrometry and Proteomics (CFMP) at the Center for Molecular Biology at Heidelberg University (ZMBH). In this case, protein extracts incubated with a specific α-SAT5 antiserum were included as an additional background control. The rabbit α-SAT5 antiserum was selected because it was generated in-house in the same manner as the α-NAA50 and α-NAA15 and was therefore expected to yield similar unspecific binding (e.g., from the His-tag used to purify SAT/NAA10/NAA50 from *E. coli* for the immunization of rabbits). Moreover, like NAA10 and NAA50, SAT5 is a cytosolic acetyltransferase. Unlike NAA10 and NAA15, however, SAT5 is not located at the ribosome and contributes to cysteine biosynthesis by catalyzing the transfer of an acetyl moiety from acetyl-CoA to free serine in order to produce activated *O*-acetylserine (Wirtz et al., 2010). Several interaction partners of SAT5 (AT5G56760.1) are known, and their co-immunoprecipitation may serve as a positive control.

The samples, which were passed on to the CFMP, were loaded on pre-cast SDS-PAGE gels. When the samples had penetrated the gels to a depth of approximately 2 cm, the relevant fractions of the gels (omitting the prominent bands at 50 kDa which represented the

heavy fragments of the antibodies) were cut out with a scalpel and processed as described by Baerenz et al. (2013). In brief, samples were reduced, alkylated and digested with trypsin. Peptides were extracted from the gel pieces, concentrated in a vacuum centrifuge and dissolved in 0.1 % TFA. Nanoflow LC-MS^2 analysis was performed with an Ultimate 3000 liquid chromatography system coupled to an Orbitrap QE HF (Thermo Fisher, Waltham). An in-house packed analytical column (75 μm x 200 mm, 1.9 μm ReprosilPur-AQ 120 C18 material) was used. Mobile phase solutions were prepared as follows:

Solvent A: 0.1 % formic acid / 1 % acetonitrile

Solvent B: 0.1 % formic acid / 89.9 % acetonitrile

Peptides were separated in a 60 min linear gradient starting from 3 % B and increased to 23 % B over 50 min and to 38 % B over 10 min, followed by a washout with 95 % B. The mass spectrometer was operated in data-dependent acquisition mode, automatically switching between MS and MS^2. MS spectra (m/z 400-1600) were acquired in the Orbitrap at 60,000 (m/z 400) resolution and MS^2 spectra were generated for up to 15 precursors with a normalized collision energy of 27 and isolation width of 1.4 m/z at 15000 (m/z 400) resolution. The MS/MS spectra were searched against the TAIR database containing 40,782 sequences and a customized contaminant database using Proteome Discoverer 2.5 with Sequest HT (Thermo Fisher, Waltham). A fragment ion mass tolerance was set to 0.02 Da and a parent ion mass tolerance to 5 ppm. Trypsin was specified as enzyme. Carbamidomethyl was set as fixed modification of cysteine and oxidation (methionine), deamidation (asparagine, glutamine), acetylation (protein N-terminus), methionine loss (protein N-terminus) and acetylation after loss of methionine (protein N-terminus) as variable modifications. Protein quantification was done using precursor ion quantifier node with summed up abundances. When compiling the list of proteins identified in the immunoprecipitates, only proteins identified by three or more peptides were taken into account.

4.5.5 Expression of recombinant proteins in *E. coli*

Transformed *E. coli* (4.2.3.1) were used to inoculate 50 ml liquid LB medium (4.1.2) supplemented with antibiotics. The cultures were incubated at 37 °C while shaking. After 16 h, 15 ml of those pre-cultures were used to inoculate 300 ml LB medium supplemented with antibiotics. This new culture was left to incubate at 37 °C while shaking. Meanwhile, the growth of the bacteria was continuously monitored. When the OD_{600} had reached 0.8-1, 1 mM IPTG was added to induce the expression of the desired transgene. The culture was

incubated at 37 °C for an additional 5 h. Subsequently, the bacteria were harvested by centrifugation at 10,000 g and 4 °C for 10 min. Most of the supernatant was discarded, leaving approximately 10 ml to resuspend the pellet. The mixture was transferred to a new, smaller reaction tube and centrifuged at 6,500 g and 4 °C for 15 min. Afterwards, the supernatant was removed completely and the pellet was snap-frozen in liquid nitrogen and stored at -80 °C until further usage.

4.5.6 Purification of recombinant proteins from *E. coli*

To purify recombinant proteins from *E. coli* (4.5.5) a HiTrap Chelating High Performance Column (GE Healthcare, Freiburg) connected to a peristaltic pump (Behr Labor-Technik, Düsseldorf) was used. The flow rate was adjusted to 1 $\mathrm{mlmin^{-1}}$. The column was washed with 10 mM EDTA and $\mathrm{ddH_2O}$ (5 min each) before loading the matrix with $\mathrm{NiCl_2}$. Afterwards, the column was equilibrated with buffer B (50 mM Tris, 250 mM NaCl, 20 mM imidazole; pH 8.0). In the meantime, the bacterial pellet (4.5.5) was resuspended in 10 ml buffer B supplemented with 40 μM PMSF. To break down the cells, the bacteria were sonicated for 5 min at 40 % activity (Sonopuls GM70, Bandelin Electronic). After a second sonication step of 4 min, the lysate was centrifuged at 13.0000 g for 10 min at 4 °C. Subsequently, the supernatant (crude extract) was transferred to a fresh reaction tube, and 50 μl 200 mM PMSF were added. The crude extract was filtered with a 45 μM syringe filter to eliminate cell debris. Then 500 μl of crude extract (CE) were transferred to a reaction tube and kept on ice until further usage. The rest of the crude extract was left to circulate on the HiTrap Chelating column for 1 h. Afterwards, 500 μl of flowthrough (FT) were collected and kept on ice until further usage. The column was washed with washing buffer W (50 mM Tris, 250 mM NaCl, 80 mM imidazole; pH 8.0) for 15 min to elute unspecifically bound proteins. To verify the success of the washing steps, samples were collected at the beginning (W1) and the end (W2) of the washing procedure and kept on ice until further usage. Subsequently, the remaining specifically bound proteins were eluted with 5 ml buffer E (50 mM Tris, 250 mM NaCl, 400 mM imidazole; pH 8.0) in ten fractions à 500 μl (E1-10). The protein concentration in all samples (CE, FT, W1, W2, E1-10) was determined (4.5.2), and the presence of the purified protein was verified via SDS-PAGE (4.5.8) followed by Coomassie staining. The column was cleaned with 10 mM EDTA for 5 min, 250 mM NaOH for 2 min and then washed with $\mathrm{ddH_2O}$ until the pH reached 7.0. To prepare the column for storage, it was sealed with parafilm and stored at 4 °C.

4.5.7 *In vitro* acetyltransferase assay

The *in vitro* activity of purified acetyltransferases was determined as described by Armbruster et al. (2020).

4.5.8 SDS-polyacrylamide gel electrophoresis (SDS-PAGE)

Proteins were separated according to their size by SDS-polyacrylamide gel electrophoresis (SDS-PAGE). Depending on the number of samples to be loaded, the Mini Protean system by BioRad, Feldkirchen (up to 15 samples) or the PerfectBlue Twin ExW system by PeqLab, Erlangen (up to 36 samples) was used to set up the SDS-PAGE gels. Each gel consisted of a resolving and a stacking gel. The concentration of polyacrylamide in the resolving gel was adjusted to the size of the target protein (Tables 16 and 17).

Table 16: Composition of SDS-PAGE gels for the Mini Protean system.

PAGE [%]	ddH_2O [ml]	Resolving gel buffer [ml]	Rotigel 30 [ml]	10 % APS [μl]	TEMED [μl
10	5.55	3.3	4.5	90	16
12.5	4.5	3.3	5.55	90	16
15	3.37	3.3	6.68	90	16
PAGE [%]	**ddH_2O [ml]**	**Stacking gel buffer [ml]**	**Rotigel 30 [ml]**	**10 % APS [μl]**	**TEMED [μl]**
7.5	2.61	0.72	1.13	45	9

Table 17: Composition of SDS-PAGE gels for the PerfectBlue Twin ExW system.

PAGE [%]	ddH_2O [ml]	Resolving gel buffer [ml]	Rotigel 30 [ml]	10 % APS [μl]	TEMED [μl
10	16.65	9.9	13.5	270	48
12.5	13.5	9.9	16.65	270	48
15	10.11	9.9	20.04	270	48
PAGE [%]	**ddH_2O [ml]**	**Stacking gel buffer [ml]**	**Rotigel 30 [ml]**	**10 % APS [μl]**	**TEMED [μl]**
7.5	7.83	2.16	3.39	90	18

Depending on the gel system and concentration of the sample, 10-60 μl of sample were

loaded in each well of the resolving gel. 10 μl of BlueStar Prestained Protein Marker (NIPPON Genetics, Düren) served as a reference for the protein molecular weight. The PAGE was performed in 1 x SDS running buffer (25 mM Tris, 192 mM glycine, 0.1 % (w/v) SDS; pH 8.3) at 80 V for the first 30 min. Subsequently, the voltage was increased to 120-200 V for 1.5 h. Afterwards, the proteins in the gel were either stained with Quick Coomassie Stain (Serva, Heidelberg), subjected to Silver Staining (4.5.9) or transferred onto a PVDF membrane for the immunological detection of target proteins (4.5.10).

4.5.9 Silver staining

Silver staining was performed with the PlusOne Silver Staining Kit (GE Healthcare, Freiburg) according to the manufacturer's instructions.

4.5.10 Western blot and immunodetection

After SDS-PAGE (4.5.8), proteins were transferred to an Immobilon-P transfer PVDF membrane (Merck Millipore, Darmstadt) activated in methanol for 30 sec. When the Mini Protean system was used for PAGE, the Mini Trans-Blot Cell system (BioRad, Feldkirchen) was used for blotting at 350 mA and 4 °C for 1.5 h. When the PerfectBlue Twin ExW system was used for PAGE, the Trans-Blot Cell system (BioRad, Feldkirchen) was used for blotting at 200 mA and 4 °C for 16 h. Both blotting systems were filled with 1x blotting buffer (1.44 % (w/v) glycine, 0.5 % (w/v) Tris, 0.1 % (w/v) SDS, 20 % (v/v) methanol) and an ice pack for cooling.

Table 18: Antibodies used in this thesis.

Name	Dilution	Catalog Nr.	Manufacturer
α-H^+ATPase	1:5,000	AS07260	Agrisera, Vännäs (SWE)
α-GFP	1:2,500	2555	CellSignalling, Danvers (USA)
α-HA-tag	1:5,000	AS122220	Agrisera, Vännäs (SWE)
α-Histone3	1:5,000	AS10710	Agrisera, Vännäs (SWE)
α-NAA10	1:2,500	N.A.	inhouse (Linster et al., 2015)
α-NAA15	1:2,500	N.A.	inhouse (Linster et al., 2015)
α-NAA50	1:2,500	N.A.	inhouse (Armbruster et al., 2020)

α-OAS-TL A	1:5,000	N.A.	inhouse (Birke et al., 2013)
α-S14	1:1,000	AS122111	Agrisera, Vännäs (SWE)
α-SAT5	1:5,000	N.A.	inhouse (Wirtz et al., 2010)
α-UBQ11	1:10,000	AS08307	Agrisera, Vännäs (SWE)
α-UGPase	1:3,000	AS05086	Agrisera, Vännäs (SWE)
α-rabbit IgG-HRP	1:25,000	AS09602	Agrisera, Vännäs (SWE)

After blotting, the proteins of interest were quantified via immunodetection with specific antibodies. For this purpose, the membranes were shortly washed with 1 x TBS-T (20 mM Tris, 137 mM NaCl, 0.1 % (v/v) Tween 20; pH 7.6) and then blocked with 5 % BSA in TBS-T for 1 h at RT or overnight at 4 °C. Alternatively, a commercial blocking reagent (Roche, Mannheim) was used according to the manufacturer's instructions. All washing steps and the incubation with the primary and secondary antibodies were carried out as suggested by the manufacturer. The dilutions used for specific antibodies are listed in Table 18. After incubation with the secondary antibody and four 15 min washes with TBS-T, the membranes were developed with SuperSignal West Extended Duration Substrate (Thermo Scientific, Walldorf) according to the manufacturer's instructions. After 1 min of incubation with the substrate, the chemiluminescence was detected with the ImageQuant LAS 4000 (GE Healthcare, Freiburg). After detection, the membranes were either washed twice for 10 min each with stripping buffer (1.5 % (w/v) glycine; 0.1 % (w/v) SDS, 1 % (v/v) Tween 20; pH 2.2), PBS-T (137 mM NaCl, 2.7 mM KCl, 10 mM Na_2HPO_4, 1.8 mM KH_2PO_4, 0.1 % (v/v) Tween 20) and TBS-T, and the immunodetection was subsequently repeated with a new antibody or the membranes were stained with Amido black staining solution (0.1 % Amido black, 45 % ethanol, 10 % acetic acid) to provide adequate loading controls.

4.5.11 Split luciferase assay

For *in planta* detection of protein-protein interactions, the full-length cDNA sequences of *At*NAA10 (AT5G13780), *At*NAA15 (AT1G80410), *At*NAA50 (AT5G11340), *At*HYPK (AT3G06610) and *At*NAA20 (AT1G03150) were PCR-amplified (4.4.4) with specific primers (Table S6). The primers harboured *Kpn*I and *Sal*I endonuclease restriction sites for restriction cloning and (in the case of NAA50) the necessary mutations to disrupt binding to NAA10, NAA15 or both. The resulting PCR fragments were separated on agarose gels (4.4.6), purified (4.4.7), digested with *KpnI*-HF and *Sal*I-HF (4.4.5) and ligated (4.4.8) into

the pCambia-NLuc vector (#1726) upstream of N-Luc or in the pCambia-CLuc vector downstream of C-Luc (#1725). The resulting vectors were transformed into the *A. tumefaciens* strain GV3101 (4.2.3.2). Subsequently, the co-transformation of NLUc and CLuc vectors and the p19 suppressor (ratio 1.5:1.5:1) into *N. benthamiana* leaves was performed (4.3.4). After three days, transformed leaves were harvested and their abaxial side was anointed with 1 mM luciferin. Subsequently, the leaves were incubated in the dark for 5 min. The luciferase signal was detected with the ImageQuant™ LAS 4000 (binning set to 8 x 16 pixels, exposure time 5-20 min). The method was adapted from Chen et al., 2008.

4.6 Physiological methods

4.6.1 Determination of translation rate with radiolabelled amino acids

To determine the protein translation rate, newly translated proteins were labelled with the EasyTag EXPRE35S35S Protein Labelling Mix 7 mCi (PerkinElmer, Waltham). For this purpose, four leaf discs per replicate were punched from six-week-old plants grown on soil (4.3.2). The discs were incubated in 800 μl 1/2 Hoagland medium (4.1.2) in a 12 well plate on a vertical shaker at RT in light for 1 h. The labelling mix was diluted to 70 μCi in 1/2 Hoagland medium. The medium in the wells was removed and substituted with 800 μl of the radioactive Hoagland solution. After 0, 30, 60 and 90 min, samples were collected by dipping leaf discs into 1/2 Hoagland medium and then washing them in fresh medium for 3 min. After washing, the leaf discs were dried on a napkin, transferred to reaction tubes filled with glass pearls (diameter 1.25 mm) and snap-frozen in liquid nitrogen. The leaf discs were ground with a FastPrepTM Homogenizer (MP Biomedicals, Graffenstaden). Proteins were extracted from the ground leaf material with 300 μl protein extraction buffer (50 mM HEPES-KOH, 10 mM KCl, 1 mM EDTA, 1 mM EGTA, 10 mM DTT, 0.5 mM PMSF; pH 7.4) as described in 4.5.1. 120 μl of protein extract were transferred to a new reaction tube and 60 μl protein extraction buffer were added. PD Spintrap gel filtration columns (GE Healthcare, Freiburg) were equilibrated with protein extraction buffer according to the manufacturer's instructions. 150 μl of the supernatant mixture were pipetted onto the column and centrifuged at 800 g for 2 min. 10 ml Ultima Gold (PerkinElmer, Waltham) liquid scintillation cocktail and 80 μl filtrated sample were mixed and measured with the Tri-Carb 2810TR Liquid Scintillation Analyser (PerkinElmer, Waltham).

4.6.2 Quantification of ubiquitination activity

In order to determine the level of ubiquitinated proteins, six leaf discs per replicate were punched from six-week-old soil-grown plants (4.3.2) and incubated in 1 ml 1/2 Hoagland medium in a six-well plate on the benchtop. As soon as all the samples were ready, the medium was exchanged for fresh 1/2 Hoagland medium (control) or 1/2 Hoagland medium supplemented with 50 μM of the proteasome inhibitor MG132 (Sigma-Aldrich, Steinheim). The discs were left to incubate on a vertical shaker at RT in light for 24 h. Afterwards, the discs were dried with paper towels and snap-frozen at -80 °C. Samples were ground with stainless steel beads in an M400 grinding system (Retsch) at 20 Hz for 30 sec. Afterwards, proteins were extracted as described in 4.5.1. The protein concentration was determined (4.5.2) and adjusted to 20-30 μg ml^{-1}. Subsequently, the proteins were denatured and loaded onto an SDS-PAGE gel (4.5.8). After Western Blotting (4.5.10), polyubiquitinated proteins were detected with an α-UBQ11 antibody (4.1.5).

4.6.3 Quantification of proteasome activity

To determine the proteasome activity in *A. thaliana* protein extracts, soluble proteins were extracted from approximately 200 μg leaf material (4.5.1) using protein extraction buffer without DTT or PMSF (50 mM HEPES-KOH, 10 mM KCl, 1 mM EDTA, 1 mM EGTA; pH 7.4). The protein concentration was determined (4.5.2) and 0.1 μg ml^{-1} protein extract, 2.5 μM artificial proteasome substrate (Z-Leu-Leu-Leu-AMC, Sigma-Aldrich, Steinheim; dissolved in DMSO) and 89 mM Tris-acetate buffer (pH 7.0, adjusted with acetic acid) were mixed in a total volume of 1 ml. The reaction was left to incubate at 37 °C for 45 min. In the negative control, the protein extract was substituted with ddH_2O. The reaction was stopped by the addition of 1 ml 90 mM Tris-acetate buffer (pH 9.0, adjusted with acetic acid) supplemented with 1 % SDS. Fluorescence generated by the proteasomal cleavage of the artificial proteasome substrate was measured using the FLUOStar Optima Microplate Reader (BMG Labtech, Ortenberg) at 380 nm (excitation) and 440 nm (emission) in an opaque 96-well plate. Measurements were taken in triplicates.

4.6.4 Quantification of free N-termini

To quantify the abundance of proteins with free N-termini, soluble proteins were extracted in citrate buffer (0.89 mM citric acid, 55.8 mM sodium citrate, 1 mM EDTA; pH 7.0)

from leaf material of six-week-old soil-grown plants. 180 μl of the protein extracts were filtered through gel filtration columns (PD SpintrapTM G-25, GE Healthcare) which had previously been equilibrated with citrate buffer according to the manufacturer's instructions. Subsequently, the protein concentration of the filtered samples was measured (4.5.2) and 75 μg of each sample were transferred to a new reaction tube. The tube was filled to 891 μl with citrate buffer, and 9 μl NBD-Cl stock solution (50 mM NBD-Cl in acetonitril) were added to each sample. The samples were incubated for 16 h at RT in the dark. The next day, samples were transferred to a 96 well plate and fluorescence was measured with a FLUOStar Optima Microplate Reader (BMG Labtech) with excitation/emission wavelengths 470/520 nm in triplicates per sample.

4.7 Mass-spectrometry analyses

4.7.1 Preparation of protease-resistant sepharose beads

To generate the protease-resistant beads required for the identification of N-terminal interactors (4.7.2), 0.5 ml streptavidin-coated sepharose beads (Cytvia Life Sciences, Chalfont St. Gilles, UK) were centrifuged for 1 min at 500 g. Subsequently, the supernatant was discarded and the beads were washed trice with 1 ml PBS-T (137 mM NaCl, 2.7 mM KCl, 10 mM Na_2HPO_4, 1.8 mM KH_2PO_4, 0.1 % (v/v) Tween 20). After the last wash, the beads were resuspended in 1.4 ml reagent CHD (76.4 mM cyclohexanedione in PBS-T; pH 13.0). Following 4 h of incubation at RT on a rotary shaker, the beads were collected via centrifugation for 1 min at 500 g and washed trice with 1 ml PBS-T. Next, the beads were resuspended in 0.7 ml reagent A (4 % formaldehyde (v/v) in PBS-T). After adding 0.7 ml reagent B (0.2 M sodium cyanoborhydride in PBS-T), the beads were left to incubate at RT for another 2 h on a rotary shaker. Subsequently, the beads were centrifuged for 2 min at 500 g and washed with 1 ml 0.1 M Tris-HCl (pH 7.5). After washing the beads trice with 1 ml PBS-T, the beads were resuspended in 1.25 mL PBS-T and stored at 4 °C until further usage.

4.7.2 Identification of N-terminal interactors

To identify proteins specifically interacting with free or acetylated N-termini, peptides mimicking the acetylated and free N-terminus of the known NatA substrate OAS-TL A (AT4G14880)

were coupled to protease-resistant sepharose beads. For this purpose, 60 μl protease-resistant streptavidin-coated beads (4.7.1) per sample were centrifuged for 1 min at 500 g and washed with 1 ml binding buffer A (150 mM NaCl, 50 mM Tris, 0.075 % NP-40; pH 8.0). Subsequently, half of the beads (30 μl) were incubated with 20 μg of custom-made biotinylated peptide (4.1.6) dissolved in binding buffer A for 30 min at RT. Afterwards, the beads were washed once with lysis buffer (150 mM KCl, 75 mM Hepes, 1.5 mM EGTA, 1.5 mM $MgCl_2$ 10 % glycerol, 1 mM DTT and 0.1 % NP-40 supplemented with protease inhibitor and PhosSTOP phosphatase inhibitors; pH 7.5) and kept on ice until further usage. The rest of the previously washed beads (30 μl) was incubated with 500 μl protein extract (2 $mgml^{-1}$ in lysis buffer) to clear the extract from proteins binding unspecifically to the beads. After the beads and the unspecifically binding proteins were removed via 1 min centrifugation at 500 g, the protein extract was added to the protease-resistant beads which had previously been coupled to the custom-made peptides and the mixture was incubated for 16 h at 4 °C on a rotary shaker. In a last step, the beads were washed twice with 1 ml lysis buffer and twice with 1 ml wash buffer (150 mM KCl, 75 mM Hepes, 1.5 mM EGTA, 1.5 mM $MgCl_2$; pH 7.5).

While one part of the samples was mixed with 5 x Laemmli-buffer (4.1.2) and separated on an SDS-PAGE gel (4.5.8) followed by Silver-staining (4.5.9) for quality control, the rest was further processed by the Core Facility for Mass Spectrometry and Proteomics (Heidelberg). There, samples were mixed with 300 ng Lys-C per replicate and incubated for four hours at 37 °C and 2.000 rpm on a thermoshaker. Subsequently, 75 μl TEAB solution (100 mM, pH 8.5) supplemented with 300 ng Trypsin were added to each sample and the digest was incubated overnight at 37 °C and 2.000 rpm on a thermoshaker. Next, the samples were centrifuged at 2.000 rpm for 2 min and the supernatant was acidified by addition of TFA to a final concentration pf 0.4 % (v/v) and a pH $\leq$ 2. The resulting peptides were separated on in-house packed C18 reverse-phase columns of 25 cm length using an 60 min gradient from 3 % to 16 % acetonitrile. Subsequently, the samples were directly injected into a Q-Exactive HF mass spectrometer. Data analysis was carried out by MaxQuant (version 1.6.12.0) with an FDR cutoff of 0.01 on peptide level and 0.01 on protein level. A label free approach based on the MaxLFQ algorithm was used for quantification (Cox et al., 2014).

4.7.3 Global quantitative mass-spectrometry

For the quantitative proteome analyses, 100 mg plant tissue were ground to a fine powder. Protein extraction, sample processing, and LC-MS/MS data acquisition were performed as described in detail by Lassowskat et al. (2017). In brief, proteins were extracted and digested according to a modified filter-assisted sample preparation protocol. Peptides were dimethyl labeled with two replicates of each genotype receiving light (+28.0313 D mass shift) and two replicates receiving medium (+32.0564 D mass shift) labels. For each replicate, equal amounts of light- and medium-labeled peptides were pooled, desalted and fractionated using SDB-RPS Stagetips followed by LC-MS/MS analyses (Kulak et al., 2014). LC-MS/MS analyses were carried out using an EASY-nLC 1200 (Thermo Fisher, Waltham) coupled to a Q Exactive HF mass-spectrometer (Thermo Fisher, Waltham). Peptides were separated on 17-cm frit-less silica emitters packed in-house with reverse-phase ReproSil-Pur C18 resin. The column was constantly kept at (50°C). Peptides were eluted in 115 min applying a segmented linear gradient of 0 % to 98 % solvent B (solvent A, 0 % acetonitrile and 0.1 % (v/v) formamide; solvent B, 80 % (v/v) acetonitrile and 0.1 % (v/v) formamide) at a flow rate of 300 $\mathrm{nL\,min^{-1}}$. Mass spectra were acquired as described in Armbruster et al., 2020. The raw data were processed with the MaxQuant software version 1.6.9.0 (Cox & Mann, 2008). Further downstream analysis was performed using Perseus version 1.6.6.0 (Tyanova et al., 2016). Differentially expressed protein groups were identified with the LIMMA package in R 3.3.1 (Ritchie et al., 2015). The analysis is described in detail in Armbruster et al. (2020).

Quantitative mass-spectrometry analyses were performed by Dr. Annika Brünje and Dr. Jürgen Eirich from the Institute for Plant Biology and Biotechnology, University of Münster, under the supervision of Prof. Dr. Iris Finkemeier.

4.7.4 Global N-terminome profiling

For the N-terminome profiling, 100 mg plant tissue was ground to a fine powder. Protein extraction, sample processing and LC-MS/MS data acquisition were performed according to the SILProNAQ method as described previously (Bienvenut et al., 2017). For this purpose, free N-termini were chemically acetylated with N-acetoxy-[2H3]-succinimide. The samples were digested with trypsin, and the N-terminal peptides were enriched by strong cation-exchange liquid chromatography before liquid chromatography-tandem mass-spectrometry (LC-MS/MS) analysis. Raw data were extracted and exported with Proteome Discoverer

(Thermo Scientific, Waltham; version 1.4). The MASCOT software (Matrix Science, London; version 2.4) was used for the identification of proteins and their cotranslational and posttranslational modifications. The EnCOUNTer tool (Bienvenut et al., 2017) was used for further downstream analysis.

N-terminome profiling was performed by Dr. Willy V. Bienvenut and Dr. Jean-Baptiste Boyer from the Institute for Integrative Biology of the Cell, University of Paris-Saclay under the supervision of Dr. Carmela Giglione and Dr. Thierry Meinnel.

4.8 Global gene expression analysis

4.8.1 Hybridization of cDNA on a gene chip

Gene expression profiling was performed using arrays of the Arabidopsis AraGene-1_0-st-type. Biotinylated antisense cDNA was prepared according to the Affymetrix standard labelling protocol with the GeneChip WT Plus Reagent Kit and the GeneChip Hybridization, Wash and Stain Kit. The hybridization on the chip was performed on a GeneChip Hybridization oven 640, then dyed in the GeneChip Fluidics Station 450 and subsequently scanned with a GeneChip Scanner 3000. All of the aforementioned chemicals were purchased from Affymetrix (High Wycombe, United Kingdom).

4.8.2 Normalization and analysis

A Custom CDF Version 22 with TAIR based gene definitions was used to annotate the arrays (Dai et. al, 2005). The raw fluorescence intensity values were normalized applying quantile normalization and RMA background correction. OneWay-ANOVA was performed to identify differentially expressed genes using a commercial software package SAS JMP10 Genomics v.6 (SAS Institute, Cary, USA). A false-positive rate of 0.05 with FDR correction was taken as the level of significance.

The global gene expression analysis was performed by Dr. Carolina De La Torre and Dr. Carsten Sticht from the NGS Core Facility, University of Heidelberg.

4.9 Analytical methods

4.9.1 Phytohormone measurement

Phytohormones were extracted from 50 mg frozen plant material which was dissolved in 750 μl MTBE by 30 min incubation at 4 °C while shaking at 1.000 rpm followed by 15 min incubation in an ultrasonic ice-bath. Subsequently, samples were centrifuged for 10 min at 4 °C and 10.000 g. The supernatants were transferred into a new reaction tube and an equal volume of 0.1 % HCl in water was added to the MTBE extract. The extract was incubated for another 30 min at 4 °C and 1.000 rpm in a shaker before being centrifuged for 10 min at 4 °C and 10.000 g. Next, the upper phase (green colour) was transferred to a new reaction tube and dried in a vacuum concentration system (SpeedVac, Eppendorf) at room temperature (Setting V-AQU). Immediately before analysis, the dried samples were reconstituted in 50 μl 50 % MeOH (in water) by vortexing for 3 min. Afterwards, the samples were centrifuged for 5 min at 12.000 g and the clear supernatant was transferred to total recovery MS-grade autosampler vials (Waters, Milford, USA).

The separation of components was performed using an ACQUITY UPLC I-class PLUS system (Waters, Milford, USA) and an ACQUITY HSS T3 column (100 mm x 2.1 mm, 1.8 μm) heated to 40 °C. 0.1 % formic acid in acetonitrile and 0.1 % formic acid in water (UHPLC-MS quality) were used as solvents A and B, respectively. 4 μl of sample were injected per replicate and the samples were kept at 6 °C during measurements. The following chromatographic parameters were applied:

Time [min]	**Flow [mlmin^{-1}]**	**%A**	**%B**
Initial	0.5	3	97
0.50	0.5	3	97
5.00	0.5	90	10
5.01	0.5	100	0
7.50	0.5	100	0
7.51	0.5	3	97
10.00	0.5	3	97

Finally, the detection of phytohormones was carried out using a QTRAP 6500+ mass-spectrometry system (Sciex, Darmstadt) equipped with an ESI IonDrive Turbo V Source using the scheduled MRM mode with the following MRM parameters:

	Q1	Q3	Dwell time [ms]	Declustering potential [V]	Collision energy [V]	Collision cell exit potential [V]
ABA	263	153	30	-25	-16	-19
JA	209	59	30	-35	-16	-9
JA-Ile	322	130	30	-55	-28	-11
OPDA	291	165	30	-100	-26	-7
SA	137	93	30	-15	-22	-11

The data was analysed with the SciexOS software (Sciex, Version 1.4.0.18067). At least 4-point calibration curves of standard mixtures were used for quantification. The phytohormone extraction and measurement was performed in cooperation with Michael Schulz from the Metabolomics Core Technology Platform (MCTP) at the Centre for Organismal Studies (COS) Heidelberg.

4.10 Microscopy methods

4.10.1 Subcellular localization of tagged proteins

To determine the subcellular localization of proteins, *N. benthamiana* plants were transiently transformed with constructs encoding for fluorescent fusion proteins (4.3.4). Leaves were either cotransfected with the ER marker VMA12-RFP (#1729, described in Viotti et al., 2013) or the nuclear marker NLS-mCherry (#1805, unpublished). The fluorescence was analyzed 48 h after transformation by confocal laser scanning microscopy using a Nikon automated Ti inverted microscope equipped with a Yokagawa CSU-X1 confocal scanning unit, a Hamamatsu C9100-02 EMCCD camera and a Nikon S Fluor 40× numerical aperture 1.3 oil-immersion objective (Nikon). Images were taken in three channels (red: 561/615, blue: 405/445 nm and green: 488/527 nm). Additionally, a brightfield image was recorded. The resulting images were processed with the open-source image-analysis software Fiji (4.1.7).

4.11 Bioinformatical methods

4.11.1 Alignment of Nat homologs from different species

Protein sequences were obtained from TAIR or UniProt and aligned with Clustal Omega applying the default settings.

4.11.2 Sequence homology modelling of the *At*NatA/E complex

Homology modelling predicts the 3D structure of proteins based on alignments with known template proteins. The structure of the putative Arabidopsis NatA/E complex was modelled with SWISS-MODEL based on the previously published cryo-EM structure of the *Hs*NatA/E complex (6pw9.1). First, 3D models of the individual Arabidopsis proteins were created (*At*NAA10, *At*NAA15, *At*NAA50 and *At*HYPK). Subsequently, those were superimposed with the cryo-EM structure of the human NatA/E complex using the PyMOL Molecular Graphics System, Version 2.4, Schrödinger, LLC (4.1.7).

4.11.3 Gene Ontology (GO) term enrichment analysis

To identify overrepresented gene ontology (GO) terms among a given set of genes or gene products, an enrichment analysis was performed with the DAVID bioinformatics resources tool v.6.8.

4.11.4 Proteome-wide prediction of putative Nat substrates

For the proteome-wide prediction of putative Nat substrates, the Arabidopsis proteome (48,271 proteoforms; downloaded from the TAIR database) was screened for potential NatA-F targets based on known substrate specificities (NatA: N-termini starting with MA, MS, MV, MG, MT; NatB: N-termini starting with ME, MD, MN, MQ; NatC/E/F: N-termini starting with ML, MK, MM, MY, MF, MI; non-acetylated: all others).

4.12 Statistical methods

4.12.1 Statistical analysis

For statistical analysis, the software SigmaPlot 12.0 was used. When two genotypes/treatments were compared, an unpaired two-tailed Student's T-test was used. Significant differences are indicated with asterisks (* $p<0.05$, ** $p<0.01$ and *** $p<0.001$). When comparing more than two genotypes/treatments, a Holm-Sidak One-Way Anova or RM Anova was used. Significant differences between groups are indicated with different letters.

List of publications

First author

Armbruster L., Huber M., Etherington D.R., De La Torre C., Hawkesford J.M., Sticht C., Gibbs J.D., Hell R. and Wirtz M.: Disruption of the N-acetyltransferase NatB causes sensitivity to reductive stress in *Arabidopsis thaliana*, 2021, *Frontiers in Plant Science*

* **Armbruster L.**, Linster E., Boyer J.B., Brünje A., Eirich J., Stephan I., Bienvenut W.V., Weidenhausen J., Meinnel T., Hell R., Sinning I., Finkemeier I., Giglione C. and Wirtz M.: NAA50 is an enzymatically active N-acetyltransferase that is crucial for development and regulation of stress responses, 2020, *Plant Physiology*

Armbruster L., Uslu V.V., Wirtz M. and Hell R.: The recovery from sulfur starvation is independent from the mRNA degradation initiation enzyme PARN in Arabidopsis, 2019, *Plants (Basel)*

* part of this thesis

Co-author

* Miklankova P., Linster E., Boyer J.B., Weidenhausen J., Mueller J., **Armbruster L.**, Lapouge K., De La Torre C., Bienvenut W.V., Sticht C., Mann M., Meinnel T., Sinning I., Giglione C., Hell R. and Wirtz M.: HYPK promotes the activity of the essential N-acetyltransferase A complex to determine proteostasis of nonAc-X/N-degron containing proteins (submitted)

* Linster E., Forero Ruiz F.L., Miklankova P., Ruppert T., Mueller J., **Armbruster L.**, Gong X., Serino G., Mann M., Hell R. and Wirtz M.: Cotranslational N-degron masking by acetylation promotes proteome stability in plants, 2022, *Nature Communications*

Kats I., Reinbold C., Kschonsak M., Khmelinskii A., **Armbruster L.**, Ruppert T. and Knop, M.: Upregulation of ubiquitin-proteasome activity upon loss of NatA-dependent N-terminal acetylation, 2021, *Life Science Alliance*

Westrich L.D., Gotsmann V.L., Herkt C., Ries F., Kazek T., Trösch R., **Armbruster L.**, Mühlenbeck J.S., Ramundo S., Nickelsen J., Finkemeier I., Wirtz M., Storchová Z., Räschle M. and Willmund F.: The versatile interactome of chloroplast ribosomes revealed by affinity purification mass spectrometry, 2021, *Nucleic Acids Research*

Weidenhausen J., Kopp J., **Armbruster L.**, Wirtz, M., Lapouge K. and Sinning I.: Structural and functional characterization of the N-terminal acetyltransferase NAA50, 2020, *Structure*

Huber M., Bienvenut W.V., Linster E., Stephan I., **Armbruster L**, Sticht C., Layer D., Lapouge K., Meinnel T., Sinning I., Giglione C., Hell R. and Wirtz M.: NatB-mediated N-terminal acetylation affects growth and biotic stress responses, 2019, *Plant Physiology*

* part of this thesis

Bibliography

Ahn H-K, Yoon J-T, Choi I, Kim S, Lee H-S, Pai H-S, 2019. Functional characterization of chaperonin containing T-complex polypeptide-1 and its conserved and novel substrates in Arabidopsis. *J. Exp. Bot.* **70**, 2741-57.

Aksnes H, Drazic A, Marie M, Arnesen T, 2016. First things first: vital protein marks by N-terminal acetyltransferases. *Trends Biochem. Sci.* **41**, 746-60.

Aksnes H, Osberg C, Arnesen T, 2013. N-terminal acetylation by NatC is not a general determinant for substrate subcellular localization in *S. cerevisiae*. *PloS one* **8**, e61012.

Aksnes H, Ree R, Arnesen T, 2019. Co-translational, post-translational, and non-catalytic roles of N-terminal acetyltransferases. *Mol. Cell* **73**, 1097-114.

Aksnes H, Van Damme P, Goris M*, et al.*, 2015. An organellar N^{α}-acetyltransferase, NAA60, acetylates cytosolic N-termini of transmembrane proteins and maintains Golgi integrity. *Cell Rep.* **10**, 1362-74.

Allagulova CR, Gimalov FR, Shakirova FM, Vakhitov VA, 2003. The plant dehydrins: structure and putative functions. *Biochem.* **68**, 945-51.

Ametzazurra A, Gazquez C, Lasa M, Larrea E, Prieto J, Aldabe R, 2009. Characterization of the human N^{α}-terminal acetyltransferase B enzymatic complex. *BMC Proc.* **3**, S4.

Ametzazurra A, Larrea E, Civeira MP, Prieto J, Aldabe R, 2008. Implication of human N^{α}-acetyltransferase 5 in cellular proliferation and carcinogenesis. *Oncogene* **27**, 7296-306.

Aoi H, Mizuguchi T, Ceroni JR*, et al.*, 2019. Comprehensive genetic analysis of 57 families with clinically suspected Cornelia de Lange syndrome. *J. Hum. Genet.* **64**, 967-78.

Armbruster L, Linster E, Boyer J-B*, et al.*, 2020. NAA50 is an enzymatically active N^{α}-acetyltransferase that is crucial for development and regulation of stress responses. *Plant*

Physiol. **183**, 1502-16.

Arnesen T, Anderson D, Baldersheim C, Lanotte M, Varhaug JE, Lillehaug JR, 2005. Identification and characterization of the human ARD1-NATH protein acetyltransferase complex. *Biochem.* **386**, 433-43.

Arnesen T, Anderson D, Torsvik J, Halseth HB, Varhaug JE, Lillehaug JR, 2006a. Cloning and characterization of hNAT5/hSAN: an evolutionarily conserved component of the NatA protein N$^{\alpha}$-acetyltransferase complex. *Gene* **371**, 291-5.

Arnesen T, Betts MJ, Pendino F*, et al.*, 2006b. Characterization of hARD2, a processed hARD1 gene duplicate, encoding a human protein N$^{\alpha}$-acetyltransferase. *BMC Biochem.* **7**, 13ff.

Arnesen T, Gromyko D, Pendino F, Ryningen A, Varhaug JE, Lillehaug JR, 2006c. Induction of apoptosis in human cells by RNAi-mediated knockdown of hARD1 and NATH, components of the protein N$^{\alpha}$-acetyltransferase complex. *Oncogene* **25**, 4350-60.

Arnesen T, Kong X, Evjenth R*, et al.*, 2005. Interaction between HIF-1α (ODD) and hARD1 does not induce acetylation and destabilization of HIF-1α. *FEBS Lett.* **579**, 5ff.

Arnesen T, Starheim KK, Van Damme P*, et al.*, 2010. The chaperone-like protein HYPK acts together with NatA in cotranslational N-terminal acetylation and prevention of Huntingtin aggregation. *J. Mol. Cell Biol.* **30**, 1898-909.

Arnesen T, Van Damme P, Polevoda B*, et al.*, 2009. Proteomics analyses reveal the evolutionary conservation and divergence of N-terminal acetyltransferases from yeast and humans. *Proc. Natl. Acad. Sci. USA* **106**, 8157.

Baerenz F, Inoue D, Yokoyama H*, et al.*, 2013. The centriolar satellite protein SSX2IP promotes centrosome maturation. *J. Cell Biol.* **202**, 81-95.

Balint-Kurti P, 2019. The plant hypersensitive response: concepts, control and consequences. *Mol. Plant Pathol.* **20**, 1163-78.

Barnabas B, Jaeger K, Feher A, 2008. The effect of drought and heat stress on reproductive processes in cereals. *Plant Cell Environ.* **31**, 11-38.

Behnia R, Barr FA, Flanagan JJ, Barlowe C, Munro S, 2007. The yeast orthologue of GRASP65 forms a complex with a coiled-coil protein that contributes to ER to Golgi traffic. *J. Cell Biol.* **176**, 255-61.

Behnia R, Panic B, Whyte JRC, Munro S, 2004. Targeting of the Arf-like GTPase Arl3p to the Golgi requires N-terminal acetylation and the membrane protein Sys1p. *Nat. Cell Biol.* **6**, 405-13.

Bharath P, Gahir S, Raghavendra AS, 2021. Abscisic acid-induced stomatal closure: an

important component of plant defense against abiotic and biotic stress. *Front. Plant Sci.* **12**, 615114ff.

Bienvenut WV, Bruenje A, Boyer J-B*, et al.*, 2020. Dual lysine and N-terminal acetyltransferases reveal the complexity underpinning protein acetylation. *Mol. Syst. Biol.* **16**, 23ff.

Bienvenut WV, Espagne C, Martinez A*, et al.*, 2011. Dynamics of post-translational modifications and protein stability in the stroma of *Chlamydomonas reinhardtii* chloroplasts. *Proteomics* **11**, 1734-50.

Bienvenut WV, Giglione C, Meinnel T, 2017a. SILProNAQ: a convenient approach for proteome-wide analysis of protein N-termini and N-terminal acetylation quantitation. In *Protein Terminal Profiling: Methods and Protocols*, 17-34.

Bienvenut WV, Scarpelli J-P, Dumestier J, Meinnel T, Giglione C, 2017b. EnCOUNTer: a parsing tool to uncover the mature N-terminus of organelle-targeted proteins in complex samples. *BMC Bioinform.* **18**, 182.

Bienvenut WV, Sumpton D, Martinez A*, et al.*, 2012. Comparative large scale characterization of plant versus mammal proteins reveals similar and idiosyncratic N^{α}-acetylation features comparison of the N^{α}-acetylomes of Arabidopsis versus humans. *Mol. Cell Proteomics* **11**, M111.015131-M111.

Birke H, Heeg C, Wirtz M, Hell R, 2013. Successful fertilization requires the presence of at least one major *O*-acetylserine(thiol)lyase for cysteine synthesis in pollen of Arabidopsis. *Plant Physiol.* **163**, 959-72.

Brockmann B, Smith MW, Zaraisky AG, Harrison K, Okada K, Kamiya Y, 2001. Subcellular localization and targeting of glucocorticoid receptor protein fusions expressed in transgenic *Arabidopsis thaliana*. *Plant Cell Physiol.* **42**, 942-51.

Buerger M, Chory J, 2019. Stressed out about hormones: how plants orchestrate immunity. *Cell Host Microbe* **26**, 163-72.

Casey JP, Stove SI, Mcgorrian C*, et al.*, 2015. NAA10 mutation causing a novel intellectual disability syndrome with long QT due to N-terminal acetyltransferase impairment. *Sci. Rep.* **5**, 16022ff.

Chen H, Zou Y, Shang Y*, et al.*, 2008. Firefly luciferase complementation imaging assay for protein-protein interactions in plants. *Plant Physiol.* **146**, 368.

Chen J-Y, Liu L, Cao C-L*, et al.*, 2016. Structure and function of human Naa60 (NatF), a Golgi-localized bi-functional acetyltransferase. *Sci. Rep.* **6**, 31425.

Chen J, Huang X-Y, Salt DE, Zhao F-J, 2020. Mutation in *Os*CADT1 enhances cadmium

tolerance and enriches selenium in rice grain. *New Phytol.* **226**, 838-50.

Choudhury KR, Raychaudhuri S, Bhattacharyya NP, 2012. Identification of HYPK-interacting proteins reveals involvement of HYPK in regulating cell growth, cell cycle, unfolded protein response and cell death. *PloS one* **7**, e51415.

Christiansen KM, Gu Y, Rodibaugh N, Innes RW, 2011. Negative regulation of defence signalling pathways by the EDR1 protein kinase. *Mol. Plant Pathol.* **12**, 746-58.

Clough SJ, Bent AF, 1998. Floral dip: a simplified method for Agrobacterium-mediated transformation of *Arabidopsis thaliana*. *Plant J.* **16**, 735-43.

Couto D, Zipfel C, 2016. Regulation of pattern recognition receptor signalling in plants. *Nat. Rev. Immunol.* **16**, 537-52.

Cox J, Hein MY, Luber CA, Paron I, Nagaraj N, Mann M, 2014. Accurate proteome-wide label-free quantification by delayed normalization and maximal peptide ratio extraction, termed MaxLFQ. *Mol. Cell Proteomics* **13**, 2513-26.

Cox J, Mann M, 2008. MaxQuant enables high peptide identification rates, individualized p.p.b.-range mass accuracies and proteome-wide protein quantification. *Nat. Biotechnol.* **26**, 1367-72.

Dao TTH, Linthorst HJM, Verpoorte R, 2011. Chalcone synthase and its functions in plant resistance. *Phytochemistry* **10**, 397-412.

Daryanto S, Wang L, Jacinthe P-A, 2016. Global synthesis of drought effects on maize and wheat production. *PloS one* **11**, e0156362-e.

Dell'aglio E, Dalvit I, Loubéry S, Fitzpatrick TB, 2019. Clarification of the dispensability of PDX1.2 for Arabidopsis viability using CRISPR/Cas9. *BMC Plant Biol.* **19**, 464.

Demetriadou C, Pavlou D, Mpekris F*, et al.*, 2019. NAA40 contributes to colorectal cancer growth by controlling PRMT5 expression. *Cell Death Dis.* **10**, 236.

Deng S, Magin RS, Wei X, Pan B, Petersson EJ, Marmorstein R, 2019. Structure and mechanism of acetylation by the N-terminal dual enzyme NatA/Naa50 complex. *Structure* **27**, 1057-70.e4.

Deng S, Mctiernan N, Wei X, Arnesen T, Marmorstein R, 2020. Molecular basis for N-terminal acetylation by human NatE and its modulation by HYPK. *Nat. Commun.* **11**, 818ff.

Dikiy I, Eliezer D, 2014. N-terminal acetylation stabilizes N-terminal helicity in lipid- and micelle-bound α-synuclein and increases its affinity for physiological membranes. *J. Biol. Chem.* **289**, 3652-65.

Dickman, M., Williams, B., Li, Y., de Figueiredo, P., and Wolpert, T. (2017). Reassess-

ing apoptosis in plants. *Nat. Plants* **3**, 773-779.

Ding H, Mo S, Qian Y, Yuan G, Wu X, Ge C, 2020. Integrated proteome and transcriptome analyses revealed key factors involved in tomato under high temperature stress. *Food Energy Secur.* **9**, e239.

Dinh-Van T, 2013. Missing links of the protein N^{α}-terminal acetylation machinery in plants. Heidelberg, Univ., Diss., 2013.

Dinh-Van T, Linster E, Feldman-Salit A, Hell R, Wirtz M, 2015. Molecular identification and functional characterization of the first N^{α}-acetyltransferase in plastids by global acetylome profiling. *Proteomics* **15**, 10ff.

Dodds PN, Rathjen JP, 2010. Plant immunity: towards an integrated view of plant-pathogen interactions. *Nature Reviews Gen.* **11**, 539-48.

Dörfel MJ, Lyon GJ, 2015. The biological functions of Naa10 - from amino-terminal acetylation to human disease. *Gene* **567**, 103-31.

Dong OX, 1998. SA, JA, ethylene, and disease resistance in plants. *Curr. Opin. Plant Biol.* **1**, 316-23.

Dong OX, Ao K, Xu F*, et al.*, 2018. Individual components of paired typical NLR immune receptors are regulated by distinct E3 ligases. *Nat Plants* **4**, 699-710.

Drazic A, Aksnes H, Marie M*, et al.*, 2018. NAA80 is actin's N-terminal acetyltransferase and regulates cytoskeleton assembly and cell motility. *Proc. Natl. Acad. Sci. USA* **115**, 4399.

Duong-Ly KC, Gabelli SB, 2014. Troubleshooting protein expression: what to do when the protein is not soluble. In *Methods Enzymol.*: Academic Press, 231-47. (541.)

Edwards K, Johnstone C, Thompson C, 1991. A simple and rapid method for the preparation of plant genomic DNA for PCR analysis. *Nucleic Acids Res.* **19**, 1349.

Eichinger CS, Kurze A, Oliveira RA, Nasmyth K, 2013. Disengaging the Smc3/kleisin interface releases cohesin from Drosophila chromosomes during interphase and mitosis. *EMBO J.* **32**, 656-65.

Esmailpour T, Riazifar H, Liu L*, et al.*, 2014. A splice donor mutation in NAA10 results in the dysregulation of the retinoic acid signalling pathway and causes Lenz microphthalmia syndrome. *J. Med. Genet.* **51**, 185-96.

Evjenth R, Hole K, Karlsen OA, Ziegler M, Arnesen T, Lillehaug JR, 2009. Human Naa50p (Nat5/San) displays both protein N^{α}- and N^{ϵ}-acetyltransferase activity. *J. Biol. Chem.* **284**, 31122-9.

Evjenth RH, Brenner AK, Thompson PR, Arnesen T, Froystein NA, Lillehaug JR, 2012.

Human protein N-terminal acetyltransferase hNaa50p (hNAT5/hSAN) follows ordered sequential catalytic mechanism: combined kinetic and NMR study. *J. Biol. Chem.* **287**, 10081-8.

Faber PW, Barnes GT, Srinidhi J, Chen J, Gusella JF, Macdonald ME, 1998. Huntingtin interacts with a family of WW domain proteins. *Hum. Mol. Genet.* **7**, 1463-74.

Falb M, Aivaliotis M, Garcia-Rizo C*, et al.*, 2006. Archaeal N-terminal protein maturation commonly involves N-terminal acetylation: a large-scale proteomics survey. *J. Mol. Biol.* **362**, 915-24.

Feng J, Hu J, Li Y, Li R, Yu H, Ma L, 2020. The N-terminal acetyltransferase NAA50 regulates Arabidopsis growth and osmotic stress response. *Plant Cell Physiol.* **61**, 1565-75.

Feng J, Li R, Yu J*, et al.*, 2016. Protein N-terminal acetylation is required for embryogenesis in Arabidopsis. *J. Exp. Bot.* **67**, 4779-89.

Feng J, Qin M, Yao L, Li Y, Han R, Ma L, 2022. The N-terminal acetyltransferase Naa50 regulates tapetum degradation and pollen development in Arabidopsis. *Plant Sci.* **316**, 111180.

Fernandez RD, Lucas HR, 2018. Mass spectrometry data confirming tetrameric α-synuclein N-terminal acetylation. *Data Br.* **20**, 1686-91.

Ferrández-Ayela A, Micol-Ponce R, Sánchez-García AB, Alonso-Peral MM, Micol JL, Ponce MR, 2013. Mutation of an Arabidopsis NatB N^{α}-terminal acetylation complex component causes pleiotropic developmental defects. *PloS one* **8**, e80697-e.

Fisher TS, Etages SD, Hayes L, Crimin K, Li B, 2005. Analysis of ARD1 function in hypoxia response using retroviral RNA interference. *J. Biol. Chem.* **280**, 17749-57.

Forero Ruiz FL, 2017. The impact of proteome imprinting by N^{α}-terminal acetylation marks for protein dynamics in *Arabidopsis thaliana*. Heidelberg, Univ., Diss., 2017.

Foyn H, Van Damme P, Støve SI*, et al.*, 2013. Protein N-terminal acetyltransferases act as N-terminal propionyltransferases *in vitro* and *in vivo*. *Mol. Cell Proteomics* **12**, 42-54.

Friedrich, U.A., Zedan, M., Hessling, B., Fenzl, K., Gillet, L., Barry, J., Knop, M., Kramer, G., and Bukau, B. (2021). N^{α}-terminal acetylation of proteins by NatA and NatB serves distinct physiological roles in *Saccharomyces cerevisiae*. *Cell Rep.* **34**, 108711.

Frye CA, Tang D, Innes RW, 2001. Negative regulation of defense responses in plants by a conserved MAPKK kinase. *Proc. Natl. Acad. Sci. USA* **98**, 373-8.

Gao Q-M, Zhu S, Kachroo P, Kachroo A, 2015. Signal regulators of systemic acquired resistance. *Front. Plant Sci.* **6**.

Gautschi M, Just S, Mun A*, et al.*, 2003. The yeast N^{α}-acetyltransferase NatA is quant-

itatively anchored to the ribosome and interacts with nascent polypeptides. *J. Mol. Cell Biol.* **23**, 7403-14.

Ghosh DK, Ranjan A, 2019. An IRES-dependent translation of HYPK mRNA generates a truncated isoform of the protein that lacks the nuclear localization and functional ability. *RNA Biol.* **16**, 1604-21.

Ghosh DK, Roy A, Ranjan A, 2018. Aggregation-prone regions in HYPK help it to form sequestration complex for toxic protein aggregates. *J. Mol. Biol.* **430**, 963-86.

Giglione C, Boularot A, Meinnel T, 2004. Protein N-terminal methionine excision. *Cell. Mol. Life Sci.* **61**, 1455-74.

Giglione C, Fieulaine S, Meinnel T, 2015. N-terminal protein modifications: bringing back into play the ribosome. *Biochimie* **114**, 134-46.

Giglione C, Meinnel T, 2021. Evolution-driven versatility of N-terminal acetylation in photoautotrophs. *Trends Plant Sci.* **26**, 375-91.

Goetze S, Qeli E, Mosimann C*, et al.*, 2009. Identification and functional characterization of N-terminally acetylated proteins in *Drosophila melanogaster*. *PLoS Biol.* **7**, e1000236-e.

Gong X, Huang Y, Liang Y*, et al.*, 2022. *Os*HYPK-mediated protein N-terminal acetylation coordinates plant development and stress responses in rice. *Mol. Plant* (accepted)

Goris M, Magin RS, Foyn H*, et al.*, 2018. Structural determinants and cellular environment define processed actin as the sole substrate of the N-terminal acetyltransferase NAA80. *Proc. Natl. Acad. Sci. USA* **115**, 4405-10.

Gottlieb L, Marmorstein R, 2018. Structure of human NatA and its regulation by the Huntingtin interacting protein HYPK. *Structure* **26**, 925-35.e8.

Gou M, Shi Z, Zhu Y, Bao Z, Wang G, Hua J, 2012. The F-box protein CPR1/CPR30 negatively regulates R protein SNC1 accumulation. *Plant J.* **69**, 411-20.

Haberland S, 2017. Die komplexen Funktionen des Cysteinsynthasekomplexes bei der Schwefelmangelantwort in *Arabidopsis thaliana*. Heidelberg, Univ., Diss., 2017.

Henderson MX, Trojanowski JQ, Lee VMY, 2019. α-synuclein pathology in Parkinson's disease and related α-synucleinopathies. *Neurosci. Lett.* **709**, 134316ff.

Hole K, Van Damme P, Dalva M*, et al.*, 2011. The human N^{α}-acetyltransferase 40 (hNaa40p/hNatD) is conserved from yeast and N-terminally acetylates histones H2A and H4. *PloS one* **6**, e24713-e.

Holland AJ, Cleveland DW, 2012. Losing balance: the origin and impact of aneuploidy in cancer. *EMBO Rep.* **13**, 501-14.

Hoshiyasu S, Kohzuma K, Yoshida K*, et al.*, 2013. Potential involvement of N-terminal acetylation in the quantitative regulation of the ϵ-subunit of chloroplast ATP synthase under drought stress. *Biosci. Biotechnol. Biochem.* **77**, 998-1007.

Hou F, Chu C-W, Kong X, Yokomori K, Zou H, 2007. The acetyltransferase activity of San stabilizes the mitotic cohesin at the centromeres in a Shugoshin-independent manner. *J. Cell Biol.* **177**, 587-97.

Hsu P-K, Dubeaux G, Takahashi Y, Schroeder JI, 2021. Signaling mechanisms in abscisic acid-mediated stomatal closure. *Plant J.* **105**, 307-21.

Huang Y, Chen X, Liu Y*, et al.*, 2013a. Mitochondrial *At*PAM16 is required for plant survival and the negative regulation of plant immunity. *Nat. Commun.* **4**, 2558.

Huang Y, Minaker S, Roth C*, et al.*, 2014. An E4 ligase facilitates polyubiquitination of plant immune receptor resistance proteins in Arabidopsis. *Plant Cell* **26**, 485-96.

Huber M, 2015. Die Funktion der N^{α}-terminalen Acetyltransferasen B und C in der Entwicklung und Stressantwort von *Arabidopsis thaliana*. Heidelberg, Univ., Diss., 2015.

Huber M, Armbruster L, Etherington RD*, et al.*, 2022. Disruption of the N^{α}-acetyltransferase NatB causes sensitivity to reductive stress in *Arabidopsis thaliana*. *Front. Plant Sci.* **12**.

Huber M, Bienvenut WV, Linster E*, et al.*, 2020. NatB-mediated N-terminal acetylation affects growth and biotic stress responses. *Plant Physiol.* **182**, 792-806.

Huesgen PF, Alami M, Lange PF*, et al.*, 2013. Proteomic amino-termini profiling reveals targeting information for protein import into complex plastids. *PloS one* **8**, e74483-e.

Hunter JD, 2007. Matplotlib: a 2D graphics environment. *Comput. Sci. Eng.* **9**, 90-5.

Hwang C-S, Shemorry A, Varshavsky A, 2010. N-terminal acetylation of cellular proteins creates specific degradation signals. *Science* **327**, 973-7.

Iyer A, Roeters SJ, Schilderink N*, et al.*, 2016. The impact of N-terminal acetylation of α-synuclein on phospholipid membrane binding and fibril structure. *J. Biol. Chem.* **291**, 21110-22.

Jeong J-W, Bae M-K, Ahn M-Y*, et al.*, 2002. Regulation and destabilization of HIF-1α by ARD1-mediated acetylation. *Cell* **111**, 709-20.

Ji Hae SEO, Cha J-H, Jun Yong HA*, et al.*, 2010. Arrest defective 1 autoacetylation is a critical step in its ability to stimulate cancer cell proliferation. *Cell Res.* **70**, 4422-32.

Jung T-Y, Ryu J-E, Jang M-M*, et al.*, 2020. Naa20, the catalytic subunit of NatB complex, contributes to hepatocellular carcinoma by regulating the LKB1–AMPK–mTOR axis. *Exp. Mol. Med.* **52**, 1831-44.

Kalderon D, Roberts BL, Richardson WD, Smith AE, 1984. A short amino acid sequence able to specify nuclear location. *Cell* **39**, 499-509.

Kang J, Chun Y-S, Huh J, Park J-W, 2018. FIH permits NAA10 to catalyze the oxygen-dependent lysyl-acetylation of HIF-1α. *Redox Biol.* **19**, 364-74.

Karasov TL, Chae E, Herman JJ, Bergelson J, 2017. Mechanisms to mitigate the trade-off between growth and defense. *Plant Cell* **29**, 666-80.

Kats I, Khmelinskii A, Kschonsak M*, et al.*, 2018. Mapping degradation signals and pathways in a eukaryotic N-terminome. *Mol. Cell* **70**, 488-501.e5.

Kats I, Reinbold C, Kschonsak M*, et al.*, 2022. Up-regulation of ubiquitin–proteasome activity upon loss of NatA-dependent N-terminal acetylation. *Life Sci. Alliance* **5**, e202000730.

Kim SH, Gao F, Bhattacharjee S, Adiasor JA, Nam JC, Gassmann W, 2010. The Arabidopsis resistance-like gene SNC1 is activated by mutations in SRFR1 and contributes to resistance to the bacterial effector AvrRps4. *PLoS Pathog.* **6**, e1001172.

Kim, W.Y., Lee, S.Y., Jung, Y.J., Chae, H.B., Nawkar, G.M., Shin, M.R., Kim, S.Y., Park, J.H., Kang, C.H., Chi, Y.H., et al. (2011). Inhibitor of apoptosis (IAP)-like protein lacks a baculovirus IAP repeat (BIR) domain and attenuates cell death in plant and animal systems. *J. Biol. Chem.* **286**, 42670-42678.

Kiselev KV, Aleynova OA, Ogneva ZV, Suprun AR, Dubrovina AS, 2021. 35S promoter-driven transgenes are variably expressed in different organs of *Arabidopsis thaliana* and in response to abiotic stress. *Mol. Biol. Rep.* **48**, 2235-41.

Knorr AG, Schmidt C, Tesina P*, et al.*, 2019. Ribosome-NatA architecture reveals that rRNA expansion segments coordinate N-terminal acetylation. *Nat. Struct. Mol. Biol.* **26**, 5S.

Koskela MM, Brünje A, Ivanauskaite A*, et al.*, 2018. Chloroplast acetyltransferase NSI is required for state transitions in *Arabidopsis thaliana*. *Plant Cell* **30**, 1695-709.

Kosugi S, Hasebe M, Tomita M, Yanagawa H, 2009. Systematic identification of cell cycle-dependent yeast nucleocytoplasmic shuttling proteins by prediction of composite motifs. *Proc. Natl. Acad. Sci. USA* **106**, 10171-6.

Kuhns KJ, Zhang G, Wang Z, Liu W, 2018. ARD1/NAA10 acetylation in prostate cancer. *Exp. Mol. Med.* **50**, 1-8.

Kramer G, Boehringer D, Ban N, Bukau B, 2009. The ribosome as a platform for co-translational processing, folding and targeting of newly synthesized proteins. *Nat. Struct. Mol. Biol.* **16**, 589-97.

Kulak NA, Pichler G, Paron I, Nagaraj N, Mann M, 2014. Minimal, encapsulated

proteomic-sample processing applied to copy-number estimation in eukaryotic cells. *Nat. Methods* **11**, 319-24.

Kunz BA, Cahill DM, Mohr PG, Osmond MJ, Vonarx EJ, 2006. Plant responses to UV radiation and links to pathogen resistance. *Int. Rev. Cytol.* **255**, 1-40.

Lamers J, Van Der Meer T, Testerink C, 2020. How plants sense and respond to stressful environments. *Plant Physiol.* **182**, 1624-35.

Lassowskat I, Hartl M, Hosp F, Boersema PJ, Mann M, Finkemeier I, 2017. Dimethyl-labeling-based quantification of the lysine acetylome and proteome of plants. *Methods Protoc.*, 65-81.

Lee C-F, Ou DSC, Lee S-B*, et al.*, 2010. hNaa10p contributes to tumorigenesis by facilitating DNMT1-mediated tumor suppressor gene silencing. *J. Clin. Investig.* **120**, 2920-30.

Li H, Testerink C, Zhang Y, 2021. How roots and shoots communicate through stressful times. *Trends Plant Sci.* **26**, 940-52.

Li X, Zhang Y, Clarke JD, Li Y, Dong X, 1999. Identification and cloning of a negative regulator of systemic acquired resistance, SNI1, through a screen for suppressors of *npr1-1*. *Cell* **98**, 329-39.

Li Z, Dogra V, Lee KP*, et al.*, 2020. N-terminal acetylation stabilizes SIGMA FACTOR BINDING PROTEIN1 involved in salicylic acid-primed cell death. *Plant Physiol.* **183**, 358-70.

Liang C, Cheng S, Zhang Y*, et al.*, 2016. Transcriptomic, proteomic and metabolic changes in *Arabidopsis thaliana* leaves after the onset of illumination. *BMC Proc.* **16**, 43.

Lim J-H, Park J-W, Chun Y-S, 2006. Human arrest defective 1 acetylates and activates β-catenin, promoting lung cancer cell proliferation. *Cell Res.* **66**, 10677-82.

Linster E, 2014. Die Bedeutung der N^{α}-terminalen Protein Acetylierung durch den NatA-Komplex für die Stressantwort von höheren Pflanzen und die Qualitätskontrolle von Proteinen. Heidelberg, Univ., Diss., 2014.

Linster E, Forero Ruiz FL, Miklankova P*, et al.*, 2022. Cotranslational N-degron masking by acetylation promotes proteome stability in plants. *Nat. Commun.* **13**, 810.

Linster E, Layer D, Bienvenut WV*, et al.*, 2020. The Arabidopsis N^{α}-acetyltransferase NAA60 locates to the plasma membrane and is vital for the high salt stress response. *New Phytol.* **228**, 554-69.

Linster E, Stephan I, Bienvenut WV*, et al.*, 2015. Downregulation of N-terminal acetylation triggers ABA-mediated drought responses in Arabidopsis. *Nat. Commun.* **6**, 7640ff.

Linster E, Wirtz M, 2018. N-terminal acetylation: an essential protein modification emerges as an important regulator of stress responses. *J. Exp. Bot.* **69**, 4555-68.

Liszczak G, Goldberg JM, Foyn H, Petersson EJ, Arnesen T, Marmorstein R, 2013. Molecular basis for N-terminal acetylation by the heterodimeric NatA complex. *Nat. Struct. Mol. Biol.* **20**, 1098-105.

Liu H-Q, Zou Y-J, Li X-F, Wu L, Guo G-Q, 2021. Stablization of ACOs by NatB mediated N-terminal acetylation is required for ethylene homeostasis. *BMC Proc.* **21**, 320ff.

Liu Z, Liu Y, Wang H*, et al.*, 2009. Patt1, a novel protein acetyltransferase that is highly expressed in liver and downregulated in hepatocellular carcinoma, enhances apoptosis of hepatoma cells. *Int. J. Biochem. Cell Biol.* **41**, 2528-37.

Llamas E, Torres-Montilla S, Lee HJ, et al., 2021. The intrinsic chaperone network of Arabidopsis stem cells confers protection against proteotoxic stress. *Aging Cell* **20**, e13446.

Lobell David B, Roberts Michael J, Schlenker W*, et al.*, 2014. Greater sensitivity to drought accompanies maize yield increase in the U.S. Midwest. *Science* **344**, 516-9.

Lopez-Salmeron V, Schuerholz A-K, Li Z*, et al.*, 2019. Inducible, cell type-specific expression in *Arabidopsis thaliana* through LhGR-mediated trans-activation. *JoVE*, e59394.

Macharia MW, Tan WYZ, Das PP, Naqvi NI, Wong S-M, 2019. Proximity-dependent biotinylation screening identifies *Nb*HYPK as a novel interacting partner of ATG8 in plants. *BMC Proc.* **19**, 326ff.

Magin RS, Deng S, Zhang H, Cooperman B, Marmorstein R, 2017. Probing the interaction between NatA and the ribosome for co-translational protein acetylation. *PloS one* **12**, e0186278 S.

Magin RS, Liszczak GP, Marmorstein R, 2015. The molecular basis for histone H4- and H2A-specific amino-terminal acetylation by NatD. *Structure* **23**, 332-41.

Magin RS, March ZM, Marmorstein R, 2016. The N-terminal acetyltransferase Naa10/ARD1 does not acetylate lysine residues. *J. Biol. Chem.* **291**, 5270-7.

Maltsev AS, Ying J, Bax A, 2012. Impact of N-terminal acetylation of α-synuclein on its random coil and lipid binding properties. *Biochem.* **51**, 5004-13.

Mangano S, Gonzalez CD, Petruccelli S, 2014. *Agrobacterium tumefaciens*-mediated transient transformation of *Arabidopsis thaliana* leaves. *Methods Mol. Biol.* **1062**, 165-73.

Mann M, Jensen ON, 2003. Proteomic analysis of post-translational modifications. *Nat. Biotechnol.* **21**, 255-61.

Mason RJ, Paskins AR, Dalton CF, Smith DP, 2016. Copper binding and subsequent aggregation of α-synuclein are modulated by N-terminal acetylation and ablated by the

H50Q missense mutation. *Biochem.* **55**, 4737-41.

Matsushita T, Mochizuki N, Nagatani A, 2003. Dimers of the N-terminal domain of phytochrome B are functional in the nucleus. *Nature* **424**, 571-4.

Mazzucotelli E, Belloni S, Marone D*, et al.*, 2006. The E3 ubiquitin ligase gene family in plants: regulation by degradation. *Curr. Genomics* **7**, 509-22.

Mcintosh JR, 2016. Mitosis. *Perspect. Biol.* **8**, a023218.

Melotto M, Underwood W, Koczan J, Nomura K, He SY, 2006. Plant stomata function in innate immunity against bacterial invasion. *Cell* **126**, 969-80.

Meyer P, Van De Poel B, De Coninck B, 2021. UV-B light and its application potential to reduce disease and pest incidence in crops. *Hortic. Res.* **8**, 194.

Miklankova P, 2019. HYPK is a novel regulator of proteostasis and stress responses by controlling N^{α}-terminal protein acetylation in *Arabidopsis thaliana*. Heidelberg, Univ., Diss., 2019.

Molina-Serrano D, Schiza V, Demosthenous C*, et al.*, 2016. Loss of Nat4 and its associated histone H4 N-terminal acetylation mediates calorie restriction-induced longevity. *EMBO Rep.* **17**, 1829-43.

Monaghan J, Xu F, Gao M*, et al.*, 2009. Two prp19-like U-box proteins in the MOS4-associated complex play redundant roles in plant innate immunity. *PLoS Pathog.* **5**, e1000526.

Mueller F, Friese A, Pathe C*, et al.*, 2021. Overlap of NatA and IAP substrates implicates N-terminal acetylation in protein stabilization. *Sci. Adv.* **7**, eabc8590.

Mullen JR, Kayne PS, Moerschell RP*, et al.*, 1989. Identification and characterization of genes and mutants for an N-terminal acetyltransferase from yeast. *EMBO J.* **8**, 2067-75.

Murthi A, Hopper AK, 2005. Genome-wide screen for inner nuclear membrane protein targeting in *Saccharomyces cerevisiae*. *Genetics* **170**, 1553.

Nasmyth K, 2002. Segregating sister genomes: the molecular biology of chromosome separation. *Science* **297**, 559-65.

Neri L, Lasa M, Elosegui-Artola A*, et al.*, 2017. NatB-mediated protein N^{α}-terminal acetylation is a potential therapeutic target in hepatocellular carcinoma. *Oncotarget* **8**.

Neubauer M, Innes RW, 2020. Loss of the acetyltransferase NAA50 induces endoplasmic reticulum stress and immune responses and suppresses growth. *Plant Physiol.* **183**, 1838-54.

Neubauer M, Serrano I, Rodibaugh N*, et al.*, 2020. Arabidopsis EDR1 protein kinase regulates the association of EDS1 and PAD4 to inhibit cell death. *Mol. Plant Microbe Interact.* **33**, 693-703.

Neuwald AF, Landsman D, 1997. GCN5-related histone N-acetyltransferases belong to a diverse superfamily that includes the yeast SPT10 protein. *Trends Biochem. Sci.* **22**, 154-5.

Ngou BPM, Ahn H-K, Ding P, Jones JDG, 2021. Mutual potentiation of plant immunity by cell-surface and intracellular receptors. *Nature* **592**, 110-5.

Ossowski S, Schwab R, Weigel D, 2008. Gene silencing in plants using artificial microRNAs and other small RNAs. *Plant J.* **53**, 674-90.

Parenti I, Kaiser FJ, 2021. Cornelia de Lange Syndrome as paradigm of chromatinopathies. *Front. Neurosci.* **15**.

Park J-H, Seo JH, Wee H-J*, et al.*, 2014. Nuclear translocation of hARD1 contributes to proper cell cycle progression. *PloS one* **9**, e105185-e.

Pavlou D, Kirmizis A, 2016. Depletion of histone N-terminal-acetyltransferase Naa40 induces p53-independent apoptosis in colorectal cancer cells via the mitochondrial pathway. *Apoptosis* **21**, 298-311.

Pei Z-M, Ghassemian M, Kwak Christine M, Mccourt P, Schroeder Julian I, 1998. Role of farnesyltransferase in ABA regulation of guard cell anion channels and plant water loss. *Science* **282**, 287-90.

Pei Z-M, Murata Y, Benning G*, et al.*, 2000. Calcium channels activated by hydrogen peroxide mediate abscisic acid signalling in guard cells. *Nature* **406**, 731-4.

Pesaresi P, Gardner NA, Masiero S*, et al.*, 2003. Cytoplasmic N-terminal protein acetylation is required for efficient photosynthesis in Arabidopsis. *Plant Cell* **15**, 1817-32.

Peters J-M, Tedeschi A, Schmitz J, 2008. The cohesin complex and its roles in chromosome biology. *Genes Dev.* **22**, 3089-114.

Pimenta-Marques A, Tostões R, Marty T, Barbosa V, Lehmann R, Martinho RG, 2008. Differential requirements of a mitotic acetyltransferase in somatic and germ line cells. *Dev. Biol.* **323**, 197-206.

Polevoda B, Cardillo TS, Doyle TC, Bedi GS, Sherman F, 2003. Nat3p and Mdm20p are required for function of yeast NatB N^{α}-terminal acetyltransferase and of actin and tropomyosin. *J. Biol. Chem.* **278**, 30686-97.

Polevoda B, Norbeck J, Takakura H, Blomberg A, Sherman F, 1999. Identification and specificities of N-terminal acetyltransferases from *Saccharomyces cerevisiae*. *EMBO J.* **18**, 6155-68.

Polevoda B, Sherman F, 2001. NatC N^{α}-terminal acetyltransferase of yeast contains three subunits, Mak3p, Mak10p, and Mak31p. *J. Biol. Chem.* **276**, 20154-9.

Polevoda B, Sherman F, 2003. Composition and function of the eukaryotic N-terminal acetyltransferase subunits. *Biochem. Biophys. Res. Commun.* **308**, 1-11.

Pollard TD, O'shaughnessy B, 2019. Molecular mechanism of cytokinesis. *Annu. Rev. Biochem.* **88**, 661-89.

Popp B, Støve SI, Endele S*, et al.*, 2015. *De novo* missense mutations in the NAA10 gene cause severe non-syndromic developmental delay in males and females. *Eur. J. Hum.* **23**, 602-9.

Rathore OS, Faustino A, Prudêncio P, Van Damme P, Cox CJ, Martinho RG, 2016. Absence of N-terminal acetyltransferase diversification during evolution of eukaryotic organisms. *Sci. Rep.* **6**, 21304.

Raychaudhuri S, Majumder P, Sarkar S, Giri K, Mukhopadhyay D, Bhattacharyya NP, 2008. Huntingtin interacting protein HYPK is intrinsically unstructured. *Proteins* **71**, 1686-98.

Ree R, Krogstad K, Mctiernan N, Jakobsson ME, Arnesen T, 2021. Hydroxylation of the acetyltransferase NAA10 Trp38 is not an enzyme-switch in human cells. *Int. J. Mol. Sci.* **22**, 11805.

Ree R, Varland S, Arnesen T, 2018. Spotlight on protein N-terminal acetylation. *Exp. Mol. Med.* **50**, 1-13.

Ribeiro AL, Silva RD, Foyn H*, et al.*, 2016. Naa50/San-dependent N-terminal acetylation of Scc1 is potentially important for sister chromatid cohesion. *Sci. Rep.* **6**, 39118ff.

Rigaut G, Shevchenko A, Rutz B, Wilm M, Mann M, Séraphin B, 1999. A generic protein purification method for protein complex characterization and proteome exploration. *Nat. Biotechnol.* **17**, 1030-2.

Ritchie ME, Phipson B, Wu D*, et al.*, 2015. Limma powers differential expression analyses for RNA-sequencing and microarray studies. *Nucleic Acids Res.* **43**, e47-e.

Rizhsky L, Liang H, Shuman J, Shulaev V, Davletova S, Mittler R, 2004. When defense pathways collide. The response of Arabidopsis to a combination of drought and heat stress. *Plant Physiol.* **134**, 1683-96.

Rong Z, Ouyang Z, Magin RS, Marmorstein R, Yu H, 2016. Opposing functions of the N-terminal acetyltransferases NAA50 and NatA in sister-chromatid cohesion. *J. Biol. Chem.* **291**, 19079-91.

Rope A, Wang K, Evjenth R*, et al.*, 2011. Using VAAST to identify an X-linked disorder resulting in lethality in male infants due to N-terminal acetyltransferase deficiency. *Am. J. Hum. Genet.* **89**, 345ff.

Rubio S, Rodrigues A, Saez A, *et al.*, 2009. Triple loss of function of protein phosphatases type 2C leads to partial constitutive response to endogenous abscisic acid. *Plant Physiol.* **150**, 1345-55.

Runfola M, De Simone A, Vendruscolo M, Dobson CM, Fusco G, 2020. The N-terminal acetylation of α-synuclein changes the affinity for lipid membranes but not the structural properties of the bound state. *Sci. Rep.* **10**, 204.

Schindelin J, Arganda-Carreras I, Frise E, *et al.*, 2012. Fiji: an open-source platform for biological-image analysis. *Nat. Methods* **9**, 676-82.

Schiza V, Molina-Serrano D, Kyriakou D, Hadjiantoniou A, Kirmizis A, 2013. N^{α}-terminal acetylation of histone H4 regulates arginine methylation and ribosomal DNA silencing. *PLoS Genet.* **9**, e1003805.

Schreiner M, Martínez-Abaigar J, Glaab J, Jansen M, 2014. UV-B induced secondary plant metabolites. *Optik and Photonik* **9**, 34-7.

Schwab R, Ossowski S, Riester M, Warthmann N, Weigel D, 2006. Highly specific gene silencing by artificial microRNAs in Arabidopsis. *Plant Cell* **18**, 1121-33.

Setty SRG, Strochlic TI, Tong AHY, Boone C, Burd CG, 2004. Golgi targeting of ARF-like GTPase Arl3p requires its N^{α}-acetylation and the integral membrane protein Sys1p. *Nat. Cell Biol.* **6**, 414-9.

Shemorry A, Hwang C-S, Varshavsky A, 2013. Control of protein quality and stoichiometries by N-terminal acetylation and the N-end rule pathway. *Mol. Cell* **50**, 540-51.

Shim JH, Chung Y-H, Kim JA, *et al.*, 2012. Clinical implications of arrest-defective protein 1 expression in hepatocellular carcinoma: a novel predictor of microvascular invasion. *J. Dig. Dis.* **30**, 6 S.

Shin DH, Chun Y-S, Lee K-H, Shin H-W, Park J-W, 2009. Arrest defective-1 controls tumor cell behavior by acetylating myosin light chain kinase. *PloS one* **4**, e7451-e.

Singer JM, Shaw JM, 2003. Mdm20 protein functions with Nat3 protein to acetylate Tpm1 protein and regulate tropomyosin-actin interactions in budding yeast. *Proc. Natl. Acad. Sci. USA* **100**, 7644-9.

Singh D, Laxmi A, 2015. Transcriptional regulation of drought response: a tortuous network of transcriptional factors. *Front. Plant Sci.* **6**, 895.

Song O-K, Wang X, Waterborg JH, Sternglanz R, 2003. An N^{α}-acetyltransferase responsible for acetylation of the N-terminal residues of histones H4 and H2A. *J. Biol. Chem.* **278**, 38109-12.

Soppa J, 2010. Protein acetylation in archaea, bacteria, and eukaryotes. *Archaea* **2010**,

820681.

Soto-Suárez M, Serrato AJ, Rojas-González JA, Bautista R, Sahrawy M, 2016. Transcriptomic and proteomic approach to identify differentially expressed genes and proteins in *Arabidopsis thaliana* mutants lacking chloroplastic 1 and cytosolic FBPases reveals several levels of metabolic regulation. *BMC Proc.* **16**, 258.

Starheim K, Arnesen T, Gromyko D, Ryningen A, Varhaug J, Lillehaug J, 2008. Identification of the human N^{α}-acetyltransferase complex B (hNatB): a complex important for cell-cycle progression. *Biochem.* **415**, 325-31.

Starheim KK, Gromyko D, Evjenth R*, et al.*, 2009. Knockdown of human N^{α}-terminal acetyltransferase complex C leads to p53-dependent apoptosis and aberrant human Arl8b localization. *J. Mol. Cell Biol.* **29**, 3569-81.

Stephan I, 2011. Identifizierung und Charakterisierung von N-terminalen Acetyltransferasen in *Arabidopsis thaliana*. Heidelberg, Univ., Diss., 2011.

Tan W, Zhang D, Zhou H, Zheng T, Yin Y, Lin H, 2018. Transcription factor HAT1 is a substrate of SnRK2.3 kinase and negatively regulates ABA synthesis and signaling in Arabidopsis responding to drought. *PLoS Genet.* **14**, e1007336.

Tang D, Christiansen KM, Innes RW, 2005. Regulation of plant disease resistance, stress responses, cell death, and ethylene signaling in Arabidopsis by the EDR1 protein kinase. *Plant Physiol.* **138**, 1018-26.

Tang H, Guo J, Linpeng S, Wu L, 2019. Next generation sequencing identified two novel mutations in NIPBL and a frame shift mutation in CREBBP in three Chinese children. *Orphanet J. Rare Dis.* **14**, 45.

Tercero JC, Dinman JD, Wickner RB, 1993. Yeast MAK3 N-acetyltransferase recognizes the N-terminal four amino acids of the major coat protein (gag) of the L-A double-stranded RNA virus. *J. Bacteriol.* **175**, 3192-4.

Timms RT, Zhang Z, Rhee DY, Harper JW, Koren I, Elledge SJ, 2019. A glycine-specific N-degron pathway mediates the quality control of protein N-myristoylation. *Science* **365**, eaaw4912.

Trexler AJ, Rhoades E, 2012. N-terminal acetylation is critical for forming α-helical oligomer of α-synuclein. *Protein Sci.* **21**, 601-5.

Tyanova S, Temu T, Sinitcyn P*, et al.*, 2016. The Perseus computational platform for comprehensive analysis of (prote)omics data. *Nat. Methods* **13**, 731-40.

Umezawa T, Sugiyama N, Mizoguchi M*, et al.*, 2009. Type 2C protein phosphatases directly regulate abscisic acid-activated protein kinases in Arabidopsis. *Proc. Natl. Acad.*

Sci. USA **106**, 17588.

Underwood W, 2012. The plant cell wall: a dynamic barrier against pathogen invasion. *Front. Plant Sci.* **3**.

Van Damme P, 2021. Charting the N-Terminal acetylome: a comprehensive map of human NatA substrates. *Int. J. Mol. Sci.* **22**.

Van Damme P, Hole K, Gevaert K, Arnesen T, 2015. N-terminal acetylome analysis reveals the specificity of Naa50 (Nat5) and suggests a kinetic competition between N-terminal acetyltransferases and methionine aminopeptidases. *Proteomics* **15**, 2436-46.

Van Damme P, Hole K, Pimenta-Marques A*, et al.*, 2011. NatF contributes to an evolutionary shift in protein N-terminal acetylation and is important for normal chromosome segregation. *PLoS Genet.* **7**, e1002169.

Van Damme P, Kalvik TV, Starheim KK*, et al.*, 2016. A role for human N^{α}-acetyltransferase 30 (Naa30) in maintaining mitochondrial integrity. *Mol. Cell Proteomics* **15**, 3361-72.

Van Damme P, Lasa M, Polevoda B*, et al.*, 2012. N-terminal acetylome analyses and functional insights of the N-terminal acetyltransferase NatB. *Proc. Natl. Acad. Sci. USA* **109**, 12449.

Vinueza-Gavilanes R, Inigo-Marco I, Larrea L*, et al.*, 2020. N-terminal acetylation mutants affect α-synuclein stability, protein levels and neuronal toxicity. *Neurobiol. Dis.* **137**, 104781.

Viotti C, Krüger F, Krebs M*, et al.*, 2013. The endoplasmic reticulum is the main membrane source for biogenesis of the lytic vacuole in Arabidopsis. *Plant Cell* **25**, 3434-49.

Virlouvet L, Ding Y, Fujii H, Avramova Z, Fromm M, 2014. ABA signaling is necessary but not sufficient for RD29B transcriptional memory during successive dehydration stresses in *Arabidopsis thaliana*. *Plant J.* **79**, 150-61.

Vlad F, Rubio S, Rodrigues A*, et al.*, 2009. Protein phosphatases 2C regulate the activation of the Snf1-related kinase OST1 by abscisic acid in Arabidopsis. *Plant Cell* **21**, 3170-84.

Vo TTL, Park J-H, Lee EJ*, et al.*, 2020. Characterization of lysine acetyltransferase activity of recombinant human ARD1/NAA10. *Molecules* **25**, 588.

Voinnet O, Rivas S, Mestre P, Baulcombe D, 2003. An enhanced transient expression system in plants based on suppression of gene silencing by the p19 protein of tomato bushy stunt virus. *Plant J.* **33**, 949-56.

Wang T, Li J, Shen Q-H, 2019. Regulation of NLR stability in plant immunity. *Front. Agr. Sci. Eng.* **6**, 97-104.

Wang W, Vinocur B, Shoseyov O, Altman A, 2004. Role of plant heat-shock proteins and molecular chaperones in the abiotic stress response. *Trends Plant Sci.* **9**, 244-52.

Wang Z-H, Gong J-L, Yu M*, et al.*, 2011. Up-regulation of human arrest-defective 1 protein is correlated with metastatic phenotype and poor prognosis in breast cancer. *Asian Pac. J. Cancer Prev.* **12**, 1973-7.

Waskom LM, 2021. Seaborn: statistical data visualization. *J. Open Source Softw.* **6**, 3021.

Watkins JM, Chapman JM, Muday GK, 2017. Abscisic acid-induced reactive oxygen species are modulated by flavonols to control stomata aperture *Plant Physiol.* **175**, 1807-25.

Watson MD, Lee JC, 2019. N-terminal acetylation affects α-synuclein fibril polymorphism. *Biochem.* **58**, 3630-3.

Wawrzynska A, Christiansen KM, Lan Y, Rodibaugh NL, Innes RW, 2008. Powdery mildew resistance conferred by loss of the EDR1 protein kinase is suppressed by a missense mutation in KEEP ON GOING, a regulator of abscisic acid signaling. *Plant Physiol.* **148**, 1510-22.

Weidenhausen J, Kopp J, Armbruster L, Wirtz M, Lapouge K, Sinning I, 2021. Structural and functional characterization of the N-terminal acetyltransferase Naa50. *Structure* **29**, 413-25.e5.

Wen W, Meinkotht JL, Tsien RY, Taylor SS, 1995. Identification of a signal for rapid export of proteins from the nucleus. *Cell* **82**, 463-73.

Westrich LD, Gotsmann VL, Herkt C*, et al.*, 2021. The versatile interactome of chloroplast ribosomes revealed by affinity purification mass spectrometry. *Nucleic Acids Res.* **49**, 400-15.

Weyer FA, Gumiero A, Lapouge K, Bange G, Kopp J, Sinning I, 2017. Structural basis of HypK regulating N-terminal acetylation by the NatA complex. *Nat. Commun.* **8**, 15726ff.

Wild K, Aleksić M, Lapouge K, et al., 2020. MetAP-like Ebp1 occupies the human ribosomal tunnel exit and recruits flexible rRNA expansion segments. *Nat. Commun.* **11**, 776.

Wilkinson JE, Twell D, Lindsey K, 1997. Activities of CaMV 35S and nos promoters in pollen: implications for field release of transgenic plants. *J Exp Bot* **48**, 265-75.

Williams BC, Garrett-Engele CM, Li Z, Williams EV, Rosenman ED, Goldberg ML, 2003. Two putative acetyltransferases, San and Deco, are required for establishing sister chromatid cohesion in Drosophila. *Curr. Biol.* **13**, 2025-36.

Wirtz M, Birke H, Heeg C*, et al.*, 2010. Structure and function of the hetero-oligomeric

cysteine synthase complex in plants. *J. Biol. Chem.* **285**, 32810-7.

Xu F, Huang Y, Li L*, et al.*, 2015. Two N-terminal acetyltransferases antagonistically regulate the stability of a nod-like receptor in Arabidopsis. *Plant Cell* **27**, 1547-62.

Xu F, Xu S, Wiermer M, Zhang Y, Li X, 2012. The cyclin L homolog MOS12 and the MOS4-associated complex are required for the proper splicing of plant resistance genes. *Plant J.* **70**, 916-28.

Yam AY, Xia Y, Lin H-TJ, Burlingame A, Gerstein M, Frydman J, 2008. Defining the TRiC/CCT interactome links chaperonin function to stabilization of newly made proteins with complex topologies. *Nat. Struct. Mol. Biol.* **15**, 1255-62.

Yang X, Yu W, Shi L*, et al.*, 2011. HAT4, a Golgi apparatus-anchored B-type histone acetyltransferase, acetylates free histone H4 and facilitates chromatin assembly. *Mol. Cell* **44**, 39-50.

Yavarna T, Al-Dewik N, Al-Mureikhi M*, et al.*, 2015. High diagnostic yield of clinical exome sequencing in Middle Eastern patients with Mendelian disorders. *Hum. Genet.* **134**, 967-80.

Ye W, Munemasa S, Shinya T*, et al.*, 2020. Stomatal immunity against fungal invasion comprises not only chitin-induced stomatal closure but also chitosan-induced guard cell death. *Proc. Natl. Acad. Sci. USA* **117**, 20932.

Yordanov I, Velikova V, Tsonev T, 2000. Plant responses to drought, acclimation, and stress tolerance. *Photosynthetica* **38**, 171-86.

Yuan L, Yang X, Auman D, Makaroff CA, 2014. Expression of epitope-tagged SYN3 cohesin proteins can disrupt meiosis in Arabidopsis. *J. Genet. Genom.* **41**, 153-64.

Yuan M, Jiang Z, Bi G*, et al.*, 2021. Pattern-recognition receptors are required for NLR-mediated plant immunity. *Nature* **592**, 105-9.

Zhang H, Gannon L, Hassall KL*, et al.*, 2018. N-terminomics reveals control of Arabidopsis seed storage proteins and proteases by the Arg/N-end rule pathway. *New Phytol.* **218**, 1106-26.

Zheng X-Y, Spivey N, Zeng W*, et al.*, 2012. Coronatine promotes *Pseudomonas syringae* virulence in plants by activating a signaling cascade that inhibits salicylic acid accumulation. *Cell Host Microbe* **11**, 587-96.

Zybailov B, Rutschow H, Friso G*, et al.*, 2008. Sorting signals, N-terminal modifications and abundance of the chloroplast proteome. *PloS one* **3**, e1994-e.

Acknowledgements

At this point, I would like to thank several people who made this dissertation possible. First of all, I would like to mention my supervisor Prof. Dr. Rüdiger Hell. With his wonderful lecture on the molecular biology of plants, he sparked my enthusiasm for botany. He gave me the opportunity to complete not only my bachelor's thesis but also my master's thesis and, last but not least, my dissertation in his research group. Thanks to his supervision, I developed from a curious student to a serious scientist during this time.

I would also like to thank my mentor Dr. Markus Wirtz. Our fruitful discussions, his clever ideas and his constructive criticism have always kept me one step ahead. During the countless hours we spent together working on publications and arguing about the optimal wording of sentences, he patiently shaped my scientific writing style.

Furthermore I want to thank my TAC members Prof. Dr. Irmgard Sinning and Prof. Dr. Thomas Greb, for their numerous suggestions and support. Similarly, I received important feedback at the Kat/Nat meetings with consortium members from Birmingham, Münster, Paris, and Turku.

Many thanks also to my collaborators for their valuable support: Dr. Thomas Ruppert and his team from the Core Facility for Mass Spectrometry and Proteomics analyzed my Co-IP samples and putative N-terminal interactors by mass spectroscopy. Prof. Dr. Xin Li and Dr. Zhongshou Wu from the Michael Smith Laboratories in Vancouver subjected my *aminaa50* lines to various pathogen treatments and thus significantly advanced my research. Dr. Gernot Poschet and his team from the Metabolomics Core Technology Platform supported me with phytohormone analyses, and Dr. Carolina de La Torre from the Next Generation Sequencing Core Facility in Mannheim assisted me with transcriptome data analysis.

Another person without whom this PhD would not have been possible is Dr. Eric Linster.

He was there to help and advise me from the very first moment in the lab and was never at a loss for an answer. Even when experiments did not work as planned, he was always there with words of encouragement. Although I met him at a much later point during my PhD, it was a similar story with Dr. Xiaodi Gong. He supported me in the planning and execution of several experiments and introduced me to the secrets of Chinese culture along the way. Another person who has contributed significantly to the success of this work is the good soul of our laboratory, Olga Keberlein. Over the course of the last four years, she has bravely pricked hundreds of plants on my behalf, pipetted countless PCRs, and prepared litres of culture medium. I would also like to mention Birgit Maresch who solved every administrative problem within seconds, Michael Schilbach who saved my plants from drying out many times, and Michael Kraft who repaired numerous broken machines and pipettes for me.

In addition, I would like to thank all former and current members of AG Hell for birthday breakfasts, barbecue afternoons, movie nights and many conversations at lunch or during coffee breaks. I greatly enjoyed working with all of you! It's a shame that Covid-19 prevented us from socializing even more, but I hope we can make up for that this summer!

I have also had the pleasure of teaching students time and again. As temporary members of AG Hell Marvin Bremer, Eugenia Guerrero, Rebecca Alvarado, Eddie Merbitz, Selina Windecker, and Anika Seppelt contributed to the success of this work.

Lastly, I would like to thank my friends, my fiancé Sebastián and my family. You always believed in me and helped me through many difficulties. I can't imagine what life would be like without you.

Supplement

7.1 Supplementary Tables

Table S1: Proteins (co)-immunoprecipitated from wildtype protein extracts incubated with a specific α-NAA15 antiserum. Protein extracts of six-week-old soil-grown (4.3.2) wildtype plants were incubated with α-NAA15 antiserum (n=3). Subsequently, the samples were mixed with protein A/G beads (4.5.4) to capture the antibodies and the proteins which interacted with them. Protein extracts incubated exclusively with protein A/G beads served as negative control. After separating the beads from the supernatant, the proteins bound to the beads were released by addition of Laemmli buffer. The samples were separated by SDS-PAGE and analyzed by mass-spectrometry. This table lists the significantly ($>$2-fold, p$<$0.05 in a Student's t-test) enriched proteins.

#	ID	fold enrichment	p-value
1	AT3G06610.1	1069.81	4.28E-02
2	AT2G38230.1	1013.12	3.62E-02
3	AT1G80410.2	772.38	1.74E-02
4	AT5G01410.1	763.47	4.65E-02
5	AT5G13780.1	528.07	3.07E-02
6	AT3G16050.1	290.13	4.33E-02
7	AT2G18960.1	81.24	3.81E-02
8	AT2G43945.1	77.21	6.29E-05
9	AT3G59870.1	55.03	7.29E-03
10	AT5G52440.1	39.11	1.34E-02
11	AT4G26510.3	37.55	1.49E-02
12	AT1G50250.1	32.69	3.49E-02

13	AT3G02320.1	30.62	1.50E-02
14	AT2G39050.1	27.54	4.40E-02
15	AT5G13420.1	24.8	1.25E-02
16	AT5G01600.1	20.51	2.36E-03
17	AT3G25530.1	17.77	1.84E-02
18	AT5G11450.2	16.01	2.80E-02
19	AT2G47940.1	15.67	2.76E-04
20	AT1G07920.1	15.36	3.87E-05
21	AT5G15810.1	14.98	6.20E-03
22	AT1G13060.1	14.24	1.08E-02
23	AT1G58380.1	12.22	5.19E-03
24	AT2G45180.1	11.37	5.11E-05
25	AT1G06530.1	11.25	8.79E-03
26	AT1G24020.1	11.09	1.42E-03
27	AT4G38740.1	10.84	4.36E-03
28	AT2G40840.1	10.24	4.27E-02
29	AT3G50560.1	10.01	7.92E-03
30	AT2G24270.4	9.81	4.18E-02
31	AT5G66510.1	9.77	1.45E-02
32	AT5G65750.1	9.55	5.34E-04
33	AT3G05530.1	8.88	2.59E-02
34	AT1G71695.1	8.65	5.42E-03
35	AT3G27830.1	8.58	6.34E-03
36	AT1G78630.1	8.33	2.85E-02
37	AT3G52200.2	8.31	4.47E-02
38	AT3G51420.1	8.22	4.32E-03
39	AT4G17720.1	8.08	2.53E-03
40	AT3G54890.1	7.88	4.60E-02
41	AT1G43670.1	7.67	5.67E-04
42	AT3G25770.1	7.44	2.22E-04
43	AT5G66190.1	7.25	3.18E-03
44	AT2G27720.1	7.23	1.32E-02
45	AT2G47110.1	7.19	8.21E-04
46	AT2G47400.1	7.14	5.44E-04
47	AT3G13930.1	7.08	2.38E-02
48	AT5G62350.1	7.05	3.88E-03
49	AT1G14610.1	7.01	1.41E-02

50	AT3G13870.1	6.8	5.59E-03
51	AT5G64370.1	6.7	3.17E-02
52	AT5G23060.1	6.53	2.12E-02
53	AT5G16050.2	6.53	1.23E-02
54	AT1G20620.1	6.5	1.53E-03
55	AT1G78680.1	6.32	1.14E-02
56	AT2G24200.2	6.2	4.91E-03
57	AT1G70820.1	6.08	3.39E-02
58	AT2G30110.1	6.04	3.53E-02
59	AT4G29010.1	6.01	1.32E-03
60	AT3G52960.1	5.96	2.13E-02
61	AT2G39470.1	5.9	1.46E-03
62	AT5G66420.2	5.85	1.20E-02
63	AT1G02780.1	5.6	1.02E-02
64	AT2G33800.1	5.57	6.98E-04
65	AT4G33510.1	5.56	1.31E-03
66	AT4G10840.1	5.5	1.77E-03
67	AT1G14345.1	5.47	4.61E-02
68	AT5G13510.1	5.45	6.64E-04
69	AT3G02360.1	5.29	1.15E-02
70	AT5G10450.4	5.26	8.06E-05
71	ATMG00070.1	5.24	2.43E-03
72	AT3G07110.2	5.17	2.24E-04
73	AT5G28540.1	5.14	1.98E-04
74	AT3G48140.1	5.04	1.12E-03
75	AT1G59610.1	4.98	7.67E-04
76	AT2G27680.1	4.98	5.40E-03
77	AT5G54600.1	4.94	2.32E-02
78	AT4G34450.1	4.83	9.19E-03
79	AT1G70410.1	4.8	2.68E-02
80	AT1G15690.1	4.55	4.55E-02
81	AT5G54750.2	4.46	1.06E-02
82	ATCG01300.1	4.43	3.15E-02
83	AT3G25920.1	4.39	2.34E-02
84	AT3G63490.1	4.35	2.04E-02
85	AT5G08050.1	4.2	1.13E-02
86	AT3G53990.1	4.13	4.95E-02

87	AT1G07320.1	4.13	4.33E-02
88	AT1G01090.1	4.03	9.58E-03
89	AT1G35160.2	3.99	5.38E-04
90	AT3G16530.1	3.96	1.49E-02
91	AT3G11820.1	3.95	1.91E-03
92	AT2G24820.1	3.93	4.20E-02
93	AT5G30510.1	3.92	4.59E-02
94	AT3G45780.1	3.87	5.04E-03
95	AT3G46740.1	3.85	2.63E-02
96	AT2G01140.1	3.81	2.56E-02
97	AT3G18890.1	3.78	1.96E-04
98	AT5G02870.1	3.78	1.27E-02
99	AT2G20450.1	3.74	4.78E-03
100	AT1G59900.1	3.73	5.37E-03
101	AT5G58140.6	3.67	1.25E-03
102	AT4G09000.2	3.67	4.70E-03
103	AT5G08300.1	3.65	1.62E-02
104	AT5G50850.1	3.57	1.24E-02
105	AT3G14310.1	3.5	3.87E-03
106	AT5G35590.1	3.5	3.86E-03
107	AT2G35780.1	3.5	9.37E-03
108	AT5G42980.1	3.49	7.91E-03
109	AT3G54110.1	3.49	1.32E-02
110	AT1G22300.1	3.41	9.90E-03
111	AT2G28000.1	3.4	7.04E-04
112	AT5G03350.1	3.36	8.07E-03
113	AT5G13440.1	3.34	2.37E-03
114	AT3G11830.1	3.33	5.70E-04
115	AT2G21170.3	3.32	5.09E-03
116	AT1G71500.1	3.31	4.07E-02
117	AT1G72910.1	3.2	4.33E-03
118	AT3G62530.1	3.2	3.09E-02
119	AT4G24800.3	3.17	5.75E-03
120	AT5G11340.1	3.15	1.35E-03
121	AT2G42540.2	3.15	4.75E-02
122	AT4G37200.1	3.15	2.26E-02
123	AT3G04120.1	3.13	4.58E-02

124	AT3G28220.1	3.11	4.68E-02
125	AT2G19940.2	3.07	1.66E-03
126	AT2G25450.1	3.04	9.21E-04
127	ATCG00780.1	2.9	1.62E-02
128	AT2G06850.1	2.88	3.22E-02
129	AT5G58070.1	2.87	5.03E-03
130	AT3G47370.3	2.86	3.05E-02
131	AT3G63520.1	2.84	4.33E-03
132	AT4G17600.1	2.83	4.63E-02
133	AT3G01340.2	2.82	2.91E-02
134	AT4G19410.1	2.77	1.79E-02
135	AT5G03880.1	2.76	2.61E-02
136	AT3G01480.1	2.75	3.20E-02
137	AT3G02200.2	2.69	1.15E-02
138	AT1G32990.1	2.61	3.53E-02
139	AT1G13440.1	2.58	4.03E-02
140	AT3G26650.1	2.54	1.40E-02
141	AT4G23850.1	2.51	1.11E-03
142	AT2G45990.2	2.45	3.67E-02
143	AT1G12900.5	2.36	2.70E-02
144	AT5G17920.1	2.27	1.06E-02
145	AT4G01900.1	2.25	2.41E-02
146	AT4G27440.1	2.19	9.41E-03
147	AT5G19940.1	2.17	3.77E-02
148	AT3G48990.1	2.05	2.49E-02
149	AT2G27730.1	2.03	1.15E-02

Table S2: Proteins (co)-immunoprecipitated from wildtype protein extracts incubated with a specific α-NAA50 antiserum. Protein extracts of six-week-old soil-grown (4.3.2) wildtype plants were incubated with α-NAA50 antiserum (n=3). Subsequently, the samples were mixed with protein A/G beads (4.5.4) to capture the antibodies and the proteins which interacted with them. Protein extracts incubated exclusively with protein A/G beads served as negative control. After separating the beads from the supernatant, the proteins bound to the beads were released by addition of Laemmli buffer. The samples were separated by SDS-PAGE and analyzed by mass-spectrometry. This table lists the significantly ($>$2-fold, p$<$0.05 in a Student's t-test) enriched proteins.

#	ID	fold enrichment	p-value
1	AT4G35830.1	538.92	6.18E-03
2	AT2G39050.1	355.22	2.40E-02
3	AT5G65750.1	279.66	1.83E-02
4	AT4G29060.1	279.11	7.02E-03
5	AT2G37660.1	257.12	1.74E-03
6	AT4G10840.1	205.71	2.60E-04
7	AT5G11340.1	195.51	4.08E-03
8	AT5G46070.1	177.71	1.19E-02
9	AT3G50560.1	149.51	8.23E-03
10	AT4G17090.1	149.45	4.16E-02
11	AT3G06040.3	147.73	1.69E-02
12	AT3G45980.1	122.79	3.22E-04
13	AT3G55410.1	102.27	2.31E-02
14	AT5G17170.1	91.67	1.36E-03
15	AT3G03980.1	87.67	6.03E-04
16	AT5G20080.1	86.61	2.07E-02
17	AT5G14220.4	86.51	6.50E-03
18	AT1G70410.1	72.92	9.04E-03
19	AT1G07110.1	71.96	1.85E-02
20	AT1G12240.1	66.15	3.05E-02
21	AT1G08250.1	61.48	3.62E-03
22	AT5G16390.1	58.89	3.77E-02
23	AT2G02740.1	57.15	4.86E-04
24	AT5G24165.1	49.48	1.93E-02
25	AT2G34480.2	49.28	8.97E-03
26	AT2G41680.1	47.96	4.52E-02
27	AT3G54960.1	41.99	8.43E-04

28	AT3G56130.1	41.88	1.41E-02
29	AT2G38270.1	41.47	4.23E-02
30	AT4G27740.1	39.39	3.46E-02
31	AT5G20280.1	37.62	7.44E-05
32	AT2G33210.1	37.14	8.83E-03
33	AT1G61250.1	36.02	2.07E-02
34	AT1G08720.1	33.01	2.70E-03
35	AT5G51970.2	31.46	1.67E-05
36	AT1G02280.2	30.94	2.08E-03
37	AT1G52670.1	29	1.53E-02
38	AT5G37850.4	26.94	1.37E-02
39	AT5G52440.1	26.4	6.67E-05
40	AT5G10470.2	25.98	1.85E-02
41	AT2G40840.1	21.14	1.13E-02
42	AT1G72550.1	19.34	1.19E-05
43	AT2G39990.1	18.62	4.44E-05
44	AT5G65270.1	18.49	4.13E-02
45	AT2G43945.1	18.41	4.48E-03
46	AT3G23990.1	16.53	1.36E-02
47	AT1G21750.1	16.48	1.39E-05
48	AT1G80410.2	16.41	4.68E-04
49	AT5G11450.2	15.46	7.50E-04
50	AT5G13780.1	15.12	4.40E-02
51	AT1G53850.1	15.06	1.62E-03
52	AT4G12060.1	14.71	5.04E-04
53	AT3G16050.1	14	2.74E-04
54	AT1G68560.1	13.39	2.09E-02
55	AT5G01600.1	13.18	2.15E-02
56	AT2G24270.4	13.07	4.63E-02
57	AT5G54750.2	12.78	2.38E-03
58	AT3G59870.1	12.23	3.75E-03
59	AT1G67280.1	11.98	1.66E-03
60	AT1G11840.6	11.88	2.22E-04
61	AT5G07030.1	11.85	3.72E-02
62	AT1G07920.1	11.61	1.31E-02
63	AT1G20020.1	11.27	2.85E-04
64	AT1G78570.1	11.04	2.96E-05

65	AT3G44310.1	10.98	2.90E-03
66	AT4G00430.1	10.97	6.03E-03
67	AT3G01390.2	10.12	1.44E-04
68	AT5G08530.1	9.83	7.71E-03
69	AT5G52920.1	9.36	1.87E-03
70	AT5G08740.1	9.28	1.28E-02
71	AT5G20950.3	8.82	5.61E-07
72	AT3G13860.1	8.39	2.37E-02
73	AT3G09980.1	8.3	1.41E-03
74	AT4G38630.1	8.14	2.83E-04
75	AT2G18960.1	8.14	2.34E-03
76	AT4G39970.1	7.79	5.28E-05
77	AT3G25530.1	7.75	3.63E-02
78	AT3G52200.2	7.26	4.32E-04
79	AT3G13930.1	7.07	1.63E-04
80	AT1G06950.1	6.95	2.17E-04
81	AT1G18070.3	6.88	1.62E-03
82	AT5G06320.1	6.64	1.06E-02
83	AT1G04710.1	6.38	3.27E-03
84	AT1G80600.1	6.22	2.21E-02
85	AT2G21390.1	6.03	4.44E-02
86	AT1G54220.1	5.96	5.48E-04
87	AT1G09630.1	5.73	3.51E-03
88	AT2G20990.3	5.45	9.23E-04
89	AT1G17290.1	5.44	2.12E-04
90	AT3G14110.3	5.43	8.51E-04
91	AT4G19710.2	5.39	3.48E-03
92	AT3G53460.4	5.25	7.87E-03
93	AT5G04740.1	5.19	3.12E-02
94	AT3G25860.1	5.1	3.79E-04
95	AT3G03710.1	5.02	3.63E-02
96	AT5G06870.1	4.75	1.42E-02
97	AT3G44110.1	4.6	2.58E-02
98	AT1G78630.1	4.52	1.24E-02
99	AT3G09840.1	4.52	7.00E-03
100	AT4G26510.3	4.46	1.35E-02
101	AT3G07720.1	4.35	2.02E-02

102	AT4G18440.1	4.35	2.20E-03
103	AT1G30120.1	4.31	2.58E-02
104	AT3G17970.1	4.27	2.37E-02
105	AT3G52380.1	4.25	1.37E-02
106	ATCG00120.1	4.2	6.99E-03
107	AT1G66970.2	4.04	4.38E-02
108	AT1G74920.1	4.03	1.78E-02
109	AT5G65010.2	3.96	4.60E-03
110	ATCG00660.1	3.88	4.32E-03
111	AT1G12410.1	3.86	1.55E-02
112	AT5G44070.1	3.85	4.13E-03
113	AT1G04530.1	3.84	5.48E-03
114	AT5G62690.1	3.83	3.95E-03
115	AT3G48930.1	3.75	6.06E-03
116	AT1G37130.1	3.65	1.49E-02
117	AT4G24280.1	3.63	2.26E-03
118	AT3G63490.1	3.54	3.40E-03
119	AT3G56910.1	3.47	2.61E-02
120	AT2G32730.1	3.43	3.67E-03
121	AT1G20620.1	3.42	5.21E-03
122	AT2G27020.2	3.39	7.17E-03
123	AT4G35450.5	3.35	6.92E-03
124	AT4G24750.1	3.32	4.57E-02
125	AT1G49750.1	3.3	8.67E-04
126	ATCG00810.1	3.29	3.27E-03
127	AT3G13120.1	3.2	9.60E-04
128	AT4G34110.1	3.18	8.67E-03
129	AT5G23060.1	3.18	3.07E-02
130	AT1G63660.1	3.13	1.43E-02
131	AT3G13790.1	3.12	8.39E-03
132	AT2G47450.1	3.02	1.97E-02
133	AT3G53430.1	2.99	2.57E-03
134	AT3G06580.1	2.96	6.83E-03
135	AT1G44575.1	2.9	5.54E-03
136	AT5G09590.1	2.9	4.37E-03
137	AT2G05070.1	2.88	8.99E-03
138	AT1G62640.2	2.87	4.68E-03

139	AT5G05010.2	2.85	1.60E-02
140	AT2G43030.1	2.83	2.55E-02
141	AT3G52180.1	2.83	1.61E-02
142	AT1G17890.1	2.81	4.73E-03
143	AT2G39800.4	2.77	7.91E-03
144	AT2G31610.1	2.76	6.47E-03
145	AT3G24830.1	2.75	3.17E-02
146	AT2G39730.2	2.74	8.92E-03
147	AT5G19140.1	2.73	2.41E-02
148	AT1G35680.1	2.73	6.89E-03
149	AT4G04040.1	2.72	4.76E-03
150	AT5G49360.1	2.72	2.82E-02
151	AT1G59900.1	2.7	1.24E-02
152	AT1G34430.1	2.66	3.67E-02
153	AT3G04120.1	2.66	7.14E-03
154	AT1G74970.1	2.65	4.60E-02
155	ATCG00800.1	2.64	4.61E-03
156	AT1G09620.1	2.63	1.06E-02
157	AT1G56580.1	2.62	4.69E-02
158	AT5G14740.7	2.62	1.67E-02
159	AT5G19760.1	2.61	6.51E-03
160	AT5G48790.1	2.6	7.42E-03
161	AT5G25980.2	2.6	4.60E-02
162	AT4G16720.1	2.58	3.58E-02
163	AT5G61170.1	2.57	6.98E-03
164	ATCG00770.1	2.56	1.06E-02
165	AT5G16840.2	2.52	1.72E-02
166	AT3G14420.1	2.5	4.38E-02
167	AT4G39150.1	2.5	2.02E-02
168	AT5G60790.1	2.48	2.79E-02
169	AT3G01480.1	2.45	4.03E-02
170	AT5G62350.1	2.45	1.27E-02
171	AT2G42130.3	2.44	3.70E-02
172	AT3G14310.1	2.38	1.07E-02
173	AT2G45180.1	2.37	2.70E-02
174	AT2G42590.1	2.35	3.72E-02
175	AT3G08940.2	2.34	1.65E-02

176	AT5G07090.1	2.34	4.73E-02
177	AT1G02560.1	2.34	2.83E-02
178	AT4G09800.1	2.32	3.59E-02
179	AT4G33510.1	2.3	9.90E-03
180	AT1G18080.1	2.29	2.09E-02
181	AT2G25450.1	2.29	1.43E-02
182	ATCG00670.1	2.28	8.60E-03
183	AT3G20820.1	2.28	6.11E-03
184	AT4G39640.2	2.28	5.04E-03
185	AT4G35000.1	2.27	2.88E-02
186	AT1G53750.1	2.23	2.43E-02
187	AT5G50850.1	2.21	1.08E-02
188	ATCG01300.1	2.18	2.79E-02
189	AT3G09440.4	2.17	1.67E-02
190	AT4G21650.1	2.16	4.69E-02
191	AT5G66420.2	2.13	2.12E-02
192	AT4G05530.1	2.13	3.66E-02
193	AT1G18500.1	2.11	4.68E-02
194	AT3G54210.1	2.09	1.95E-02
195	AT5G40950.1	2.08	4.98E-02
196	AT5G56010.1	2.07	3.73E-02
197	AT1G09130.3	2.07	4.22E-02
198	ATCG00680.1	2.07	2.41E-02
199	AT5G20890.1	2.06	2.52E-03
200	AT1G33140.1	2.06	3.56E-02
201	AT3G04840.1	2.05	1.17E-02
202	AT3G54900.1	2.05	2.07E-02
203	AT4G39960.2	2.03	4.75E-02
204	AT1G12900.5	2.02	1.89E-02
205	AT1G13440.1	2.02	1.21E-02
206	AT3G46970.1	2.02	2.03E-02
207	AT1G23740.1	2.01	4.69E-02
208	AT4G00570.1	2.01	2.23E-02
209	AT4G11150.1	2.01	1.40E-02

Table S3: GO-Term enrichment analysis of transcripts downregulated in *aminaa50* #13.6. The significantly (>2-FC, p<0.05) downregulated transcripts as identified in Fig. 28 were subjected to a GO-Term enrichment analysis with the DAVID functional annotation tool v.6.8.

GO Term	Count	p-value	fold enrichment
response to jasmonic acid	21	1.14E-15	11.80
response to wounding	17	1.08E-09	7.49
response to gibberellin	8	1.35E-04	7.08
regulation of growth	7	1.03E-03	6.08
response to chitin	9	1.41E-04	5.93
auxin-activated signaling pathway	12	1.15E-05	5.54
circadian rhythm	6	4.98E-03	5.42
unidimensional cell growth	6	9.73E-03	4.61
response to auxin	15	6.07E-06	4.53
response to bacterium	5	2.90E-02	4.30
ethylene-activated signaling pathway	7	1.66E-02	3.43
response to abscisic acid	15	1.72E-04	3.34
abscisic acid-activated signaling pathway	7	2.41E-02	3.15
response to salt stress	14	3.66E-03	2.54
multicellular organism development	10	3.17E-02	2.28
defense response to fungus	12	1.74E-02	2.27
transcription, DNA-templated	48	1.64E-07	2.23

Table S4: GO-Term enrichment analysis of transcripts upregulated in *aminaa50* #13.6. The significantly (>2-FC, p<0.05) upregulated transcripts as identified in Fig. 28 were subjected to a GO-Term enrichment analysis with the DAVID functional annotation tool v.6.8

GO Term	Count	p-value	fold enrichment
response to mechanical stimulus	5	6.35E-05	20.19
response to chitin	38	4.18E-27	10.38
trehalose metabolism in response to stress	5	2.32E-03	8.65
response to brassinosteroid	8	3.19E-05	8.55
xyloglucan metabolic process	9	1.59E-05	7.79
defense response, incompatible interaction	5	4.50E-03	7.27
trehalose biosynthetic process	5	4.50E-03	7.27
regulation of proteolysis	7	4.02E-04	7.07
cellular response to hypoxia	5	5.20E-03	6.99
response to absence of light	5	5.20E-03	6.99
cell wall biogenesis	11	4.91E-06	6.66
polysaccharide biosynthetic process	5	6.82E-03	6.49
pectin biosynthetic process	5	1.10E-02	5.68
plant-type hypersensitive response	11	3.32E-05	5.4
response to bacterium	14	4.36E-06	4.99
defense response to virus	5	1.98E-02	4.78
response to hydrogen peroxide	7	3.52E-03	4.71
response to salicylic acid	20	5.27E-08	4.69
glucosinolate metabolic process	5	2.16E-02	4.66
response to fungus	9	7.84E-04	4.54
hexose transmembrane transport	5	2.55E-02	4.43
response to wounding	24	6.57E-09	4.38
vesicle docking involved in exocytosis	5	2.76E-02	4.33
cell death	5	3.21E-02	4.13
glucose import	5	3.70E-02	3.95
regulation of defense response	7	8.76E-03	3.91
carbohydrate biosynthetic process	5	3.96E-02	3.87
brassinosteroid mediated signaling pathway	6	2.27E-02	3.7
abscisic acid-activated signaling pathway	19	7.60E-06	3.54

protein autophosphorylation	13	3.51E-04	3.5
response to jasmonic acid	13	1.27E-03	3.03
response to osmotic stress	10	6.52E-03	2.98
cell wall organization	25	6.74E-06	2.89
ethylene-activated signaling pathway	14	1.37E-03	2.84
leaf senescence	7	4.10E-02	2.77
defense response	46	1.87E-08	2.54
signal transduction	31	7.76E-06	2.5
response to cold	20	6.41E-04	2.43
response to abscisic acid	26	9.77E-05	2.4
response to water deprivation	18	1.91E-03	2.34
response to auxin	18	2.85E-03	2.26
response to oxidative stress	18	2.99E-03	2.25

Table S5: Proteins exclusively detected in wildtype protein extracts. A global mass-spectrometry analysis (4.7.3) of proteins extracted from leaves of seven-week-old soil-grown wildtype and *aminaa50* #13.6 plants revealed that apart from NAA50, 15 proteins were detected in all of the wildtype but none of the *aminaa50* #13.6 protein extracts (n=4).

Identifier	Symbol	N-terminus	Putative modifying Nat
AT1G12360.1	SEC11	MSYS	NatA
AT1G20340.1	PETE2	MASV	NatA
AT1G23180.1	-	MSLS	NatA
AT2G17280.1	-	MDNE	NatB
AT2G33470.1	GLTP1	MEGT	NatB
AT2G43235.1	-	MNMT	NatB
AT3G55630.3	DFD	MATE	NatA
AT4G01080.1	TBL26	MEQQ	NatB
AT4G34570.1	THY-2	MRCL	non-acetylated
AT5G06120.1	XPO7	MQNS	NatB
AT5G06160.1	ATO	MSST	NatA
AT5G35180.4	-	MTSP	NatA
AT5G58440.1	SNX2a	MMGS	NatC/E/F
AT5G63180.1	-	MFRP	NatC/E/F
AT5G63190.1	-	MASG	NatA

Table S6: Primers used for cloning in this thesis.

#	Name	Sequence
849	pRS300-A	ctgcaaggcgattaagttcggtaac
850	pRS300-B	gcggataacaatttcacacaggaaacag
4687	KpnI_SMC3_fwd	gcatggtaccatgtttatcaagcaggttataatcgaag
4726	NAA50_miRNA_1	gatgtcattatataaactcgccttctctctttgtattcc
4727	NAA50_miRNA_2	gaaggcgagtttatataatgacatcaaagagaatcaatga
4728	NAA50_miRNA_3	gaagacgagtttataaaatgacttcacaggtcgtgatatg
4729	NAA50_miRNA_4	gaagtcattttataaactcgtcttctacatatatattcct
4864	EYFP_SalI_rev	ccatgtcgacttacttgtacagctcgtccatg
4865	KpnI_NLS_f	atgcggtaccgtcgacatggaagagcaagc
4866	NLS_BamHI_r	gcatggatccagcaattgctgcggcagcc
4867	BamHI_NAA50_f	attgctggatccatgggagctgggagagaag
4868	NAA50_Sal_r	gcatgtcgactcatttgttggcttcagattgagcaaag

4876	KpnI_NES_f	tgcaggtaccatgctgcagaacgagcttgctcttaag- ttggctggacttgatattaacaagactggaggactgc- agaacgagcttgctcttaagttggctggac
4877	NES_BamHI_r	tcgtggatcctcctccagtcttgttaatatcaagtccag- ccaacttaagagcaagctcgttctgcagtcctccagtc- ttgttaatatcaagtccagccaacttaagagcaag
4948	HYPK_cLuc_f	ctagggtaccgagggagcagaggaagctg
4949	HYPK_cLuc_r	gatagtcgactcatagaggatatcgtgaaagcaatt
4950	HYPK_nLuc_f	ctagggtaccatggagggagcagaggaag
4951	HYPK_nLuc_r	gatagtcgactagaggatatcgtgaaagcaattg
4952	NAA10_cLuc_f	ctatggtaccgtttgcatcaggcgagcga
4953	NAA10_cLuc_r	gtaagtcgacctatttggaaactgctttaccatc
4954	NAA10_nLuc_f	ctatggtaccatggtttgcatcaggcgagc
4955	NAA10_nLuc_r	gtaagtcgactttggaaactgctttaccatctac
4956	NAA15_cLuc_f	ctagggtaccggggcttcgcttcctcc
4957	NAA15_cLuc_r	gattgtcgacttatatagaaaaacaattatacacatttgg
4958	NAA15_nLuc_f	ctagggtaccatgggggcttcgcttcctc
4959	NAA15_nLuc_r	gattgtcgactatagaaaaacaattatacacatttggcat
4960	NAA50_cLuc_f	tatcggtaccggagctgggagagaagtcag
4961	NAA50_cLuc_r	gatcgtcgactcatttgttggcttcagattgagc
4962	NAA50_nLuc_f	tatcggtaccatgggagctgggagagaag
4963	NAA50_nLuc_r	gatcgtcgactttgttggcttcagattgagcaa
4995	XhoI_linker_SYN4_f	ctatctcgagggtgcgtcagagaacctctatttcc- aaggtgagttagagcttggggccggtgggagtg- agcttgaaaacctctacttccaggggcatctttt- tattcgcagtttatatt
4996	SMC3_linker_XhoI_r	caccctcgagatagagattttctcgtgccctagtac- ctcccgccccagatccggcaccagaaccacctg- ctccggtatcgtgggactgatctttc
4997	SYN4_SalI_r	gactgtcgacctagaagatggatttgg
5204	NAA15_cLuc_r	gattgtcgacctagaggctcttgaatgcttcgag
5205	NAA15_nLuc_r	gattgtcgacgaggctcttgaatgcttcgag
5206	NAA50_Y53T_C58A_V59A_r	ccccactttctttcttctccagccgacaggcgat- agctccagcagctatgtcattgtaagttgc
5207	NAA50_Y87T_f	ggagaagaaagaaagtggggccatgcgagtt- atataatgacgcttggtgttcttgcacccactcgtggg

5208	NAA50_Y53T_C58A_V59A_-nLuc_f	ctctgactccatctagcgatacgctgacttctctccca-gctcccatggtaccgata
5209	NAA50_Y87_T_nLuc_r	gatcgtcgactttgttggcttcagattgagcaaaggac-ttgctgacaacgtagcaatctcttggctc
5210	NAA50_Y53T_C58A_V59A_-cLuc_f	tatcggtaccggagctgggagagaagtcagcgtatc-gctagatggagtcagagacaaaaac
5211	NAA50_Y87T_cLuc_r	gatcgtcgactcatttgttggcttcagattgagcaaag-gacttgctgacaacgtagcaatctcttggc
5212	NAA50_S10A_D56A_nLuc_f	tatcggtaccatgggagctgggagagaagtcagcgt-agcgctagatgg
5213	NAA50_S10A_D56A_r	cccactttctttcttctccagccgacaggcgatagctcc-aacacatatggcattgtaatatg
5214	NAA50_2nd_f	ctggagaagaaagaaagtggg
5215	NAA50_S10A_D56A_cLuc_f	tatcggtaccggagctgggagagaagtcagcgtagc-gctagatgg
5317	NAA50_Y53T_D56A_C58A_-V59A_r	ccccactttctttcttctccagccgacaggcgatagctc-cagcagctatggcattgtaagttgc

7.1 Supplementary Tables

Table S7: Primers used for genotyping in this thesis.

#	Name	Sequence
321	SAIL_LB3	tagcatctgaatttcataaccaatctcgatacac
603	N843868_LP	tcacttttgtgaaacccttgg
604	N843868_RP	aacaagcaaaactcggaaacc
645	N844130_LP	gaccaacatttacaaacacgatg
646	N844130_RP	aatggattgacttcctctcagc
3166	aminaa10_r	cgtcgcatcgttggctatgta
3915	35S_f	acaatcccactatccttcgc
4661	SYN4_r	tagaagatggatttggtgagctttgg
4662	SMC3_f	atgtttatcaagcaggttataatcgaagg
4839	aminaa50_r	ccatggcgatgccttaaataaag
5446	Linker_f	cgggaggtactagggcac
5447	Linker_r	gtgccctagtacctcccg

Table S8: Primers used for qRT-PCR in this thesis.

#	Name	Sequence
2359	NAA10_f	cggtctcgccactaagctc
2360	NAA10_r	ctcggttacttctcctcacat
2457	TIP41_f	gatgaggcaccaactgttcttcgtg
2458	TIP41_r	ctgactgatggagctcgggtcg
2459	PP2A_f	cttctcgctccagtaatgggatcc
2460	PP2A_r	gcttggtcgactatcggaatgagag
2641	NAA50_f	tacgccgatgcaatcgctgc
2642	NAA50_r	tacgccgatgcaatcgctgc
2697	NAA15_f	gcttgcattccaggctgtc
2698	NAA15_r	cttatcgattctgtcatgagaaag
2881	RD21B_f	cagtggtgtatctaattatcagtc
2882	RD21B_r	tttcattctaccaagagactcag
3508	CHS_f	cgtgttgagcgagtatggaaac
3509	CHS_r	tgacttcctcctcatctcgtctagt
3854	HYPK_f	gatctgaatgctaagaggttgag
3855	HYPK_r	ccttagagttctttccgccac
5388	PBA1_f	ggagccgactcacgtacc
5389	PBA1_r	gaaggaagtagcggacatag

7.2 Supplementary Figures

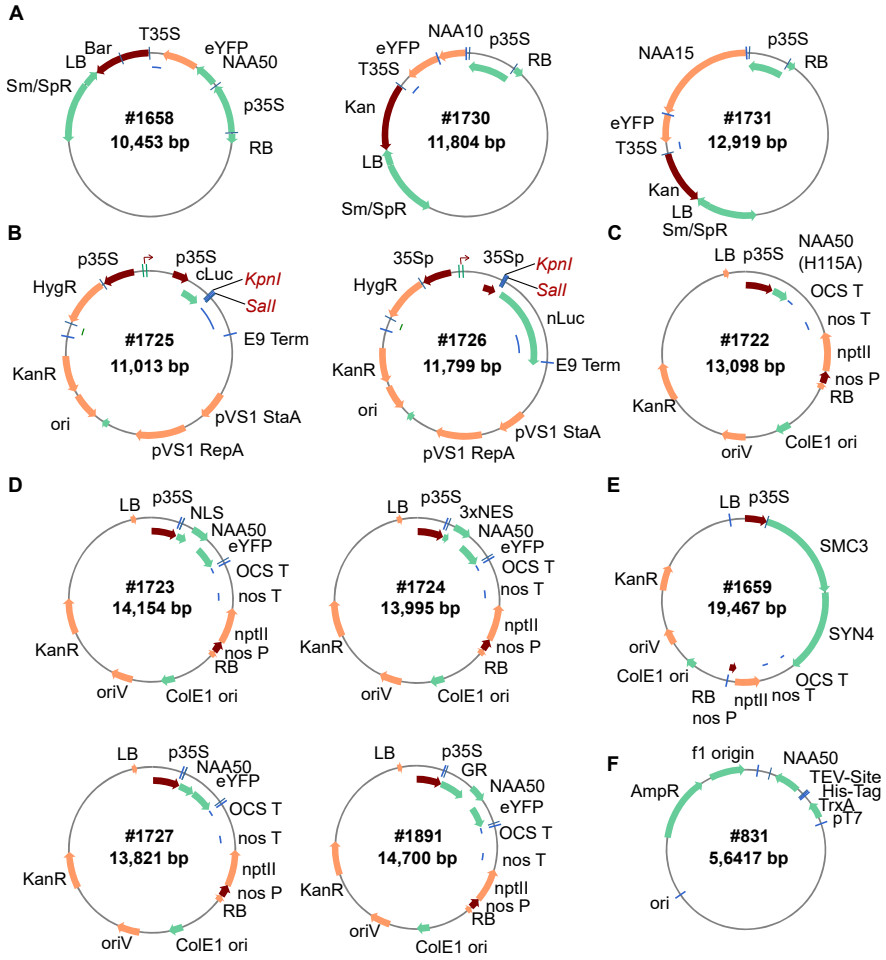

Figure S1: Maps of vectors described in this thesis. **(A)** Constructs used to determine the subcellular localization of NAA10, NAA15 and NAA50. **(B)** Empty CLuc and NLuc constructs for luciferase split assays. **(C)** Construct for the expression of a NAA50 variant with diminished enzymatic activity in plants. **(D)** Constructs for the complementation of *naa50* knockout mutants with NAA50 versions localizing exclusively to the nucleus, the cytoplasm or both. **(E)** Construct for the complementation of *naa50* knockout mutants with an SMC3-SYN4 fusion protein. **(D)** Construct for the expression of NAA50 in *E. coli* (#831).

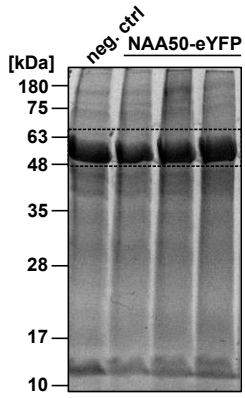

Figure S2: Coomassie stained SDS-PAGE showing protein extracts of *N. benthamiana* plants which transiently express *At*NAA50-eYFP. Proteins were extracted with modified RIPA-buffer (Zhang et al., 2018). An untransformed plant served as negative control (neg. ctrl.). The dotted lines indicate the fraction of the membrane which was shown in the main body of the thesis.

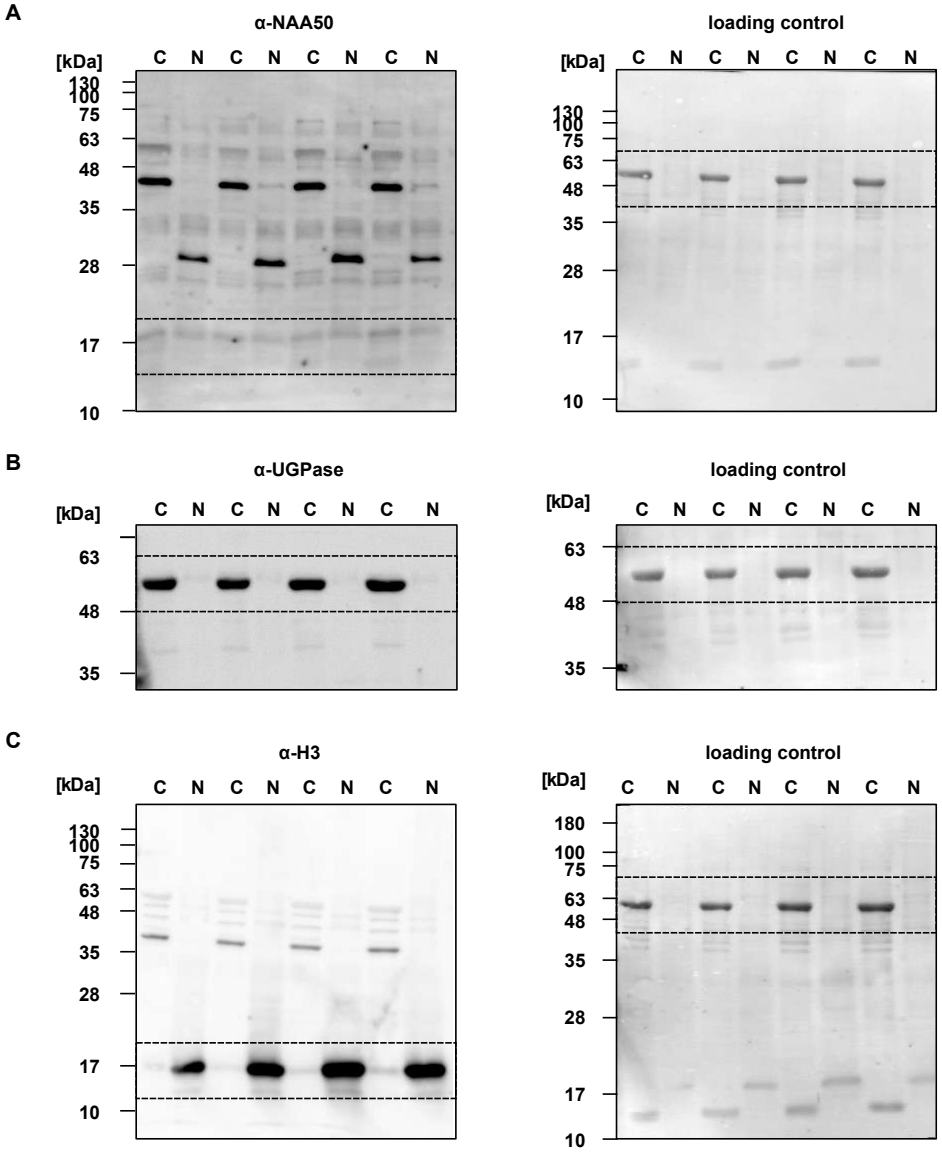

Figure S3: *At*NAA50 localizes to the nucleus in wildtype plants. Col-0 wildtype plants were grown on soil for eight weeks under short day conditions. Subsequently, proteins were extracted from 1.5 g of leaf material. The protein extracts were separated into cytosolic (C) and nuclear (N) fractions (4.5.3). **(A)** The NAA50 protein was detected with a specific antiserum. **(B)** UDP-glucosepyrophosphorylase (UGPase) and **(C)** Histon3 (H3) were used as markers for the cytosolic and nuclear fraction respectively. The dotted lines indicate fractions of the membranes which were shown in the main body of the thesis. Amido black stainings of the membranes (right panel) serve as loading controls (LC).

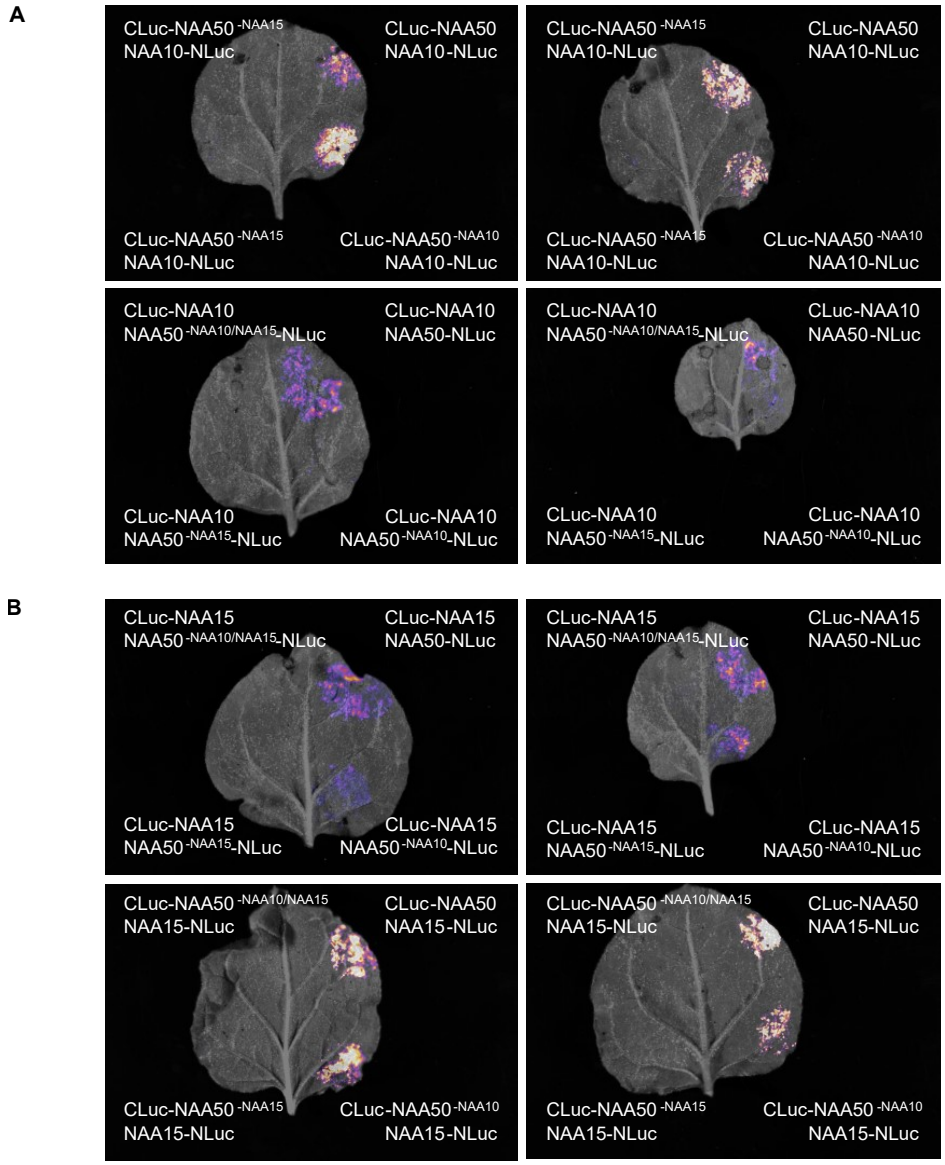

Figure S4: Repetitions of luciferase complementation assay to assess the interactions between putative *At*NatA/E subunits. *N. benthamiana* leaves were transformed with different luciferase split constructs (4.5.11). **(A)** Interaction between *At*NAA10 and *At*NAA50. **(B)** Interaction between *At*NAA15 and *At*NAA50.

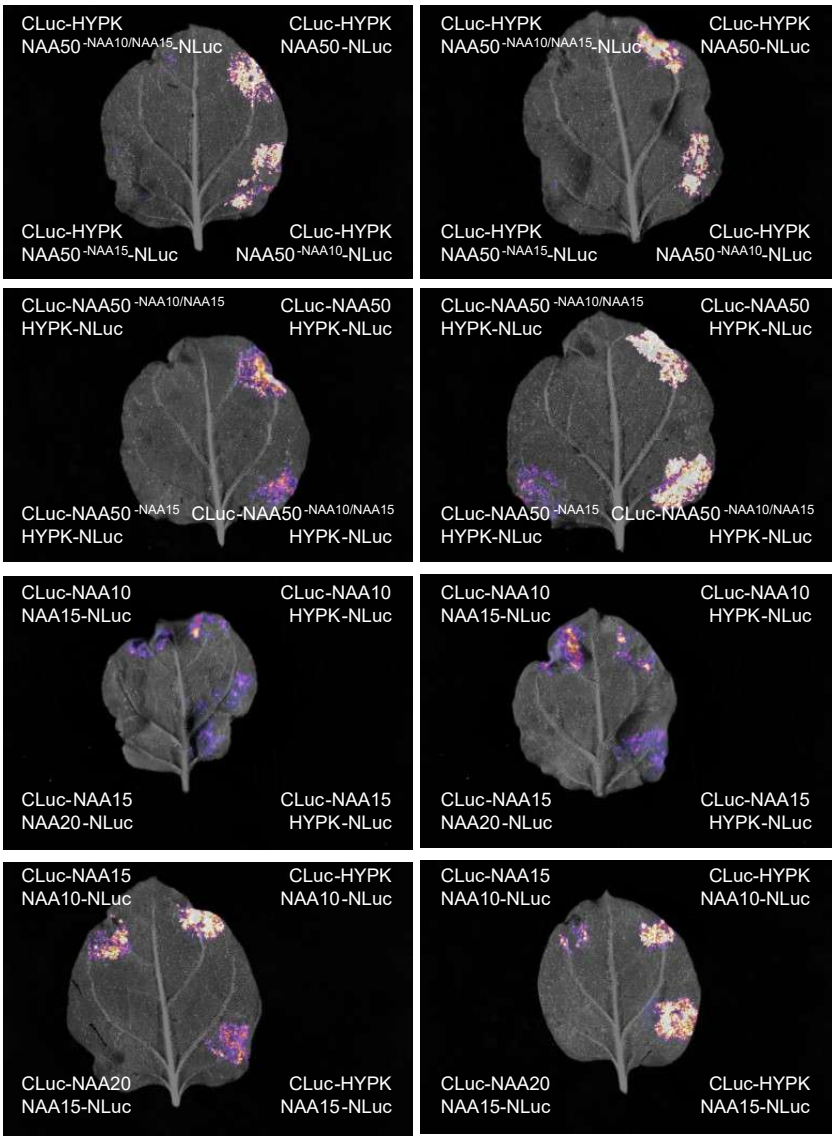

Figure S5: Repetitions of luciferase complementation assay to assess the interactions between putative *At*NatA/E subunits. *N. benthamiana* leaves were transformed with different luciferase split constructs (4.5.11). Interaction between *At*HYPK and *At*NAA50.

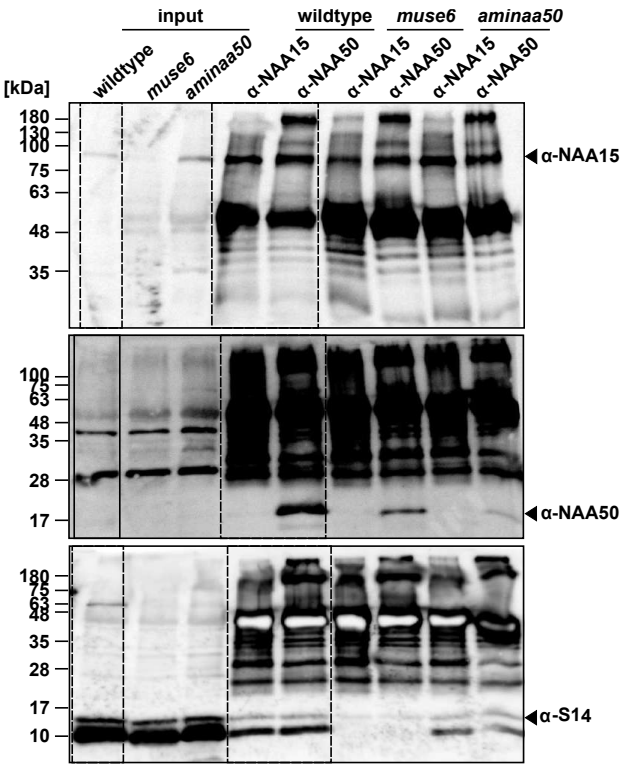

Figure S6: Immunoprecipitation of NatA/E subunits. Protein extracts of six-week-old soil-grown (4.3.2) wildtype, *muse6* and *aminaa50* #13.6 plants were incubated with antibodies against *At*NAA15 or *At*NAA50 (Tab. 18). Subsequently, the antibodies and the proteins which interacted with them were captured with protein A/G beads (4.5.4) and separated by SDS-PAGE (4.5.8). The proteins which co-precipitated with the antibodies were detected with specific antisera against *At*NAA15, *At*NAA50 and the 40S ribosomal subunit S14 (Tab. 18). The dotted lines indicate fractions of the membranes which were shown in the main body of the thesis.

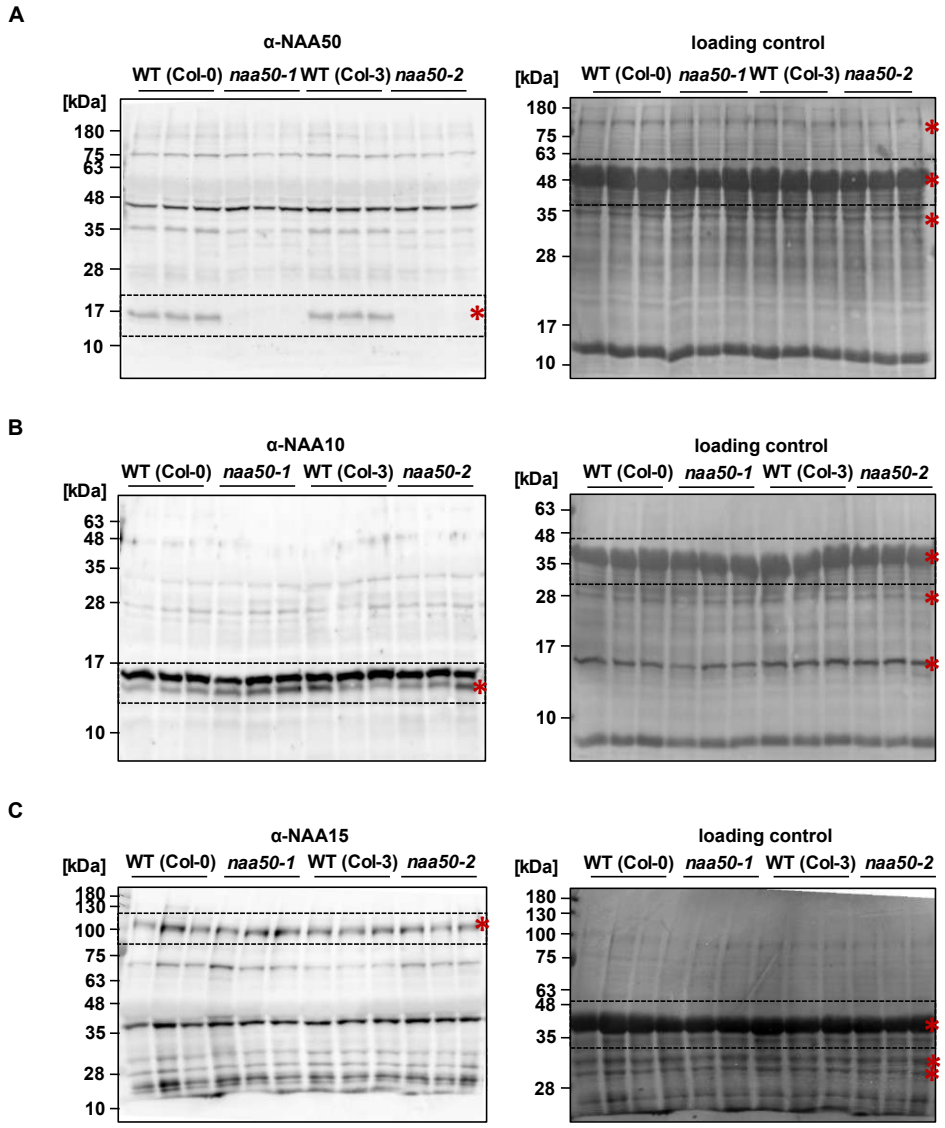

Figure S7: Knockout of *NAA50* does not impact the abundance of other *At*NatA/E subunits on the protein level. Protein levels of **(A)** NAA50, **(B)** NAA10 and **(C)** NAA15 were determined with specific antisera (4.5.10) in four-week-old *naa50* mutants and wildtype plants cultivated on 1/2 MS plates under short-day conditions. The dotted lines indicate fractions of the membranes which were shown in the main body of the thesis. Asterisks indicate bands which were used for quantification and normalization. Amido black stainings of the membranes (right panel) served as loading controls (LC).

A

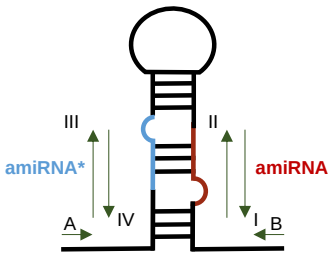

C

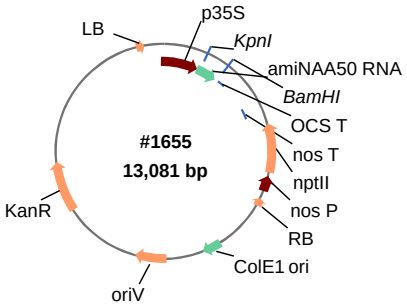

B

amiRNA			primer sequence
amiNAA50	I	#4726	gaTGTCATTATATAAACTCGCCT tctctcttttgtattcc
	II	#4727	gaAGGCGAGTTTATATAATGACA tcaaagagaatcaatga
	III	#4728	gaAGACGAGTTTATAAAATGACT tcacaggtcgtgatatg
	IV	#4729	gaAGTCATTTTATAAACTCGTCT tctacatatattcct
pRS3000	A	#849	CTGCAAGGCGATTAAGTTCGGTAAC
	B	#850	GCGGATAACAATTTCACACAGGAAACAG

Figure S8: Generation of a *NAA50* amiRNA precursor. **(A)** Schematic representation of amiRNA with primer binding sites. **(B)** Vector map of the pBinAR-aminaa50 construct (#1655). **(C)** Primer sequences for the generation of the NAA50 amiRNA. The amiRNA and amiRNA* coding regions are marked in red and blue respectively.

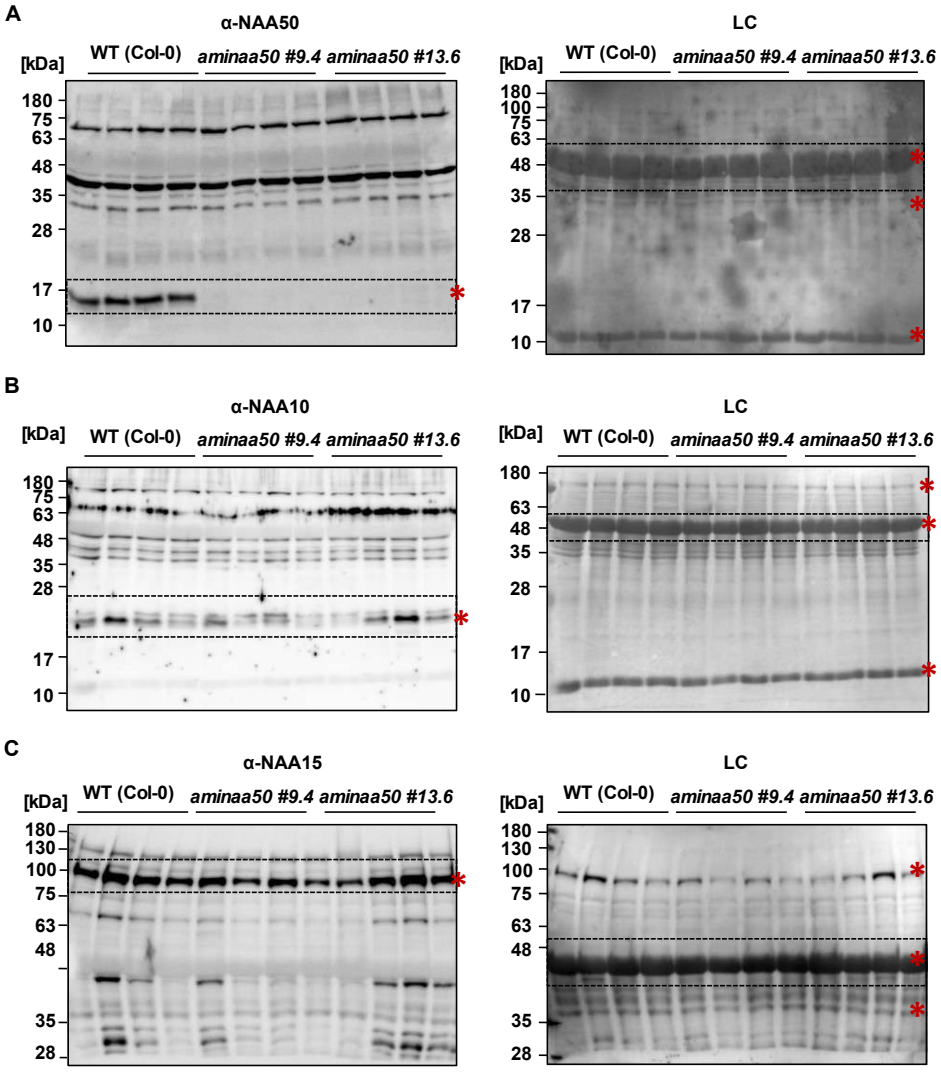

Figure S9: Knockdown of *NAA50* does not impact the abundance of other *At*NatA/E subunits on the protein level. Protein levels of **(A)** NAA50, **(B)** NAA10 and **(C)** NAA15 were determined with specific antisera (4.5.10) in eight-week-old *aminaa50* mutants and wildtype plants cultivated on soil under short-day conditions. The dotted lines indicate fractions of the membranes which were shown in the main body of the thesis. Asterisks indicate bands which were used for quantification and normalization. Amido black stainings of the membranes (right panel) served as loading controls (LC).

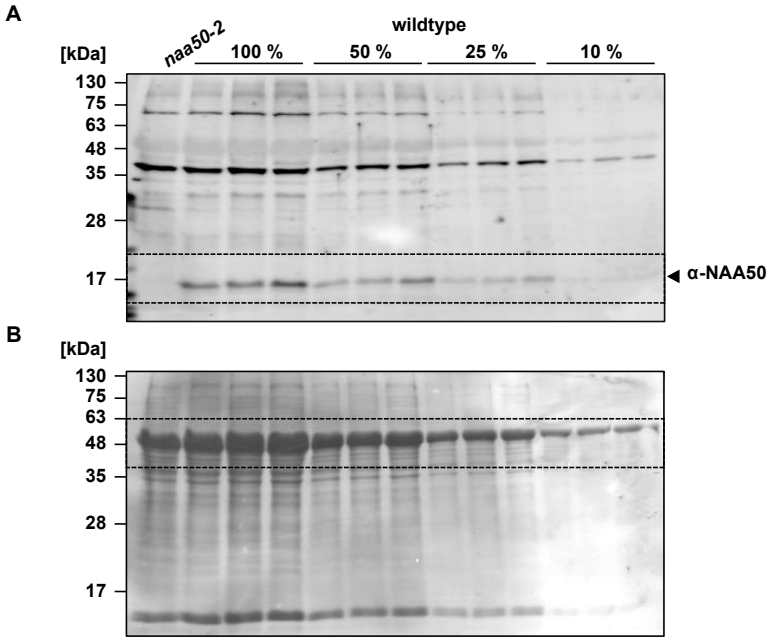

Figure S10: Detection limit of the specific antiserum against *At*NAA50. **(A)** Proteins were extracted from *naa50-2* and wildtype (n=3) plants. Starting from 30 µg of crude extract (= 100 %) dilutions were prepared. The *At*NAA50 level was detected with a specific antiserum (diluted 1:2.500 in TBS-T supplemented with 0.5 % BSA, 3 h incubation at RT). The dotted lines indicate fractions of the membranes which were shown in the main body of the thesis. **(B)** An Amido black staining of the membrane (lower panel) served as loading control (LC).

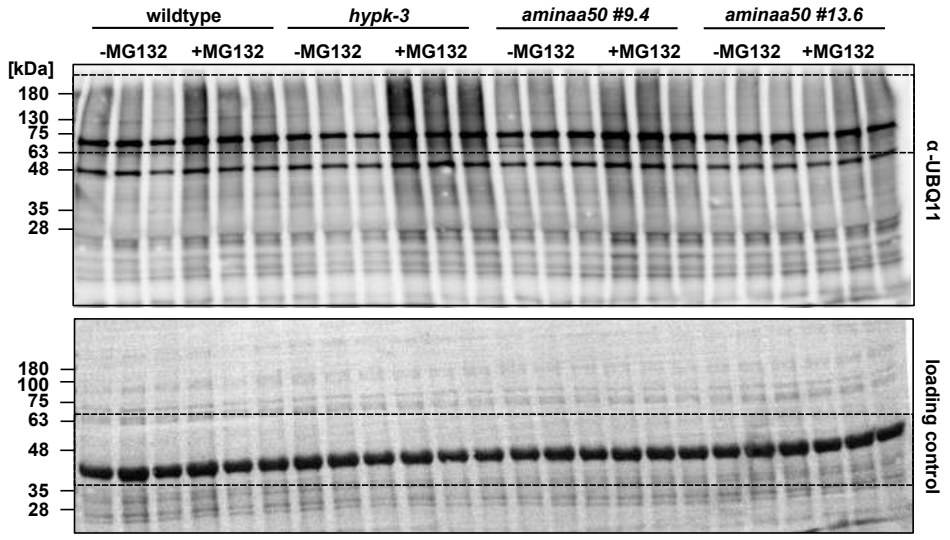

Figure S11: Accumulation of polyubiquitinylated proteins in *hypk-3*. Leaf discs of seven-week-old soil grown plants were incubated in 1/2 Hoagland medium (4.1.2) supplemented with 50 μM of the proteasome inhibitor. After 24 h, proteins were extracted from the leaf discs (4.5.1), loaded on an SDS-PAGE gel (4.5.8) and blotted onto a PVDF membrane (4.5.10). Polyubiquitinylated proteins were detected with a specific antiserum (diluted 1:5.000 in TBS-T supplemented with 0.5 % BSA, 1.5 h incubation at room temperature). The dotted lines indicate fractions of the membranes which were shown in the main body of the thesis. **(B)** An Amido black staining of the membrane (lower panel) served as loading control (LC).

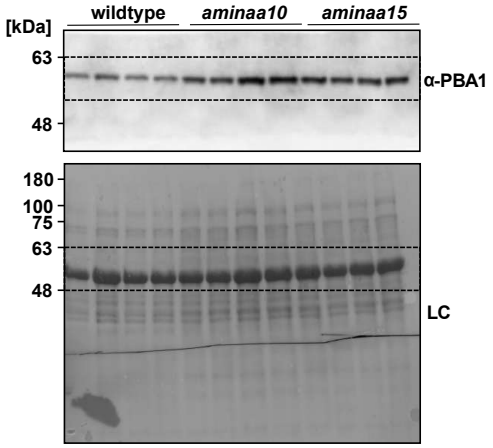

Figure S12: Expression of the 20S proteasome subunit PBA1. (A) Proteins were extracted (4.5.1) from leaves of six-week-old plants grown on soil (4.3.2) under short day conditions, separated by SDS-PAGE (4.5.8) and transferred onto a PVDF membrane (4.5.10) where PBA1 was detected with a specific antiserum (Tab. 18). An Amido black staining of the membrane served as loading control (LC). The dotted lines indicate fractions of the membranes which were shown in the main body of the thesis.

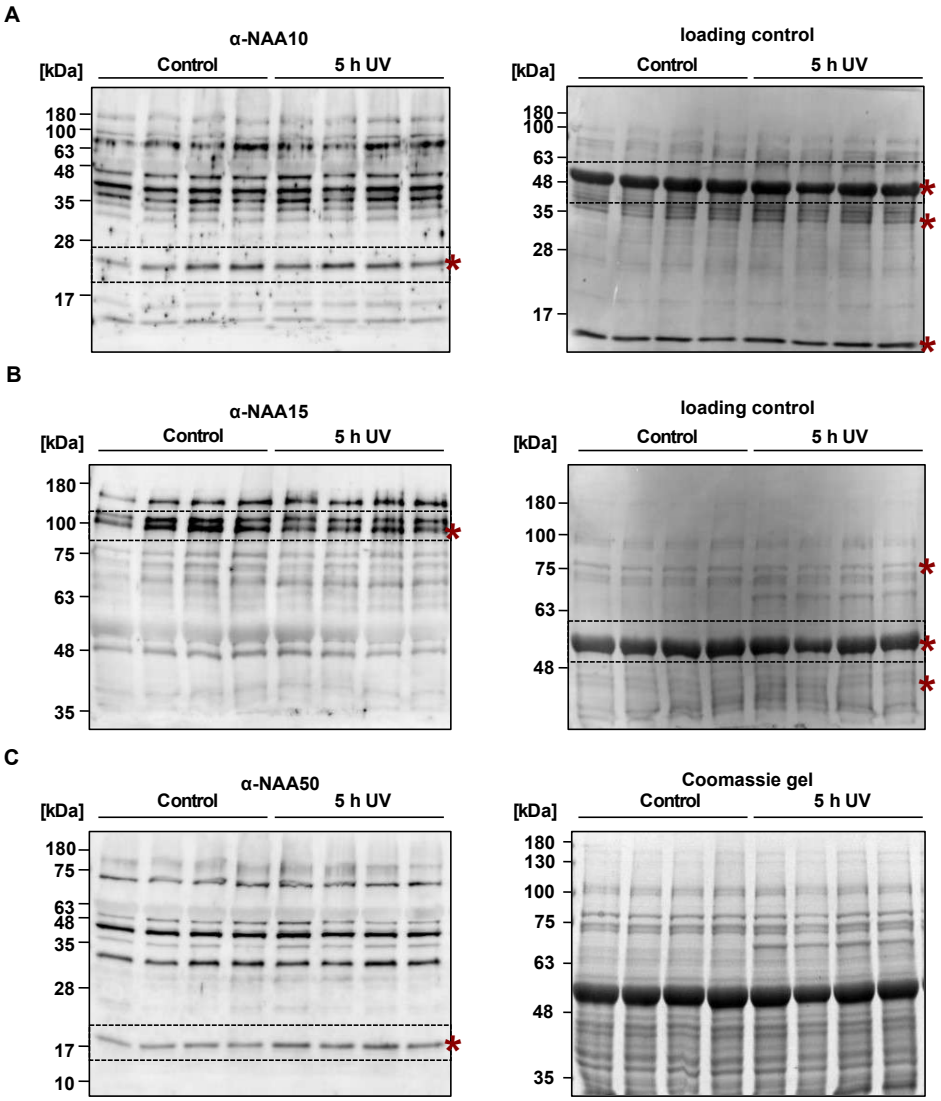

Figure S13: NatA/E subunits accumulate upon UV-B treatment. Proteins were extracted (4.5.1) from eight-week-old soil-grown (4.3.2) plants treated for 5 h with UV-B light (4.3.12). Subsequently, protein levels of **(A)** NAA10, **(B)** NAA15 and **(C)** NAA50 were determined with specific antisera. The dotted lines indicate fractions of the membranes which were shown in the main body of the thesis. Asterisks indicate bands which were used for quantification and normalization. Amido black stainings of the membranes (right panel) served as loading controls (LC). Since the membrane where NAA10 was detected was stripped for the detection of NAA50, only one Amido black staining is available and was used as loading control for both membranes.

Figure S14: Control plants for drought stress experiment. To address whether NAA50 as a component of the NatA/E complex was involved in the drought stress response, plants were grown on soil for six weeks under short-day conditions (4.3.2) and subsequently exposed to 19 days of drought (4.3.10). The control plants displayed above were watered further. The drought stressed plants are displayed in Fig. S15. During this experiment, the physical appearance of the plants was monitored. To account for the difference in size between the wildtype-like *aminaa50* plants and *hypk-3*, eight-week-old *hypk-3* plants were included.

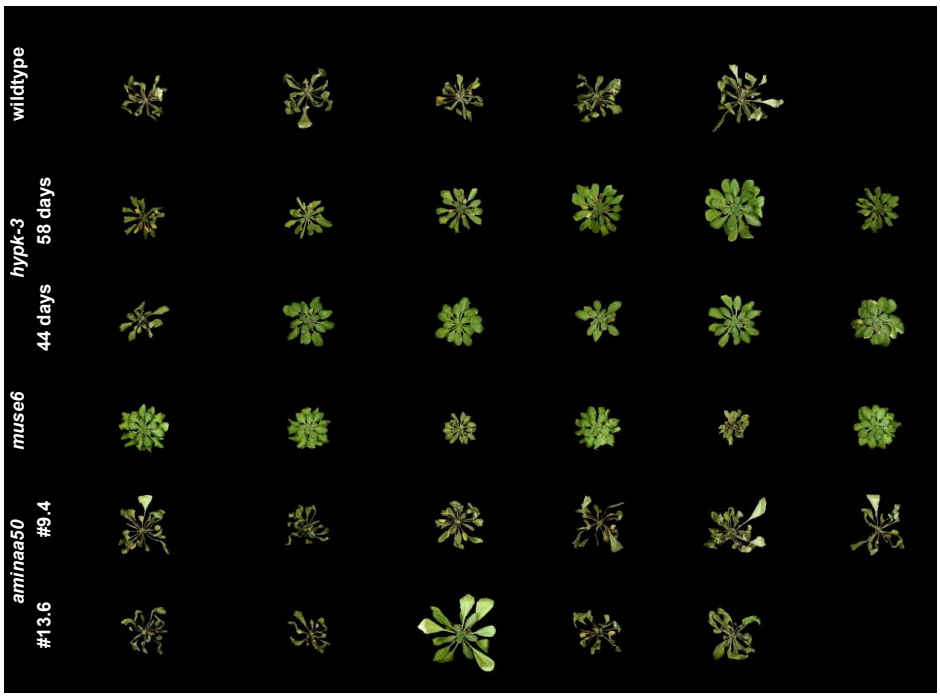

Figure S15: Drought stressed plants. To address whether NAA50 as a component of the NatA/E complex was involved in the drought stress response, plants were grown on soil for six weeks under short-day conditions (4.3.2) and subsequently exposed to 19 days of drought (4.3.10). The control plants displayed in Fig. S14 were watered further. During this experiment, the physical appearance of the plants was monitored. To account for the difference in size between the wildtype-like *aminaa50* plants and *hypk-3*, eight-week-old *hypk-3* plants were included.

```
AtNAA50   MGAGREVSVSLDGVRDKNLMQLKILNTVLFPVRYNDKYYADAIAA--------------- 45
HsNAA50   ---MKGSRIELGDVTPHNIKQLKRLNQVIFPVSYNDKFYKDVLEV--------------- 42
ScNAA50   ---MGRDICTLDNVYANNLGMLTKLAHVTVPNLYQDAFFSALFAEDSLVAKNKKPSSKKD 57

AtNAA50   GEFTKLAYYNDICVGAIACRLEKKESGA---MRVYIMTLGVLAPYRGIGIGSNLLNHVLD 102
HsNAA50   GELAKLAYFNDIAVGAVCCRVDHSQ-NQ---KRLYIMTLGCLAPYRRLGIGTKMLNHVLN 98
ScNAA50   VHFTQMAYYSEIPVGGLVAKLVPKKQNELSLKGIQIEFLGVLPNYRHKSIGSKLLKFAED 117

AtNAA50   MCSKQN-MCEIYLHVQTNNEDAIKFYKKFGFEITDTIQNYYI-NIE--PRDCYVVSKSFA 158
HsNAA50   ICEKDGTFDNIYLHVQISNESAIDFYRKFGFEIIETKKNYYK-RIE--PADAHVLQKNLK 155
ScNAA50   KCSECH-QHNVFVYLPAVDDLTKQWFIAHGFEQVGETVNNFIKGVNGDEQDAILLKKHIS 176

AtNAA50   QSEANK-------- 164
HsNAA50   VPSGQNADVQKTDN 169
Sc        -------------- 176
```

Figure S16: Alignment between NAA50 homologs from different species. Alignment of *At*NAA50 (Q9LFM3), *Hs*NAA50 (Q9GZZ1) and *Sc*NAA50 (Q08689) protein sequences with Clustal Omega. The catalytic residues which are conserved between human and Arabidopsis, but not yeast, are shaded in red.